

Important Notice

This copy may be used only for the purposes of research and private study, and any use of the copy for a purpose other than research or private study may require the authorization of the copyright owner of the work in question. Responsibility regarding questions of copyright that may arise in the use of this copy is assumed by the recipient.

THE UNIVERSITY OF CALGARY

**P- AND S-WAVE SEPARATION USING THREE-
COMPONENT MODAL FILTERS**

by

Maria Silvia Donati

A THESIS

**SUBMITTED TO THE FACULTY OF GRADUATE STUDIES
IN PARTIAL FULFILLMENT OF THE REQUIREMENTS FOR THE
DEGREE OF MASTER OF SCIENCE**

DEPARTMENT OF GEOLOGY AND GEOPHYSICS

CALGARY, ALBERTA

JUNE, 1996

©Maria S. Donati 1996

THE UNIVERSITY OF CALGARY
FACULTY OF GRADUATE STUDIES

The undersigned certify that they have read, and recommend to the Faculty of Graduate Studies for acceptance, a thesis entitled "P- and S- Wave Separation Using Three-Component Modal Filters " submitted by Maria Silvia Donati in partial fulfilment of the requirements for the degree of Master of Science.



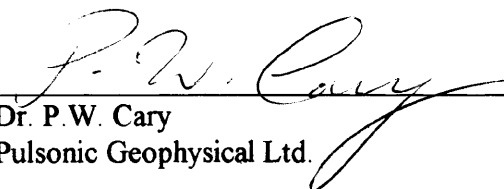
Supervisor, Dr. R.R. Stewart
Department of Geology and Geophysics



Dr. G. Margrave
Department of Geology and Geophysics



Dr. E.S. Krebs
Department of Geology and Geophysics



Dr. P.W. Cary
Pulsonic Geophysical Ltd.

July 11, 1996

Date

ABSTRACT

Separation of individual P and S arrivals is often a problem on three-component seismic data since P and S data are recorded on both the vertical and horizontal geophones. Due to the intrinsic response of an elastic interface, P and S waves are observed on vertical and radial geophones. A method of separating P and S waves in the τ - p domain is presented which inverts the three-component records using the interface (or geophone) responses, thereby separating the two wavetypes. The P - S modal filter coefficients in the 2-D case are calculated from the geophone responses and the near-surface P and S wave velocities V_p and V_s .

For the 3C-2D case we consider two types of data: one acquired locating the geophone on the surface (free-surface case) and a second one considering the geophones located in the liquid-solid contact. For both cases, the geophone responses of the vertical and radial geophones are different but the modal filter method is unchanged. The P - S separation is tested using synthetic and real data showing that it is capable of separating pure P , S and converted reflections. It also appears to have low sensitivity to errors in the near-surface P and S wave velocity and to noise in the data.

Two different approaches to the 2-D τ - p transform used in the modal filter are used: the slant stack algorithm proposed by Stoffa et al. (1981) developed in the x - t domain, and the method proposed by Wade and Gardner (1988) which works in the f - k domain. It is found that the second method provides a faster, cleaner and easier way to perform τ - p filtering of seismic data than Stoffa's method.

A 3-D τ - p transform is also developed. No geometric symmetry is assumed. The 3-D τ - p transform is tested using synthetic data which includes P and converted waves, with and without random noise and ground roll added. The 3-D τ - p transform appears to

perform well by reconstructing the original data and attenuating the noise and ground roll present in the data.

ACKNOWLEDGMENTS

This thesis would not have been possible without the help of many others. My husband, Nicolas, his continuous support, patient and enlightening discussions helped me in the moments of difficulty and frustration. MUCHAS GRACIAS NICO. My thanks to Dr. Robert Stewart for sharing his ideas and giving me the opportunity to participate in different activities and learn new technologies. My gratitude to Intevep S.A. (Venezuela) for their financial support and their confidence in my work. I want to express my gratitude to Corpoven S.A. and CREWES Project for providing the 3C-2D seismic data from Barinas (Venezuela) and Blackfoot (Alberta), respectively. Thanks to the Staff of the CREWES Project, specially to Henry Bland and Darren Foltinek for all their help particularly the days when the computer didn't want to cooperate with me. Louise Forgues and Regina Shedd for her continuous support and friendship. Special thanks to my mother, Maggiorina, for her words of support and encouragement. I would also like to acknowledge those companies which provided the software used in this work: SIERRA and Landmark (Promax 2D). I sincerely appreciate the contribution of all who have assisted.

TABLE OF CONTENTS

Approval Page.....	ii
Abstract.....	iii
Acknowledgments.....	v
Table of Contents.....	vi
List of Tables.....	viii
List of Figures.....	ix
Chapter 1.- Introduction.....	1
1.1 Background.....	1
1.2 The need for three-component recording in surface seismic.....	2
1.3 Thesis objective.....	3
1.4 Data sets used in the thesis.....	4
1.4.1 Synthetic surface data set.....	4
1.4.1.1 Free-surface solid P - S separation filter case.....	4
1.4.1.2 Liquid-solid P - S separation filter case.....	6
1.4.1.3 2-D τ - p case.....	6
1.4.1.4 3-D τ - p case.....	6
1.4.2 Field surface seismic data.....	9
1.4.2.1 Barinas, Venezuela.....	9
1.4.2.2 Blackfoot, Alberta.....	11
Chapter 2.- Modal separation of 3C-2D seismic data.....	16
2.1 Introduction.....	16
2.2 Theory.....	17
2.3 Expressions and characteristics of the geophone responses.....	19
2.4 Expressions and characteristics of the tau-p domain in 2-D domain.....	27
2.4.1 The (x,t) method - forward and inverse slant stack process.....	33
2.4.1.1 Construction of slant stack.....	33
2.4.1.2 Alias suppression by semblance windowing.....	35
2.4.1.3 Inverse.....	39
2.4.2 The (K,F) method - forward and inverse slant stack process.....	41
2.4.2.1 Interpolation process.....	47
2.5 Filter coefficients.....	52
2.5.1 Raw filter coefficients.....	52
2.5.2 Instabilities.....	54
2.5.3 Tapered filter coefficients.....	54
2.6 Application of the separation filter in the tau-p domain.....	58
2.6.1 Synthetic data.....	58
2.6.2 Real data.....	87
2.6.1 Barinas data.....	87
2.6.2 Blackfoot data.....	116
2.7 Discussion.....	147

Chapter 3.- Modal separation of 3C-2D subsea seismic data	154
3.1 Introduction	154
3.2 Theory	156
3.3 Geophone response definitions and characteristics	156
3.4 Filter coefficients	162
3.4.1 Raw filter coefficients	162
3.4.2 Instabilities	163
3.4.3 Tapered filter coefficients	164
3.5 Application of the filter in the tau-p domain	169
3.5.1 Synthetic application	169
3.6 Discussion	191
Chapter 4.- Conclusions	195
Chapter 5.- Future work	197
Appendix.- 3-D Tau-p	198
References	221

LIST OF TABLES

Table 1.1. Geometry and recording parameters of survey	13
Table 2.1. Refraction statics used for P - P and S - S reflections	77
Table 2.2. Refractions statics used for the converted waves considering 110% (case 1) and 150% (case 2) of the P - P refraction statics	84

List of Figures

Fig. 1.1. A horizontally layered model used for testing the P - S separation filter in the free-surface case (after Dankbaar, 1985)	5
Fig. 1.2. Depth model used for testing the P - S separation filter in the free-surface case under strong changes in elevation conditions	5
Fig. 1.3. Horizontally layered earth model used for testing the separation filter in the fluid-solid case (after Dankbaar, 1985)	7
Fig. 1.4. Two-dimensional model that contains a relatively thin lens. On this model was acquired a 3C-2D data set used for testing the separation filter in the fluid-solid case (after McCormack and Tatham, 1987)	7
Fig. 1.5. Dipping depth model which basically consists in two homogeneous layers used for testing the 2-D τ - p algorithms	8
Fig. 1.6. Depth model representing a horizontally layered earth with constant P and S wave velocities used for testing the 3-D τ - p algorithm.	10
Fig. 1.7. Plan view of the acquisition geometry for a 3-D shot record	10
Fig. 1.8. Location map of the three 3C-2D seismic lines (Lines 1, 2 and 3) acquired in the Barinas area, Venezuela	12
Fig. 1.9. Location map of 3C-2D seismic line 950278, well control and incised valley isopach in Blackfoot area (isopach map from Politylo, 1985)	15
Fig. 2.1. Effect of the receiving characteristic on an incident SV wave. (a) SV wave incident at the surface for equidistant offsets, (b) and (c) receiving characteristics of vertical and horizontal geophones, (d) and (e) shear wave as recorded on vertical and horizontal geophones (after Dankbaar, 1985)	21
Fig. 2.2. Response, in polar diagram form, of the vertical (a) and horizontal (b) geophones located on the surface of the solid (stress-free) for P waves and S waves as a function of angle of incidence. Parameter values are: $V_p=1500$ m/s and $V_s=650$ m/s	23
Fig. 2.3. (a,b) Response, in polar diagram form, of the vertical (a) and horizontal (b) geophones, located on the surface of a solid (stress-free) for P and S waves as a function of the angle of incidence. Parameter values for this case are: $V_p=1275$ m/s and $V_s=552.50$ m/s. (c,d) Response, in polar	

diagram form, of the vertical (a) and horizontal (b) geophones, located on the surface of a solid (stress-free) for P and S waves as a function of the angle of incidence. Parameter values for this case are: $V_p= 2000$ m/s and $V_s= 1000$ m/s..... 24

Fig. 2.4. Radiation pattern of a model-seismic source (piezoelectric transmitter) normally used. The source is placed on the free surface of a two-dimensional model (after Kim and Behrens, 1985)..... 26

Fig. 2.5. Radiation pattern of a model-seismic source (piezoelectric transmitter) normally used. The source is placed upon a two-dimensional model plate (after Kim and Behrens, 1985) 26

Fig. 2.6. (a) A seismic source generates waves that propagate in all directions; waves traveling in different directions are recorded at different locations. (b) A vertically incident plane wave is generated by setting off many shots in unison. (c) A plane wave that travels at angle θ from vertical is generated by setting many shots (starting from left) at appropriate time intervals. (d) Computation of time interval between shots (S) to generate the oblique plane wave in (c)..... 28

Fig. 2.6. (e) The reciprocity principle applied to the geometry of Fig. 2.d to replace shots (S) with receivers (R). (f) If the ray parameter p is specified, then the ray can be traced in an horizontally layered earth model with a known velocity function $v(z)$. (g) Some raypaths for a given p value, corresponding to a single trace in the (τ, p) plane (after Yilmaz, 1987)..... 30

Fig. 2.7. (a) A hyperbola on a shot gather maps onto an ellipse on the p -gather. (b) Various arrivals on a shot gather mapped onto the corresponding p -gather. Events A, B, C, and D map onto A', B', C', and D' (after Yilmaz, 1985)..... 31

Fig. 2.8. Detail of the derivation and application of the semblance derived window function. (a) Slowness stack for a horizontal ray parameter of .445 s/km. The arrivals after about 12.6s are alias contributions from the sea floor reflection. (b) Semblance calculated for every time sample for the same ray parameter. The principal contributions are from the primary wavelet. (c) Results from the application of 0-10 Hz bandpass filter to the unit sample semblance trace. (d) A rectangular window is then derived by defining all values of the band-passed semblance trace. (e) The recovered primary wavelet before deconvolution. (f) The recovered primary wavelet after deconvolution (from Stoffa et al., 1981)..... 37

Fig. 2.9. (a) Data in the τ - p domain. (b) Filtered semblance. (c) Filtered semblance multiplied by the threshold value. (d) Data in the τ - p domain multiplied by (c).....	38
Fig. 2.10. Flowchart of the slant stack processing in the x - t domain.....	40
Fig. 2.11a. The Fourier slice theorem is illustrated here.....	43
Fig. 2.11b. (a) This figure illustrates a projection of a function $f(x,y)$. (b) Taking the Fourier transforms of projections taken at different angles one can fill up the frequency domain.....	44
Fig. 2.12. Scheme for constructing slant-stack with 2-D Fourier transforms (after Wade and Gardner, 1991).....	45
Fig. 2.13. Scheme for reconstructing (x,t) data from (p,τ) data with Fourier transforms (after Wade and Gardner, 1991).....	46
Fig. 2.14. A (p,τ) slant stack can be constructed with a wide range of p values. The p values of “interest” are those traces for which no frequency filtering is desired. High-cut frequency filtering is then applied by muting outside the interval $1/(Fdx)$ for each frequency. The resulting (p,τ) slant stack contains enough information to recover the original function (after Wade and Gardner, 1988).....	49
Fig. 2.15. Dip-angle model used to test two different approaches of the 2-D τ - p transform.....	50
Fig. 2.16a. Data from the dip-angle model transformed in to the τ - p domain using the (x,t) method as proposed by Stoffa (1981).....	51
Fig. 2.16b. Data from the dip-angle model transformed in to the τ - p domain using the (k,w) method.....	51
Fig. 2.17. (a) Stacked input section from the dip-angle model. (b) Reconstructed section after applying the τ - p transform in the (x,t) domain. (c) Corresponding stacked section by using the proposed τ - p transform in the (k,w) domain.....	53
Fig. 2.18. Value of the filter coefficients F as a function of horizontal slowness for pass- P and pass- S filter considering $V_p= 1500$ m/s and $V_s= 650$ m/s, without constrains.....	55

Fig. 2.19. Value of the filter coefficients F as a function of horizontal slowness for pass- P and pass- S filter considering $V_p= 1500$ m/s and $V_s= 650$ m/s, with constrains	55
Fig. 2.20a. Value of the filter coefficients F as a function of horizontal slowness for pass- P and pass- S filter considering $V_p= 1275$ m/s and $V_s= 552.5$ m/s, with constrains	56
Fig. 2.20b. Value of the filter coefficients F as a function of horizontal slowness for pass- P and pass- S filter considering $V_p= 2000$ m/s and $V_s= 1000$ m/s, with constrains	56
Fig. 2.21. Flowchart of the P - S separation filter for the free-stress case in the τ - p domain.....	57
Fig. 2.22. Subsurface model used for synthetic data calculation (after Dankbaar, 1985).....	59
Fig. 2.23. Vertical and horizontal geophone response from the model in Fig. 2.22. (a) P - P and S - S reflections, with no receiver response. (b) Vertical and horizontal geophone output from incident P - P and S - S reflections. (c) Pass- P and pass- S sections obtained from both vertical and horizontal records (Fig. 2.23b) using $V_p= 1500$ m/s and $V_s= 650$ m/s	60
Fig. 2.24. (a) Filtered pass- P and pass- S records, respectively, obtained using $V_p= 1650$ m/s and $V_s= 715$ m/s. (b) Filtered pass- P and pass- S records, respectively, obtained using $V_p= 1875$ m/s and $V_s= 812.5$ m/s. (c) Filtered pass- P and pass- S records, respectively, obtained using $V_p= 1275$ m/s and $V_s= 552.5$ m/s	63
Fig. 2.25. Vertical and horizontal geophone response from the model in Fig. 2.22. (a) P - P and S - S reflections with 10% of random noise added, no receiver response considered. (b) Vertical and horizontal geophone output from incident P - P and S - S reflections. (c) Pass- P and pass- S sections obtained from both vertical and horizontal records (Fig. 2.25b) using $V_p= 1500$ m/s and $V_s= 650$ m/s.....	64
Fig. 2.26. (a) Filtered pass- P and pass- S records, respectively, obtained using $V_p= 1650$ m/s and $V_s= 715$ m/s. (b) Filtered pass- P and pass- S records, respectively, obtained using $V_p= 1875$ m/s and $V_s= 812.5$ m/s. (c) Filtered pass- P and pass- S records, respectively, obtained using $V_p= 1275$ m/s and $V_s= 552.5$ m/s	65
Fig. 2.27. Vertical and horizontal geophone response from the model in Fig. 2.22.	

(a) *P-P* and *P-S* reflections, with no receiver response. (b) Vertical and horizontal geophone output from incident *P-P* and *P-S* reflections. (c) Pass-*P* and pass-*S* sections obtained from both vertical and horizontal records (Fig. 2.27b) using $V_p= 1500$ m/s and $V_s= 650$ m/s 66

Fig. 2.28. (a) Filtered pass-*P* and pass-*S* records, respectively, obtained using $V_p= 1650$ m/s and $V_s= 715$ m/s. (b) Filtered pass-*P* and pass-*S* records, respectively, obtained using $V_p= 1875$ m/s and $V_s= 812.5$ m/s. (c) Filtered pass-*P* and pass-*S* records, respectively, obtained using $V_p= 1275$ m/s and $V_s= 552.5$ m/s 67

Fig. 2.29. Vertical and horizontal geophone response from the model in Fig. 2.22. (a) *P-P* and *P-S* reflections with 10% of random noise added, no receiver response considered. (b) Vertical and horizontal geophone output from incident *P-P* and *P-S* reflections. (c) Pass-*P* and pass-*S* sections obtained from both vertical and horizontal records (Fig. 2.29b) using $V_p= 1500$ m/s and $V_s= 650$ m/s 69

Fig. 2.30. (a) Filtered pass-*P* and pass-*S* records, respectively, obtained using $V_p= 1650$ m/s and $V_s= 715$ m/s. (b) Filtered pass-*P* and pass-*S* records, respectively, obtained using $V_p= 1875$ m/s and $V_s= 812.5$ m/s. (c) Filtered pass-*P* and pass-*S* records, respectively, obtained using $V_p= 1275$ m/s and $V_s= 552.5$ m/s 70

Fig. 2.31. Vertical and horizontal geophone response from the model in Fig. 2.22. (a) *P-P*, *S-P*, *S-S* and *P-S* reflections, with no receiver response. (b) Vertical and horizontal geophone output from incident *P-P*, *S-P*, *S-S* and *P-S* reflections. (c) Pass-*P* and pass-*S* sections obtained from both vertical and horizontal records (Fig. 2.31b) using $V_p= 1500$ m/s and $V_s= 650$ m/s 71

Fig. 2.32. (a) Filtered pass-*P* and pass-*S* records, respectively, obtained using $V_p= 1650$ m/s and $V_s= 715$ m/s. (b) Filtered pass-*P* and pass-*S* records, respectively, obtained using $V_p= 1875$ m/s and $V_s= 812.5$ m/s 72

Fig. 2.33. (a) Filtered pass-*P* and pass-*S* records, respectively, obtained using $V_p= 1275$ m/s and $V_s= 552.5$ m/s. (b) Filtered pass-*P* and pass-*S* records, respectively, obtained using $V_p= 1500$ m/s and $V_s= 780$ m/s 73

Fig. 2.34. Depth model using for calculating the *P-P* refraction statics 76

Fig. 2.35. Vertical and horizontal geophone response from the model of Fig. 2.34 considering *S-S* refraction statics equal 200% of the *P-P* refraction statics. (a) *P-P* and *S-S* reflections, with n receiver response. (b) Vertical and horizontal geophone output from the incident *P-P* and *S-S* reflections 78

Fig. 2.36. Pass- <i>P</i> and pass- <i>S</i> sections obtained from both vertical and horizontal records (Fig. 2.35b) using (a) $V_p= 1500$ m/s and $V_s= 650$ m/s. (b) $V_p= 1875$ m/s and $V_s= 812.5$ m/s.....	79
Fig. 2.37. Vertical and horizontal geophone response from the model of Fig. 2.34 considering <i>P-S</i> refraction statics equal 110% of the <i>P-P</i> refraction statics. (a) <i>P-P</i> and <i>P-S</i> reflections, with n receiver response. (b) Vertical and horizontal geophone output from the incident <i>P-P</i> and <i>P-S</i> reflections	82
Fig. 2.38. Pass- <i>P</i> and pass- <i>S</i> sections obtained from both vertical and horizontal records (Fig. 2.37b) using (a) $V_p= 1500$ m/s and $V_s= 650$ m/s. (b) $V_p= 1875$ m/s and $V_s= 812.5$ m/s.....	83
Fig. 2.39. Vertical and horizontal geophone response from the model of Fig. 2.34 considering <i>P-S</i> refractions statics equal 150% of the <i>P-P</i> refraction statics. (a) <i>P-P</i> and <i>P-S</i> reflections, with no response. (b) Vertical and horizontal geophone output from incident <i>P-P</i> and <i>P-S</i> reflections	85
Fig. 2.40. Pass- <i>P</i> and pass- <i>S</i> sections obtained from both vertical and horizontal records (Fig. 2.39b) using (a) $V_p= 1500$ m/s and $V_s= 650$ m/s. (b) $V_p= 1875$ m/s and $V_s= 812.5$ m/s.....	86
Fig. 2.41a. Raw shot gather from the vertical component showing the strong superposition between the ground roll and reflections.....	89
Fig. 2.41b. Raw shot gather from the horizontal component showing the strong superposition between the ground roll and reflections.....	89
Fig. 2.42a. Uphole time values of the Barinas survey.....	90
Fig. 2.42b. Source depth in the Barinas survey	90
Fig. 2.43. Schematic summary of the raypaths and parameters used in deriving the uphole correction	91
Fig. 2.44a. Raw shot gather from the vertical component	92
Fig. 2.44b. Filtered pass- <i>P</i> record obtained from vertical and horizontal records (Fig. 2.41) using $V_p= 856$ m/s and $V_s= 428$ m/s.....	92
Fig. 2.45a. Raw shot gather from the horizontal component	93
Fig. 2.45b. Filtered pass- <i>S</i> record obtained from the vertical and horizontal records (Fig. 2.41) using $V_p= 856$ m/s and $V_s= 428$ m/s.....	93

Fig. 2.46. Processing flowchart for <i>P</i> wave without and with modal filter.....	96
Fig. 2.47a. Shot gather of the vertical component after applying the processing flow shown in Fig. 2.46 without modal filter.....	97
Fig. 2.47b. Pass- <i>P</i> output obtained from both vertical and horizontal records (Fig. 2.41) after applying the processing flow shown in Fig. 2.46 with modal filter.....	97
Fig. 2.48a. Velocity analysis for the CDP 2340 without modal filter applied.....	98
Fig. 2.48b. Velocity analysis for the CDP 2340 after modal filtering.....	99
Fig. 2.49. Processing flowchart for <i>S</i> waves in the Barinas data without and with modal filter.....	100
Fig. 2.50a. Shot gather of the horizontal component after applying the processing flow shown in Fig. 2.49 without modal filter.....	101
Fig. 2.50b. Pass- <i>S</i> output obtained from both vertical and horizontal records (Fig. 2.41) after applying the processing flow shown in Fig. 2.49 with modal filter.....	101
Fig. 2.51a. Velocity analysis for the CCP 2330 without modal filter applied.....	102
Fig. 2.51b. Velocity analysis for the CCP 2330 after modal filtering.....	103
Fig. 2.52. Brute stack of the vertical component data from Barinas, southwest Venezuela, processed without separation filter.....	104
Fig. 2.53. Stacked section of the filtered pass- <i>P</i> output obtained from the vertical and horizontal records using $V_p= 856$ m/s and $V_s= 428$ m/s.....	105
Fig. 2.54. Brute stack of the horizontal component data from Barinas, southwest Venezuela, processed without separation filter.....	106
Fig. 2.55. Stacked section of the filtered pass- <i>S</i> output obtained from the vertical and horizontal records using $V_p= 856$ m/s and $V_s= 428$ m/s.....	107
Fig. 2.56a. A detailed picture of the area of interest from the brute stack of the vertical component data acquired in Barinas, southwest Venezuela, processed without separation filter.....	108

Fig. 2.56b. A detailed picture of the area of interest from the filtered pass- <i>P</i> output from the vertical and horizontal data acquired in Barinas, southwest Venezuela, using $V_p= 856$ m/s and $V_s= 428$ m/s.....	109
Fig. 2.57a. A detailed picture of the area of interest from the brute stack of the horizontal component data acquired in Barinas, southwest Venezuela, processed without separation filter	110
Fig. 2.57b. A detailed picture of the area of interest from the filtered pass- <i>S</i> output from the vertical and horizontal data acquired in Barinas, southwest Venezuela, using $V_p= 856$ m/s and $V_s= 428$ m/s.....	111
Fig. 2.58a. Stacked section of the filtered pass- <i>P</i> output obtained from the vertical and horizontal records using $V_p= 984.4$ m/s and $V_s= 492.2$ m/s.....	112
Fig. 2.58b. Stacked section of the filtered pass- <i>S</i> output obtained from the vertical and horizontal records using $V_p= 984.4$ m/s and $V_s= 492.2$ m/s.....	113
Fig. 2.59a. Stacked section of the filtered pass- <i>P</i> output obtained from the vertical and horizontal records using $V_p= 727.6$ m/s and $V_s= 363.8$ m/s.....	114
Fig. 2.59b. Stacked section of the filtered pass- <i>S</i> output obtained from the vertical and horizontal records using $V_p= 727.6$ m/s and $V_s= 363.8$ m/s.....	115
Fig. 2.60a. Stacked section of the filtered pass- <i>P</i> output obtained from the vertical and horizontal data acquired in Barinas, southwest Venezuela, using $V_p= 984.4$ m/s and $V_s= 492.2$ m/s.....	117
Fig. 2.60b. Stacked section of the filtered pass- <i>S</i> output obtained from the vertical and horizontal data acquired in Barinas, southwest Venezuela, using $V_p= 984.4$ m/s and $V_s= 492.2$ m/s.....	118
Fig. 2.61a. A detailed picture of the area of interest from the filtered pass- <i>P</i> output obtained from the vertical and horizontal data acquired in Barinas, southwest Venezuela, using $V_p= 727.6$ m/s and $V_s= 363.8$ m/s.....	119
Fig. 2.61b. A detailed picture of the area of interest from the filtered pass- <i>S</i> output obtained from the vertical and horizontal data acquired in Barinas, southwest Venezuela, using $V_p= 727.6$ m/s and $V_s= 363.8$ m/s.....	120
Fig. 2.62. Location of the 3C-2D seismic line 950278, well control and incised valley isopach in Blackfoot area (isopach map from Politylo, 1995).....	121
Fig. 2.63a. Raw shot gather from the vertical component showing acquired in Blackfoot, Alberta.....	122

Fig. 2.63b. Raw shot gather from the horizontal component acquired in Blackfoot field.....	122
Fig. 2.64a. Uphole time values of the Blackfoot survey.....	126
Fig. 2.64b. Source depth in the Blackfoot survey.....	126
Fig. 2.65a. Raw shot gather from the vertical component.....	127
Fig. 2.65b. Filtered pass- <i>P</i> record obtained from the vertical and horizontal records (Fig. 2.63) using $V_p= 985$ m/s and $V_s= 492$ m/s.....	127
Fig. 2.66a. Raw shot gather from the horizontal component.....	128
Fig. 2.66b. Filtered pass- <i>S</i> record obtained from the vertical and horizontal records (Fig. 2.41) using $V_p= 985$ m/s and $V_s= 492$ m/s.....	128
Fig. 2.67. <i>P</i> -wave processing flow for Blackfoot data without and with modal filter.....	129
Fig. 2.68a. Shot gather of the vertical component after applying the processing flow shown in Fig. 2.67 without modal filter.....	130
Fig. 2.68b. Pass- <i>P</i> output obtained from both vertical and horizontal records (Fig. 2.63) after applying the processing flow shown in Fig. 2.67 with modal filter.....	130
Fig. 2.69a. Velocity analysis for the CDP 390 without modal filter applied.....	131
Fig. 2.69b. Velocity analysis for the CDP 390 after modal filtering.....	132
Fig. 2.70. <i>S</i> -wave processing flow for Blackfoot data without and with modal filter.....	133
Fig. 2.71a. Shot gather of the horizontal component after applying the processing flow shown in Fig. 2.49 without modal filter.....	134
Fig. 2.71b. Pass- <i>S</i> output obtained from both vertical and horizontal records (Fig. 2.41) after applying the processing flow shown in Fig. 2.49 with modal filter.....	134
Fig. 2.72a. Velocity analysis for the CCP 460 without modal filter applied.....	135
Fig. 2.72b. Velocity analysis for the CCP 460 after modal filtering.....	136

Fig. 2.73. Brute stack of the vertical component data from Blackfoot field, Alberta, processed without separation filter	137
Fig. 2.74. Stacked section of the filtered pass- <i>P</i> output obtained from the vertical and horizontal records using $V_p= 985$ m/s and $V_s= 492$ m/s.....	138
Fig. 2.75. Brute stack of the horizontal component data from Blackfoot field, Alberta, processed without separation filter	139
Fig. 2.76. Stacked section of the filtered pass- <i>S</i> output obtained from the vertical and horizontal records using $V_p= 985$ m/s and $V_s= 492$ m/s.....	140
Fig. 2.77a. A detailed picture of the area of interest from the brute stack of the vertical component data acquired in Blackfoot field, Alberta, processed without separation filter.....	141
Fig. 2.77b. A detailed picture of the area of interest from the filtered pass- <i>P</i> output from the vertical and horizontal data acquired in Barinas, southwest Venezuela, using $V_p= 985$ m/s and $V_s= 492$ m/s	142
Fig. 2.78a. A detailed picture of the area of interest from the brute stack of the horizontal component data acquired in Blackfoot field, Alberta, processed without separation filter.....	143
Fig. 2.78b. A detailed picture of the area of interest from the filtered pass- <i>S</i> output from the vertical and horizontal data acquired in Barinas, southwest Venezuela, using $V_p= 985$ m/s and $V_s= 492$ m/s	144
Fig. 2.79a. Stacked section of the filtered pass- <i>P</i> output obtained from the vertical and horizontal records using $V_p= 1083.5$ m/s and $V_s= 542.5$ m/s	145
Fig. 2.79b. Stacked section of the filtered pass- <i>S</i> output obtained from the vertical and horizontal records using $V_p= 1083.5$ m/s and $V_s= 542.5$ m/s.....	146
Fig. 2.80a. Stacked section of the filtered pass- <i>P</i> output obtained from the vertical and horizontal records using $V_p= 886.5$ m/s and $V_s= 443.7$ m/s.....	148
Fig. 2.80b. Stacked section of the filtered pass- <i>S</i> output obtained from the vertical and horizontal records using $V_p= 886.5$ m/s and $V_s= 443.7$ m/s.....	149
Fig. 2.81a. A detailed picture of the area of interest from the filtered pass- <i>P</i> output obtained from the vertical and horizontal data acquired in Blackfoot field, Alberta, using $V_p= 1083.5$ m/s and $V_s= 542.3$ m/s.....	150

Fig. 2.81b. A detailed picture of the area of interest from the filtered pass- <i>S</i> output obtained from the vertical and horizontal data acquired in Blackfoot field, Alberta, using $V_p= 1083.5$ m/s and $V_s= 542.3$ m/s.....	151
Fig. 2.82a. A detailed picture of the area of interest from the filtered pass- <i>P</i> output obtained from the vertical and horizontal data acquired in Blackfoot field, Alberta, using $V_p= 886.5$ m/s and $V_s= 443.7$ m/s.....	152
Fig. 2.81b. A detailed picture of the area of interest from the filtered pass- <i>S</i> output obtained from the vertical and horizontal data acquired in Blackfoot field, Alberta, using $V_p= 886.5$ m/s and $V_s= 443.7$ m/s.....	153
Fig. 3.1. (a) Schematic SUMIC (subsea seismic) 2-D acquisition (after Berg et al., 1994). (b) Geometry of waves impinging on a vertical and horizontal geophone at the fluid-solid interface (after Ferber, 1989).....	155
Fig. 3.2. Response, in polar diagram form, of the vertical (a) and horizontal (b) geophones, located at a liquid-solid contact, for <i>P</i> waves and <i>S</i> waves as a function of angle of incidence. Parameter values for this case are: $V_p= 1500$ m/s, $V_s= 650$ m/s, and $\rho= 1.6$ g/cc (in the solid), and $V_p= 1455$ m/s and $\rho= 1.135$ g/cc in the liquid.....	159
Fig. 3.3. Response, in polar diagram form, of the vertical (a) and horizontal (b) geophones located on the surface of a solid (stress-free) for <i>P</i> waves and <i>S</i> waves as a function of angle of incidence. Parameter values are: $V_p= 1500$ m/s, $V_s= 650$ m/s and $\rho= 1.6$ g/cc.....	160
Fig. 3.4. (a,b) Response, in polar diagram form, of the vertical (a) and horizontal (b) geophones, located at a liquid-solid contact, for <i>P</i> and <i>S</i> waves as a function of the angle of incidence. Parameter values for this case are: $V_p= 1650$ m/s, $V_s= 715$ m/s and $\rho= 1.76$ g/cc (in the solid), and $V_p= 1455$ m/s and $\rho= 1.135$ g/cc (in the liquid). (c,d) Response, in polar diagram, of the vertical (c) and horizontal (d) geophones, locates at a liquid-solid contact, for <i>P</i> and <i>S</i> waves as a function of the angle of incidence. Parameter values for this case are: $V_p= 1600$ m/s, $V_s= 800$ m/s and $\rho= 1.3$ g/cc (in the solid), and $V_p= 1350$ m/s and $\rho= 1.0$ g/cc (in the liquid).....	161
Fig. 3.5. Value of the filter coefficients <i>F</i> as a function of horizontal slowness for pass- <i>P</i> and pass- <i>S</i> filter considering $V_p= 1500$ m/s, $V_s= 650$ m/s and $\rho= 1.6$ g/cc (in the solid), and $V_p= 1455$ m/s and $\rho= 1.135$ g/cc (in the liquid), without constraints.....	164
Fig. 3.6a. Filter coefficients <i>F</i> as a function of horizontal slowness for pass- <i>P</i> and pass- <i>S</i> filter for a geophone located at a liquid-solid contact as described in Fig. 3.2.....	165

Fig. 3.6b. Filter coefficients F as a function of horizontal slowness for pass- P and pass- S filter for a geophone on the surface at a solid (stress-free case) using the model of Fig. 3.3.....	165
Fig. 3.7a. Value of the filter coefficients F as a function of horizontal slowness for pass- P and pass- S filter considering $V_p= 1650$ m/s, $V_s= 715$ m/s and $\rho= 1.76$ g/cc (in the solid), and $V_p= 1455$ m/s and $\rho= 1.135$ g/cc (in the liquid), with constraints.....	167
Fig. 3.7b. Value of the filter coefficients F as a function of horizontal slowness for pass- P and pass- S filter considering $V_p= 1600$ m/s, $V_s= 800$ m/s and $\rho= 1.3$ g/cc (in the solid), and $V_p= 1350$ m/s and $\rho= 1.0$ g/cc (in the liquid), with constraints.....	167
Fig. 3.8. Flowchart of the P - S separation filter for the liquid-solid case in the τ - p domain.....	168
Fig. 3.9. Subsurface model used for synthetic data calculation (after Dankbaar, 1985).....	170
Fig. 3.10. Vertical and horizontal geophone response from the model of Fig. 3.9. (a) P - P and P - S reflections, with no receiver responses. (b) Vertical and horizontal geophone output from incident P - P and P - S reflections. (c) Pass- P and pass- S sections obtained from both vertical and horizontal records (Fig. 3.10b) using $V_p= 1500$ m/s, $V_s= 650$ m/s and $\rho= 1.6$ g/cc (in the solid), and $V_p= 1455$ m/s and $\rho= 1.135$ g/cc (in the liquid).....	171
Fig. 3.11. (a) Filtered pass- P and pass- S record, respectively, obtained using $V_p= 1650$ m/s, $V_s= 715$ m/s and $\rho= 1.76$ g/cc (in the solid), and $V_p= 1455$ m/s and $\rho= 1.135$ g/cc (in the liquid). (b) Filtered pass- P and pass- S record, respectively, obtained using $V_p= 1350$ m/s, $V_s= 585$ m/s and $\rho= 1.44$ g/cc (in the solid), and $V_p= 1455$ m/s and $\rho= 1.135$ g/cc (in the liquid). (c) Filtered pass- P and pass- S record, respectively, obtained using $V_p= 1600$ m/s, $V_s= 800$ m/s and $\rho= 1.3$ g/cc (in the solid), and $V_p= 1350$ m/s and $\rho= 1.0$ g/cc (in the liquid).....	172
Fig. 3.12. Vertical and horizontal geophone response from the model of Fig. 3.9. (a) P - P and P - S reflections with 10% of random noise added, no receiver response considered. (b) Vertical and horizontal geophone output from incident P - P and P - S reflections. (c) Pass- P and pass- S sections obtained from both vertical and horizontal records (Fig. 3.12b) using $V_p= 1500$ m/s, $V_s= 650$ m/s and $\rho= 1.6$ g/cc (in the solid), and $V_p= 1455$ m/s and $\rho= 1.135$ g/cc (in the liquid).....	174

Fig. 3.13. (a) Filtered pass-*P* and pass-*S* record, respectively, obtained using $V_p=1650$ m/s, $V_s=715$ m/s and $\rho=1.76$ g/cc (in the solid), and $V_p=1455$ m/s and $\rho=1.135$ g/cc (in the liquid). (b) Filtered pass-*P* and pass-*S* record, respectively, obtained using $V_p=1350$ m/s, $V_s=585$ m/s and $\rho=1.44$ g/cc (in the solid), and $V_p=1455$ m/s and $\rho=1.135$ g/cc (in the liquid). (c) Filtered pass-*P* and pass-*S* record, respectively, obtained using $V_p=1600$ m/s, $V_s=800$ m/s and $\rho=1.3$ g/cc (in the solid), and $V_p=1350$ m/s and $\rho=1.0$ g/cc (in the liquid)..... 175

Fig. 3.14. Vertical and horizontal geophone response with source and receivers on the fluid-solid interface from the model of Fig. 3.9.
 (a) *P-P* and *S-S* reflections, with no receiver response. (b) Vertical and horizontal geophone output from incident *P-P* and *S-S* reflections. (c) Pass-*P* and pass-*S* sections obtained from both vertical and horizontal records (Fig. 3.14b) using $V_p=1500$ m/s, $V_s=650$ m/s and $\rho=1.6$ g/cc (in the solid), and $V_p=1455$ m/s and $\rho=1.135$ g/cc (in the liquid). 178

Fig. 3.15. (a) Filtered pass-*P* and pass-*S* record, respectively, obtained using $V_p=1650$ m/s, $V_s=715$ m/s and $\rho=1.76$ g/cc (in the solid), and $V_p=1455$ m/s and $\rho=1.135$ g/cc (in the liquid). (b) Filtered pass-*P* and pass-*S* record, respectively, obtained using $V_p=1350$ m/s, $V_s=585$ m/s and $\rho=1.44$ g/cc (in the solid), and $V_p=455$ m/s and $\rho=1.135$ g/cc (in the liquid). (c) Filtered pass-*P* and pass-*S* record, respectively, obtained using $V_p=1600$ m/s, $V_s=800$ m/s and $\rho=1.3$ g/cc (in the solid), and $V_p=1350$ m/s and $\rho=1.0$ g/cc (in the liquid)..... 179

Fig. 3.16. Vertical and horizontal geophone response with source and receivers on the fluid-solid interface from the model of Fig. 3.9.
 (a) *P-P* and *S-S* reflections with 10% of random noise added, no receiver response considered. (b) Vertical and horizontal geophone output from incident *P-P* and *S-S* reflections. (c) Pass-*P* and pass-*S* sections obtained from both vertical and horizontal records (Fig. 3.16b) using $V_p=1500$ m/s, $V_s=650$ m/s and $\rho=1.6$ g/cc (in the solid), and $V_p=1455$ m/s and $\rho=1.135$ g/cc (in the liquid). 180

Fig. 3.17. (a) Filtered pass-*P* and pass-*S* record, respectively, obtained using $V_p=1650$ m/s, $V_s=715$ m/s and $\rho=1.76$ g/cc (in the solid), and $V_p=1455$ m/s and $\rho=1.135$ g/cc (in the liquid). (b) Filtered pass-*P* and pass-*S* record, respectively, obtained using $V_p=1350$ m/s, $V_s=585$ m/s and $\rho=1.44$ g/cc (in the solid), and $V_p=1455$ m/s and $\rho=1.135$ g/cc (in the liquid). (c) Filtered pass-*P* and pass-*S* record, respectively, obtained using $V_p=1600$ m/s, $V_s=800$ m/s and $\rho=1.3$ g/cc (in the solid), and $V_p=1350$ m/s and $\rho=1.0$ g/cc (in the liquid)..... 181

Fig. 3.18. Vertical and horizontal geophone response with source and receivers on the fluid-solid interface from the model of Fig. 3.9. (a) <i>P-P</i> , <i>S-S</i> , <i>P-S</i> and <i>S-P</i> reflections, with no receiver response. (b) Vertical and horizontal geophone output from incident <i>P-P</i> , <i>S-S</i> , <i>P-S</i> and <i>S-P</i> reflections. (c) Pass- <i>P</i> and pass- <i>S</i> sections obtained from both vertical and horizontal records (Fig. 3.18b) using $V_p=1500$ m/s, $V_s=650$ m/s and $\rho=1.6$ g/cc (in the solid), and $V_p=1455$ m/s and $\rho=1.135$ g/cc (in the liquid).....	182
Fig. 3.19. (a) Filtered pass- <i>P</i> and pass- <i>S</i> record, respectively, obtained using $V_p=1650$ m/s, $V_s=715$ m/s and $\rho=1.76$ g/cc (in the solid), and $V_p=1455$ m/s and $\rho=1.135$ g/cc (in the liquid). (b) Filtered pass- <i>P</i> and pass- <i>S</i> record, respectively, obtained using $V_p=1350$ m/s, $V_s=585$ m/s and $\rho=1.44$ g/cc (in the solid), and $V_p=1455$ m/s and $\rho=1.135$ g/cc (in the liquid). (c) Filtered pass- <i>P</i> and pass- <i>S</i> record, respectively, obtained using $V_p=1600$ m/s, $V_s=800$ m/s and $\rho=1.3$ g/cc (in the solid), and $V_p=1350$ m/s and $\rho=1.0$ g/cc (in the liquid).....	183
Fig. 3.20. Vertical and horizontal geophone response with source and receivers on the fluid-solid interface from the model of Fig. 3.9. (a) <i>P-P</i> , <i>S-S</i> , <i>P-S</i> and <i>S-P</i> reflections with 10% of random noise added, no receiver response considered. (b) Vertical and horizontal geophone output from incident <i>P-P</i> , <i>S-S</i> , <i>P-S</i> and <i>S-P</i> reflections. (c) Pass- <i>P</i> and pass- <i>S</i> sections obtained from both vertical and horizontal records (Fig. 3.20b) using $V_p=1500$ m/s, $V_s=650$ m/s and $\rho=1.6$ g/cc (in the solid), and $V_p=1455$ m/s and $\rho=1.135$ g/cc (in the liquid).....	185
Fig. 3.21. (a) Filtered pass- <i>P</i> and pass- <i>S</i> record, respectively, obtained using $V_p=1650$ m/s, $V_s=715$ m/s and $\rho=1.76$ g/cc (in the solid), and $V_p=1455$ m/s and $\rho=1.135$ g/cc (in the liquid). (b) Filtered pass- <i>P</i> and pass- <i>S</i> record, respectively, obtained using $V_p=1350$ m/s, $V_s=585$ m/s and $\rho=1.44$ g/cc (in the solid), and $V_p=1455$ m/s and $\rho=1.135$ g/cc (in the liquid). (c) Filtered pass- <i>P</i> and pass- <i>S</i> record, respectively, obtained using $V_p=1600$ m/s, $V_s=800$ m/s and $\rho=1.3$ g/cc (in the solid), and $V_p=1350$ m/s and $\rho=1.0$ g/cc (in the liquid).....	186
Fig. 3.22. Depth model with a thin-lens used for synthetic data calculation (after McCormack and Tatham, 1989).....	187
Fig. 3.23a. Stacked section of the <i>P-P</i> reflections, with no receiver response.....	188
Fig. 3.23b. Stacked section of the <i>P-SV</i> reflections, with no receiver response.....	188
Fig. 3.24a. Stacked section of the vertical records.....	189

Fig. 3.24b. Stacked section of the horizontal records.....	189
Fig. 3.25a. Stacked section of the filtered pass- P output obtained using $V_p= 2273$ m/s, $V_s= 945$ m/s and $\rho= 1.6$ g/cc (for the solid), and $V_p= 1455$ m/s and $\rho= 1.135$ g/cc (for the liquid).	190
Fig. 3.25b. Stacked section of the filtered pass- S output obtained using $V_p= 2273$ m/s, $V_s= 945$ m/s and $\rho= 1.6$ g/cc (for the solid), and $V_p= 1455$ m/s and $\rho= 1.135$ g/cc (for the liquid).	190
Fig. 3.26a. Stacked section of the filtered pass- P output obtained using $V_p= 2499$ m/s, $V_s= 1042$ m/s and $\rho= 1.6$ g/cc (for the solid), and $V_p= 1455$ m/s and $\rho= 1.135$ g/cc (for the liquid).	192
Fig. 3.26b. Stacked section of the filtered pass- S output obtained using $V_p= 2499$ m/s, $V_s= 1042$ m/s and $\rho= 1.6$ g/cc (for the solid), and $V_p= 1455$ m/s and $\rho= 1.135$ g/cc (for the liquid).	192
Fig. 3.27a. Stacked section of the filtered pass- P output obtained using $V_p= 1875$ m/s, $V_s= 813$ m/s and $\rho= 1.6$ g/cc (for the solid), and $V_p= 1455$ m/s and $\rho= 1.135$ g/cc (for the liquid).	193
Fig. 3.27b. Stacked section of the filtered pass- S output obtained using $V_p= 1875$ m/s, $V_s= 813$ m/s and $\rho= 2.0$ g/cc (for the solid), and $V_p= 1455$ m/s and $\rho= 1.135$ g/cc (for the liquid).	193
Fig. A.1 The slant stack $\psi(\tau,p)$ at any point (τ,p) is obtained by adding $u(x,t)$ along the line $t= \tau+px$. The value of the ψ at the points where the line intersects each trace of u is obtained by interpolation (after Wade and Gardner, 1988).....	201
Fig. A.2 A hyperbola on a shot gather maps onto an ellipse on the p -gather (after Yilmaz, 1987)	201
Fig. A.3a. Schematic view of a 3-D slant stack defined over a surface data.....	204
Fig. A.3b. Schematic view of a 3-D slant stack defined over a surface data considering axial symmetry.....	204
Fig. A.4a Scheme for constructing slant stack with 2-D Fourier transforms (after Wade and Gardner, 1988)	208
Fig. A.4b. Scheme for reconstructing (x,t) data from (τ,p) data with 2-D Fourier transforms (after Wade and Gardner, 1988).....	209

Fig. A.5. Schematic view of 3-D tau-p transform applied on data distributed over an areal coverage without assuming any geometric symmetry	210
Fig. A.6a. Depth model representing a horizontally layered earth with constant P and S velocities	211
Fig. A.6b. Acquisition geometry for a 3-D shot record. The inlines are oriented along the North-South direction and the crosslines along the East-West direction. The source is represented by the symbol (*) and the receivers by (#) on thus display.....	211
Fig. A.7a. The input 3-D shot record showing the P - P arrivals.....	213
Fig. A.7b. The representation of the 3-D shot record for the inline 1 in the τ - p domain.....	213
Fig. A.7c. The reconstructed 3-D shot record after applying the 3-D τ - p transform considering 50 slowness values in each x and y direction.....	214
Fig. A.7d. The reconstructed 3-D shot record after applying the 3-D τ - p transform considering 100 slowness values in each x and y direction.....	214
Fig. A.8a. 3-D shot record input showing the P - P arrivals with 15% of background noise added for the three flat layers in the depth model shown in Fig. A.7a	216
Fig. A.8b. Reconstruction of the 3-D shot record shown in Fig. A.8a after applying the 3-D τ - p transform in the presence of noise.....	216
Fig. A.9a. 3-D shot record showing the P - P and P - SV arrivals (free-noise condition).....	217
Fig. A.9b. Reconstructed 3-D shot record after applying the 3-D τ - p transform.....	217
Fig. A.10a. 3-D shot record showing the P - P and P - SV arrivals with 15% of random noise added for the three layers in the depth model shown in Fig. A.9a.....	218
Fig. A.10b. Reconstructed 3-D shot record after applying 3-D τ - p transform in the presence of noise.....	218
Fig. A.11a. 3-D shot record from the depth model shown in Fig. A.7a with ground roll noise added.....	220
Fig. A.11b. Reconstructed 3-D shot record after applying 3-D τ - p transform under the presence of ground roll.....	220

Chapter 1 - Introduction

1.1 Background

Surface seismic data, both 2-D and 3-D, have been enormously useful in obtaining important information on subsurface structure and its rock properties such as lithology, porosity, porefill, etc. These data are usually acquired using a single-component, vertical geophone which works very well for what it was designed to do: record the particle motion associated with nearly vertically traveling P waves. This assumption works well as long as the subsurface is fairly flat, the near surface has low-velocities, and there is little shallow structure. But structural deformations occur in many sorts of basins. Seismic waves, scattered from high-angle features, will not necessarily arrive at the surface along nearly vertical rays. Converted modes occur which interfere with P - P data and complicate the records making them difficult to analyze.

In the seismograms obtained from three-component (3-C) geophones it is possible to see different types of events: refractions, surface waves, and shear waves, along with primary P waves. These waves are recorded in their “true amplitude” motion (Ameely et al., 1985).

Usually, we assume that all the information related to P waves is contained on the vertical channel, but due to the interface (or geophone) responses and emergence angle, P and S waves are observed on both horizontal and vertical geophones. Then the recognition and separation of the individual P and S arrivals forms a considerable problem. “The disturbing events” present in both channels are in most cases so intermingled that they cannot be separated visually and therefore are often regarded as “noise”. The “noise” could be converted into signal if we found a way to discriminate individual waves components and describe them by laws of wave propagation. Separation of wave modes can improve our description and definition of the subsurface.

Many papers have shown that shear waves complement the information given by the P waves due to their different behavior especially in the presence of fluid saturation and fractures related to reservoirs (Helbig and Mesdag, 1982; Meissner and Hegazy, 1981).

1.2 The need for three-component recording in surface seismic

Application of shear (S)-waves in seismic petroleum exploration is in a critical stage of development. Propagation of these waves and of the historically applied compressional (P)-waves in a sedimentary section are affected differently by rock physical properties. The propagation velocity and, in turn, reflection amplitude of P -waves are affected by both rock incompressibility and rigidity, whereas, that of S -waves is affected by rock rigidity only. Because of this difference it is possible, for example, to associate P -wave reflection amplitude variation due to pore fluid change (e.g., brine to a gas-brine mixture), that affects rock compressibility and not rigidity, by the absence of variation in amplitude of the corresponding S -wave reflection. Additionally, this difference makes it possible to distinguish for example, clastic from calcareous portions of the sedimentary section by comparison of P - and S -wave interval velocities derived from corresponding P - and S -wave reflections bracketing the interval.

Much effort has been expended to establish the practicality and reliability of determining sedimentary rock properties from a combination of P - and S -wave surface and borehole data. This goal required the development of multicomponent sources and receivers, as well as large-capacity recording systems. The effect of velocity anisotropy on S -wave propagation, especially that associated with shale, requires additional study. Also required are studies of differences in P - and S -wave reflection correlation (Domenico and Danbom, 1987).

Due to the steady increase in the number of channels, two- and three-component recording now are much more affordable for the seismic industry. The seismic source array and the seismometer spread design are very similar to conventional P -wave recording. Three-component acquisition (i.e., vertical, horizontal inline and transverse crossline geophone sensors) provides a triple seismic image, the conventional one from vertical components, the converted-wave ($P-S_1$) image and a $P-S_2$ image from the horizontal recordings. The interpretation of the conventional and $P-S_1$ seismic sections mostly involves correlation of reflections appearing on the two sections. When correlation is possible, the value of the V_p / V_s ratio can be derived and related to lithology. Some information also can be obtained in the case of noncorrelated events, especially for the detection of fluid boundaries (Garotta, 1987).

The full potential of these data is still not being fully exploited; for example, polarization or velocity anisotropy, which are closely related to lithology and stratification. However interpretive methods are improving.

1.3 Thesis objective

The objective of this thesis is to develop processing algorithms that use both the vertical and radial components, for the 2-D case, and the vertical, radial and transverse components, for the 3-D case, to image the structure and lithology of the subsurface. Chapter 2 deals with the P - S separation filter when the geophone is located at the free-surface which uses the vertical and radial components. The P -and S -wave separation at a liquid-solid contact from the vertical and radial components is presented in Chapter 3. A new 3-D τ - p transform is presented in the appendix.

1.4 Data sets used in the thesis

All the algorithms that are derived in this thesis are tested with two different data sets: a synthetic data set and three-component data from the field.

1.4.1 Synthetic surface seismic data set

1.4.1.1 Free-surface solid *P-S* separation filter case

A horizontally layered earth model (Dankbaar, 1985) is used for testing the separation filter in the free-surface case. This model consists of five homogeneous layers on top of a half-space. The maximum reflector depth in this model is 200 m (Fig. 1.1). We consider a geometry with one shot and 40 geophones spaced every 5m, with an offset range of 5 - 200 m. Both shot and receivers are located at the top of the first layer. The synthetic data are calculated using the SIERRA seismic modeling package which employs ray tracing and spherical spreading.

Real seismic data contains refraction static problems especially if they are acquired in complex topographic areas. The filter was tested under these circumstances. A model was constructed which contains two homogeneous layers on top of a half-space medium. The second layer has a strong change in thickness. The maximum reflector depth in this model is located around 60 m (Fig. 1.2). The acquisition geometry consisted on a single shot and receiver at the same location (zero-offset data) located in the top of the model. The refraction statics calculated on this model were applied on the synthetic data acquired on the model shown in the Fig. 1.1.

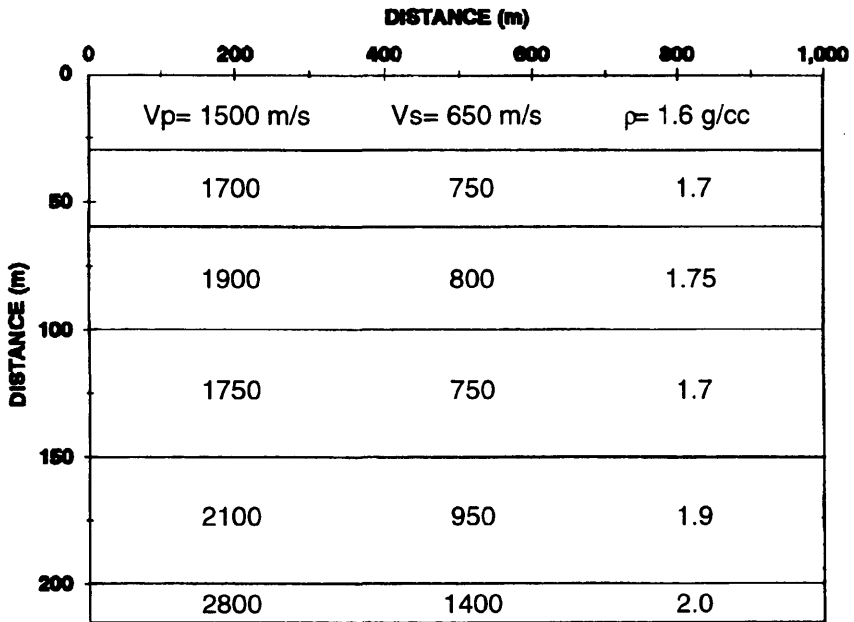


Fig. 1.1. A horizontally layered model used for testing the P - S separation filter in the free-surface case (after Dankbaar, 1985).

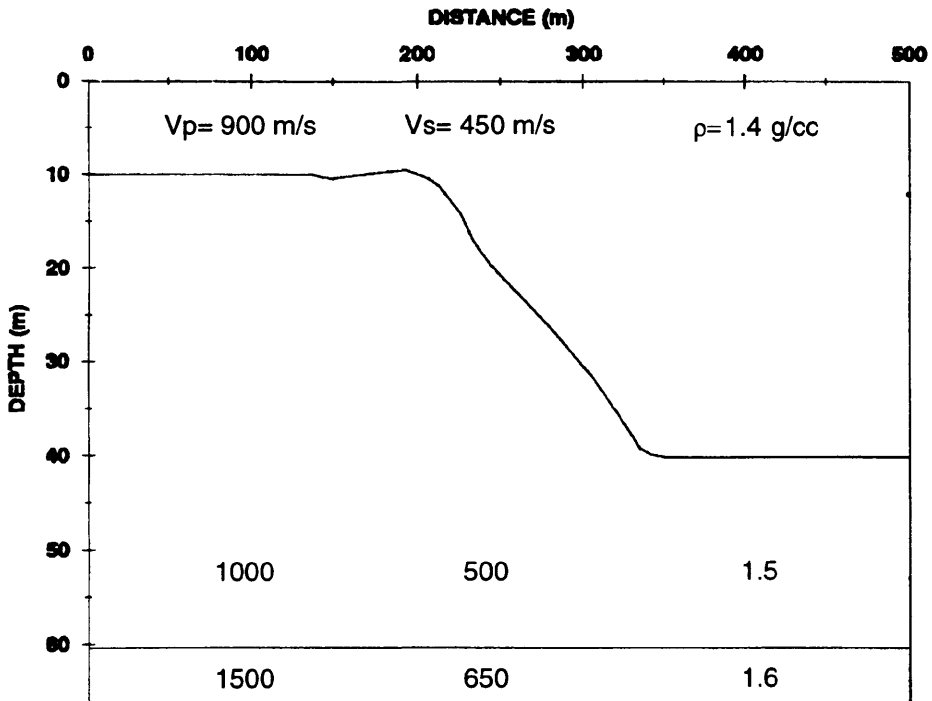


Fig. 1.2. Depth model used for testing the P - S separation filter in the free-surface case under strong problems in refraction statics.

1.4.1.2 Liquid-solid P - S separation filter case

A horizontally layered earth model (after Dankbaar, 1985) is used to test the separation filter in the fluid-solid case (Fig. 1.3). There are six flat homogeneous layers on top of a half-space. The first layer consists of a water layer 10 m deep and the maximum reflector depth in this model is 210 m. Geophone offsets are from 5 - 200 m, spaced every 5 m. The synthetic data are calculated using the SIERRA seismic modeling package which employs ray tracing and spherical spreading.

An additional 3C-2D data set was acquired over a two-dimensional model that contains a relatively thin lens. This model has six layers where the first consists of a water layer 30 m deep; all layers are laterally homogeneous except for a thin lens-like unit near the center (Fig. 1.4). The synthetic seismic data were generated in a shot-gather mode using the SIERRA ray tracing package. The survey consists in 25 shots extended from 500 to 5500 m on the model, separated 200 m each other and located in the top of the water layer. For each shot we have 80 geophones, spaced every 25 m, located in the bottom of the water layer.

1.4.1.3 2-D τ - p case

To test the 2-D τ - p algorithms implemented in this thesis a dipping-layer model was used where a single shot was acquired as is shown in the Fig. 1.5. The model basically consists in two layers with P -wave velocities of 2300 m/s and 3500 m/s, respectively.

1.4.1.4 3D τ - p case

To test the 3-D τ - p transform algorithm, a horizontally layered earth model with three flat homogeneous layers. Fig. 1.6 shows the depth model and the P wave velocities of each layer. This model was generated with the SIERRA modeling package. A

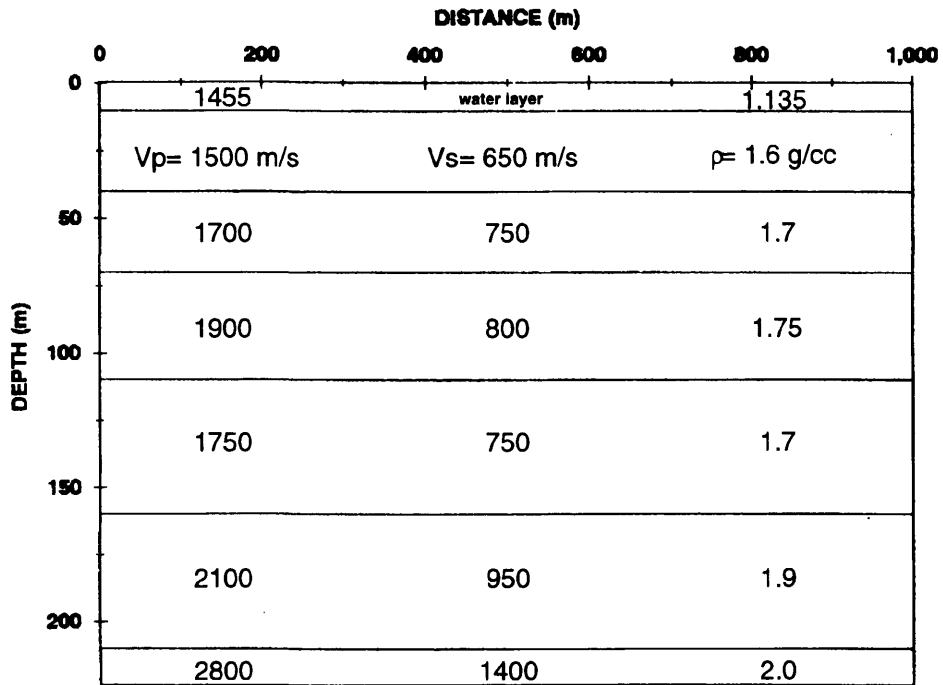


Fig. 1.3. Horizontally layered earth model used for testing the separation filter in the fluid-solid case (after Dankbaar, 1985).

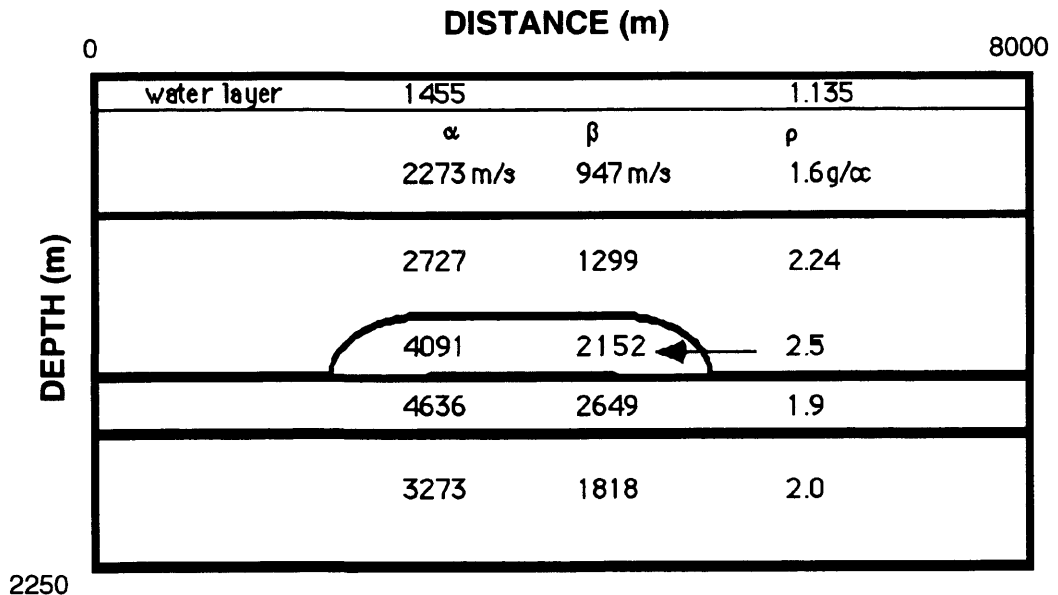


Fig. 1.4. Two dimensional model that contains a relatively thin lens. On this model was acquired a 3C-2D data set used for testing the separation filter in the fluid-solid case (after McCormack and Tatham, 1987).

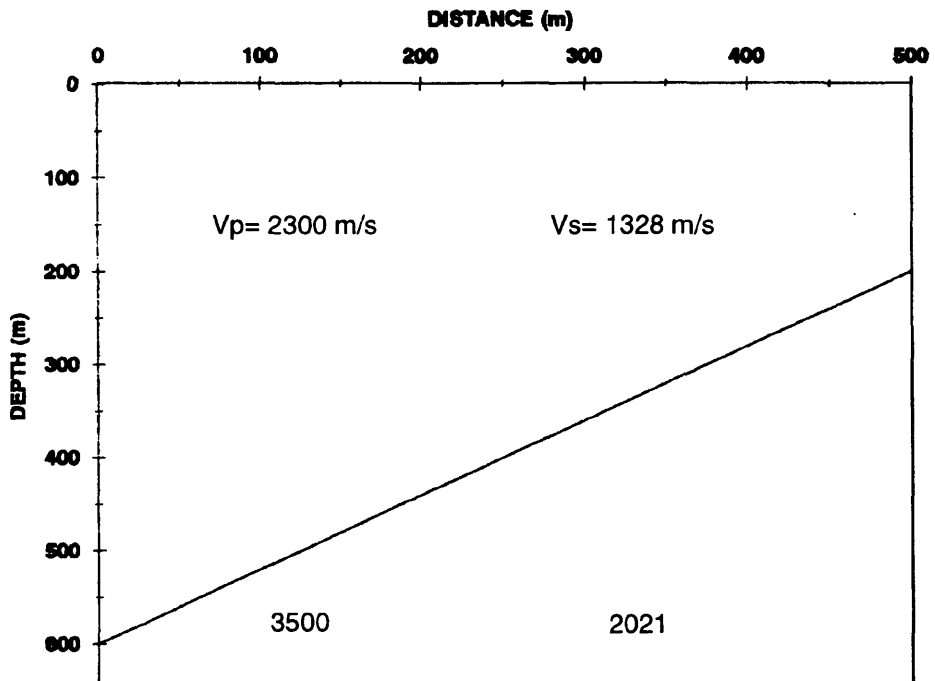


Fig. 1.5. Dip depth model which basically consists in two homogeneous layers used for testing the 2-D τ - p algorithms.

single 3-D shot record was acquired which consisted of 60 receivers distributed along six inline lines in the North-South direction and ten crosslines oriented East-West. The source was located at the bottom left corner of this patch (Fig. 1.7). The distance between inline and crossline lines was kept fixed at 75 m.

1.4.2 Field surface seismic data

1.4.2.1 Barinas, Venezuela

The objective of this survey was to estimate anisotropy parameters in a deep (approximately 3000 m) reservoir, through the acquisition of a 3C-2D data set. The data were collected in southwest Venezuela to map the strike, density, and extent of fractures in the hydrocarbon bearing formation of a reservoir. Well information indicates that the hydrocarbon bearing formation is a fractured limestone with a depth of approximately 3000 m, and gently dipping in NE-SW direction. Based on previous seismic *P* wave data, subtle lithological structures and small normal faults dominate the reflection horizons of the target zone. These structures appear to control the production history of the existing wells in the field, which implies the necessity of high resolution data for better definition of the seismic events.

Three 10 km multicomponent lines were centered over the reservoir along three different azimuths. The survey was designed to maximize the data quality with respect to resolution, signal-to-noise ratio, sufficient spatial and temporal sampling, correct near and far offsets, and maximum dip. This was to eliminate variations in amplitude or traveltimes that could be confused with lithological effects. Lines were positioned to intersect existing well control and surface seismic data in the area. Contour maps, from *P*-wave seismic data, show two systems of normal faults: one runs in northeast-southwest and the other in northwest-southeast directions. The azimuths of the two lines were set parallel to the two fault systems, and the third line bisected the first two, forming an angle of approximately

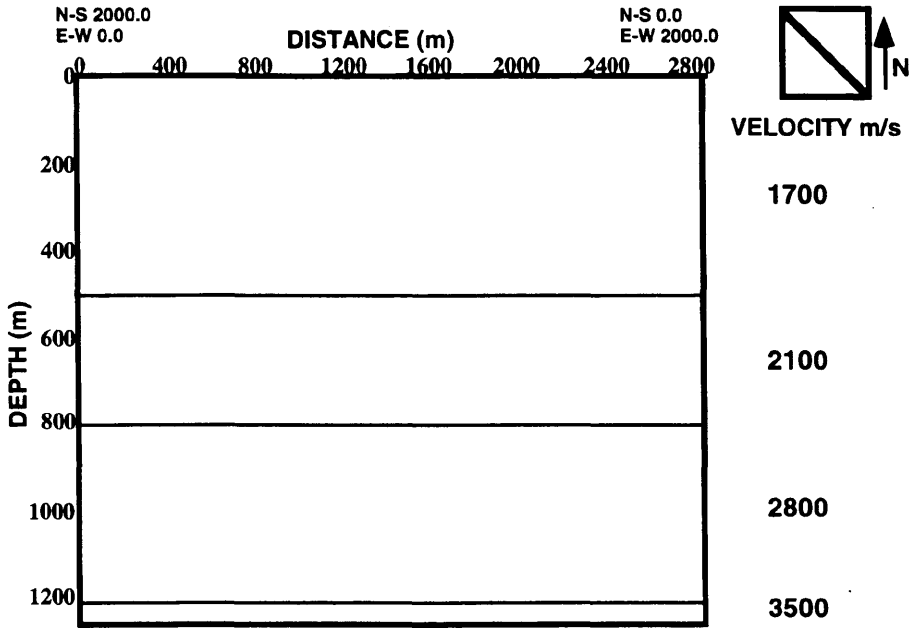


Fig. 1.6. Depth model representing a horizontally layered earth with constant P and S wave velocities used for testing the 3-D τ - p algorithm.

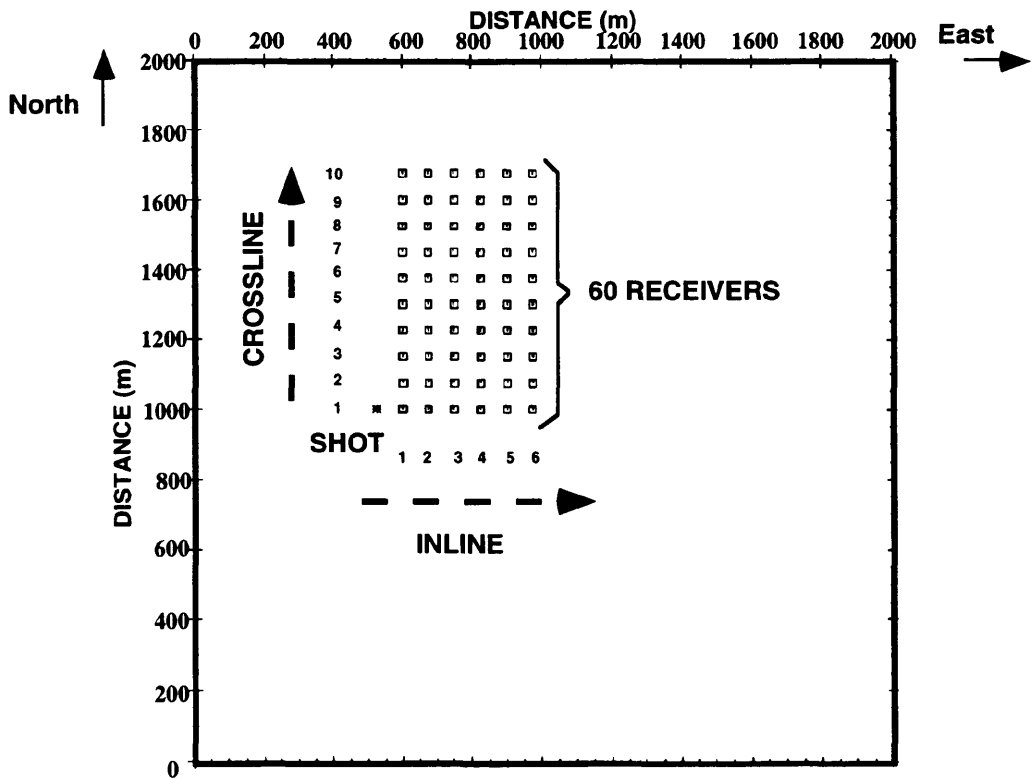


Fig. 1.7. Plan view of the acquisition geometry for a 3-D shot record.

41° with respect to line 1. Fig. 1.8 is an illustration of survey geometry with respect to the fault systems.

A noise-spread test was performed to examine the quality of converted waves, severity of ambient noise, surface wave amplitude and frequency, and optimum source and receiver spacing. This information was used to design an acquisition geometry that would prevent aliasing. The noise spread test consisted of a geophone spread of 240 strings (6 elements per string) and six shotpoints. The geophones were bunched with group interval of 3m for a total spread length of 720 m. The shotpoint interval was 720 yielding a maximum offset of 3.6 km (only 3 shotpoints were recorded due to field conditions yielding a maximum offset of 2.1 km). From a charge size and depth test it was determined that a charge of one kilogram at 10 m depth gave the best S/N ratio. To avoid aliasing of surface waves, the geophone group interval was set at 17 m with a linear array between stations. The far offset was extended to 3600 m, so the converted waves events would arrive outside the surface-wave cone. Geometry of the survey and recording parameters are given in Table 1.1.

1.4.2.2 Blackfoot, Alberta

A set of 2-D seismic lines were acquired over the Blackfoot field near Strathmore, Alberta. These lines included a variety of geophones: 2-C 2 Hz, 3-C 4.5 Hz, 3-C 10 Hz and vertical 10 Hz strings. The separation filter was used with the 10 Hz 3-C recordings which are standard industry receivers. The line was 4 km long with receiver stations at every 20 m and shot points of 6 kg charge of dynamite at 18 m depth, at every half station. The spread was fixed, and all 200 receivers were live for each shot. The ARAM-24 recording system, with 1660 line channels, was used as it could record to less than 1 Hz. The survey was acquired to image a Glauconitic sandstone reservoir and test whether *P-S* data could help elucidate the sand channels. Further testing objectives were to differentiate seismically between sand, shale and shale plug lithologies encased in the regional silts.

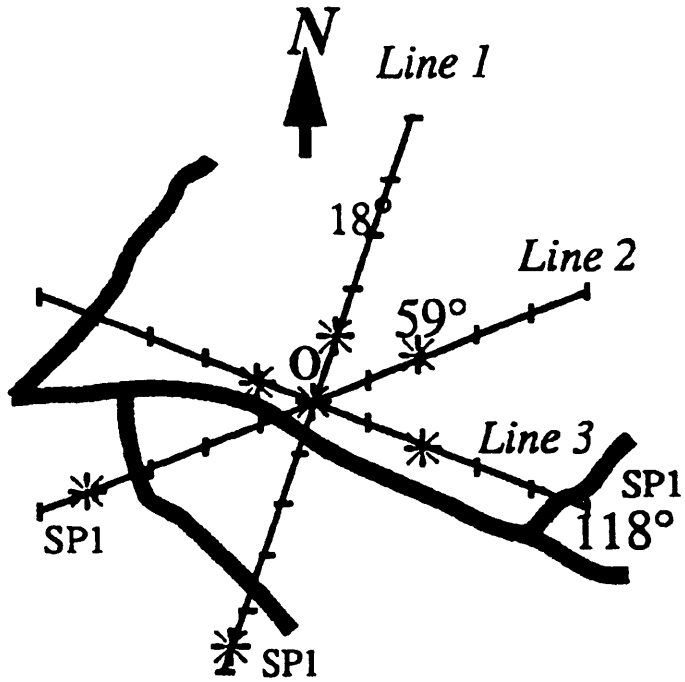


Fig. 1.8. Location map of the three 3C-2D seismic lines (Line 1, 2 and 3) acquired in Barinas area, Venezuela.

GEOMETRY	
Number of traces/component	216
Total number of 3-C receivers	648
Near offset trace	17 m (~ 55 ft)
Far-offset trace	3672 m (~ 12,000 ft)
Number of elements per string	6
Separation of geophone elements	3.4 m (~ 11 ft)
Total geophone spread	10 km (~ 33,000 ft)
Total number of shotpoints per line	124
Shotpoint space interval	51 m (~ 167 ft)
Charge depth	10 m (~ 33 ft)
Charge size	1 kg (~ 2.2 lb)
Source offset	17 m (~ 55 ft)
Geophone pattern	6 elements centered around the flag over 17 m (~ 55 ft)
RECORDING	
Total number of traces	648
Sample interval	2 ms
Low cut	out
High cut	128 Hz
Notch filter	out
Record length	6 s

Table 1.1 Geometry and recording parameters of survey

The Blackfoot oil pool is in a fluvial/estuarine Glauconite sand which is represented by incised valleys in the Lower Mannville Group of the Lower Cretaceous. Sands of this type comprise some of the most prolific oil and gas reservoirs in Alberta (Syhlonyk, 1995). They are at a depth of about 1550 m and can have thickness up to 43 m. Their importance and potential make them ideal reservoirs to study. They also are somewhat difficult to see on conventional *P* wave seismic. The 3C-2D seismic line 950278 crosses one such valley as shown in Fig. 1.9. The map is an isopach of channel thickness based on well control and 3-D seismic data.

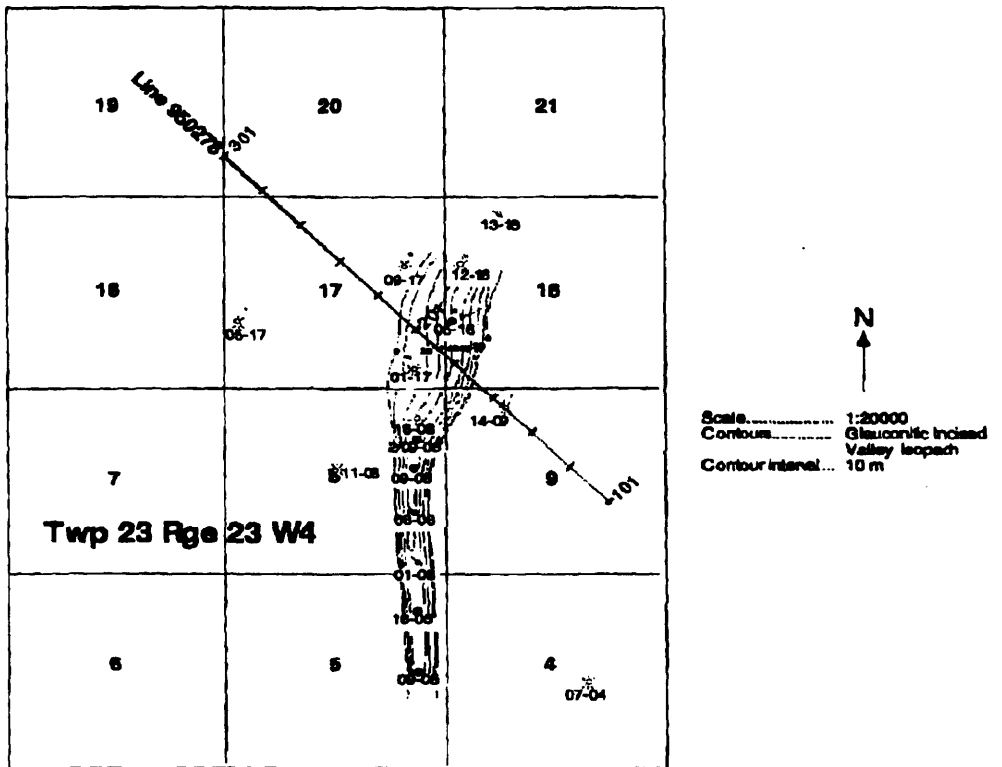


Fig. 1.9. Location map of 3C-2D seismic line 950278, well control and incised valley isopach in Blackfoot area (isopach map from Politylo, 1995).

Chapter 2 - Modal separation of 3C-2D surface seismic data

2.1 Introduction

The separation of the individual P and S arrivals may be considered a problem since both waves are recorded in both vertical and horizontal (in-line) geophones. In fact, it was shown by Miller and Pursey (1954) that in isotropic solids, a purely longitudinal (or purely shear) radiator stress field produces both longitudinal and shear wave radiation into the solid. Thus, shear and longitudinal radiation in isotropic solids cannot generally be considered separately. Also, due to the intrinsic response of an interface to impinging P and S waves as measured by vertical and horizontal geophones, P and S waves are observed on both geophones. A method of separating P and S waves in the τ - p domain is presented which inverts both vertical and horizontal records for the interface (or for short geophone) responses, thereby separating the two wavetypes. It will be shown that the P - S filter coefficients are function of the near-surface P - and S -wave velocities.

This work is an extension of the main ideas proposed by Dankbaar (1985) about the development of a new P - S separation filter. Dankbaar (1985) proposed the separation of the P and S waves from 3C-2D data through removing of the effects of the geophone responses in the f - k domain. In the present study the P - S separation filter is developed in the τ - p domain.

Both domains f - k and τ - p let us isolate P and S waves as well as remove noise (ground roll, multiple reflections, etc.) using specific properties of these waves after the transformation. In particular, the τ - p domain exploits the behavior of the apparent slowness p associated with each wave. But, working in τ - p domain offers some advantages: i) the coherent noise mute is more easily chosen in this domain, due to the data is seen directly in a time-like (i.e. τ) domain (Benoliel et al., 1987), ii) the application of frequency filtering fails when event frequencies are very similar. Also, the f - k filtering

operates linearly and cannot discriminate events which are of similar velocity (Evans, 1991). In contrast, the τ - p domain discriminates by velocity (or slowness p), and iii) it is possible to apply the local slant stack technique in the τ - p domain. The technique is effective for preserving event characters, for handling conflicting dips, and for reducing line spacing for 3-D surveys (Lu, 1990)

The P - S separation is tested using synthetic and real data. In both cases, the method demonstrates to be capable of separating P and converted reflections, even in presence of noise, and appears to be stable and have low sensitivity to errors in the near-surface P - and S -wave velocities.

2.2 Theory

The P - S separation method is based on the interface response as measured by a geophone. The resultant geophone response describes the amplitude at a receiver due to an incident wave, as a function of its angle of incidence (Dankbaar, 1985). Following this definition, we define by geophone responses the behavior of the amplitude at a receiver on an interface as a function of the angle of incidence for a range of values of this angle (Figs. 2.2 and 2.3).

In the P - S case considered here, only four types of geophone responses are involved, distinct for vertical and horizontal geophones and for incident P and S waves.

A useful way to express the P - S separation filter is represented by the horizontal and vertical geophone records in terms the geophone responses and incident P and incident S waves (Dankbaar, 1985). Since the geophone responses are a function of frequency and horizontal wavenumber, it is advantageous to decompose the data into plane waves, i.e. to transform the data to the τ - p domain. Then the expressions take quite simple forms as

$$U_V(\tau, p) = P_{in}(\tau, p)R_V^P(p) + S_{in}(\tau, p)R_V^S(p), \quad (2.1)$$

$$U_H(\tau, p) = P_{in}(\tau, p)R_H^P(p) + S_{in}(\tau, p)R_H^S(p), \quad (2.2)$$

where U_V and U_H are the vertical and horizontal geophone records transformed on the τ - p domain and P_{in} and S_{in} the incident P and S wavefields, respectively.

Once acquired the vertical and the horizontal records and given the near-surface P - and S -wave velocities, the geophone responses are determined, resulting in two equations with two unknowns which represent the incident P and S waves. The solution of these equations is straightforward

$$P_{in}(\tau, p) = F_V^P(p)U_V(\tau, p) + F_H^P(p)U_H(\tau, p), \quad (2.3)$$

$$S_{in}(\tau, p) = F_V^S(p)U_V(\tau, p) + F_H^S(p)U_H(\tau, p), \quad (2.4)$$

where the coefficients F are functions of the geophone responses R and can be considered as filter coefficients.

The outputs of the filter will be the pass- P (P_{in}) and pass- S (S_{in}), where the pass- P mode output consists of all waves that arrived at the surface as P wave, with the correct amplitude and phase of the incident waves; all S wave energy is removed. The same principle is applied over the pass- S mode, which consist of all waves that arrived at the surface as S wave, with the correct amplitude and phase of the incident waves; all P wave energy is removed.

2.3 Expressions and characteristics of the geophone responses

In order to relate the receiver responses of a geophone at the free surface of a homogeneous half-space to the radiation characteristic of a surface point source, the statement of the reciprocity relation given by White (1965) can be used. This statement goes back to the reciprocity relation for the Helmholtz equation (Morse and Feshbach, 1953). It says that the far field of a displacement of a single horizontal or vertical force (point source) is identical to the (horizontal or vertical) displacement at the surface caused by a distant source. In other words: the radiation characteristic of a distant (horizontal or vertical) surface point source is identical to the receiver responses of a (horizontal or vertical) geophone. Hence White's statement provides the possibility of using well-known formulae for the incidence characteristics of point sources acting on the free surface (e.g. Meissner, 1965) to calculate also the radiation pattern of horizontally and vertically directed point sources. The plane-wave approximation for the far field is used.

The geophone responses for single vertical and horizontal surface-forces which are equivalent to the geophone responses of vertical and horizontal geophones are given by Miller and Pursey (1954) and Cherry (1962), respectively.

The expressions of the geophone responses R_V^P , R_V^S , R_H^P , and R_H^S as derived by Miller and Pursey (1954) and White (1965) for a single geophone are given by

$$R_V^P = \frac{\cos \theta \left[1 - 2(V_s / V_p)^2 \sin^2 \theta \right]}{\left\{ \left[1 - 2(V_s / V_p)^2 \sin^2 \theta \right]^2 + 4(V_s / V_p)^3 \sin^2 \theta \cos \theta \left[1 - (V_s / V_p)^2 \sin^2 \theta \right]^{1/2} \right\}}, \quad (2.5)$$

$$R_V^S = \frac{\sin \theta \cos \theta \left[(V_s / V_p)^2 - \sin^2 \theta \right]^{1/2}}{\left\{ (1 - 2 \sin^2 \theta)^2 + 4 \sin^2 \theta \cos \theta \left[(V_s / V_p)^2 - \sin^2 \theta \right]^{1/2} \right\}}, \quad (2.6)$$

$$R_H^P = \frac{\sin \theta \cos \theta \left[1 - (V_s / V_p)^2 \sin^2 \theta \right]^{1/2}}{\left\{ \left[1 - 2(V_s / V_p)^2 \sin^2 \theta \right]^2 + 4 (V_s / V_p)^3 \sin^2 \theta \cos \theta \left[1 - (V_s / V_p)^2 \sin^2 \theta \right]^{1/2} \right\}}, \quad (2.7)$$

$$R_H^S = \frac{\cos \theta (1 - 2 \sin^2 \theta)}{\left\{ (1 - 2 \sin^2 \theta)^2 + 4 \sin^2 \theta \cos \theta \left[(V_s / V_p)^2 - \sin^2 \theta \right]^{1/2} \right\}}, \quad (2.8)$$

The effect of the geophone responses on an incident S wave, radiated by a point source and reflected at horizontal interface, as a function of angle of incidence θ , between 0 and 50 degrees, is shown in the Fig. 2.1a. Due to the geophone response of the vertical and horizontal geophones the S -wave displacement is recorded with different behavior on both records showing changes in amplitude and phase (Fig. 2.1d,e). It is evident from this figure that both incident P and incident S waves are observed on vertical and horizontal geophone records due to the overlapping of the radiation characteristics associated with both waves for certain angles of incidence θ , between 30 and 60 degrees.

If we consider the horizontal slowness which is defined as the reciprocal of velocity along the horizontal direction ($p = \sin \theta / V$, θ is the incidence angle measured from the vertical) then the geophone responses can be written as a function of horizontal slowness p , given:

$$R_V^P(p) = 2\gamma^{-1} \xi (2V_s^2 p^2 - 1) / R_o(p), \quad (2.9)$$

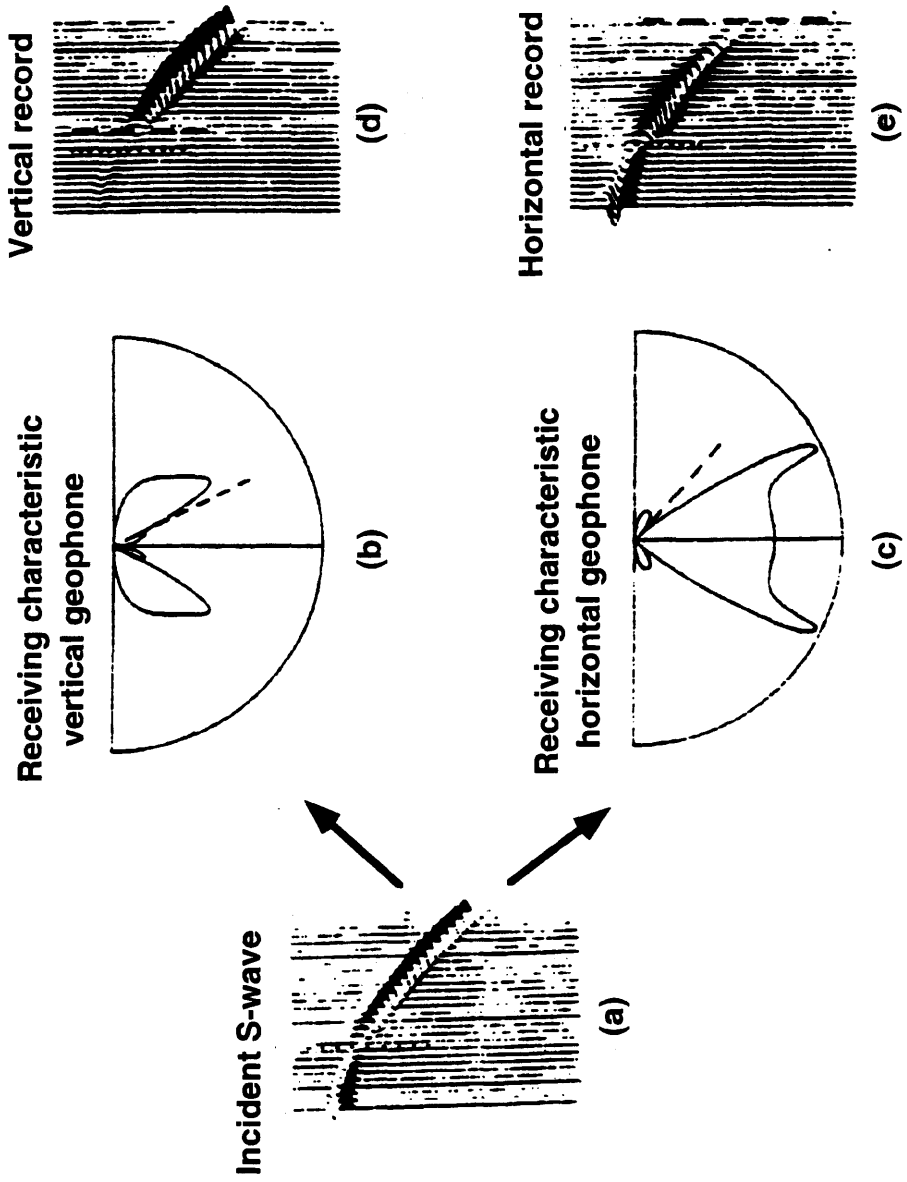


Fig. 2.1. Effect of receiving characteristic on an incident SV wave. (a) SV wave incident at the surface for equidistant offsets, (b) and (c) receiving characteristics of vertical and horizontal geophones, (d) and (e) shear wave as recorded on vertical and horizontal geophones (after Dankbaar, 1985).

$$R_{V_o}^S(p) = 4V_s p \xi \eta / R_o(p), \quad (2.10)$$

$$R_{H_o}^P(p) = 4V_p p \xi \eta / R_o(p), \quad (2.11)$$

$$R_{H_o}^S(p) = 2\eta(1 - 2V_s^2 p^2) / R_o(p), \quad (2.12)$$

where $\gamma = V_s/V_p$, $\xi = (\gamma^2 - V_s^2 p^2)^{1/2}$, $\eta = (1 - V_s^2 p^2)^{1/2}$, and

$$R_o(p) = (1 - 2V_s^2 p^2)^2 + 4p^2 V_s^2 \xi \eta.$$

It is evident from eq.(2.9) to eq.(2.12) that the geophone responses only depend on the P -wave and S -wave velocities at the near-surface (Fig. 2.2). In Fig. 2.2a the radial motion is entirely compressional, with amplitude real and independent of frequency. The tangential motion travels at shear speed, with amplitude independent of frequency but subject to a phase shift for angles beyond the critical angle $\eta (= \sin^{-1}(V_s/V_p))$. In the vertical plane containing the direction of the force, radial and tangential displacements vary as shown in Fig. 2.2b for a horizontal force. The shear curve again indicates that the amplitudes in eq. (2.12) is complex.

In order to show the effect of the P - and S -wave velocities on the geophone responses, two different velocity values were selected as shown in the Fig. 2.3. The response of the vertical geophone is not much affected by the selected P - and S -wave velocities, but the response associated with the horizontal geophone shows moderated changes, particularly for the geophone responses of the SV wave. In fact, the amplitude at the critical angle η (25° for Fig. 2.3b and 30° for Fig. 2.3d) increases when the V_p/V_s ratio (Poisson's ratio) decreases (increases). For angles of incidence beyond the critical

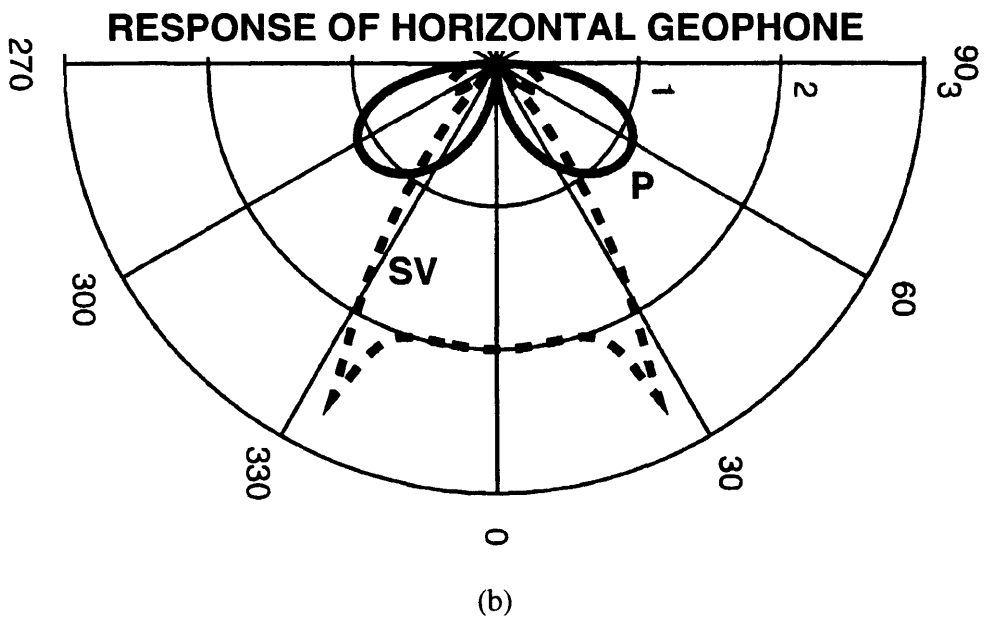
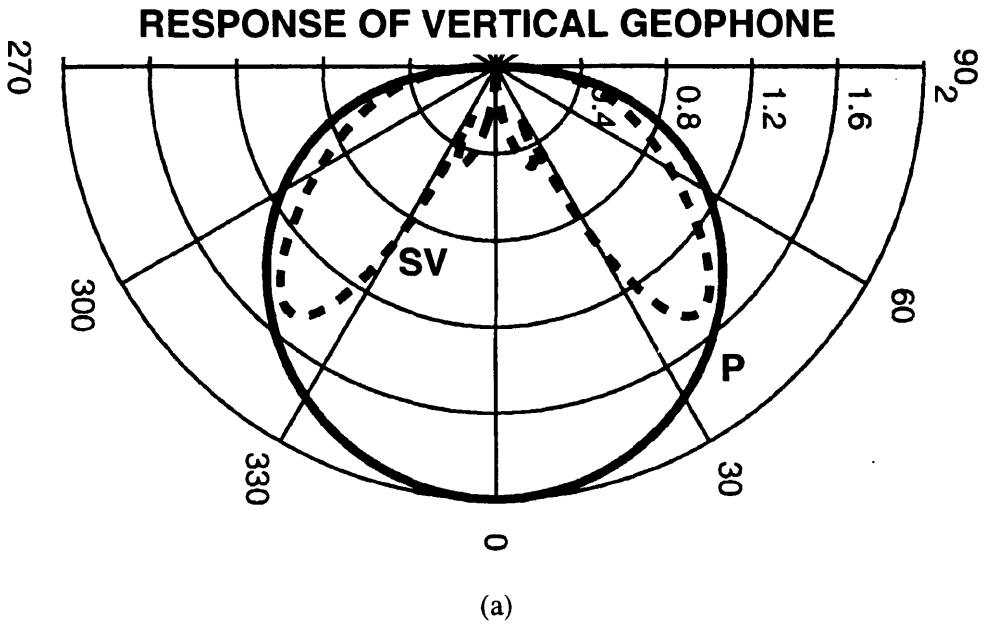


Fig. 2.2 Response, in polar diagram form, of the vertical (a) and horizontal (b) geophones located on the surface of a solid (stress-free) for P waves and S waves as a function of angle of incidence. Parameter values are: $V_p = 1500$ m/s and $V_s = 650$ m/s.

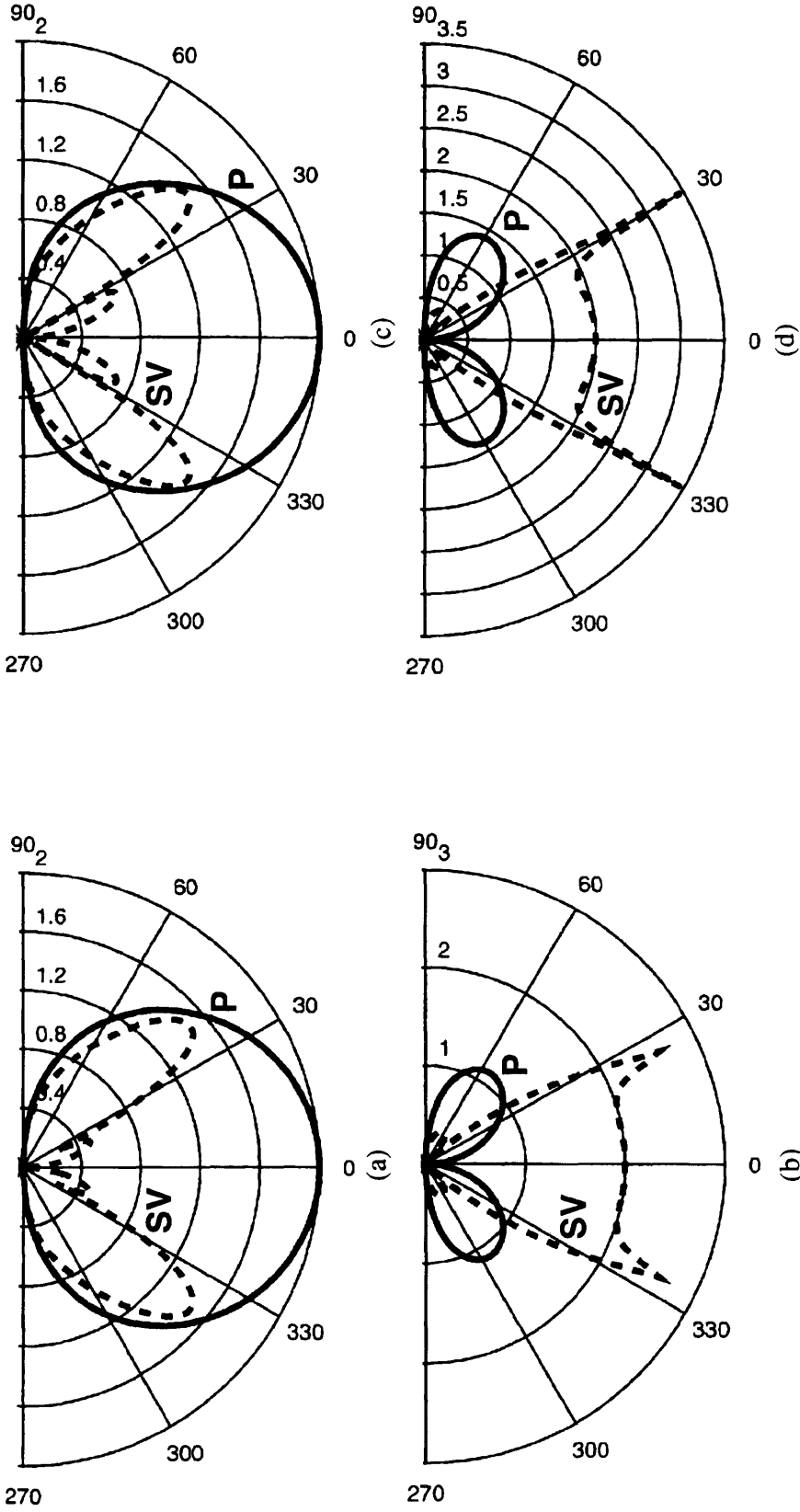


Fig. 2.3. (a,b) Response, in polar diagram form, of the vertical (a) and horizontal (b) geophones, located on the surface of a solid (stress-free) for P and S waves as a function of the angle of incidence. Parameter values for this case are: $V_p=1275$ m/s and $V_s=552.50$ m/s.
 (c,d) Response, in polar diagram form, of the vertical (c) and horizontal (d) geophones, located on the surface of a solid (stress-free) for P and S waves as a function of the angle of incidence. Parameter values for this case are: $V_p=2000$ m/s and $V_s=1000$ m/s.

angle the response for SV wave remains unaffected. Then, from these observations is expected that the P - S separation filtering will be not significantly affected by errors in the estimation of the P - and S -wave near-surface velocities.

Above have been used a theoretical approach to the geophone responses but can we expect the same geophone responses in a real acquisition?. The answer is given by the physical modeling technique which uses piezoelectric transmitter as source and receiver and represents the subsurface by scaled models. A description of the physical modeling technique and measuring devices normally used are given by Behrens and Waniek (1972) and Behrens and Dresen (1982).

In physical modeling work, the piezoelectric transmitters (sources) act as an approximate point source creating P - and S -wave radiation. Fig. 2.4 depicts a typical example of a radiation pattern from a normally used source for P and S waves, when the source is placed on the free surface of a two-dimensional model. The S -wave radiation pattern is composed of two almost symmetrical lobes with two maximum intensities, indicating its dependence on the radiation angle. It is shown that the greatest amplitude of S wave radiation is comparable to that of the P wave radiation (Kim and Behrens, 1985).

When the same source is placed upon a two-dimensional model plate, another typical example of a radiation pattern for P and S waves is obtained, as shown in Fig. 2.5. Within the radiation (or incident) angle range (194° - 225°) indicated with arrows, the shear wave radiation is clearly dominant in comparison to the P wave radiation.

From Figs. 2.4 and 2.5 it is evident that we can see that both theoretical and experimental geophone responses have almost the same behavior with a slight differences. This result suggests that the P - S separation filter using the theoretical approach to the vertical and horizontal geophone responses will provide accurate results.

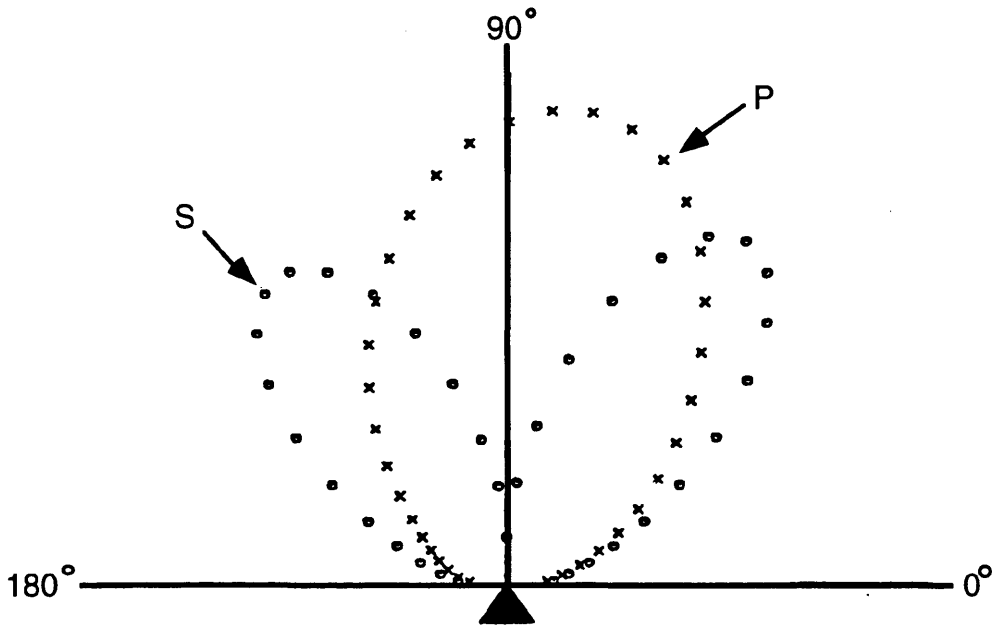


Fig. 2.4. Radiation pattern of a model-seismic source (piezoelectric transmitter) normally used. The source is placed on the free surface of a two-dimensional model (after Kim and Behrens, 1985).

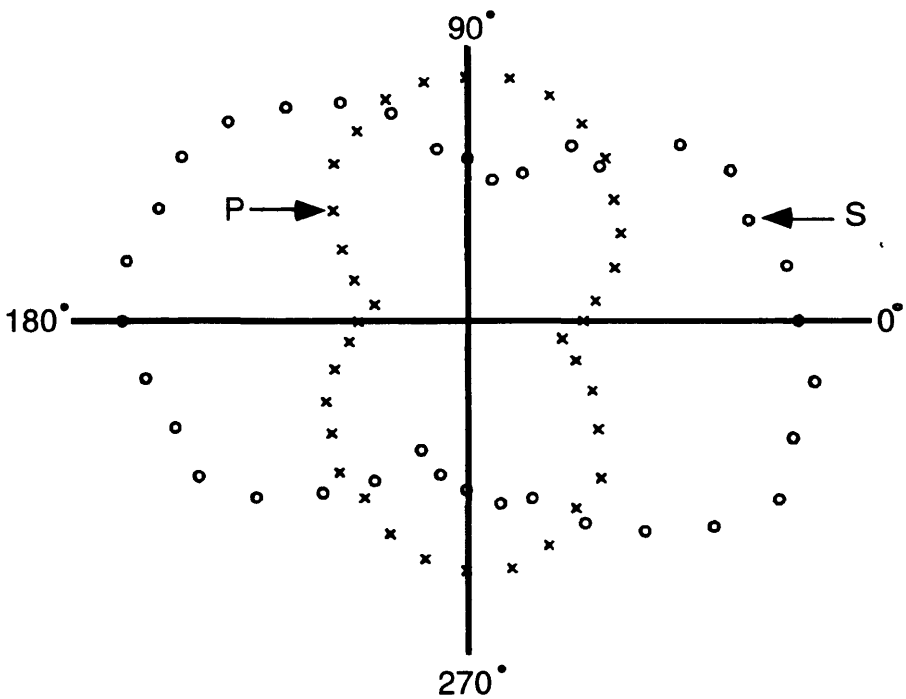


Fig. 2.5. Radiation pattern of a model-seismic source (piezoelectric transmitter) normally used. The source is placed upon a two-dimensional model plate (after Kim and Behrens, 1985).

2.4 Expressions and characteristics of the tau-p transform in the 2-D domain

Plane-wave decomposition of a wave field can be achieved by applying linear moveout (LMO) and summing amplitudes over the offset axis. This procedure is called slant stacking or τ - p transformation (Yilmaz, 1987; Claerbout, 1978). Slant stacking replaces the offset axis with the ray parameter p axis where the ray parameter is the inverse of the horizontal phase velocity.

Each trace in the tau- p gather represents a plane wave that propagates with a certain slowness. In reality when a source explodes, the energy propagates at all angles (Fig. 2.6a). The reflected energy arrives at different receiver groups at different angles because of the offset between source and receiver locations. The farther the offset or the shallower the reflecting interface, the more oblique the angle of the upcoming wavefront.

First we will consider how plane waves can be generated. Fig. 2.6b shows a line of point sources. Assume that this line of sources is activated so that all points on the line are excited simultaneously and each point generates a spherical wave field. Some distance from the surface, the spherical waveforms superimpose and result in a plane wave that travels vertically downward. This plane wave reflects from an interface and is recorded by a receiver at the surface.

The superimposed response is recorded on a single receiver (Fig. 2.6c). This response is in the form of a plane wave that is reflected from an interface. Superposition means summing over the shot axis for a receiver location. Using reciprocity, the summation also can be performed over the receiver axis for a given shot location. This reciprocity indicates how a common shot gather, as a single wave field, can be decomposed into its plane-wave components. By replacing the shot axis in Fig. 2.6d with the receiver axis, the raypath geometry in Fig. 2.6e results. The time delay associated with the plane wave that travels at angle θ from the vertical is given by:

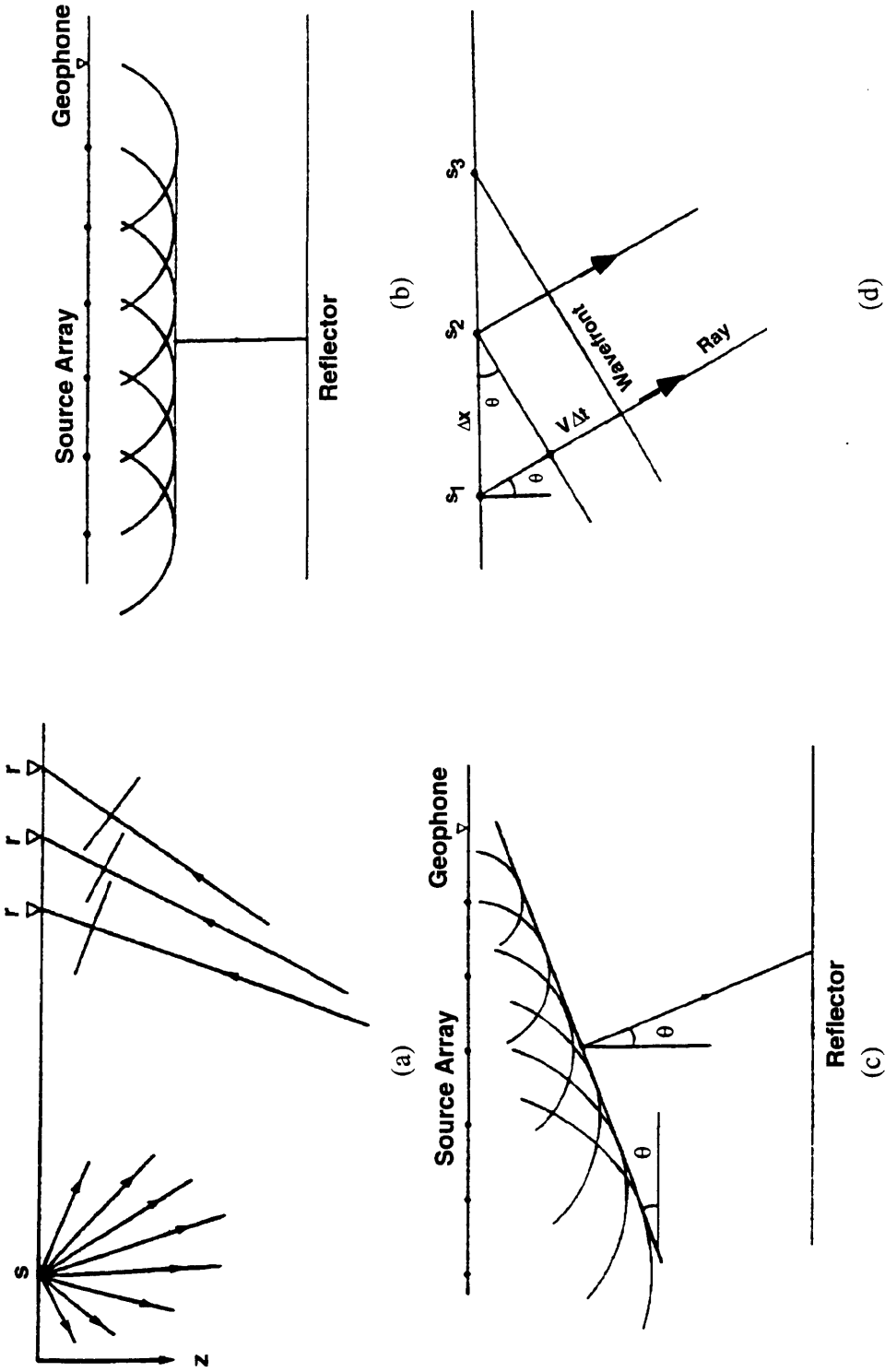


Fig. 2.6. (a) A seismic source generates waves that propagate in all directions; waves traveling in different directions are recorded at different locations. (b) A vertically incident plane wave is generated by setting off many shots in unison. (c) A plane wave that travels at angle θ from vertical is generated by setting off many shots (starting from left) at appropriate time intervals. (d) Computation of time interval between shots (S) to generate the oblique plane wave in (c). (after Yilmaz, 1987).

$$\Delta t = (\sin \theta / V) \Delta x \quad (2.13)$$

Snell's law says that the quantity $\sin \theta / V$, which is the inverse of the horizontal phase velocity, is constant along a raypath in a layered medium (Fig. 2.6f). This constant is called the ray parameter p . Eq. (2.13) then is rewritten as:

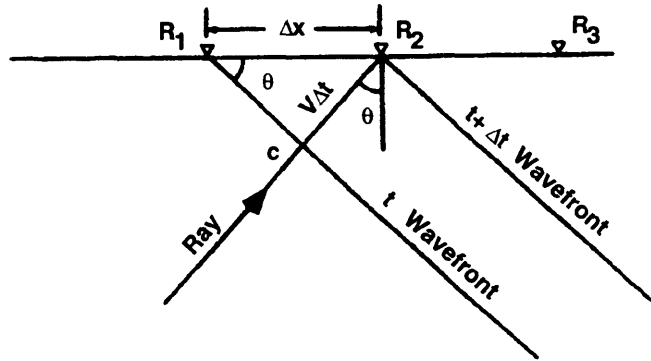
$$\Delta t = p \Delta x \quad (2.14)$$

The angle of propagation of the plane wave is controlled by adjusting the p value. Setting $p=0$ corresponds to a plane wave that travels vertically. Given p and the velocity model for the layered earth, the family of raypaths associated with a particular p value can be traced as shown in Fig. 2.6g. For a single p value, the signal is recorded at many offsets. In general, receivers at all offsets record plane waves of many p values. To decompose the offset gather into plane-wave components, all the trace amplitudes in the gather must be summed along several slanted paths, each with a unique time delay defined by eq. (2.14). The equation used to define a slant stack (Stoffa et al., 1981) can be written

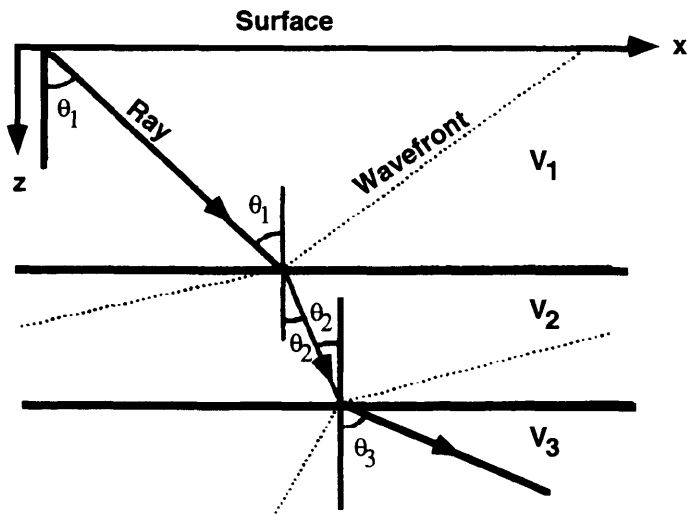
$$h(p, \tau) = \sum_{i=1}^{nx} g(x_i, \tau + px_i) \quad (2.15)$$

where g is the seismic data consisting of nx traces and h is the slant stack data. The value of h at the point (p, τ) is obtained by adding the data $g(x, t)$ along the straight line $t = \tau + px$, where p is the slope of this line and τ is the intercept time where $x=0$.

A schematic description of the plane-wave mapping described by equations (2.14) and (2.15) is shown in Fig. 2.7a. We start by summing amplitudes in the offset domain along the horizontal path, $p=0$. This line intersects the reflection hyperbola in the vicinity of the apex A. Thus, point A maps onto point A' on the (p, τ) plane. By tilting the summation line, the hyperbola is intersected at location B, which maps onto B'. Note that

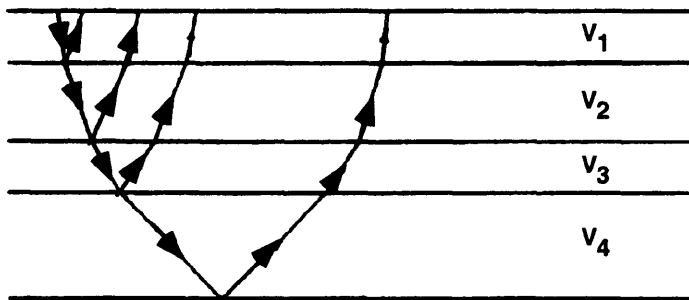


(e)



$$\frac{\sin \theta_1}{v_1} = \frac{\sin \theta_2}{v_2} = \dots = \frac{\sin \theta(z)}{v(z)} = p$$

(f)



(g)

Fig. 2.6. (e) The reciprocity principle applied to the geometry of Fig. 2.6d to replace shots (S) with receivers (R). (f) If the ray parameter p is specified, then the ray can be traces in a horizontally layered earth model with a known velocity function $v(z)$. (g) Some raypaths for a given p value, corresponding to a single trace in the (τ, p) plane (after Yilmaz, 1987).

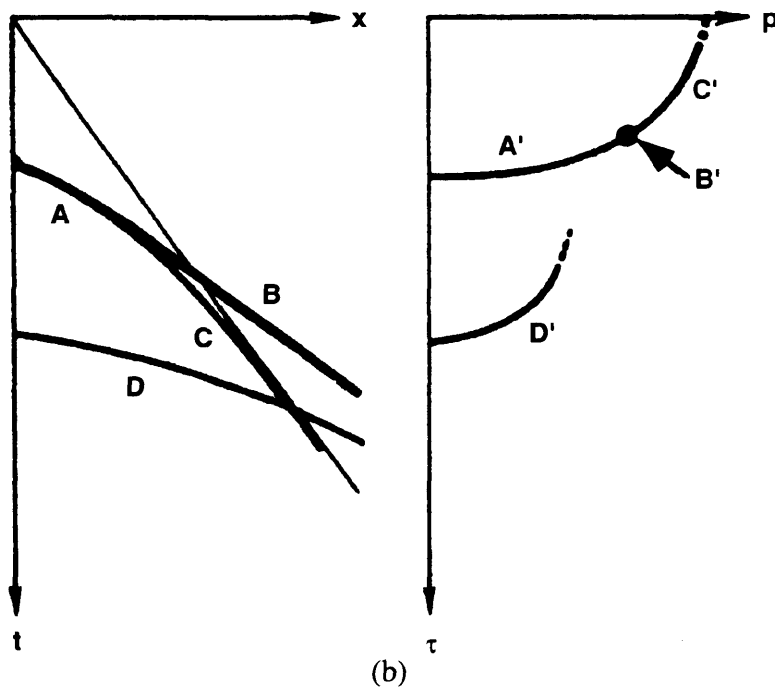
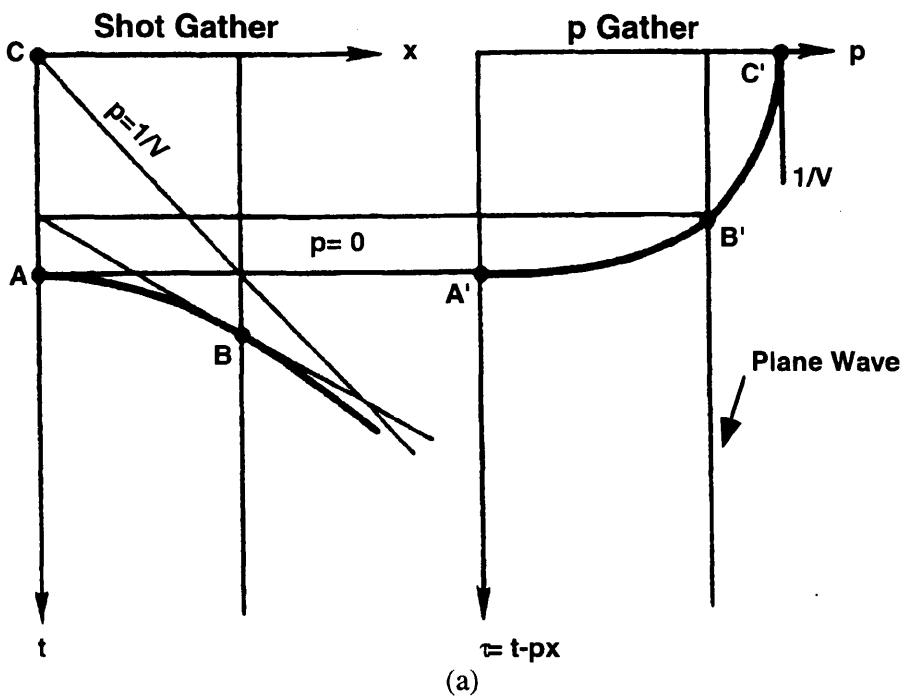


Fig. 2.7. (a) A Hyperbola on a shot gather maps onto an ellipse on the p -gather.
 (b) Various arrivals on a shot gather mapped onto the corresponding p -gather.
 Events A, B, C, and D map onto A', B', C', and D' (after Yilmaz, 1985).

a major contribution to summation along the slanted path comes in the area of tangential point B. The steepest necessary path of summation is along $p=1/V$, which is the asymptote to the hyperbola. This path corresponds to rays that are 90° to the vertical. The energy along the hyperbolic trajectories in the (x, t) domain are mapped to elliptical trajectories in the (p, τ) domain (Schultz and Claerbout, 1978). In reality, we never record a hyperbola with infinite extent nor a zero-offset trace. Therefore, the elliptical path in the slant-stack domain never is complete from A' to C' (Yilmaz, 1987).

A more complicated situation is shown in Fig. 2.7b. Subcritical reflections A and D (those with an angle of incidence smaller than the critical angle) map into the region of lower p values, while supercritical reflections C (wide-angle reflections) map into the region of higher p values. Ideally, a linear event in the offset domain, such as a refraction arrival B, maps to a point in the slant stack domain. Conversely, a linear event in the slant stack domain maps to a point in the offset domain.

The mathematical transform defined by equation (2.15) has an inexact inverse which can be written

$$g(x, t) = \sum_{i=1}^{np} h(p_i, t - xp_i) \quad (2.16)$$

The equation (2.16) represents an inverse of the slant stack process which let us move from the (p, τ) domain to (x, t) domain. This inverse is quick and easy to implement but not exact.

A variety of schemes can be used to construct both the forward and inverse slant stacks of a discrete, two-dimensional data set. Each technique has advantages and disadvantages corresponding to its particular implementation. One of the main differences between the various schemes is the domain in which they are carried out. For example, forward and inverse slant stacks performed in the space-frequency, (x, f) , domain can be

accurate (Beylkin, 1987), but difficulties with singularities and the solution of large systems of equations must be dealt with.

Regardless of the method used, reconstructing the (x, t) data from the (p, τ) data is more complex problem than the forward process. Some methods involve performing a second forward slant stack in combination with the application of a filter (Thorson, 1978 Tatham, 1984). Heuristically, performing the second slant stack invokes the notion of points transforming to line and vice-versa. Thus, starting with a single point in (x, t) space produces a single line in (p, τ) space. The second slant stack then reproduces the point from the line. However, slant stacks of lines for finite-length, discrete data do not transform exactly into points (Phinney et al., 1981). This property is independent of the slant stack method used.

Basically we will discuss two methods for developing the slant stack process, these are: (x, t) method and (f, k) method. Both methods will be tested with a data obtained on a steep dip model. The results obtained from that experiment let us decide which method will be better for being used in the P - S separation filter.

2.4.1 The (x, t) method - forward and inverse slant stack process

2.4.1.1 Construction of slant stack

Two step typically are used in synthesizing plane waves by summing amplitudes in the offset domain along slanted paths. First, a linear moveout (LMO) correction is applied to the data through a coordinate transformation (Claerbout, 1978):

$$\tau = t - px \tag{2.17}$$

where p is the ray parameter, x is the offset, t , is the two-way traveltime, and τ is the linearly moved out time. After LMO, an event with slope p on input is flat. Next, the data are summed over the offset axis to obtain:

$$F(p, \tau) = \sum_x P(x, \tau + px) \quad (2.18)$$

Here, $S(p, \tau)$ represents a plane wave with ray parameter $p = \sin\theta/V$. By repeating the LMO for various values of p and performing the sum [eq. (2.18)], the complete slant-stack gather (or p -gather), which consists of all the dip components in the original offset data, is constructed.

In addition to the slowness stack [eq. (2.18)], another useful function is semblance. This function has found wide use in detecting coherent arrivals across an array (Taner and Koehler, 1969). The definition of semblance is

$$S = \frac{\sum_W \left(\sum_{k=1}^N y_k \right)^2}{N \sum_W \sum_{k=1}^N y_k^2} \quad (2.19)$$

where y_k is the sample of the k th trace which lies along a trajectory through the x - t plane, and W represents a time window centered about the trajectory. The time window W adds stability to the semblance statistic, but has the disadvantage of decreasing the time resolution of event detection. For this study we chose the window to be one sample in width, thereby dropping the sums over W . In addition, we chose linear x - t trajectories as defined by equally spaced horizontal ray parameters. This is a natural selection since for a given waveform it is proportional to the reciprocal of the velocity of the arrival across the array. Thus, the resolution of a subarray is characterized by a data, semblance is defined by an equation similar to eq. (2.18)

$$S(p_j, \tau_i) = \frac{\sum_{k=1}^N \left[\sum_{k=1}^N P(x_k, \tau_i + p_j x_k) \right]^2}{N \sum_{k=1}^N \left[\sum_{k=1}^N P(x_k, \tau_i + p_j x_k) \right]^2} \quad (2.20)$$

Semblance can be considered to ratio of output to input energy aligned along the proposed trajectory (Neidell and Taner, 1971). It also has the important property that its value is independent of the amplitude of the arrival to be detected. That is the normalized statistic which has a maximum value of 1 and minimum value approaching $1/N$ (Stoffa et al., 1981).

The slowness stack and semblance may each be considered the result of a filtering operation on the original $x-t$ data.

2.4.1.2 Alias suppression by semblance windowing

The slowness stack and semblance are both useful functions, each with its own desirable characteristics. The stack preserves amplitudes and waveforms but can be severely aliased (Stoffa et al., 1981). Aliased energy of strong arrivals may often be stronger than the primary energy of weak arrivals. Semblance yield uniform, high amplitudes for arrivals with even modest signal-to-noise (S/N) ratios provided they are not dominated by interfering coherent events. It also suppresses aliased energy, except for narrow band signals. These properties suggest that semblance can be used to derive a window functions $W(\tau, p)$ which, when applied to individual slowness stacks, yields true amplitude, unaliased $\tau-p$ stacks for individual subarrays (Stoffa et al., 1981). The final $\tau-p$ data can then be found by summing each windowed $\tau-p$ stack

$$R(p_j, \tau_i) = \sum_{l=1}^M W_l(p_j, \tau_i) F_l(p_j, \tau_i) \quad (2.21)$$

where the sum on l is over M subarrays.

The ideal window function would have a value of one where there were primary arrivals in τ - p space and zero elsewhere.

Semblance itself could be used directly as the window function, but it is not zero in the presence of random noise, approaching $1/N$ where N is the number of traces. In addition, it tends to small values near zero crossings of the waveform which would cause pulse distortion. This suggests that the window function be derived by smoothing the semblance data, followed by thresholding.

Fig. 2.8 shows in detail the windowing procedure for the slowness stack corresponding to the ray parameter 445 s/km. On the left is the original slowness stack. The high-frequency arrivals greater than about 12.4 s of the two-way traveltime re all arises from the sea floor reflection. To the right of the slowness stack is the corresponding unit sample semblance trace which has significant values for only the unliased primary arrival. The next trace is semblance after the application of the 0-10 Hz low-pass filter. The only significant amplitude in this trace is now centered on the envelope of the primary arrival. Next, a rectangular window based on a minimum acceptable semblance value of 0.35 is shown. The final traces in this figure are the windowed and deconvolved slowness stack, respectively.

Fig. 2.9(a,d) is a second example of the windowing procedure for a synthetic data. The original data in the τ - p domain is shown in the graphic at the left and the next display is the semblance after the application of the 2-8 Hz low-pass filter, calculated for every sample time and for the same ray parameters in the Fig. 2.9a. Again the only significant amplitudes in this data are now centered on the envelope of the primary arrivals. A threshold of 1.6E-02 was applied over the filtered semblance (Fig. 2.9c), and finally it was multiplied by the original slowness stack (Fig. 2.9a). This new slowness stack has removed all alias contributions and it is cleaner than the original one.

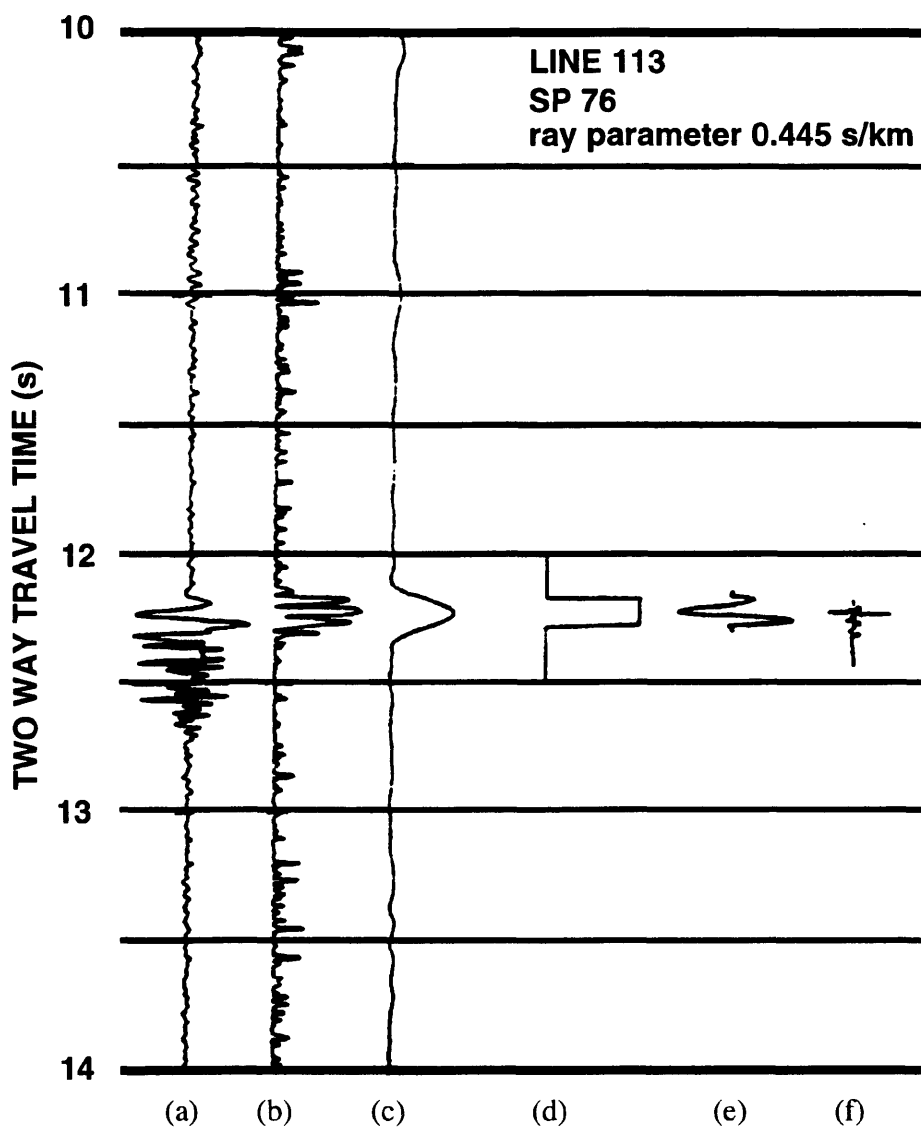


Fig. 2.8. Detail of the derivation and application of the semblance derived window function.

- (a) Slowness stack for a horizontal ray parameter of .445 s/km. The arrivals after about 12.6 s are alias contributions from the sea floor reflection.
- (b) Semblance calculated for every trace time sample for the same ray parameter. The principal contributions are from the primary wavelet.
- (c) Results from the application of a 0-10Hz bandpass filter to the unit sample semblance trace.
- (d) A rectangular window is then derived by defining all values of the band-passed semblance trace above .35 as a unity and all over values as 0.
- (e) The recovered primary wavelet before deconvolution.
- (f) The recovered primary wavelet after deconvolution (from Stoffa et al., 1981).

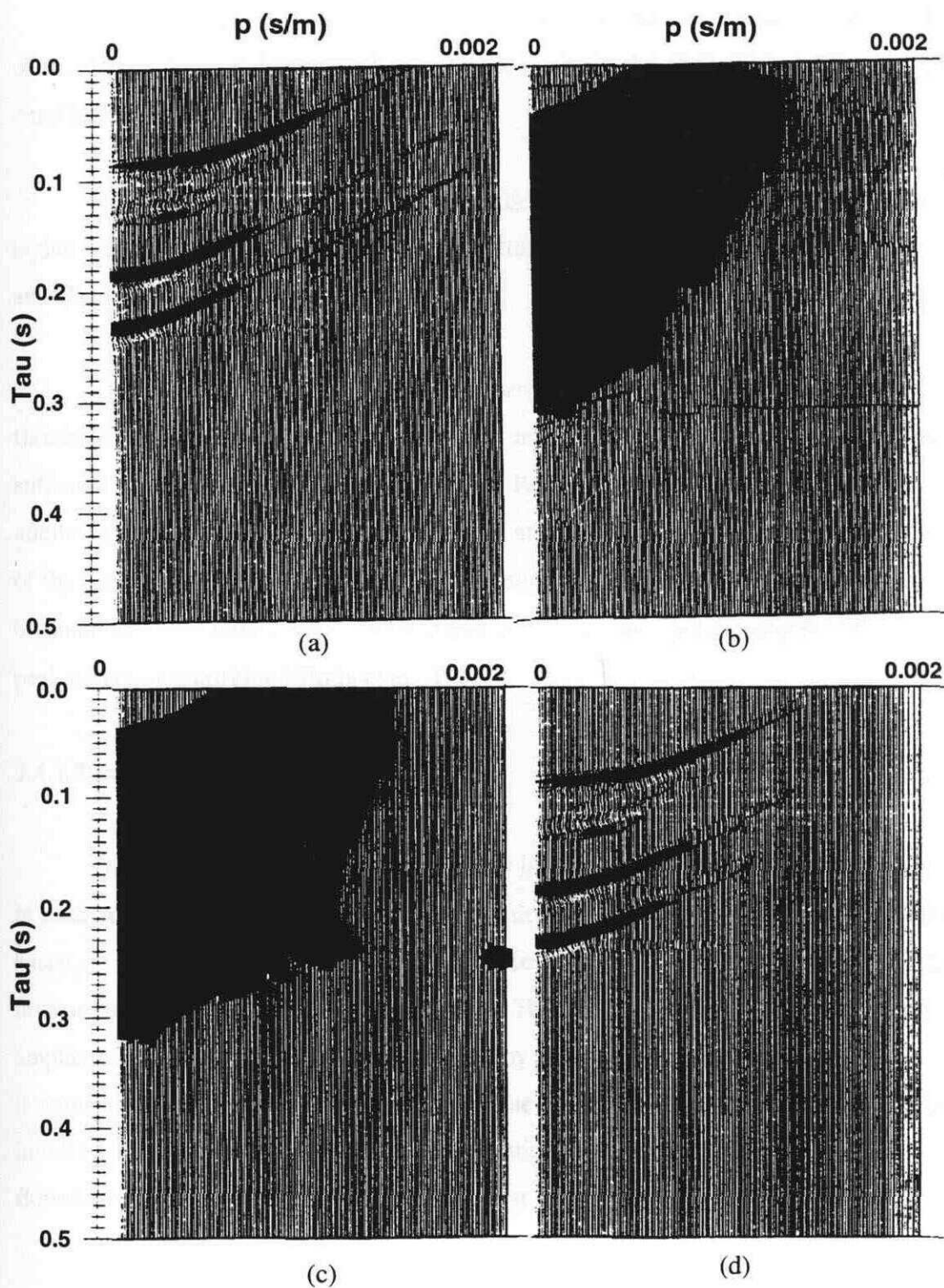


Fig. 2.9. (a) Data in the τ - p domain. (b) Filtered semblance. (c) Filtered semblance multiplied by the threshold value. (d) Data in the τ - p domain multiplied by (c).

The threshold value, it is calculated from the maximum amplitude on the first trace of the data in the τ - p domain and after that it is obtained a percentage of the maximum amplitude value which is selected by the user.

We can increase resolution as a function of ray parameter and time by using a higher semblance threshold. This results in better definition of loci of the principal arrivals and also in distortion of the waveforms.

The mapping without the semblance-derived window is severely aliased. With the threshold the aliases are diminished. Even a modest threshold of 0.1 for these data is sufficient to eliminate most of the aliasing. Raising the threshold above 0.1 removes additional aliasing but leaves only the principal arrivals. This results in improved resolution of the loci of wide-angle reflections and refractions in the τ - p plane. These data can now be manually interpreted or the τ - p locations of the arrivals can be recognized by a simple peak detection algorithm (Stoffa et al., 1981).

2.4.1.3 Inverse

Once a particular process is carried out in the slant-stack domain, inverse mapping is used to reconstruct the data in the offset domain. The inverse process is developed based on equation (2.17). To restore amplitudes properly, *rho* filtering is applied before inverse mapping (Claerbout, 1978; 1985). This is accomplished by multiplying the amplitude spectrum of each slant-stack trace by the absolute value of the frequency. This is somewhat analogous to differentiation of the wave field before the summation that is involved in the integral formulation of migration (Yilmaz, 1987). Fig. 2.10 shows the flowchart of the (x, t) slant-stack processing just described.

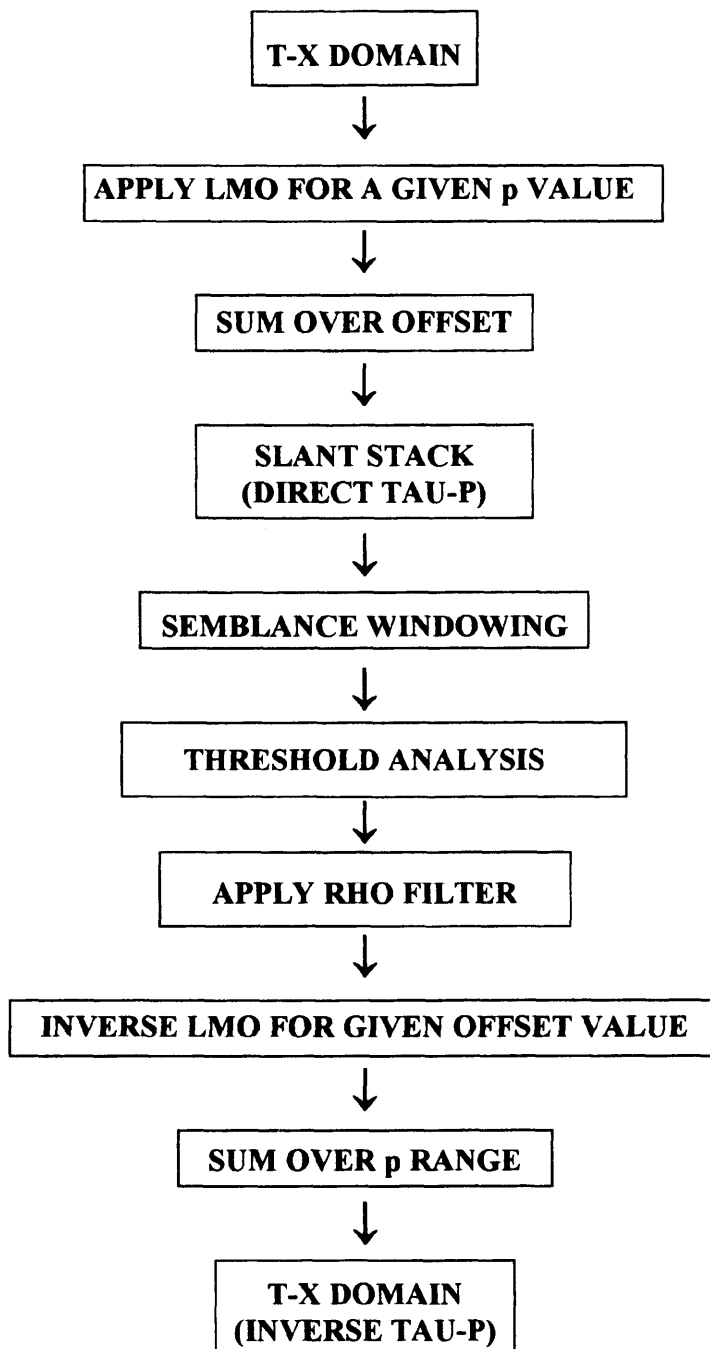


Fig. 2.10. Flowchart of the slant stack processing in the $x-t$ domain.

2.4.2 The (K, F) method - forward and inverse slant stack process

Let the seismic data be a single frequency sinusoid with frequency f and with no dip. Then $g(x, t) = \exp(2\pi i F t)$. Let x range from $-N(dx)$ to $N(dx)$ so that are $2N+1$ identical traces with spacing dx . In this particular case, the slant stack summation (Gardner and Lu, 1991)

$$h(p, \tau) = \sum_{\alpha=-N}^N \exp[2\pi i F (\tau + p(dx)\alpha)] \quad (2.22)$$

is just a geometric progression with constant factor $\exp[2\pi i F p(dx)]$, and the result in closed form is (Gardner and Lu, 1991)

$$h(p, \tau) = \frac{\sin(2N+1) [\pi F p dx]}{\sin[\pi F p dx]} \exp[2\pi i F \tau] \quad (2.23)$$

If we sample p at equal increments given by

$$dp = \frac{1}{(2N+1)Fdx} \quad (2.24)$$

starting at $p=0$, then $h(p, \tau)$ is zero for all p except when both sine terms in eq. (2.24) vanish, i.e., when

$$p = 0, \pm \frac{1}{Fdx}, \pm \frac{2}{Fdx}, \dots \quad (2.25)$$

Thus if we regard the data as a single-frequency horizontal “line”, the slant stack is a single-frequency “point” at $p=0$, with repetitions at multiples of $1/Fdx$. To recover the original data it is enough to use the slant stack around $p=0$ and omit the repetitions.

This example makes clear that to properly sample the slant stack the increment in p should be satisfy the inequality

$$dp < \frac{1}{F(2N+1)dx} \quad (2.26)$$

From equation (2.22) we can see that the slant stack process can be performed in the two-dimensional Fourier transform space or (k, f) space. Performing slant stack in this domain is facilitated by the “Fourier slice theorem” or “projection slice theorem” (Kak and Rosenfeld, 1982) (Fig. 2.11a,b). This means that for p constant, the one-dimensional Fourier transform of the slant stack of the function $g(x, t)$ is equivalent to a slice of the two-dimensional Fourier transform given by $G(k=-pf, f)$ (Pan and Gardner, 1984). A collection of such slices defines the (p, f) domain. Individual slices constructed in this manner are then processed though a one-dimensional inverse Fourier transform in frequency to form the (p, τ) domain. Fig. 2.12 illustrate this procedure and the relationship of the four spaces utilized: (x, t) , (k, f) , (p, f) and (p, τ) . Note the negative frequencies need not be processed because of the symmetry in the (k, f) domain involved with real-valued data. Equivalent results are obtained by doubling the value of the positive frequency components and leaving out the negative frequency components.

Any radial line in (k, f) space is a column in (p, f) space. Conversely, any column in (k, f) space is a hyperbola in (p, f) (Wade and Gardner, 1988). Thus, the forward and inverse computations can be carried out in the same manner. Specifically, the (k, f) data can be reconstructed from the (p, f) data by simply picking out values for k constant (along an hyperbola) as illustrated in Fig. 2.13. This of course will only reconstruct (k, f) values within the range, $p_{\min} \leq p \leq p_{\max}$. For some applications, this is exactly the desired effect. For example, a velocity filter removes velocities above and/or below some values according to p_{\max} and p_{\min} respectively by computing the slant stack within the

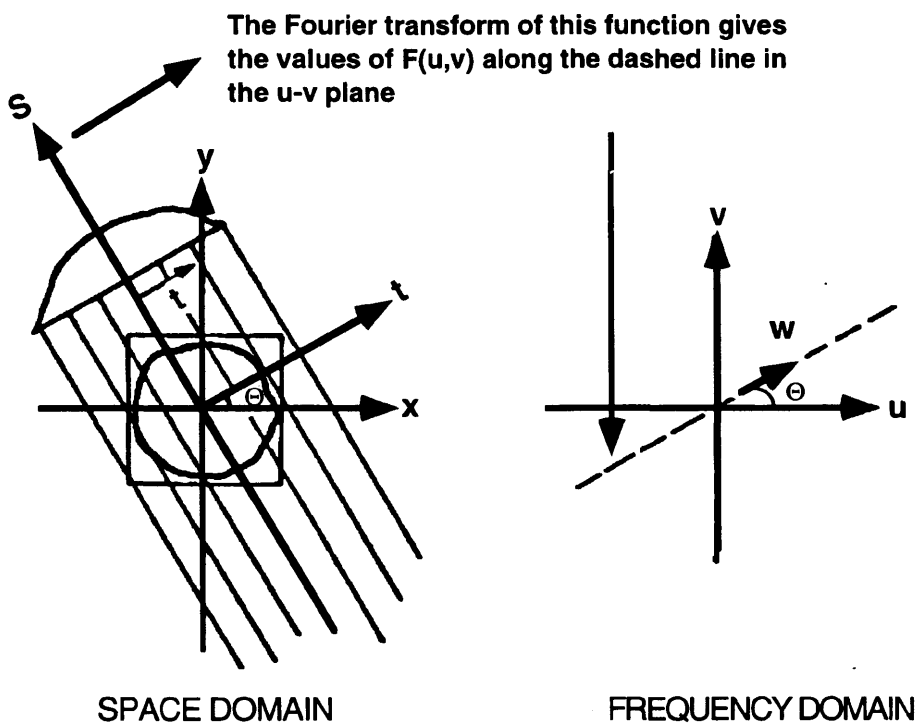


Fig. 2.11a. The Fourier slice theorem is illustrated here

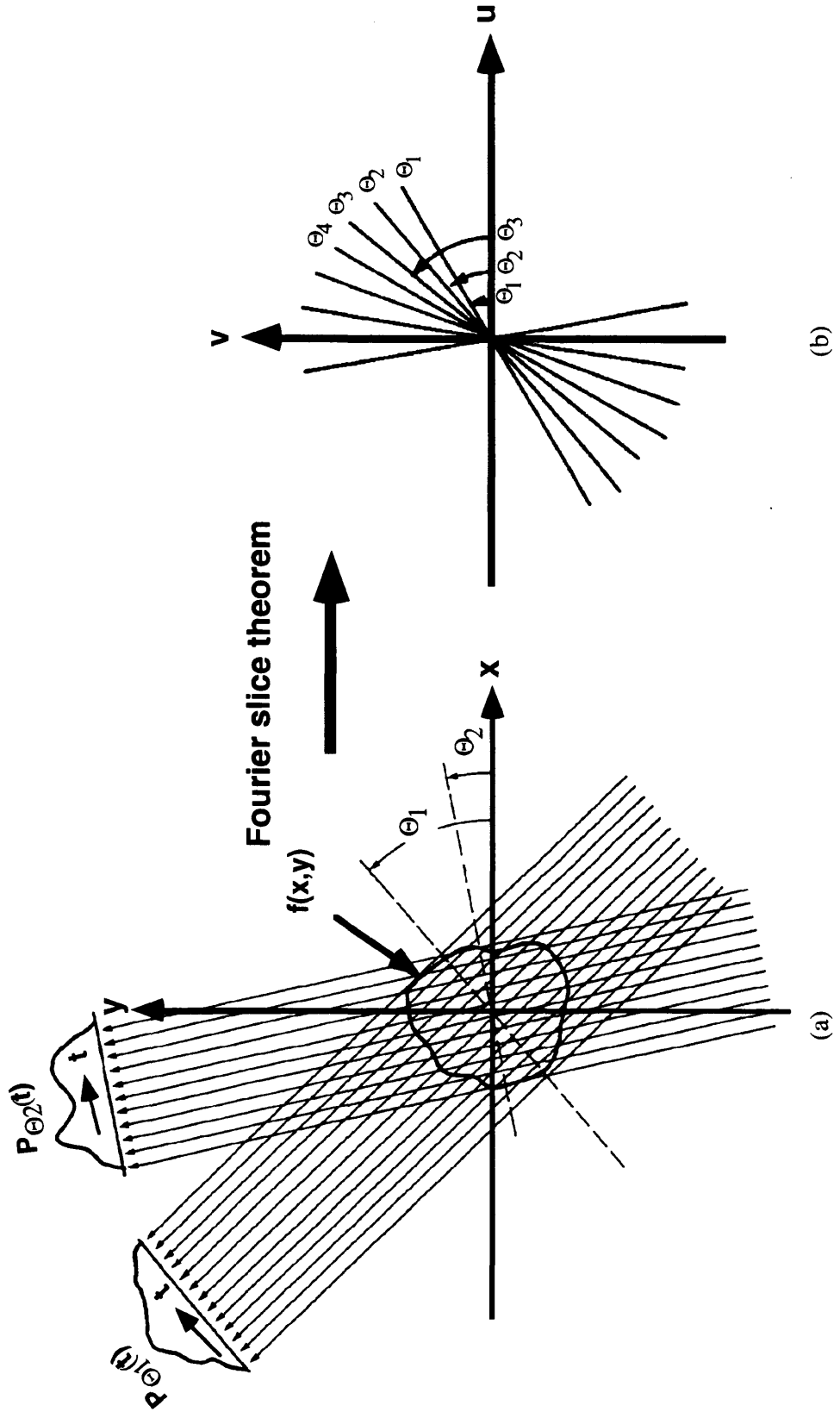


Fig. 2.11b. (a) This figure illustrates a projection of a function $f(x,y)$.
(b) Taking the Fourier transforms of projections taken at different angles one can fill up the frequency domain.

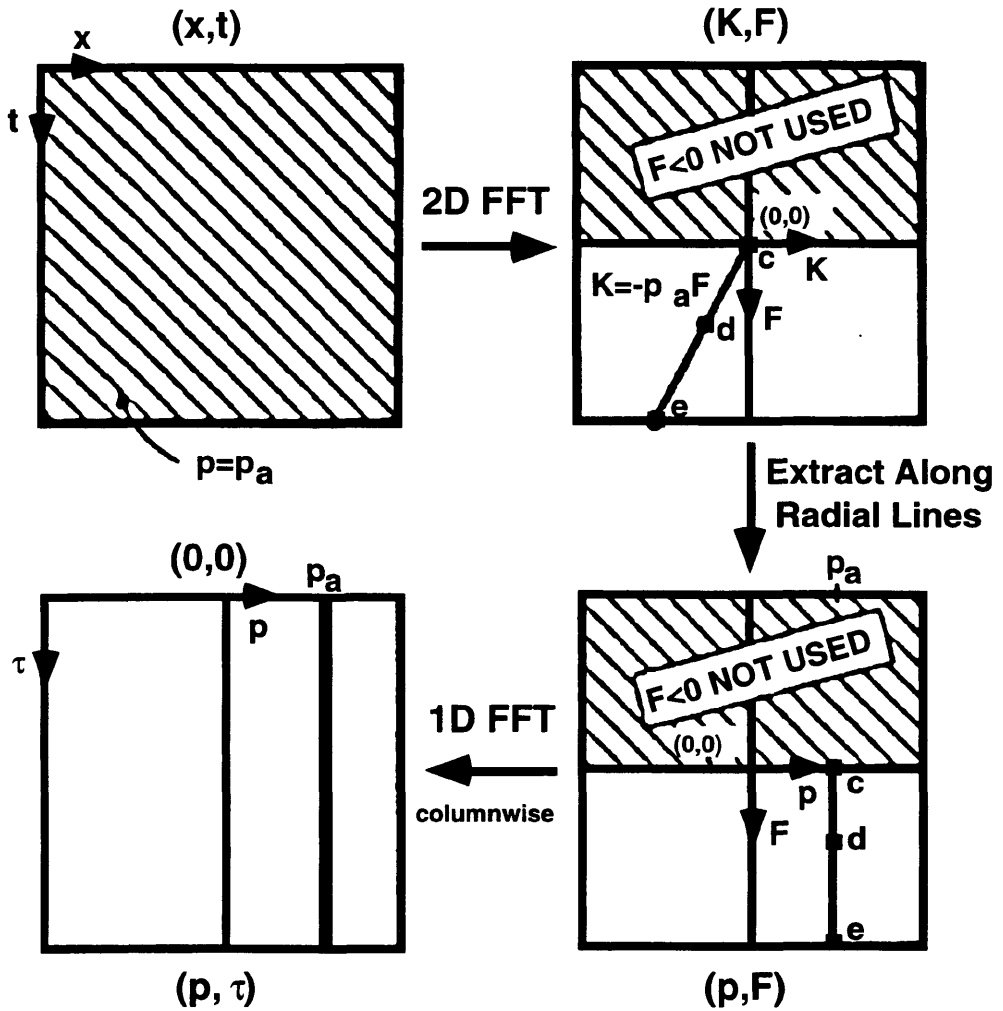


Fig. 2.12. Scheme for constructing slant stacks with 2-D Fourier transforms (after Wade and Gardner, 1991).

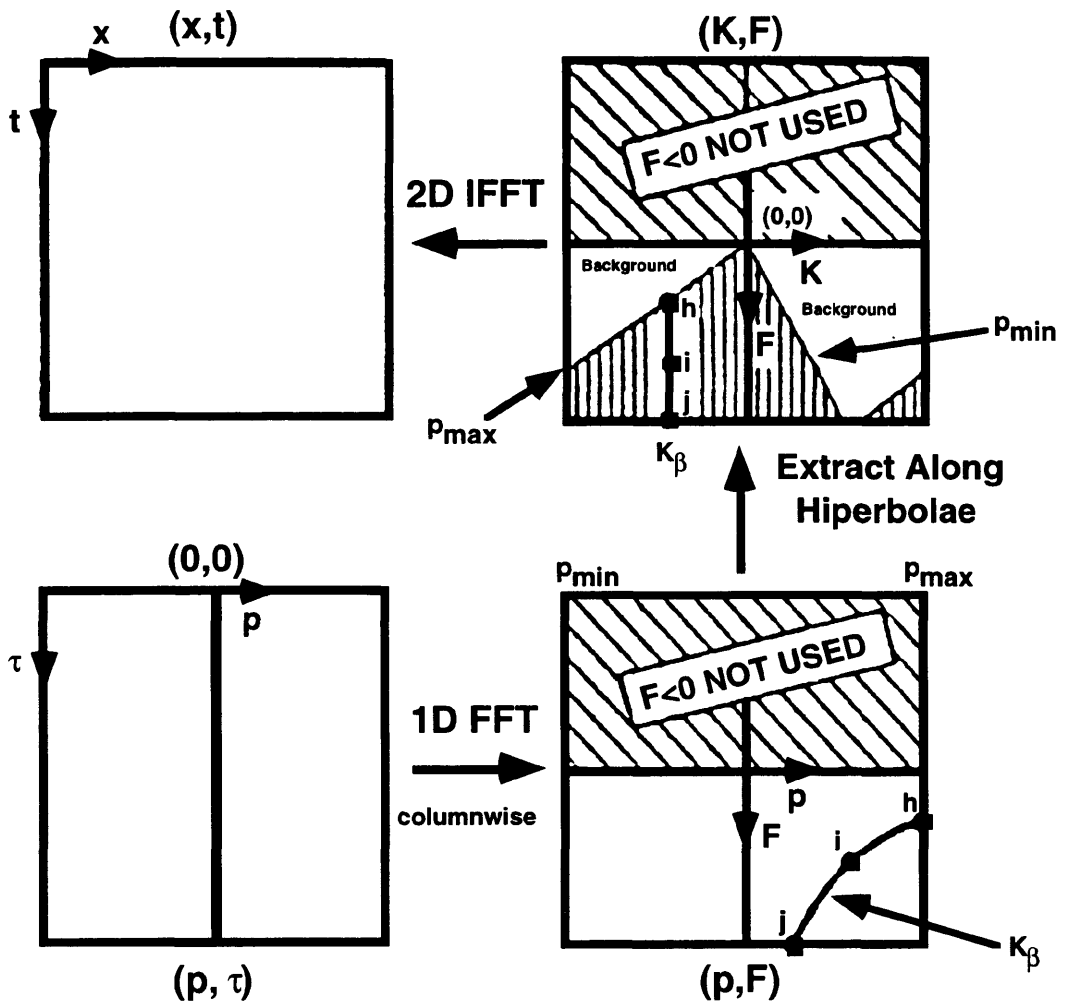


Fig. 2.13. Scheme for reconstructing (x,t) data from (p,τ) data with Fourier transforms (after Wade and Gardner, 1991).

range and then performing the inversion. For other applications, it is desirable to perhaps compute a wide range of p values and then manipulate a small region in (p, τ) space before inversion.

2.4.2.1 Interpolation process

As with (x, t) implementations of the slant stack, the (k, f) method requires interpolations to obtain the desired result since both radial lines in the (k, f) space and hyperbolae in the (p, f) space rarely intersect the respective grids and grid-points. However, there is added difficulty that the numbers to be interpolated are complex-valued. One way to accomplish this is to perform row-wise interpolation using a complex-valued series interpolation operator (Wade and Gardner, 1988). The expression for this interpolation operator is derived from the basic definition of the discrete Fourier transform with the spatial data length doubled with padded zeros and the inclusion of a triangular weighting function:

$$D(\sigma) = \sum_{\gamma=-N}^N C_{\gamma} e^{i(\gamma-\sigma)\pi/2} \left(\frac{\sin[(\gamma-\sigma)\pi/4]}{(\gamma-\sigma)\pi/4} \right)^2 \left(\frac{\sin(\gamma-\sigma)\pi}{(\gamma-\sigma)\pi} \right) \quad (2.27)$$

where σ is the floating point index at which the interpolation is desired, and γ is the integer index of the available Fourier series coefficients (Wade and Gardner, 1988). Note that the terms of this series diminish like $1/n^3$. Consequently, only six terms yield very accurate results. Furthermore, the geometric nature of this process lends itself to establishing an adequately small Δp for accurate reconstruction given by

$$\Delta p \leq \frac{Nt\Delta t}{2\psi Nx\Delta x} \quad (2.28)$$

ψ is the integer index of the maximum temporal frequency of interest (i.e. $\psi = (Nt)(\Delta t)(f_{max})$), and the two in the denominator results from the spatial zero-padding.

The forward transform is constructed over a large range of p , i.e., from $-1/2(F_{min} dx)$ to $1/2(F_{max} dx)$. We pick out of $h(p, \tau)$ a range of p of magnitude to f . Mute out all the coefficients at frequency f that lie outside the range $1/Fdx$ as indicated in Fig. 2.14. As we can see from the figure the p values of “interest” are those traces for which no frequency filtering is desired. High-cut frequency filtering is then applied by muting outside the interval for each frequency. The resulting (p, τ) slant stack contains enough information to recover the original function. The muting of the Fourier coefficients outside the range at each frequency f can be done in many ways by centering the range at different p values. Each selection gives a slant stack $h(p, \tau)$ from which the function $g(x, t)$ can be recovered.

One advantage of performing slant stack in the (k, f) domain is that the inverse procedure can be addressed in a similar manner as the forward procedure. That is, an extraction process from the (p, f) domain can be employed to reconstruct the (k, f) domain. This is exactly analogous to the extraction process from the (k, f) domain to form the (p, f) domain originally. Therefore, this process is an arithmetic reversal rather than an inversion. Consequently, the difficulty alluded to earlier concerning inverting inexact line-to-point and point-to-line transformation is avoided.

Both methods were tested using a steep model (Fig. 2.15). The model consists of two homogeneous layers with velocities $V_p = 2300$ m/s for layer 1 and $V_p = 3500$ m/s for layer 2. The acquisition geometry consisted on a single shot and receiver at the same location (zero-offset data) located in the top of the model. A total of 40 different locations along the model were considered. Fig. 2.16(a,b) show the data in the τ - p domain using (x, t) and (k, f) slant stack methods, respectively. It is evident from the Fig. 2.16a the presence of symmetric fans of lower-amplitude radial lines intersecting at the center of this

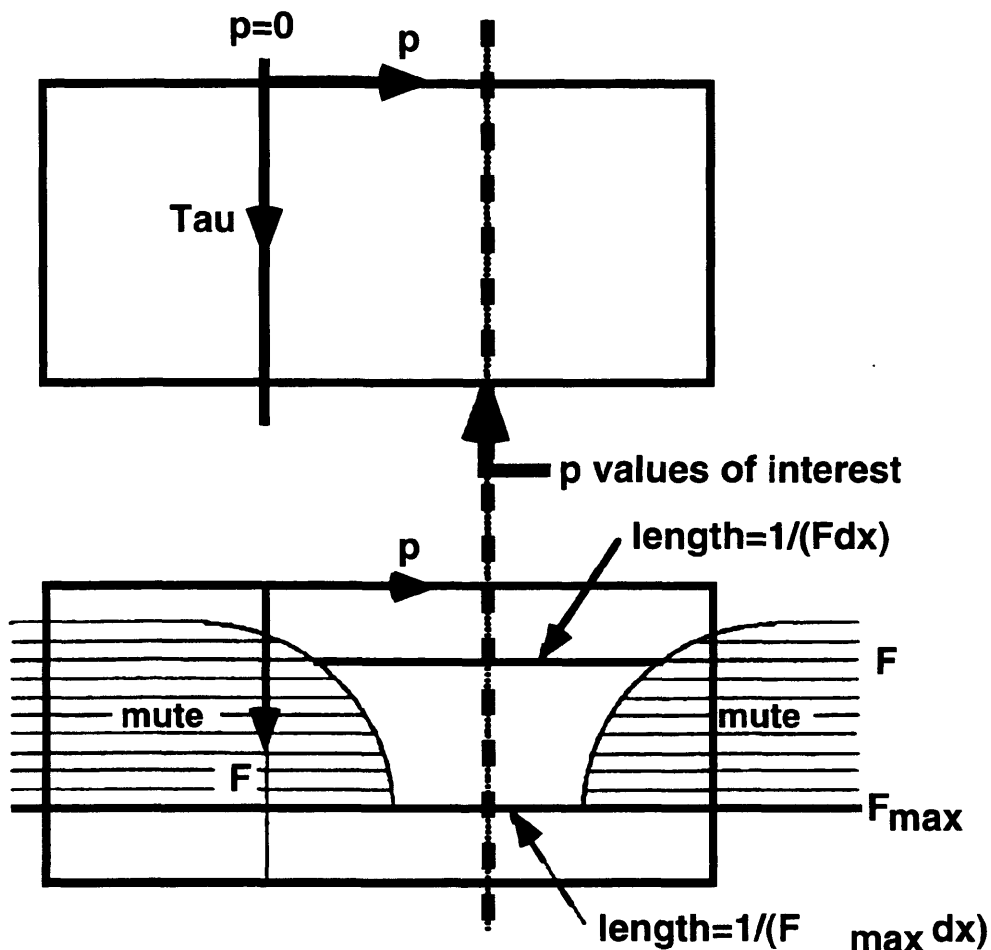


Fig. 2.14. A (p, τ) slant stack can be constructed with a wide range of p values. The p values of "interest" are those traces for which no frequency filtering is desired. High-cut frequency filtering is then applied by muting outside the interval $1/(F dx)$ for each frequency. The resulting (p, τ) slant stack contains enough information to recover the original function.

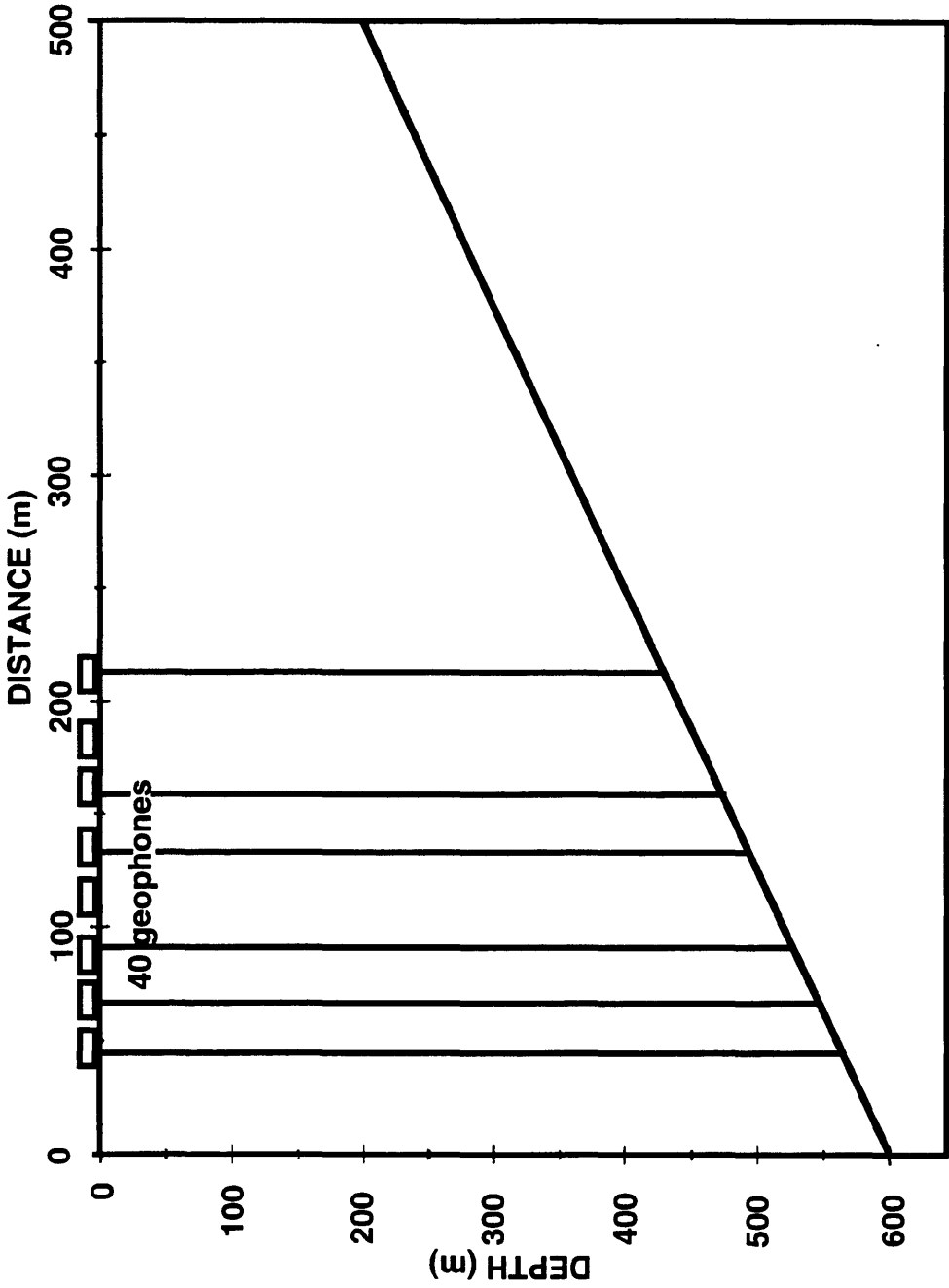


Fig. 2.15. Dip-angle model used to test two different approaches of the 2-D τ - p transform.

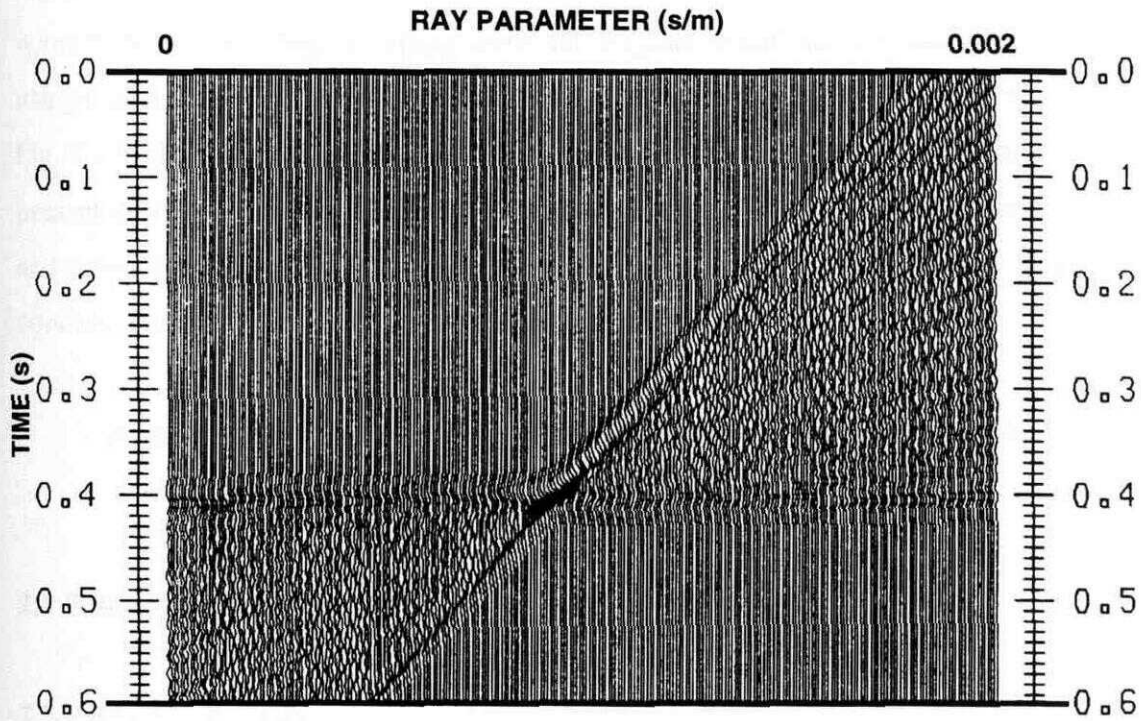


Fig. 2.16a. Data from the dip-angle model transformed in to the τ - p domain using the (x,t) method as proposed by Stoffa (1981).

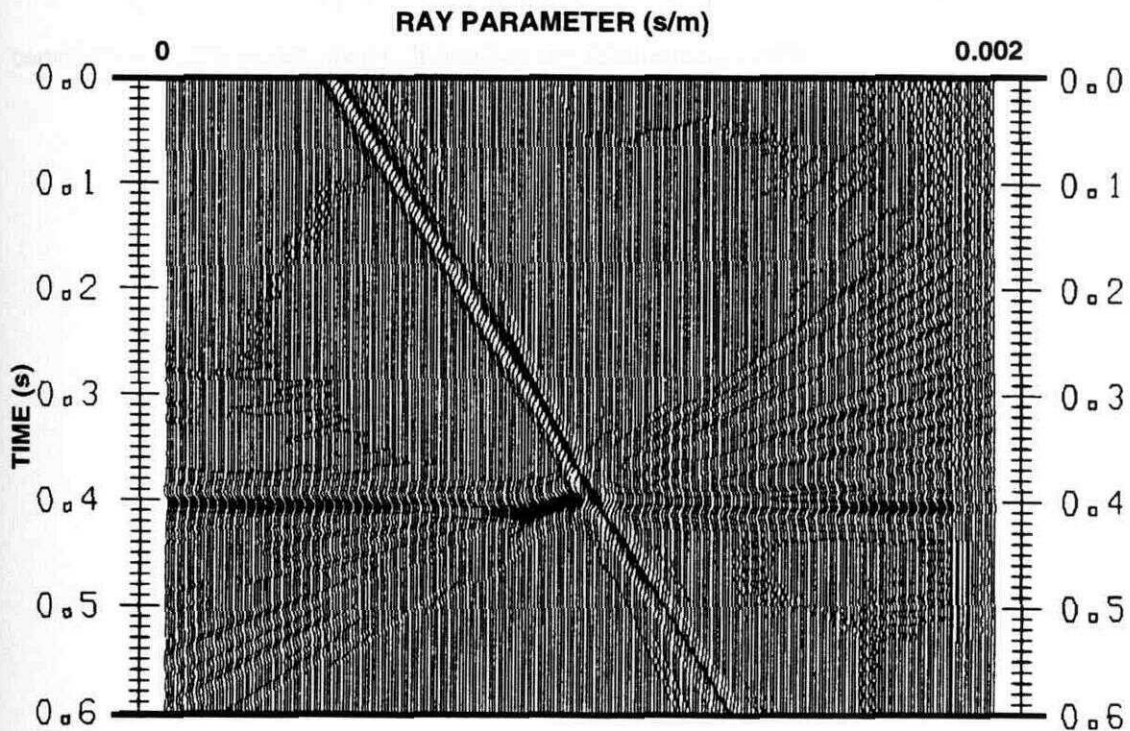


Fig. 2.16b. Data from the dip-angle model transformed in to the τ - p domain using the (k,w) method.

region. In other hand Fig. 2.16b shows a clear picture of the data in the τ - p domain without radial lines. Fig. 2.17(a,c) show the original model and the reconstructed data using (x,t) and (k,f) slant stack methods, respectively. Comparing the figures we can see in Fig. 2.17b the presence of noise introduced during the inverse transform by the fans lines present in the τ - p domain. The τ - p transform in the (k,f) domain (Fig. 2.17c) gives a clear and better image of the data due to this kind of transformation avoid the inaccuracy concern with the inversion of line-to-point and point-to-line.

An extension of the τ - p transform for a 3-D volume is described in the Appendix.

2.5 Filter coefficients

2.5.1 Raw coefficients

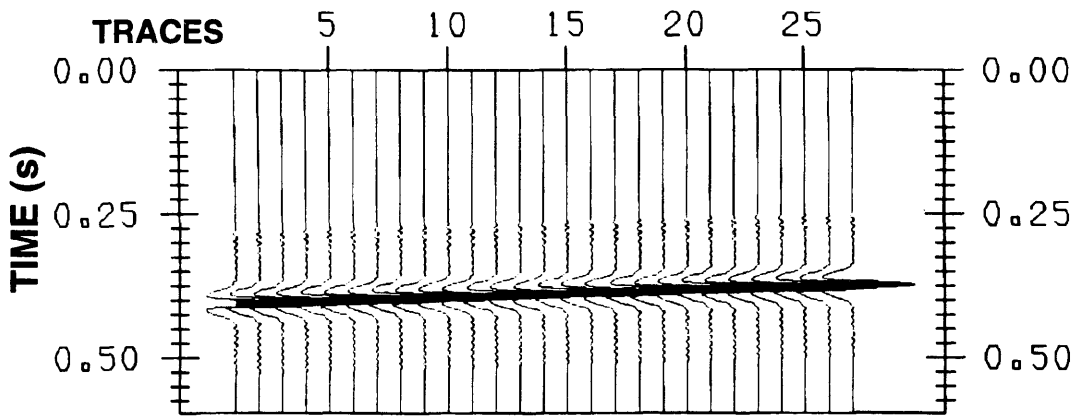
The filter coefficients are functions of the geophone responses, their expressions considering single geophones will be given by (Dankbaar, 1985)

$$F_V^P(p) = (1 - 2V_s^2 p^2) / 2(1 - V_p^2 p^2)^{1/2}, \quad (2.29)$$

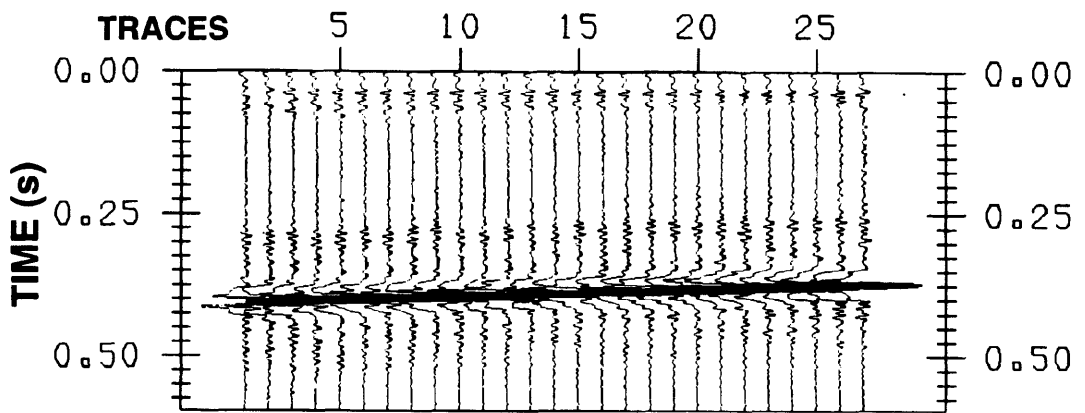
$$F_H^S(p) = V_s^2 p / V_p \quad (2.30)$$

$$F_V^S(p) = V_s p \quad (2.31)$$

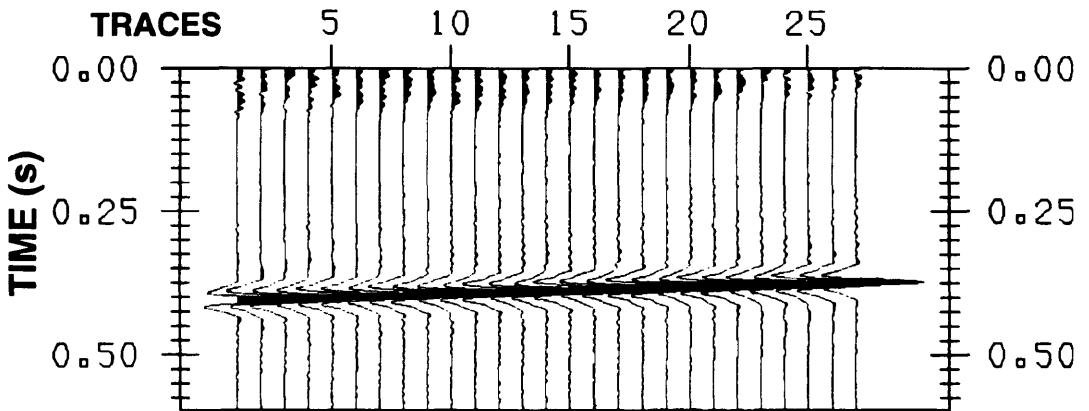
$$F_H^S(p) = (1 - 2V_s^2 p^2) / 2(1 - V_s^2 p^2)^{1/2} \quad (2.32)$$



(a)



(b)



(c)

Fig. 2.17. (a) Stacked input section from the dip-angle model. (b) Reconstructed section after applying the τ - p transform in the (x,t) domain. (c) Corresponding stacked section by using the proposed τ - p transform in the (k,w) domain.

The above equations were derived for a single geophones whose geophone responses are considered independent of frequency and completely determined by the near-surface P and S wave velocity V_p and V_s .

2.5.2 Instabilities

The behavior of the filter coefficients for a range of values the near-surface velocities V_p and V_s is shown in the Fig. 2.18. The filter coefficients F_V^P and F_H^S reach anomalous values in comparison with F_H^P and F_V^S causing instabilities in the separation filter. Perhaps the relations that express the pass- P and pass- S wavefield (eqs. (2.3)-(2.4)) are strongly affected altering the coupled relation between both equations.

2.5.3 Tapered coefficients

The ideal situation is indicated in the Fig. 2.19 where the coefficients are limited between -1 and +1. The maximum slowness displayed corresponds to that of incident S waves. The additional condition on slowness p values for P - P waves limits the behavior for F_V^P and F_H^P . In both cases, F_H^P and F_V^P filter coefficients are limited by the maximal slowness of the incident P waves which represents horizontal incidence. The values of the filter coefficients have been limited to avoid instabilities in the P - S separation filter.

Figs. 2.20(a,b) shown the behavior of the coefficients F_V^P , F_V^S , F_H^P and F_H^S considering different values of the P - and S -waves velocities at the near-surface where the geophones are located. Finally, Fig. 2.21 shows the basic steps followed by the P - S separation filter in the τ - p domain.

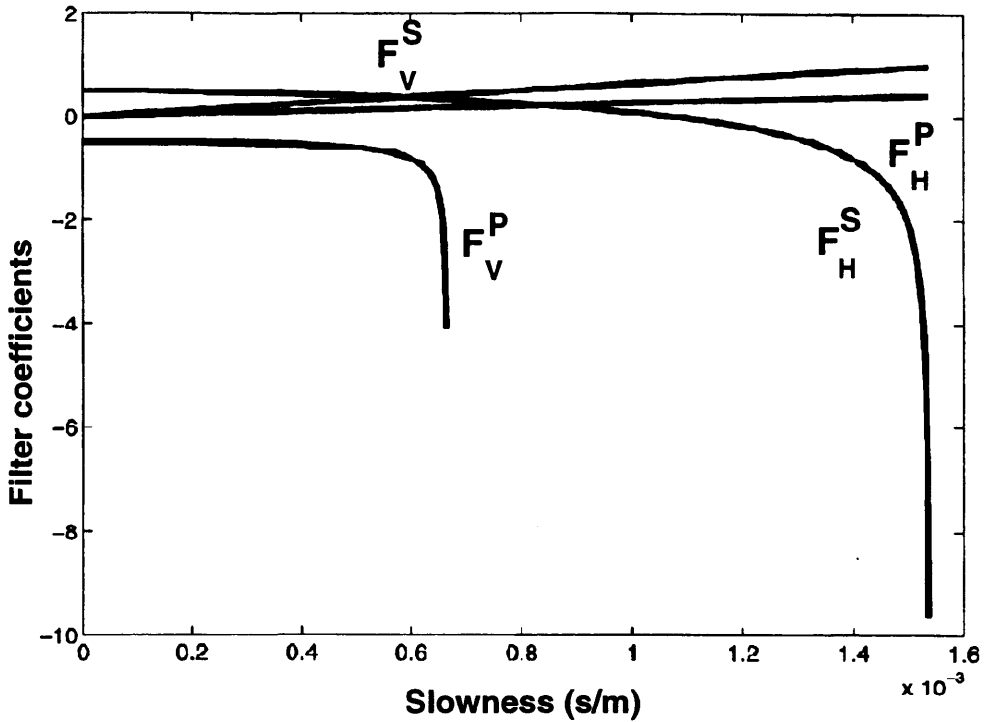


Fig. 2.18. Value of the filter coefficients F as a function of horizontal slowness for pass- P and pass- S filter considering $V_p=1500$ m/s and $V_s=650$ m/s, without constrains.

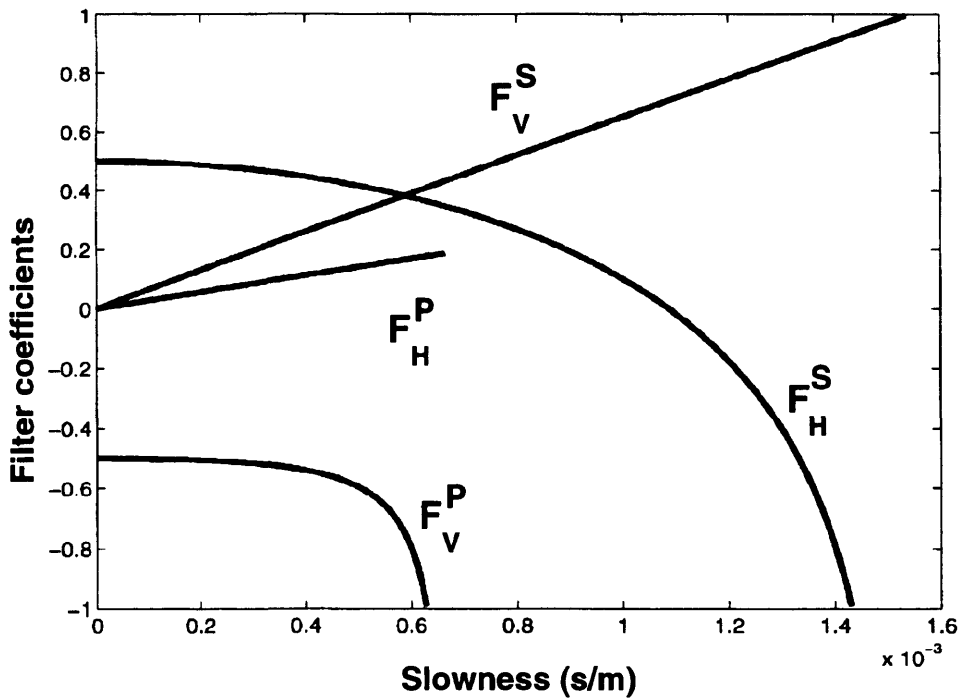


Fig. 2.19. Value of the filter coefficients F as a function of horizontal slowness for pass- P and pass- S filter considering $V_p=1500$ m/s and $V_s=650$ m/s, with constrains.

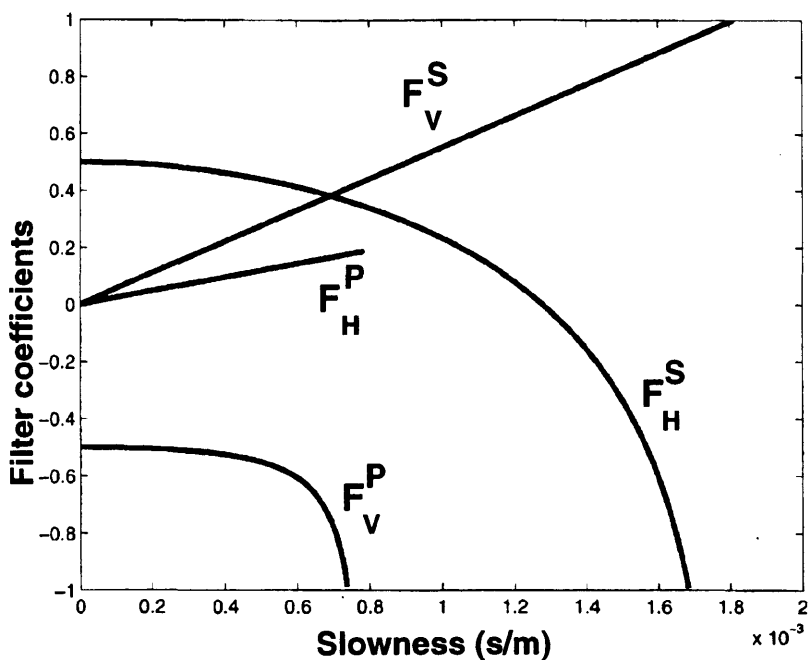


Fig. 2.20a. Value of the filter coefficients F as a function of horizontal slowness for pass- P and pass- S filter considering $V_p=1275$ m/s and $V_s=552.5$ m/s, with constrains.

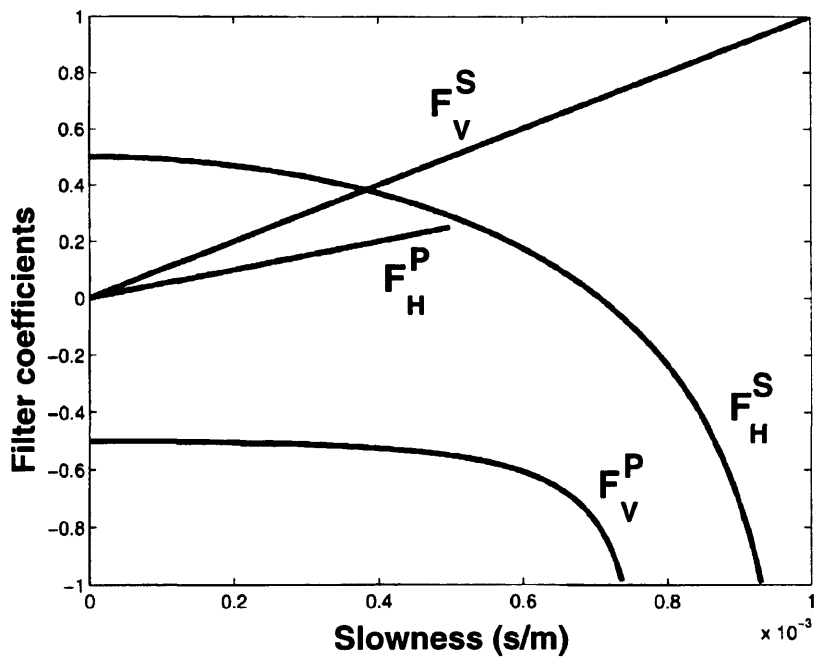


Fig. 2.20b. Value of the filter coefficients F as a function of horizontal slowness for pass- P and pass- S filter considering $V_p=2000$ m/s and $V_s=1000$ m/s, with constrains.

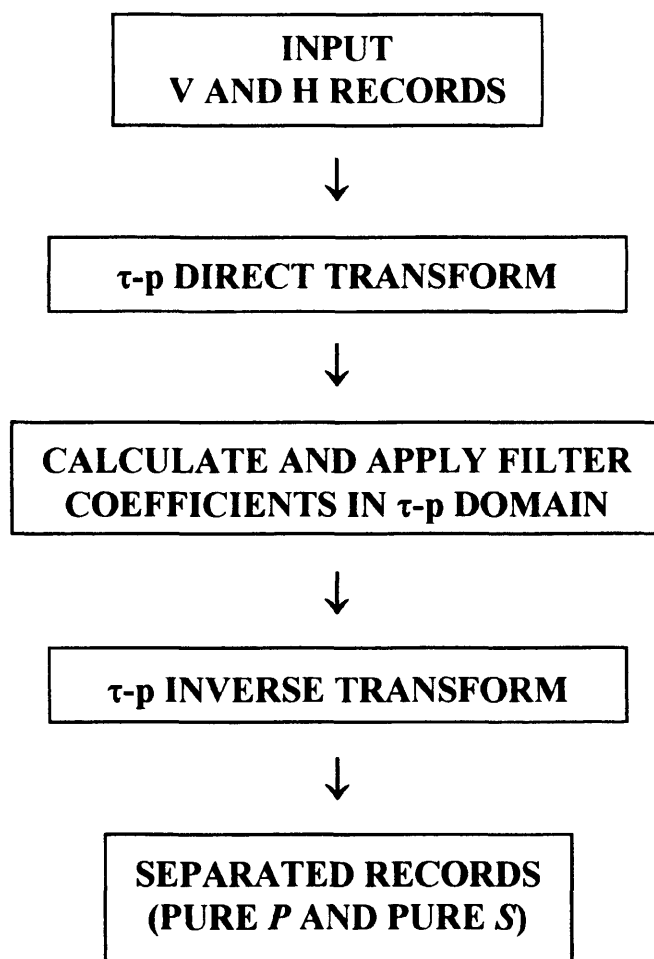


Fig. 2.21. Flowchart of the P - S separation filter for the free-stress case in the τ - p domain.

2.6 Application of the separation filter in the tau-p domain

2.6.1 Synthetic data

Some filter operations on synthetic data follow. The model consists of five flat homogeneous layers with a maximum reflector depth of this model is 200 m. Geophone offsets are from 5-100m spaced 5m and the source is located on the top of the first layer at the air-solid contact (Fig. 2.22). The modeling package (SIERRA) used did not calculate the geophone responses. Eqs. (2.1) and (2.2) which express the vertical and horizontal records as a function of the geophone responses and the P - and S -incident waves and eqs. (2.9)-(2.12) using the P - and S -wave velocities at the near-surface were used to calculate the synthetic seismograms. The P - P , S - S , P - S and S - P seismograms were independently generated in the x - t domain and transformed to the τ - p domain: then, by using the eqs. (2.1)-(2.2) were simulated the vertical and horizontal records.

First, only P - P and S - S reflections were calculated, where both P and S waves were radiated by the source, which radiated energy uniformly from 0° to 180° . Figure 2.23a shows the P - P and S - S seismograms without geophone responses. Here the incident S waves have a zero point at certain offsets followed by a 180° phase shift for large offsets. The associated vertical and horizontal records are shown in the Fig. 2.23b as would be recorded by realistic 3-C geophones. All P and S arrivals shown up on both records. The shallow SS -2 reflection appears interfering the PP -5 reflection and showing the expected behavior for pure S waves on both records.

The results of the P - S separation applied on both vertical and horizontal records is indicated in the Fig. 2.23c, using near-surface velocities $V_p = 1500$ m/s and $V_s = 650$ m/s, which are the velocities for the first layer in the synthetic model.

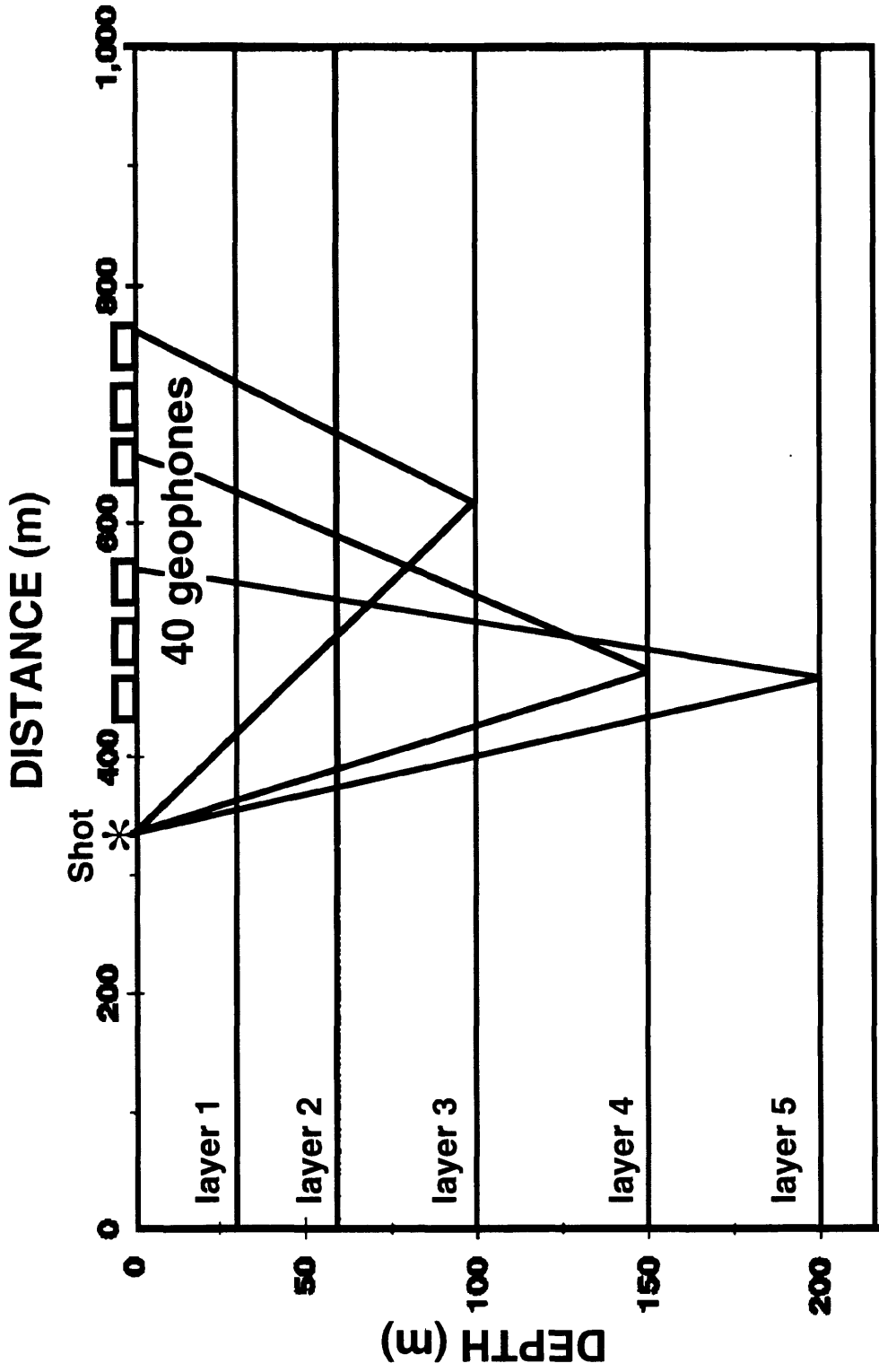


Fig. 2.22. Subsurface model used for synthetic data calculation (after Dankbaar, 1985)

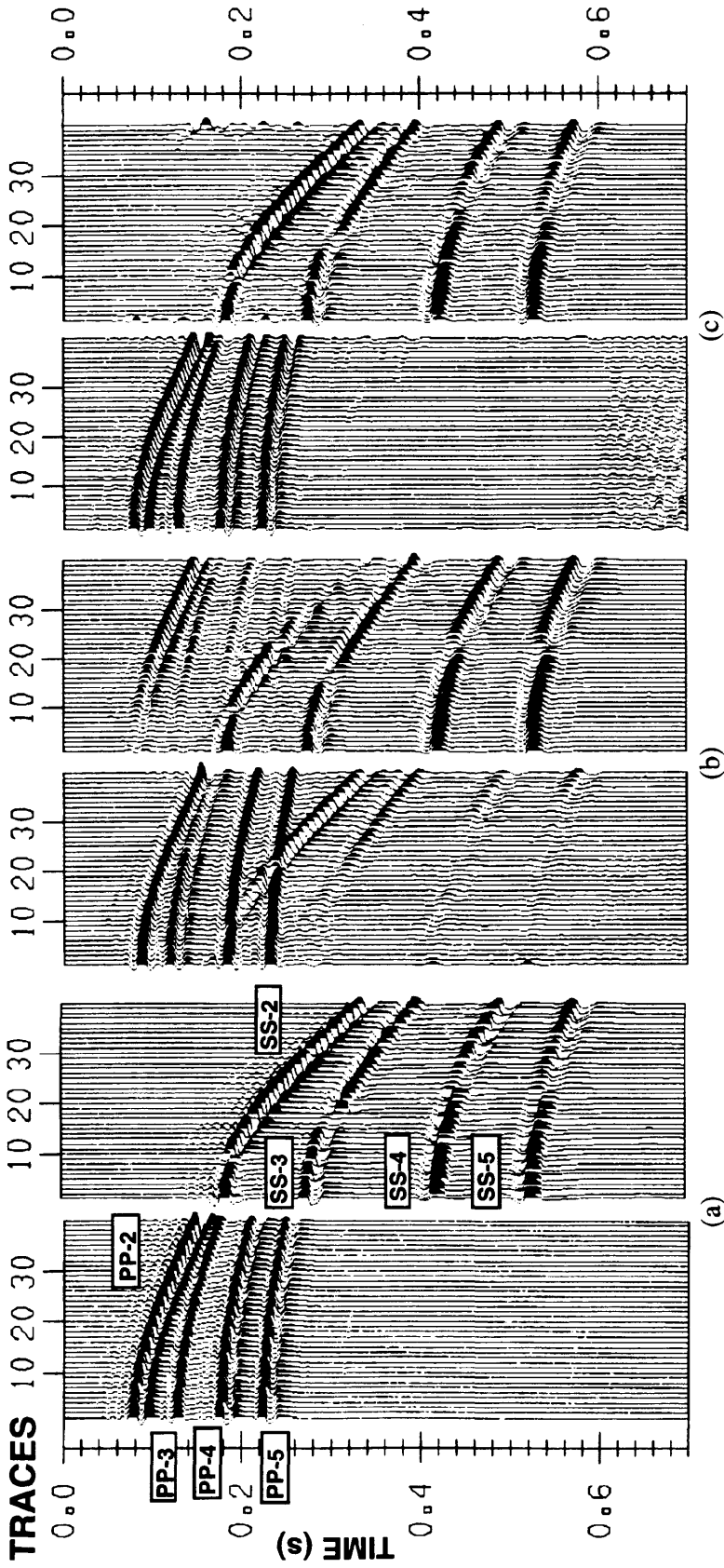


Fig. 2.23. Vertical and horizontal geophone response from the model of Fig. 2.22.

(a) P - P and S - S reflections, with no receiver response.

(b) Vertical and horizontal geophone output from incident P - P and S - S reflections.

(c) Pass- P and pass- S sections obtained from both vertical and horizontal records (Fig. 2.23b) using

$V_p = 1500$ m/s and $V_s = 650$ m/s.

The comparison with the filters pass- P and pass- S records with the incident seismograms shows a very good performance of the separation filter recovering the original P - P and S - S seismograms without any interference (SS -2 and PP -5 reflections). Only minor remnant amplitudes of the removed wavetypes are left on each record for near offsets after the P - S separation and could be explained for errors of the τ - p transform due to the truncation of the events in the x - t domain. Some noise is present on both pass- P and pass- S records as consequence of the limitations during the summation process in the τ - p domain for obtaining the inverse x - t sections, associated with a intrinsic limitation of the summation process in the τ - p domain and the limitations included in the filter coefficients calculation.

The performance of the P - S separation filter for erroneous estimates of the near-surface velocities V_p and V_s of the layer 1 is shown in the Fig. 2.24. The vertical and horizontal records from Fig. 2.23b were filtered using erroneous values as follows: first we use $V_p = 1650$ m/s and $V_s = 715$ m/s for layer 1 (which represent an overestimation of 10% in the velocities). The filtered sections are shown in Fig. 2.24a. Next, an overestimation of 25% in the velocities are used giving $V_p = 1875$ m/s and $V_s = 812.5$ m/s. The resultant sections are shown in Fig. 2.24b. Finally, an underestimation of 15% in the velocities are used giving $V_p = 1275$ m/s and $V_s = 552.5$ m/s. The filtered sections are shown on Fig. 2.24c.

The results presented in Figs. 2.24(a,c) can be compared with the records from Fig. 2.23a. We got similar results of the filter when erroneous velocities were used for the separation indicating the robustness of the separation filter. It is evident that the pass- P records is less effected by errors in the velocities than the pass- S records, where there is still some residual P -wave energy.

Real data contain noise and the filter was tested with random noise added. Fig. 2.23a shows the same P - P and S - S seismograms as in Fig. 2.25a, but now with 10% random noise added. Fig. 2.25b shows how these incident waves are observed on vertical and horizontal geophones. These records were again filtered pass- P and pass- S . The result is shown in Fig. 2.25c and can be compared with the incident wave records from Fig. 2.25a. Apparently, the P - S separation filter is not affected by noise in the data. The noise has even decreased at larger offset. The effect on the filter of erroneous estimates of the layer 1 velocities was tested on the vertical and horizontal records shown in Fig. 2.25b. Figs. 2.26(a,c) display the filtering effects when erroneous velocities V_p and V_s are used. Once again, the filter is robust with respect to errors in the velocity estimates.

In the second case, only P - P and converted waves (P - S) primary reflections are considered. Fig. 2.27a shows the P - P and P - S seismograms without geophone responses, where there are only P wave arrivals on the vertical geophone and only S wave arrivals on the horizontal geophone. The P - P and P - S seismograms were generated using a minimum phase wavelet with a center frequency of 45 Hz. Next, taking into account the geophone responses and using incident P and converted waves gives traces as shown in the Fig. 2.27b. On the horizontal and vertical geophone records all P - P and P - S reflections are evident.

The filtered pass- P and pass- S are shown in Fig. 2.27c, which can be compared with the incident seismograms in Fig. 2.27a. There is a reasonable agreement between the corresponding records indicating fairly good wave-type separation.

The effect on the filter of erroneous estimates of the P - and S -wave velocities in the layer 1 is shown in Fig. 2.28a,c. The similar results of the filter when using erroneous velocities for the calculation of the filter coefficients indicate a robust operation.

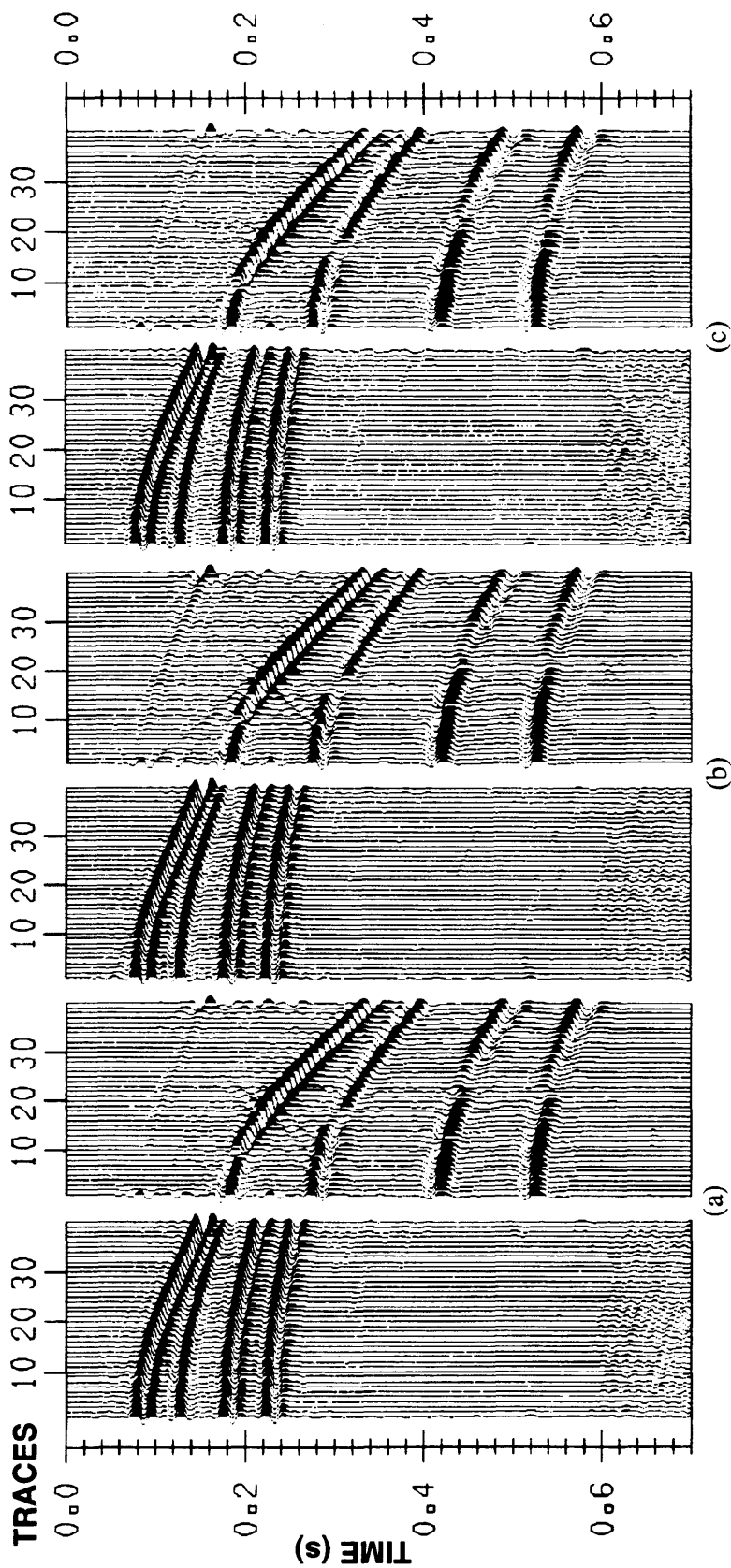


Fig. 2.24. (a) Filtered pass- P and pass- S records, respectively, obtained using $V_p=1650$ m/s and $V_s=715$ m/s.
 (b) Filtered pass- P and pass- S records, respectively, obtained using $V_p=1875$ m/s and $V_s=812.5$ m/s.
 (c) Filtered pass- P and pass- S records, respectively, obtained using $V_p=1275$ m/s and $V_s=552.5$ m/s.

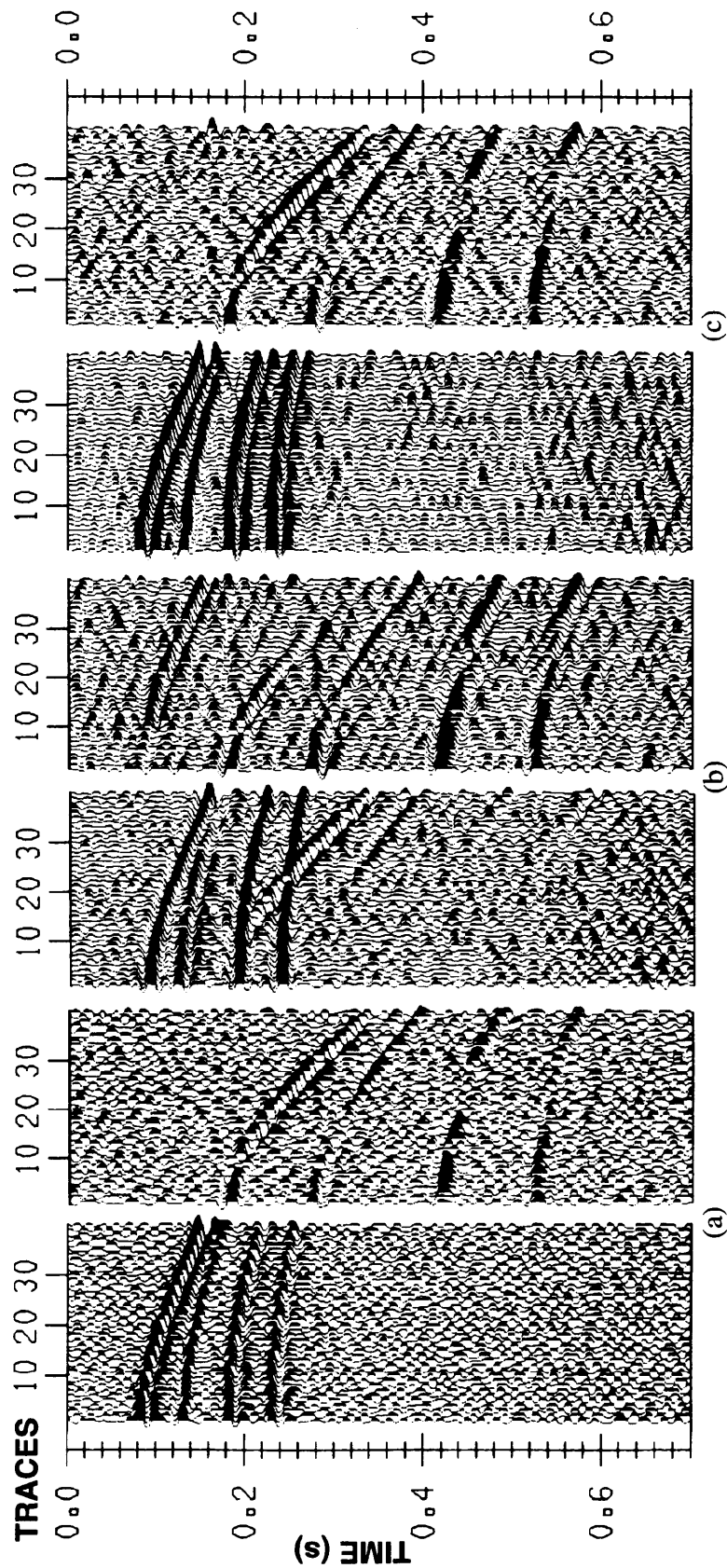


Fig. 2.25. Vertical and horizontal geophone response from the model of Fig. 2.22.
 (a) *P-P* and *S-S* reflections with 10% of random noise added, no receiver response considered.
 (b) Vertical and horizontal geophone output from incident *P-P* and *S-S* reflections.
 (c) Pass-*P* and pass-*S* sections obtained from both vertical and horizontal records (Fig. 2.25b) using $V_p=1500$ m/s and $V_s=650$ m/s.

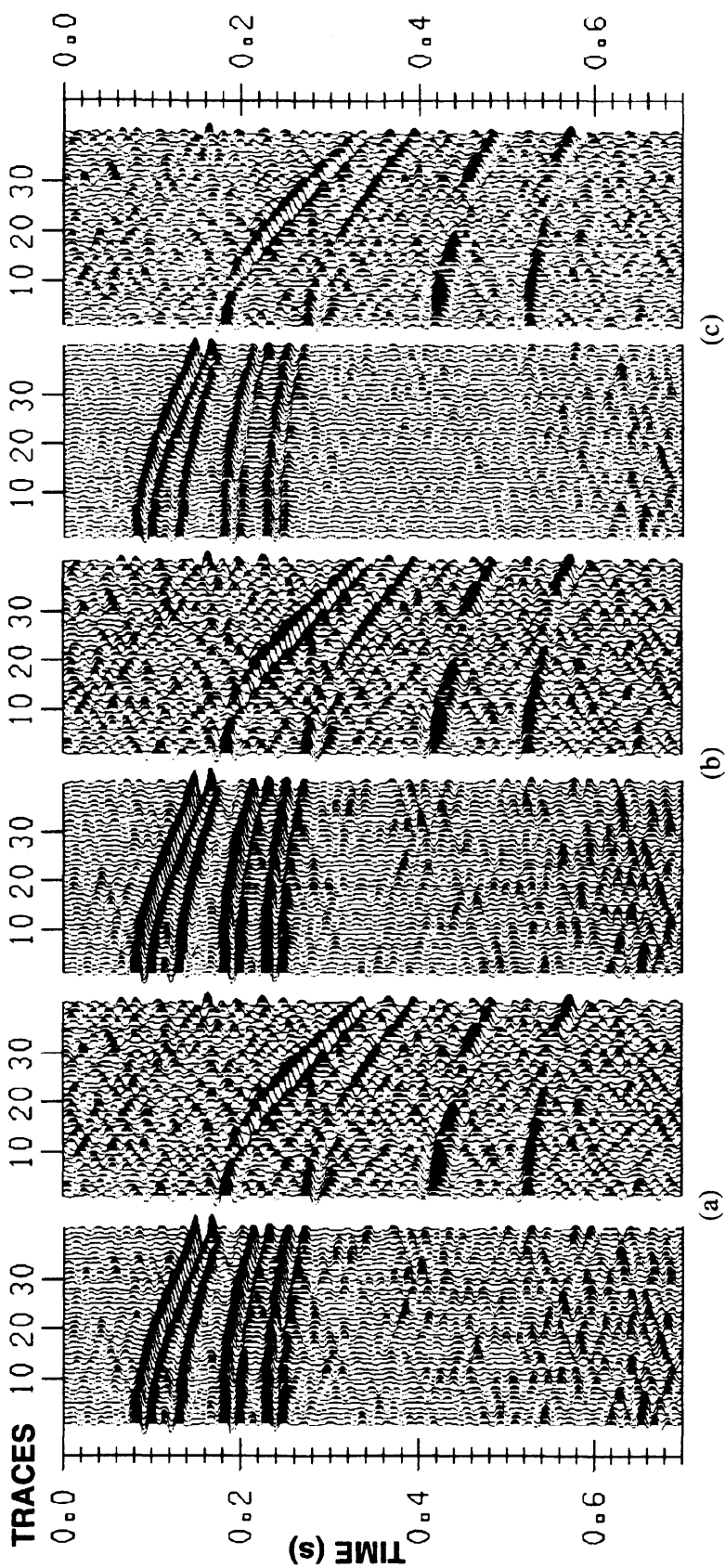


Fig. 2.26. (a) Filtered pass- P and pass- S records, respectively, obtained using $V_p = 1650$ m/s and $V_s = 715$ m/s.
 (b) Filtered pass- P and pass- S records, respectively, obtained using $V_p = 1875$ m/s and $V_s = 812.5$ m/s.
 (c) Filtered pass- P and pass- S records, respectively, obtained using $V_p = 1275$ m/s and $V_s = 552.5$ m/s.

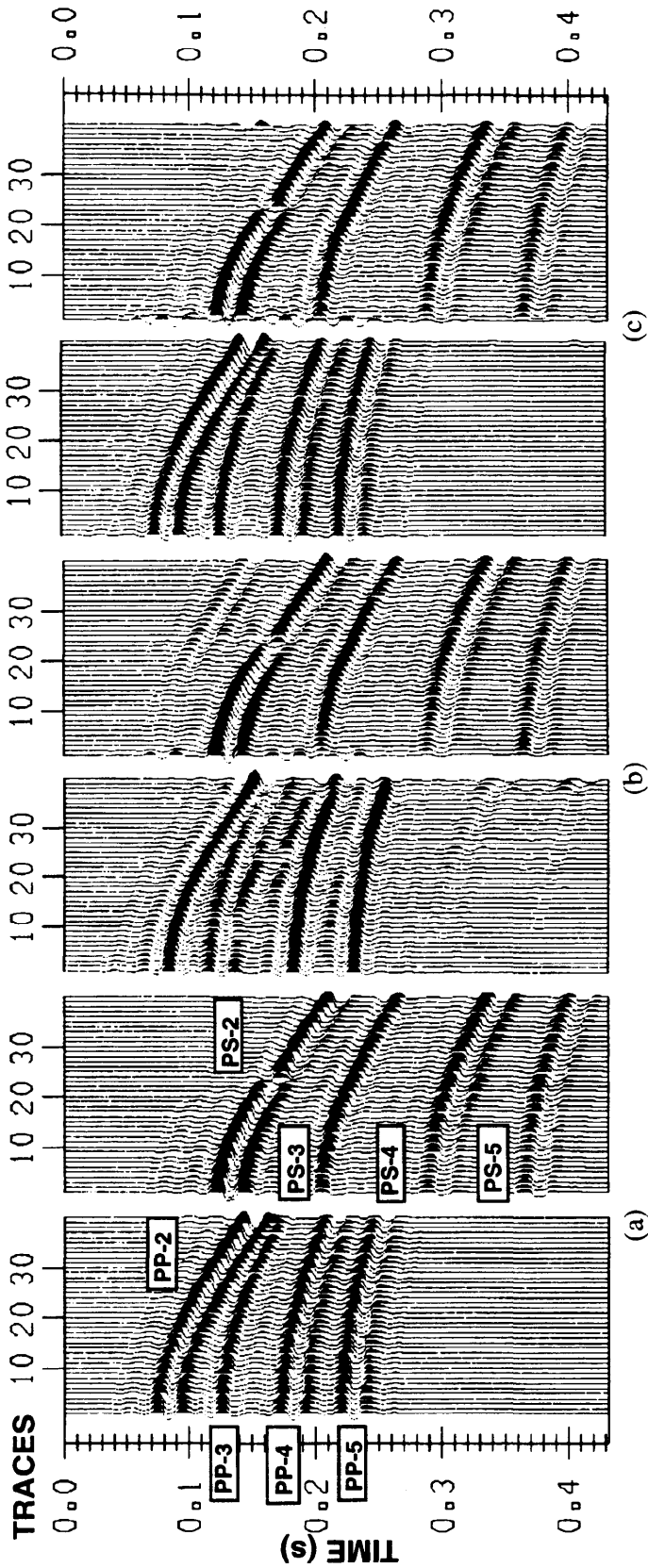


Fig. 2.27. Vertical and horizontal geophone response from the model of Fig. 2.22.

(a) *P-P* and *P-S* reflections, with no receiver response.

(b) Vertical and horizontal geophone output from incident *P-P* and *P-S* reflections.

(c) Pass-*P* and pass-*S* sections obtained from both vertical and horizontal records (Fig. 2.27b) using $V_p = 1500$ m/s and $V_s = 650$ m/s.

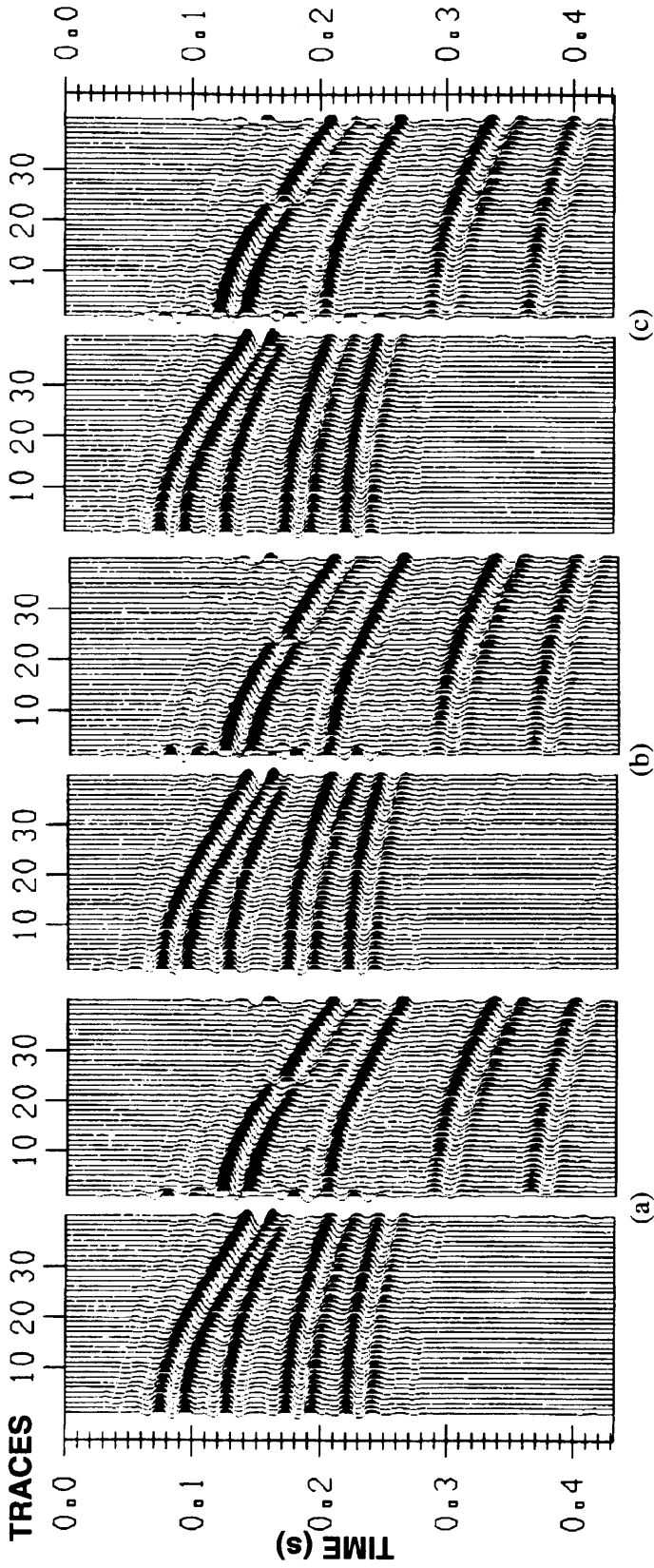


Fig. 2.28. (a) Filtered pass- P and pass- S records, respectively, obtained using $V_p=1650$ and $V_s=715$ m/s.
 (b) Filtered pass- P and pass- S records, respectively, obtained using $V_p=1875$ and $V_s=812.5$ m/s.
 (c) Filtered pass- P and pass- S records, respectively, obtained using $V_p=1275$ and $V_s=552.5$ m/s.

Adding 10% of random noise to the P - P and P - S seismograms shown in Fig. 2.27a were generated the seismograms shown in Fig. 2.29a. The correspondent vertical and horizontal records are shown in Fig. 2.29b where it is evident the superposition of the noisy P and S waves. The pass- P and pass- S outputs considering the correct and wrong P - and S -wave velocities in the near-surface are shown in Figs. 2.29c and 2.30(a,c), respectively. Again the separation filter provides good results.

The next example represents a case which is more problematic in separating P and S waves. Now converted P - S and S - P reflections are also included. Since we have a horizontally layered earth model, P - S and S - P reflections have equal slowness and traveltimes at all offsets. The P - P and P - S seismograms were generated using a minimum phase wavelet with a center frequency of 45 Hz. The Fig. 2.31a shows the incident P -(P - P and S - P) and incident S -(S - S and P - S) waves. The S - P converted reflections have quite low amplitudes whereas the converted P - S waves have large amplitudes. The vertical and horizontal geophone records resulting from the incident P and S waves are shown in the Fig. 2.31b. On the vertical geophone the converted reflections PS -2 and PS -3 have zero amplitudes due to the destructive interference of P - S and S - P . On the horizontal geophone record all P - P and converted reflections show up next the S - S reflections.

The resultant filtered pass- P and pass- S (Fig. 2.31c) were compared with the incident seismograms (Fig. 2.31a). It is evident that good agreement was obtained between the corresponding records. The incident P and S waves are retrieved correctly, although SS -2 and SS -3 appear with low amplitudes after the filtering process.

Figs. 2.32 and 2.33 show the effect on the filtering process with a wrong estimation of the near-surface velocities V_p and V_s for the separation of the vertical and horizontal records in Fig. 2.31b. In the Fig. 2.32 the data was filtered using erroneous values as follows: first we use $V_p = 1650$ m/s and $V_s = 715$ m/s for layer 1 (which represent an overestimation of 10% in the velocities), and next, an overestimation of 25% in the

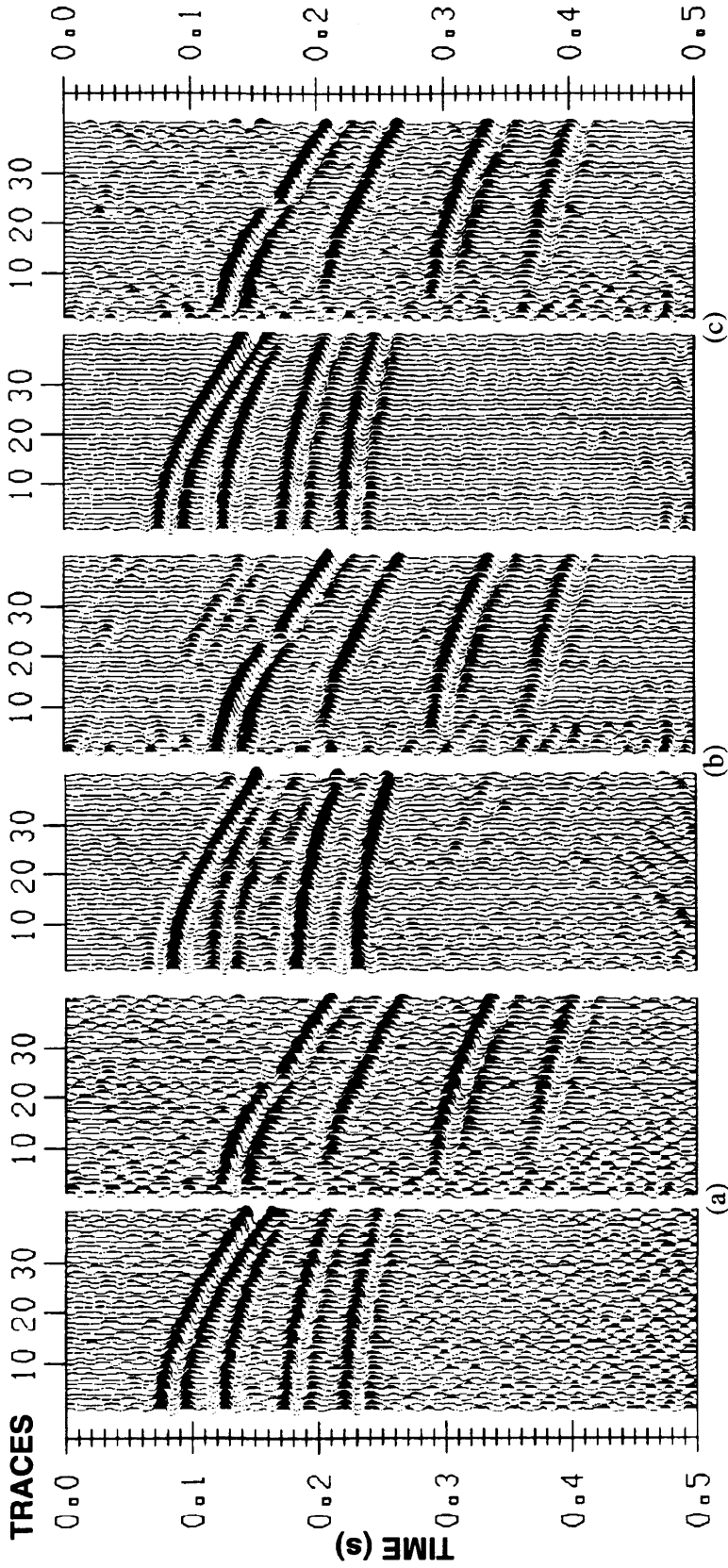


Fig. 2.29. Vertical and horizontal geophone response from the model of Fig. 2.22.

(a) *P-P* and *P-S* reflections with 10% of random noise added, no receiver response considered.

(b) Vertical and horizontal geophone output from incident *P-P* and *P-S* reflections.

(c) Pass-*P* and pass-*S* sections obtained from both vertical and horizontal records (Fig. 2.29b) using $V_p = 1500$ m/s and $V_s = 650$ m/s.

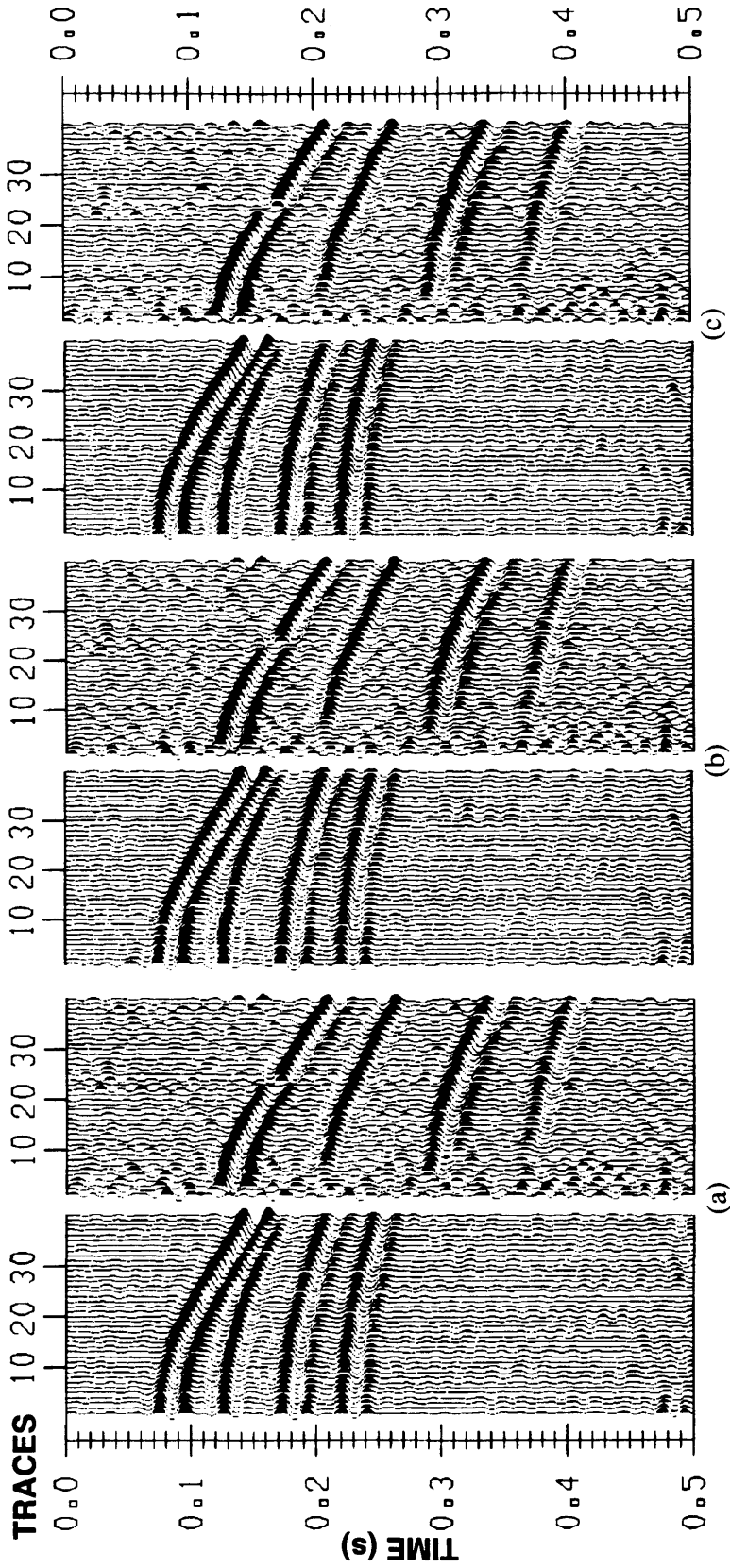


Fig. 2.30. (a) Filtered pass- P and pass- S records, respectively, obtained using $V_p = 1650$ m/s and $V_s = 715$ m/s.
 (b) Filtered pass- P and pass- S records, respectively, obtained using $V_p = 1875$ m/s and $V_s = 812.5$ m/s.
 (c) Filtered pass- P and pass- S records, respectively, obtained using $V_p = 1275$ m/s and $V_s = 552.5$ m/s.

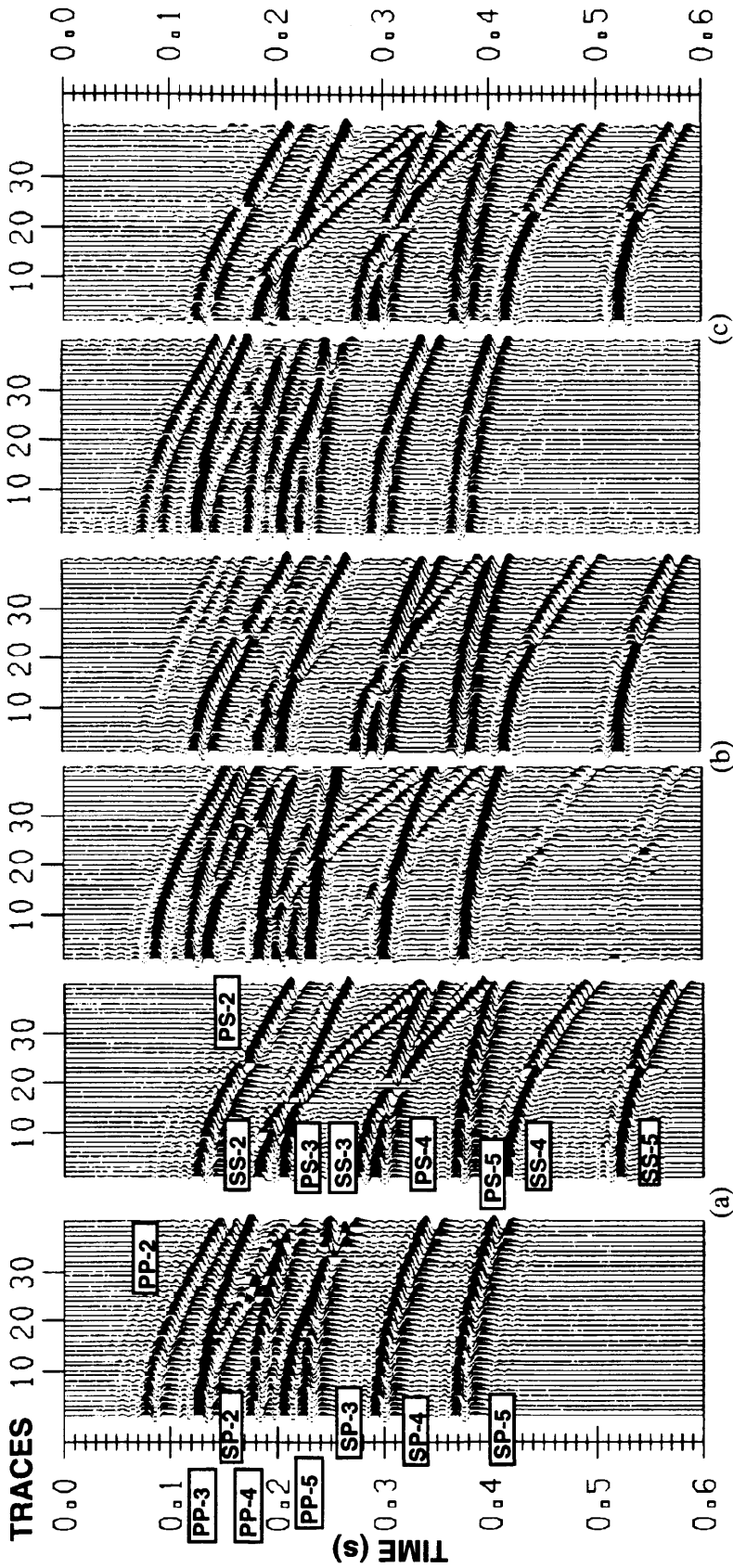


Fig. 2.31. Vertical and horizontal geophone response from model of Fig. 2.22.

(a) P - P , S - P , S - S and P - S reflections, with no receiver response.

(b) Vertical and horizontal geophone output from incident P - P , S - P , S - S and P - S reflections.

(c) Pass- P and pass- S sections obtained from both vertical and horizontal records (Fig. 2.31b) using $V_p = 1500$ m/s and $V_s = 650$ m/s.

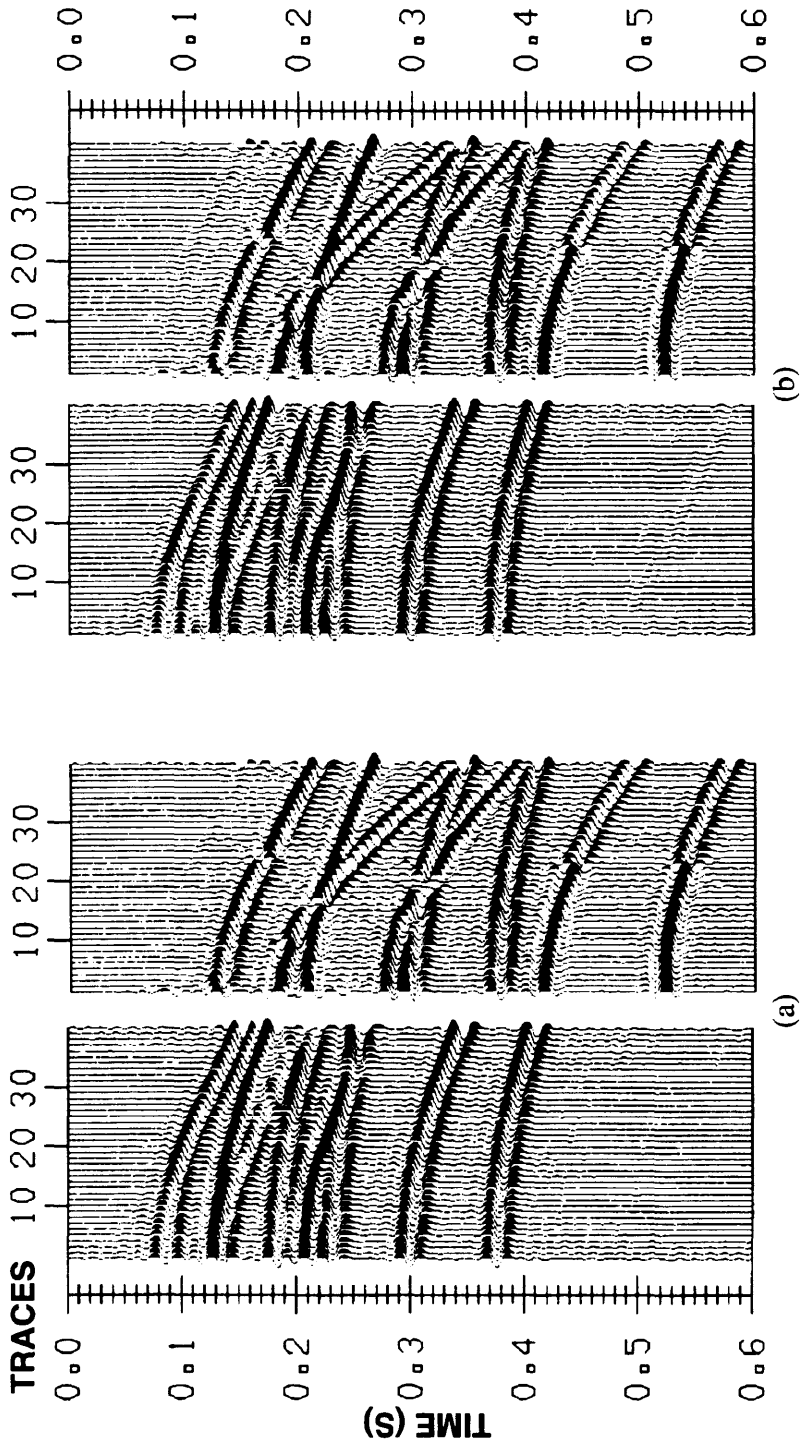


Fig. 2.32. (a) Filtered pass- P and pass- S records, respectively, obtained using $V_p = 1650$ m/s and $V_s = 715$ m/s.
 (b) Filtered pass- P and pass- S records, respectively, obtained using $V_p = 1875$ m/s and $V_s = 812.5$ m/s.

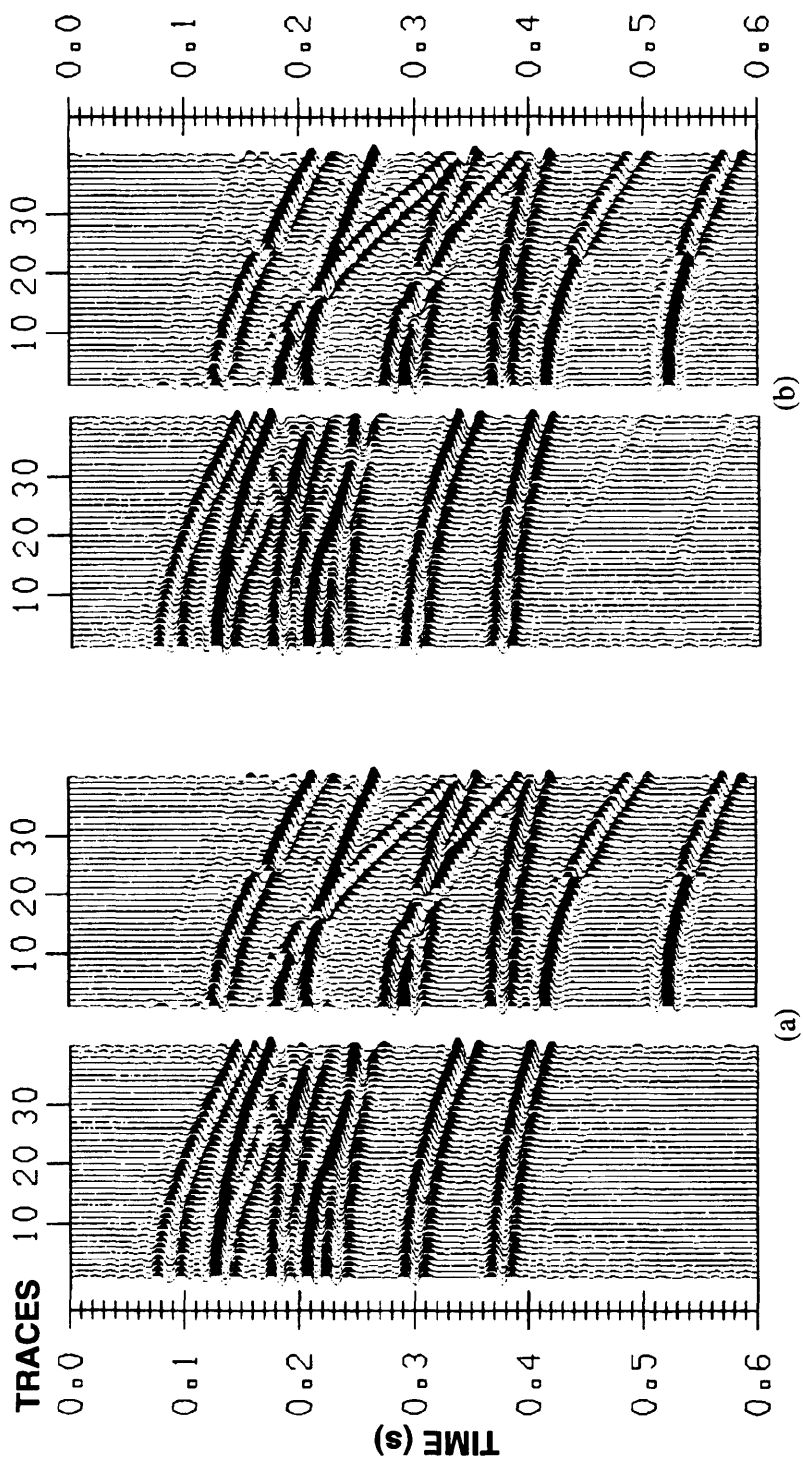


Fig. 2.33. (a) Filtered pass-*P* and pass-*S* records, respectively, obtained using $V_p=1275$ m/s and $V_s=552.5$ m/s.
 (b) Filtered pass-*P* and pass-*S* records, respectively, obtained using $V_p=1500$ m/s and $V_s=780$ m/s.

velocities in the near-surface are used giving $V_p = 1875$ m/s and $V_s = 812.5$ m/s. The resultant sections shown in Fig. 2.33 were processed using first an underestimation of 15% in the velocities of the near-surface giving $V_p = 1275$ m/s and $V_s = 552.5$ m/s, and second, velocity values of $V_p = 1500$ m/s and 780 m/s where the V_p/V_s is equal to 1.92.

The comparison of the filtered pass- P and pass- S records with the incident seismograms shows a reasonable performance. Most of the S -wave energy is removed from the pass- P section. However, there is some P wave leakage onto the pass- S section.

In the last synthetic example, we will deal with data that present static problems. The purpose of the statics correction is to remove the disturbing effects due to the near-surface low-velocity layer on the continuity of deep seismic reflections improving its interpretation, but when we have P and S data combined in the same channel due to the geophone responses is very difficult to know an initial estimation of the refraction static solutions that will be applied to each trace. These circumstances suggest that the P - S separation filter has to be applied on the raw data without P - or S -refraction static solutions.

The basic idea is testing the performance of the P - S separation filter under the presence of static problems. For achieving this goal a P - P data set was acquired on the model shown in Fig. 2.34. The acquisition geometry consisted on a single shot and receiver at the same location (zero-offset data) located in the top of the model. A total of 40 different locations along the model were considered. The P -wave statics values were calculated as follows: i) a normal raytracing between the top of the first layer and the reference reflector (bottom of the layer 2) was performed for obtaining the travel time between both reflectors, ii) a similar raytracing was done between top and bottom of layer 2, and iii) the difference between both travel times for each surface position represents the final P - P statics to be applied on the traces recorded at this location. This procedure was applied along the line to obtain the P - P statics profile. The corresponding refraction statics

for S - S and P - S waves were calculated on assumptions based on the P - P refraction statics data. For S waves was assumed a factor of 2 of the P - P statics while for P - S waves were considered two different cases. The first case considers 10% more of the P -wave statics and in the second case 50% more of the P statics. These statics values were applied on the P - P , S - S and P - S synthetic records acquired on the model shown in Fig. 2.22. The analysis of each case will be considered in the following steps.

First, only P - P and S - S reflections were calculated, where both P and S waves were radiated by the source, which radiated energy uniformly from 0° to 180° . The Fig. 2.35a shows the P - P and S - S seismograms without geophone responses. The refraction statics considered in this case are shown in Table 2.1. Here the incident S waves have a zero point at certain offsets followed by a 180° phase shift for large offsets. Associated vertical and horizontal records are shown in the Fig. 2.35b as would be recorded by realistic 3-C geophones. All P and S arrivals show up on both records. The shallow SS -2 reflection interferes with the PP -5 reflection and shows the expected behavior for pure S waves on both records. The results of the P - S separation applied on both vertical and horizontal records is indicated in the Fig. 2.36a, using near-surface velocities $V_p = 1500$ m/s and $V_s = 650$ m/s, as correspond to the velocities for the first layer in the synthetic model.

The comparison with the filters pass- P and pass- S records with the incident seismograms shows a very good performance of the separation filter recovering the original P - P and S - S seismograms without any interference (SS -2 and PP -5 reflections). Only minor remnant amplitudes of the removed wavetypes are left on each record for near offsets after the P - S separation and could be explained by errors of the τ - p transform due to the truncation of the events in the x - t domain. Also it is important to notice a smoothing effect introduced by the filter on the pass- P and pass- S outputs but the refraction static problems are kept intact and now, after the separation filter, we can apply the correct refraction P - and S -statics to each output. After the separation filter some noise is present

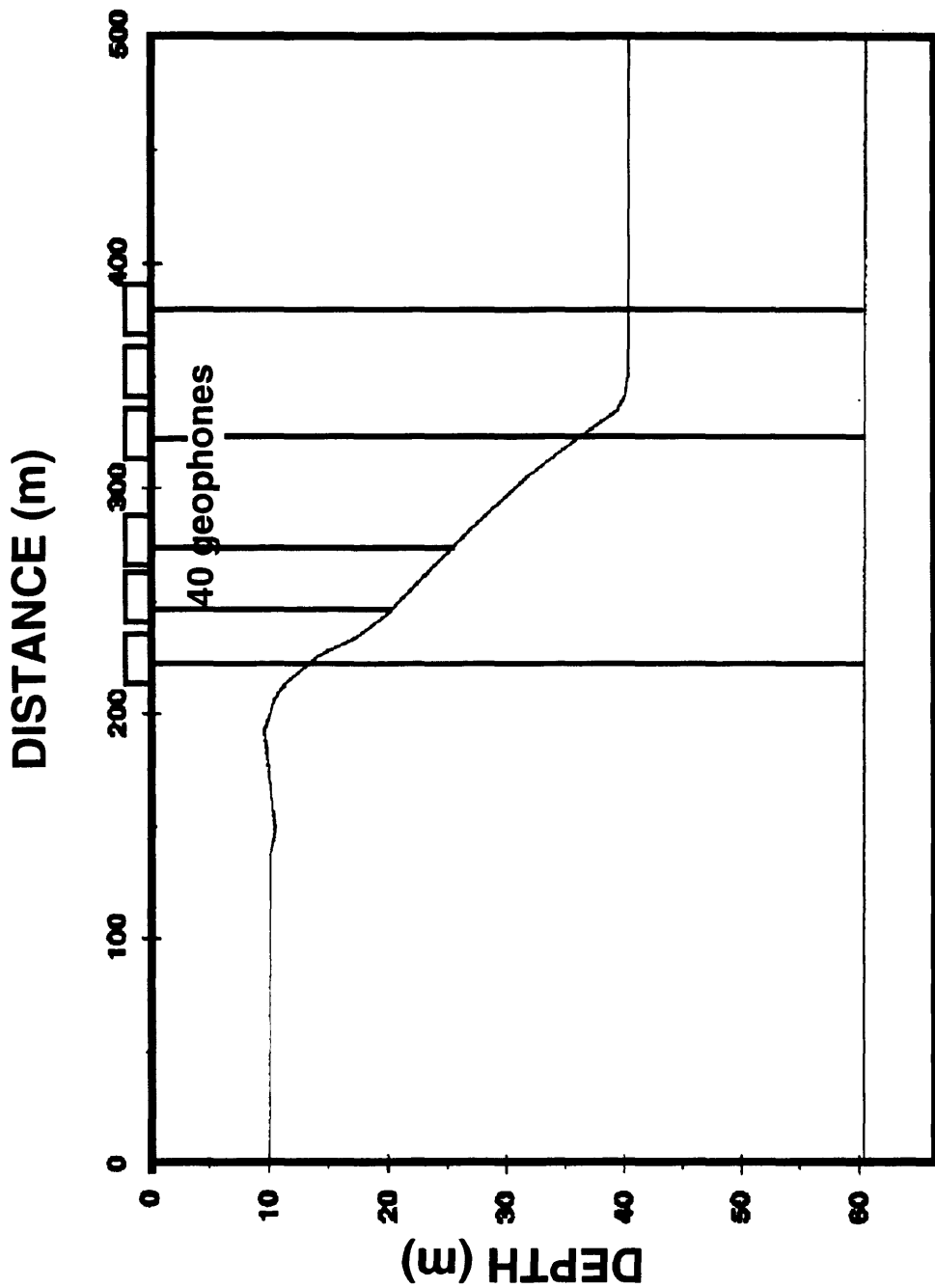


Fig. 2.34. Depth model used for testing the P-S separation filter in the free-surface case under strong changes in refraction statics.

STATION	OFFSET(m)	P-P Refraction statics (ms)	S-S Refraction statics (ms)
1	5	100	200
2	10	100	200
3	15	100	200
4	20	96	192
5	25	92	184
6	30	92	184
7	35	88	176
8	40	84	168
9	45	80	160
10	50	80	160
11	55	76	152
12	60	80	160
13	65	76	152
14	70	76	152
15	75	72	144
16	80	68	136
17	85	68	136
18	90	64	128
19	95	64	128
20	100	60	120
21	105	60	120
22	110	56	112
23	115	56	112
24	120	52	104
25	125	48	96
26	130	44	88
27	135	44	88
28	140	44	88
29	145	44	88
30	150	40	80
31	155	40	80
32	160	40	80
33	165	44	88
34	170	44	88
35	175	44	88
36	180	44	88
37	185	44	88
38	190	44	88
39	195	44	88
40	200	44	88

Table 2.1. Refraction statics used for the *P-P* and *S-S* reflections

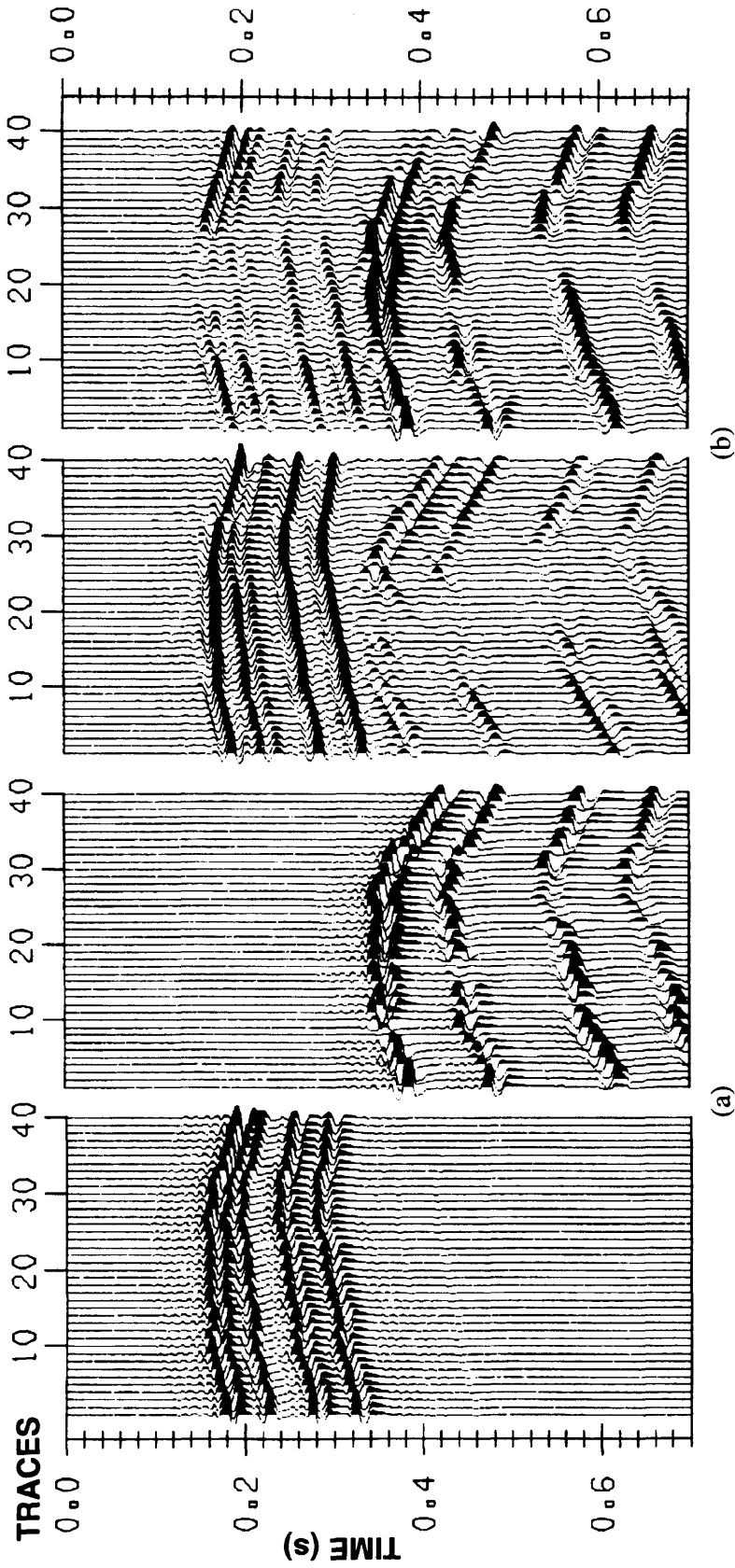


Fig. 2.35. Vertical and horizontal geophone response from the model of Fig. 2.34 considering S-S refraction statics equal 200% of the P-P refraction statics.

(a) P-P and S-S reflections, with no receiver statics.

(b) Vertical and horizontal geophone output from incident P-P and S-S reflections.

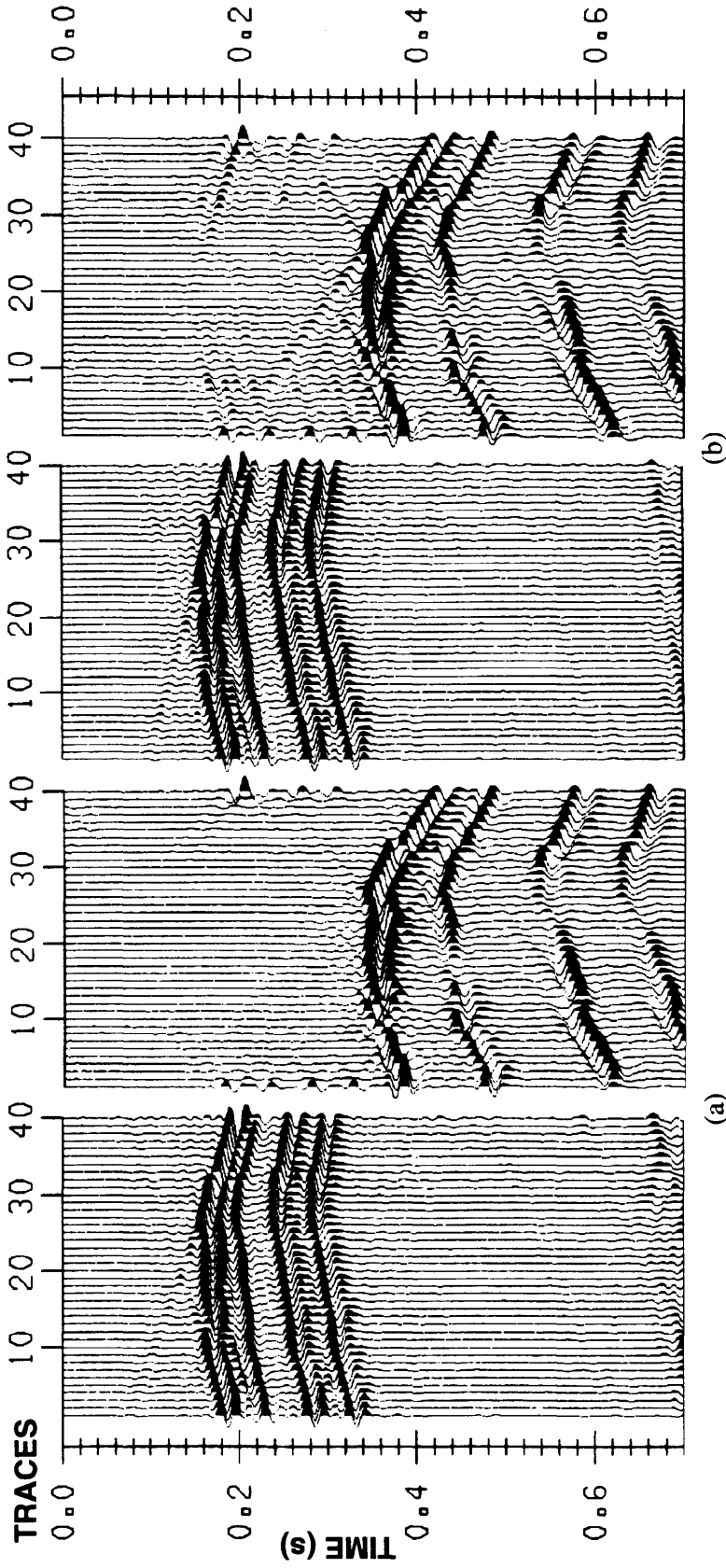


Fig. 2.36. Pass- P and pass- S sections obtained from both vertical and horizontal records (Fig. 2.35b) using
 (a) $V_p=1500$ m/s and $V_s=650$ m/s.
 (b) $V_p=1875$ m/s and $V_s=812.5$ m/s.

on both pass- P and pass- S records as consequence of the limitations during the summation process in the inverse τ - p transform to obtain the x - t sections and the limitations related to the filter coefficients calculation.

The effect on the performance of the P - S separation filter considering erroneous estimates of the near-surface velocities V_p and V_s of the layer 1 is shown in the Fig. 2.36b. The vertical and horizontal records from Fig. 2.35b were filtered using erroneous values as $V_p = 1875$ m/s and $V_s = 812.5$ m/s for layer 1 (which represent an overestimation of 25% in the velocities). The results presented in Figs. 2.36b can be compared with the records from Fig. 2.35a. We got similar results of the filter when erroneous velocities were used for the separation indicating the robustness of the separation filter. It is evident that the pass- P records is less effected by errors in the velocities than the pass- S records, where there is still some residual P -wave energy.

As a second case, an explosive source (P waves only) radiated energy uniformly from 0° to 180° downward. Only P - P and P - S primary reflections are considered. Figs. 2.37a and Fig. 2.39a show the P - P and P - S seismograms without geophone responses, where there are only P wave arrivals on the vertical geophone and only S wave arrivals on the horizontal geophone. The P - P and P - S seismograms were generated using a minimum phase wavelet with a center frequency of 50 Hz. Then, the P - P seismogram represents the response of the vertical geophone taking R_V^S equal zero; likewise with the P - S seismogram with R_H^P equal zero. For these incident P - P and P - S seismograms we will consider two different refraction static solutions for the S -wave data which are shown in Table 2.2, where the S -wave refraction static solution represents 110% (case 1 - Fig. 2.37a) and 150% (case 2 - Fig.2.39a) of the P -wave refraction static solution, respectively.

Taking the geophone responses and the incident P and converted waves (Fig. 2.37a) gives the vertical and horizontal geophone records as shown in Fig. 2.37b, where P and S reflections shown up in both channels.

The filtered pass- P and pass- S are shown in Fig. 2.38a. They can be compared with the incident seismograms (Fig. 2.37a). There is a reasonable agreement between the corresponding records indicating fairly good wave-type separation.

The vertical and horizontal geophone records from Fig. 2.37b were filtered using erroneous values of P - and S -velocities in the near-surface as $V_p = 1875$ m/s and $V_s = 812.5$ m/s for layer 1 (which represent an overestimation of 25% in the velocities). The filtered sections are shown in Fig. 2.38b.

Next, the P - P and P - S seismograms considering the refraction statics for case 2 (Table 2.2) are shown in Fig. 2.39a. Associated vertical and horizontal records are shown in the Fig. 2.39b as would be recorded by realistic 3-C geophones. All P and S arrivals show up on both records.

The results of the P - S separation applied on both vertical and horizontal records is indicated in the Fig. 2.40a, using near-surface velocities $V_p = 1500$ m/s and $V_s = 650$ m/s, which are the velocities for the first layer in the synthetic model. Fig. 2.40b shows the filtered results using erroneous velocities values in the near-surface.

These results (Figs. 2.38b and 2.40b) are compared with the incident P and S waves shown in Figs. 2.37a and 2.39a. The similar results of the filter when using erroneous velocities for the calculation indicate a robust operation. We can see that the pass- P record is less effected by errors in the velocities than the pass- S record, where there is still some residual P -wave energy. Also it is important to point out that the separation filter doesn't alter the shape of the incident data keeping the static problems

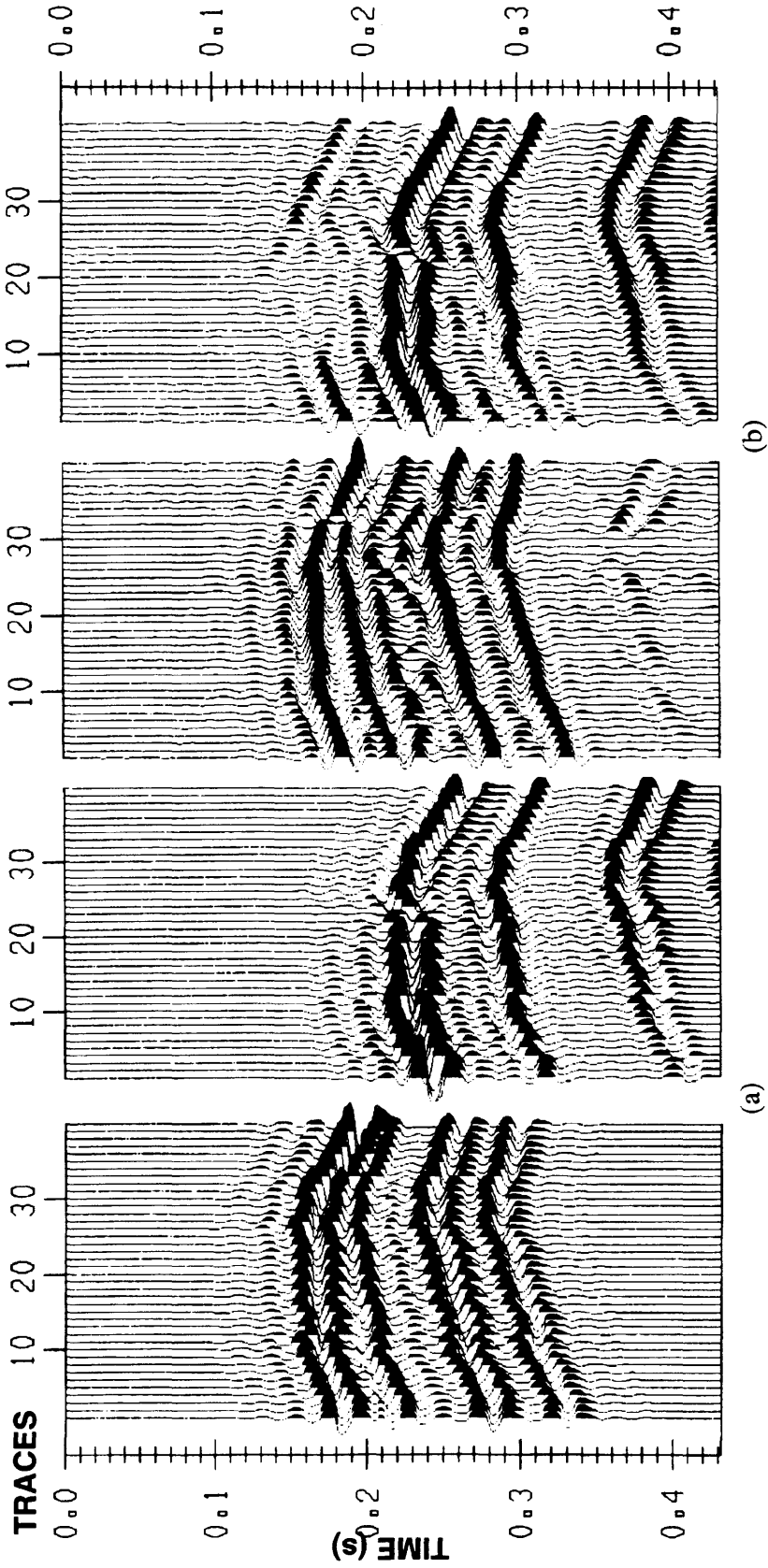


Fig. 2.37. Vertical and horizontal geophone response from the model of Fig. 2.34 considering P - S refraction statics equal 110% of the P - P refraction statics.

(a) P - P and P - S reflections, with no receiver response.

(b) Vertical and horizontal geophone output from incident P - P and P - S reflections.

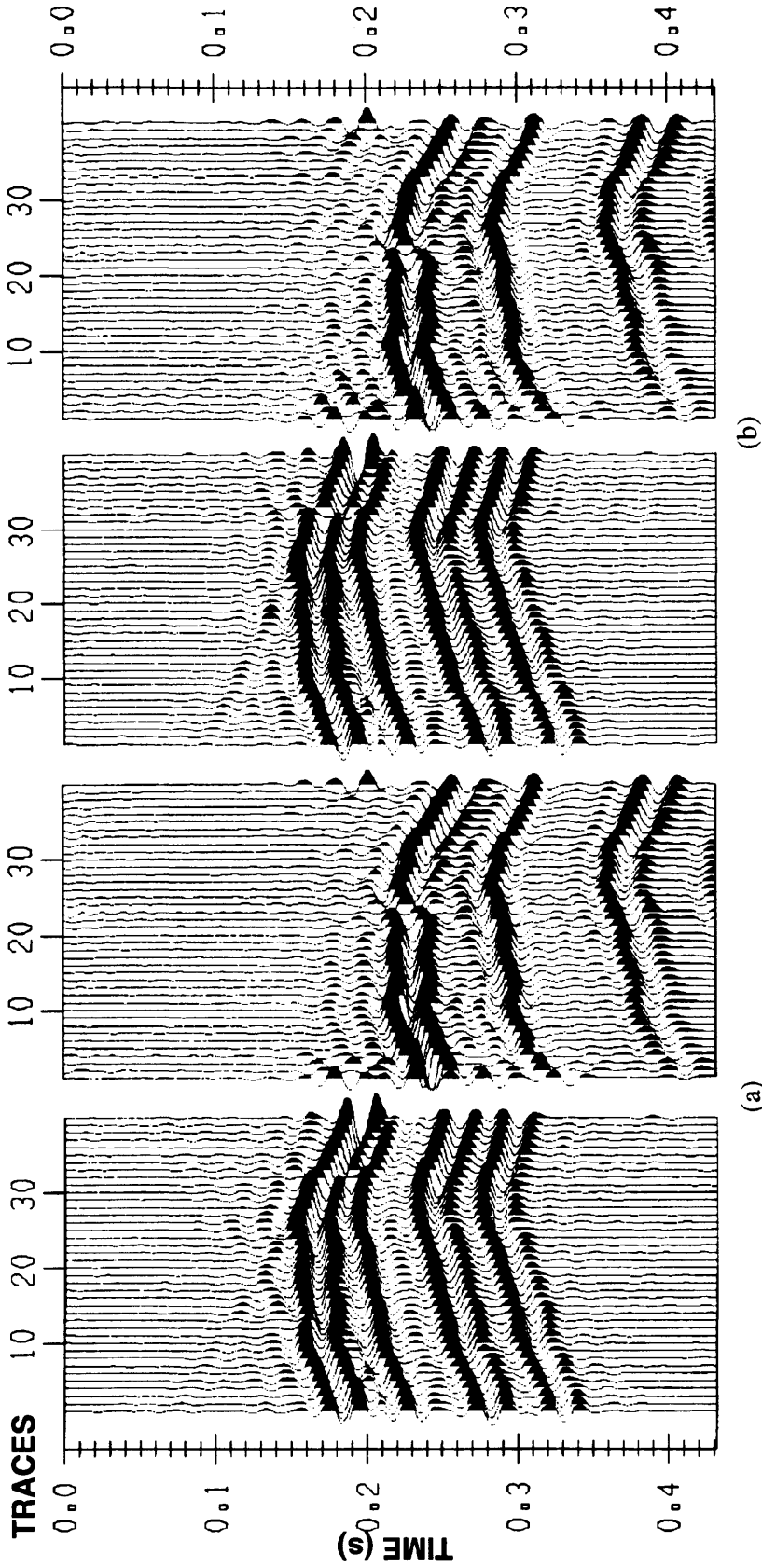


Fig. 2.38. Pass- P and pass- S sections obtained from both vertical and horizontal records (Fig. 2.37b) using
 (a) $V_p = 1500$ m/s and $V_s = 650$ m/s.
 (b) $V_p = 1875$ m/s and $V_s = 812.5$ m/s.

Station	Offset (m)	P-P refraction statics (ms)	P-S refraction statics (ms) - Case 1	P-S refraction statics (ms) - Case 2
1	5	100	110	150
2	10	100	110	150
3	15	100	110	150
4	20	96	105.6	144
5	25	92	101.2	138
6	30	92	101.2	138
7	35	88	96.8	132
8	40	84	92.4	126
9	45	80	88	120
10	50	80	88	120
11	55	76	83.6	114
12	60	80	88	120
13	65	76	83.6	114
14	70	76	83.6	114
15	75	72	79.2	108
16	80	68	74.8	102
17	85	68	74.8	102
18	90	64	70.4	96
19	95	64	70.4	96
20	100	60	66	90
21	105	60	66	90
22	110	80	88	120
23	115	56	61.6	84
24	120	56	61.6	84
25	125	52	57.2	78
26	130	48	52.8	72
27	135	44	48.4	66
28	140	44	48.4	66
29	145	44	48.4	66
30	150	40	44	60
31	155	40	44	60
32	160	40	44	60
33	165	44	48.4	66
34	170	44	48.4	66
35	175	44	48.4	66
36	180	44	48.4	66
37	185	44	48.4	66
38	190	44	48.4	66
39	195	44	48.4	66
40	200	44	48.4	66

Table 2.2. Refraction statics used for the converted waves considering 110% (case 1) and 150% (case 2) of the *P* refraction statics.

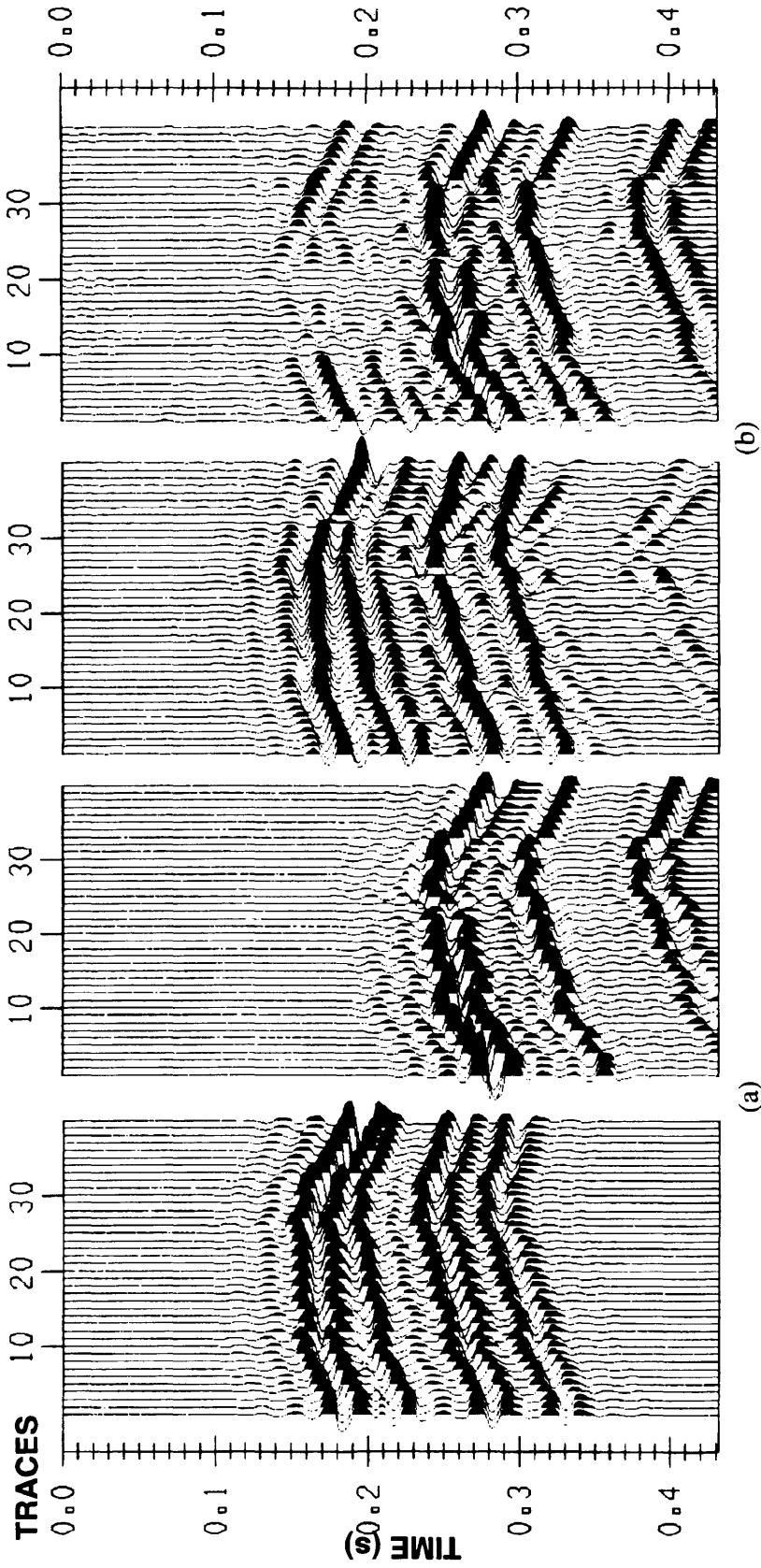


Fig. 2.39. Vertical and horizontal geophone response from the model of Fig. 2.34 considering P - S refraction statics equal 150% of the P - P refraction statics.

(a) P - P and P - S reflections, with no receiver response.

(b) Vertical and horizontal geophone output from incident P - P and P - S reflections.

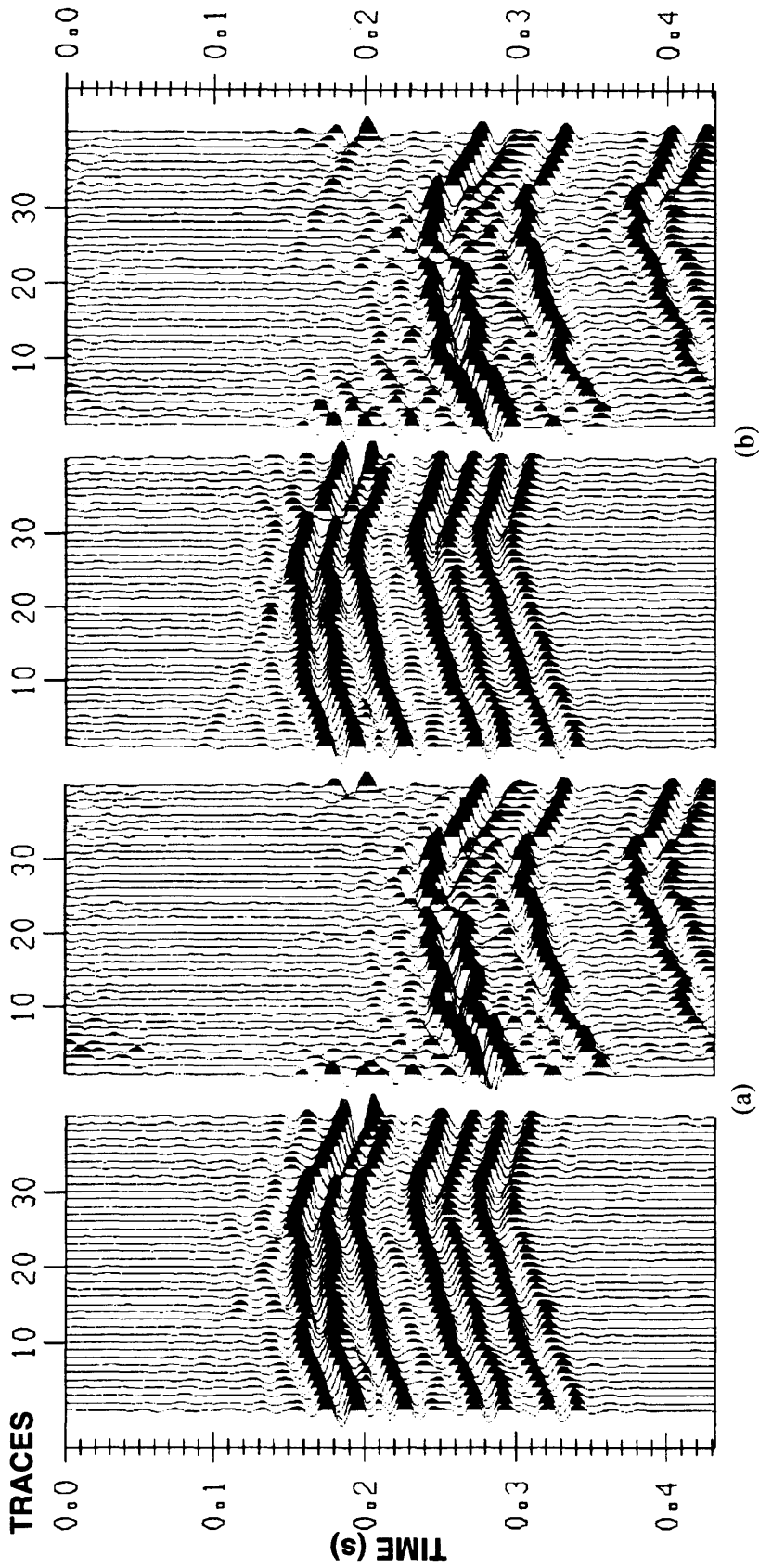


Fig. 2.40. Pass- P and pass- S sections obtained from both vertical and horizontal records (Fig. 2.29b) using
 (a) $V_p = 1500$ m/s and $V_s = 650$ m/s.
 (b) $V_p = 1875$ m/s and $V_s = 812.5$ m/s.

and eliminating the superposition of the P and S waves effectively even it have not been refraction static corrected. This result gives the confidence that the modal filter could be applied to the raw data without an alteration in amplitude, frequency and phase in the wavefields guarantying better results and the end of the processing sequence.

2.6.2 Real data

2.6.2.1 Barinas data

This real case is from a potential stratigraphic production area in Venezuela. Fig. 2.41a,b shows the vertical and horizontal raw records acquired using 3-C geophones along a 2-D test in this area. Evident in the vertical and horizontal records are reflections with good continuity in the P and P - S data interpreted at 2.0 - 3.0 s and 3.3 - 4.5 s, respectively, which are strongly contaminated by ground roll noise. The ground roll interferes with the reflections, diminishing them, and preventing us from seeing clearly the data contained in the recorded records.

Also it is important to point out the presence of good first breaks for both P - P and converted data which let us to pick and calculate adequately refraction statics. The refraction static solutions used in this work were provided by Intevop S.A. The velocity information at the near-surface required for the P - S separation filter was obtained from the uphole time information and the depth of the shots which are shown in Fig. 2.42(a,b).

In Fig. 2.43 we have a schematic summary of the raypaths of a refracted wavelet where the shot S and the detector G located at the ground surface, h defines the depth at which the source was located during the survey, i_n defines the angle of incidence of the wave generated by the source to the unweathered layer, and V_o is the velocity of the near surface. The uphole time correction defines the travel time taken by the refracted wavelet

generated by the source to reach the geophone located at the ground surface. The uphole correction is given by (Palmer, 1986)

$$\text{Uphole correction} = \frac{h \cos(i_n)}{V_o} \quad (2.40)$$

In seismic is normally assumed that i_n is equal to zero. Then, if we know the value of the uphole time, which could be obtained from a refraction survey performed in the area, and the depth of the sources through the survey we can determine the value of the P -wave velocity at the near surface. Then the expression of the velocity takes the simple form (Palmer, 1986)

$$V_o = \frac{h}{\text{Uphole correction}} \quad (2.41)$$

Taking a mean value of 10.94 m for the depth of the sources and a mean uphole time value of 12.78 ms for the ^{entire} ~~entire~~ survey, we get that $V_o = 856$ m/s for the P wave and $V = 428$ m/s for the S wave ^{assuming a} ~~considering the~~ V_p/V_s ratio equal 2.

The filtered records pass- P and pass- S corresponding to both raw records are shown in Figs. 2.44b and 2.45b using $V_p = 856$ m/s and $V_s = 428$ m/s obtained from the uphole time information and assuming a V_p/V_s ratio 2.0. In the Fig. 2.44(a,b), is shown the effect of the P - S separation filter in the τ - p transformation on a single shot from the vertical record which removes the strong amplitudes of the ground roll present in the data, preserves the amplitude and phase of the reflection, and improves the continuity of the reflections. The same results were obtained for a single shot of the radial record shown in Fig. 2.45(a,b). Although the analysis of the raw data indicated a low superposition between P and P - S waves, it is evident the good performance of the P - S separation filter

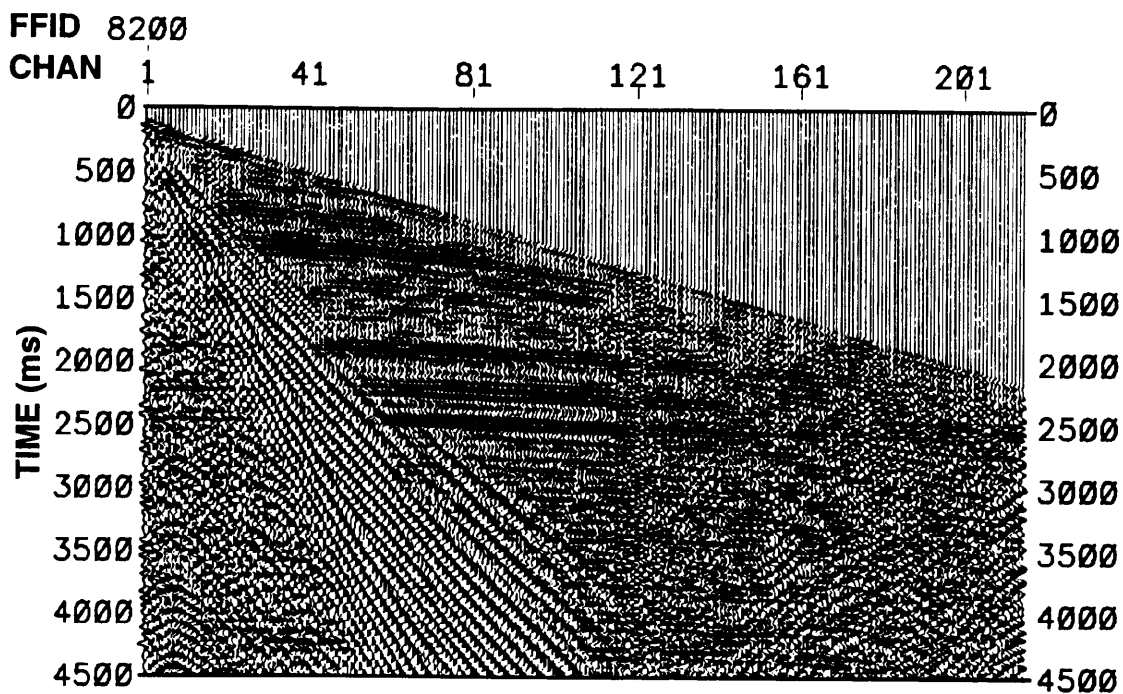


Fig. 2.41a. Raw shot gather from the vertical component showing the strong superposition between the ground roll and reflections.

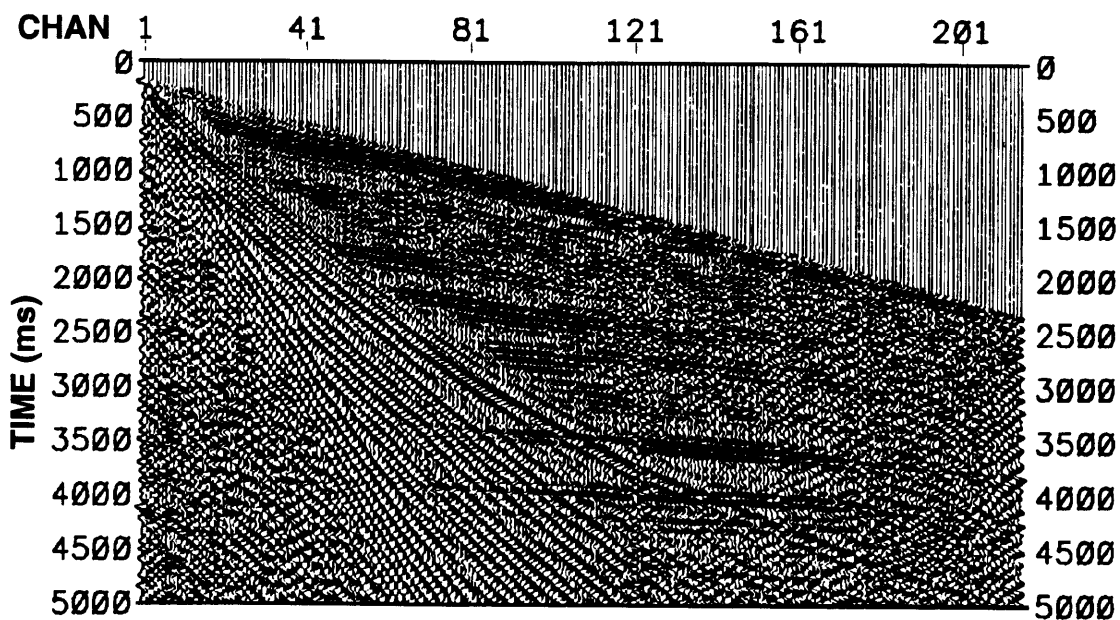


Fig. 2.41b. Raw shot gather from the horizontal component showing the strong superposition between the ground roll and reflections.

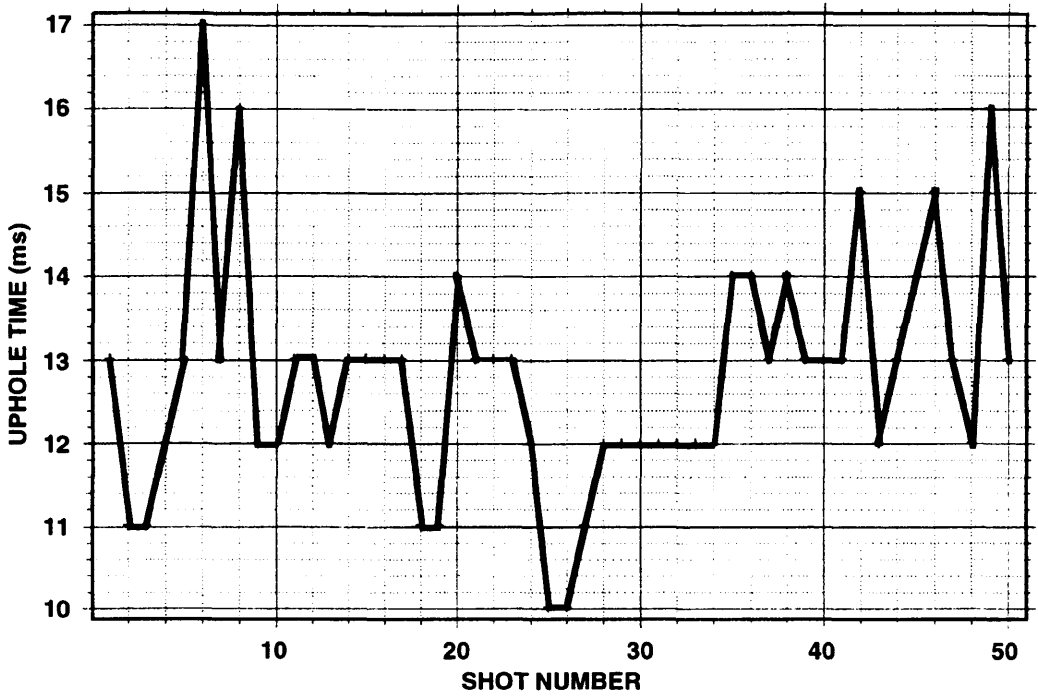


Fig. 2.42a. Uphole time values of the Barinas survey.



Fig. 2.42b. Source depth in the Barinas survey.

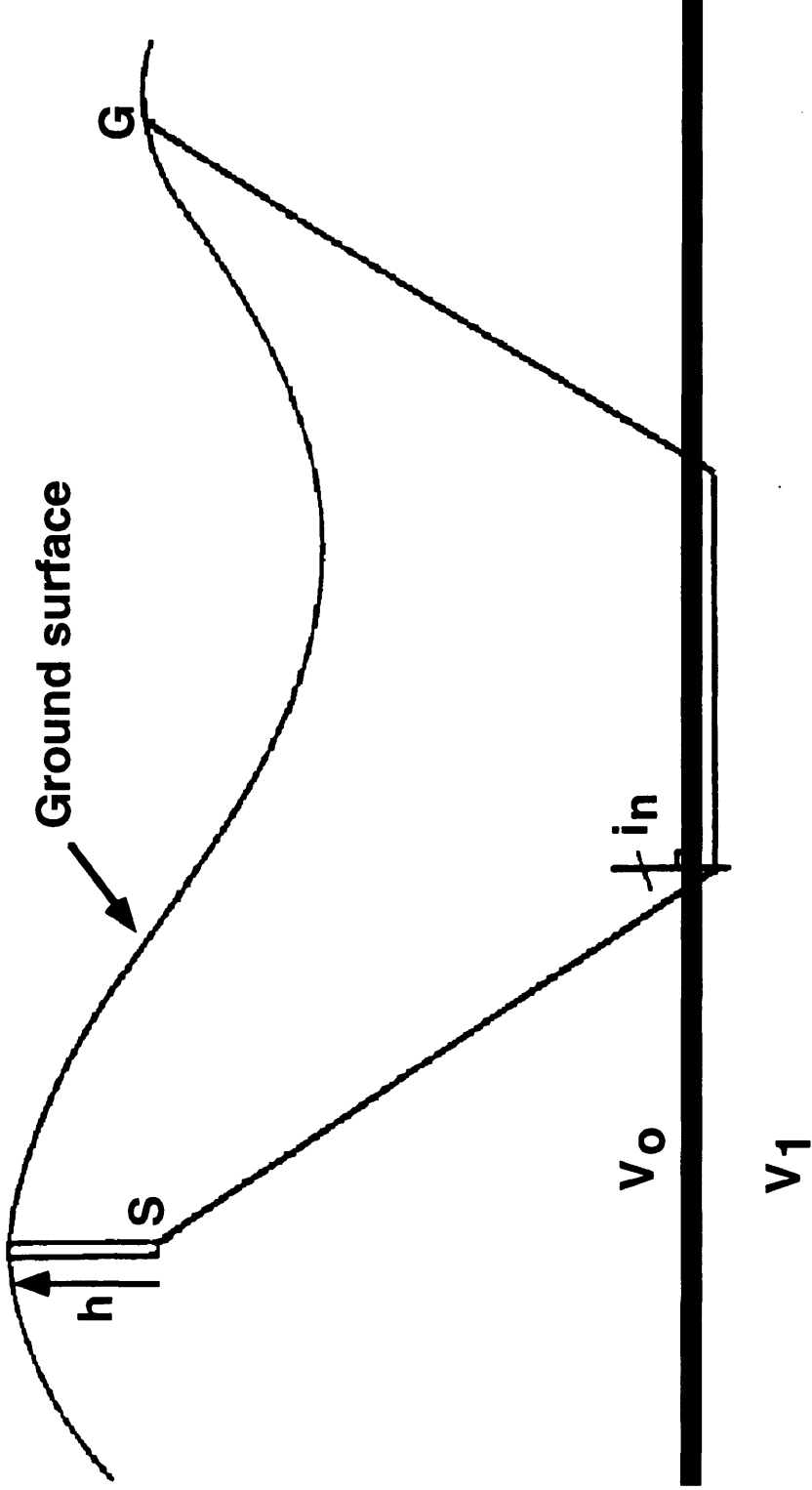


Fig. 2.43. Schematic summary of the raypaths and parameters used in deriving the uphole correction.

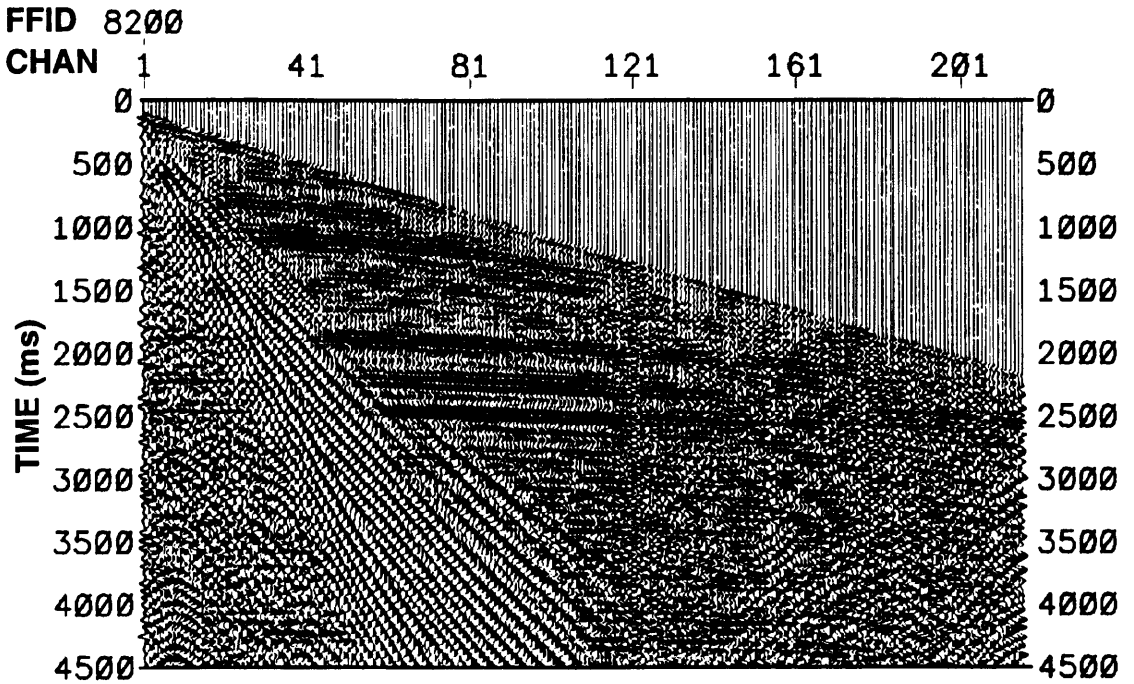


Fig. 2.44a. Raw shot gather from the vertical component.

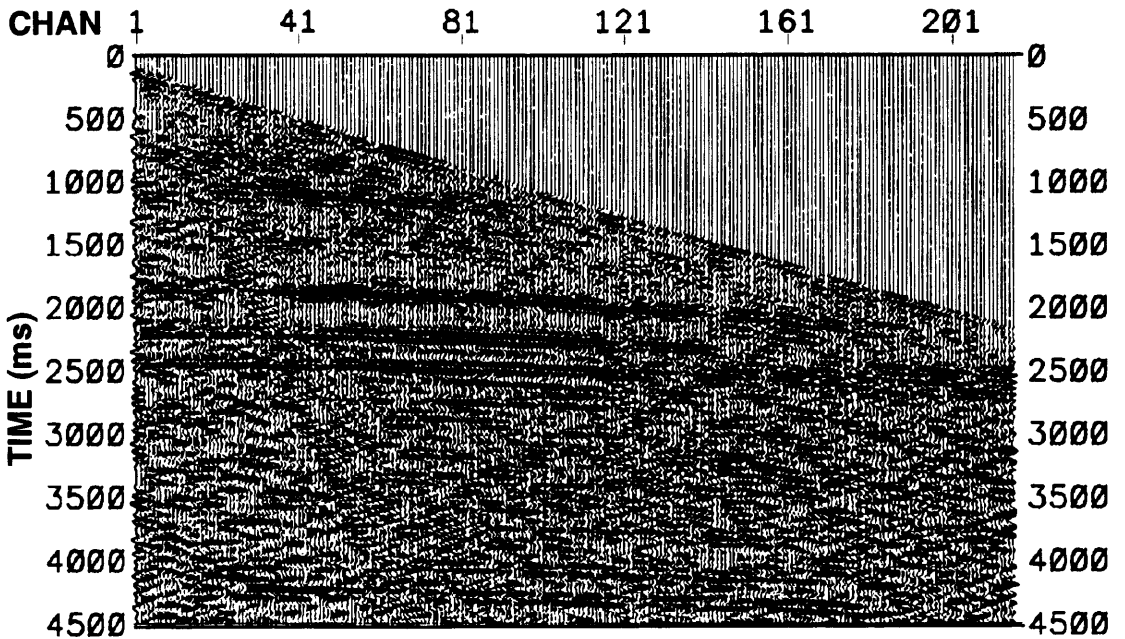


Fig. 2.44b. Filtered pass-*P* record obtained from vertical and horizontal records (Fig. 2.41) using $V_p = 856$ m/s and $V_s = 428$ m/s.

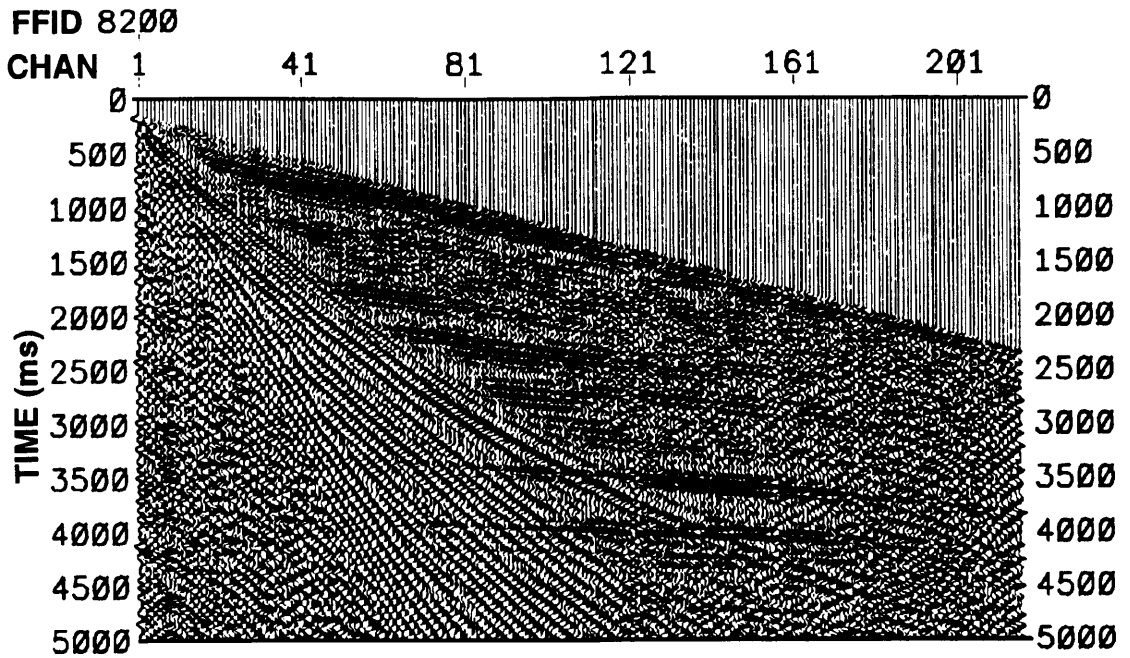


Fig. 2.45a. Raw shot gather from the horizontal component.

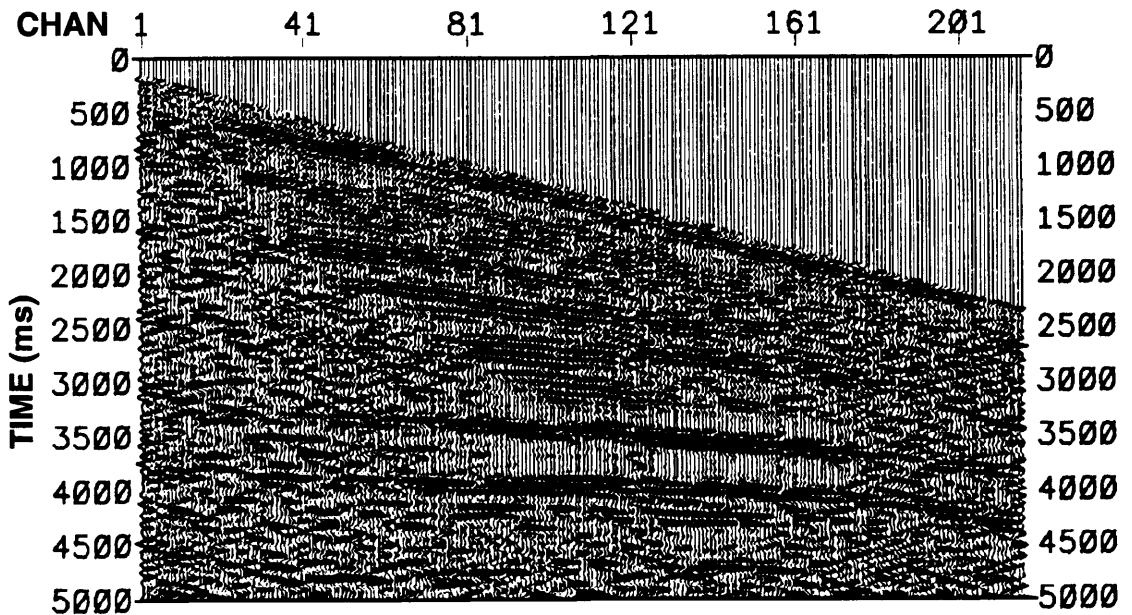


Fig. 2.45b. Filtered pass-S-record obtained from vertical and horizontal records (Fig. 2.41) using $V_p = 856$ m/s and $V_s = 428$ m/s.

in isolating the principal P and P - S events. Some remnant P - S in the pass- P data between 3.4 - 3.6 s at large offsets is present. In the same record are several reflection between 4 - 4.5 s that are not evident on the vertical raw record. The analysis of the slopes associated with these reflections seem to indicate any relation with converted waves observed at the same window time on the pass- S record.

In base on the previous results we plan to obtain a brute stack of each component. We processed both set of data with and without modal filter for comparing the improvement introduced by the separation filter. For processing the vertical channel we use the processing flow shown in Fig. 2.46.

As we can see in the processing flow without separation filter we applied a f - k filter which allows us to eliminate the ground roll, rejecting all noise and giving clean records. From the autocorrelograms performed before and after deconvolution we could obtain the best parameters for the deconvolution process which compress the wavelet and clean the data. For the deconvolution we used a minimum phase wavelet with an operator length of 100 ms and prediction lag of 5 ms, and a design window between 2000 and 2500 ms. Finally, f - x deconvolution was applied for removing the remnant random noise present improving the continuity in the data.

Fig. 2.47 shows a shot after applying all the sequence defined just before brute stack without and with P - S separation filter, respectively. Here we can see the big improvement introduced by the separation filter in the continuity of the P - P reflections, definition of the wavelet and removing noise from the data.

After sorting the data by CDP's a velocity analysis was performed on both data sets, without and with modal filter. From the velocity analysis (Fig. 2.48) we found a better definition of the P -wave velocities when it is used the data from the separation filter due to this process remove noise and converted wave present originally in the data.

The processing sequence used for processing the radial component is shown in Fig. 2.49 and is similar to the processing sequence for P -waves. For removing the ground roll the data was $f-k$ filtered. The parameters for the deconvolution were determined using autocorrelograms. The final solution after applying geometry, elevation and refraction statics, $f-k$ filter, amplitude recovery and balancing, deconvolution, $f-x$ deconvolution and band-pass filtering is shown in Fig. 2.50a. This result is compared with the data processed with the separation filter (Fig. 2.50b), it is evident a very good performance of the filter clean data free of noise and a better definition of converted reflections.

Again an important difference is noted in the velocity analysis after CCP binning between data with and without the modal filter. The velocity analysis performed on the filtered data provides a better velocity estimation then a better picture of the stack section (Fig. 2.51).

The brute stacked sections for P waves obtained from conventional and modal filtered data are shown in Fig. 2.52 and 2.53 respectively. Again we can see from these stacked sections an improvement in the continuity and definition of the P - P reflections on the pass- P section due to the elimination of noise and converted waves present in the raw data that the P - S separation filter does. The same good performance is observed for the S wave on the brute stacked sections obtained from conventional and modal filtered data (Figs. 2.54 and 2.55).

A detailed picture of the interest area (carbonates) is shown on Figs. 2.56 and 2.57 for both pass- P and pass- S sections.

The effect on the performance of the P - S separation filter considering wrong estimates of the near-surface velocities V_p and V_s is shown in the Figs. 2.58 and 2.59. The vertical and horizontal records were filtered using erroneous values as follows: first we

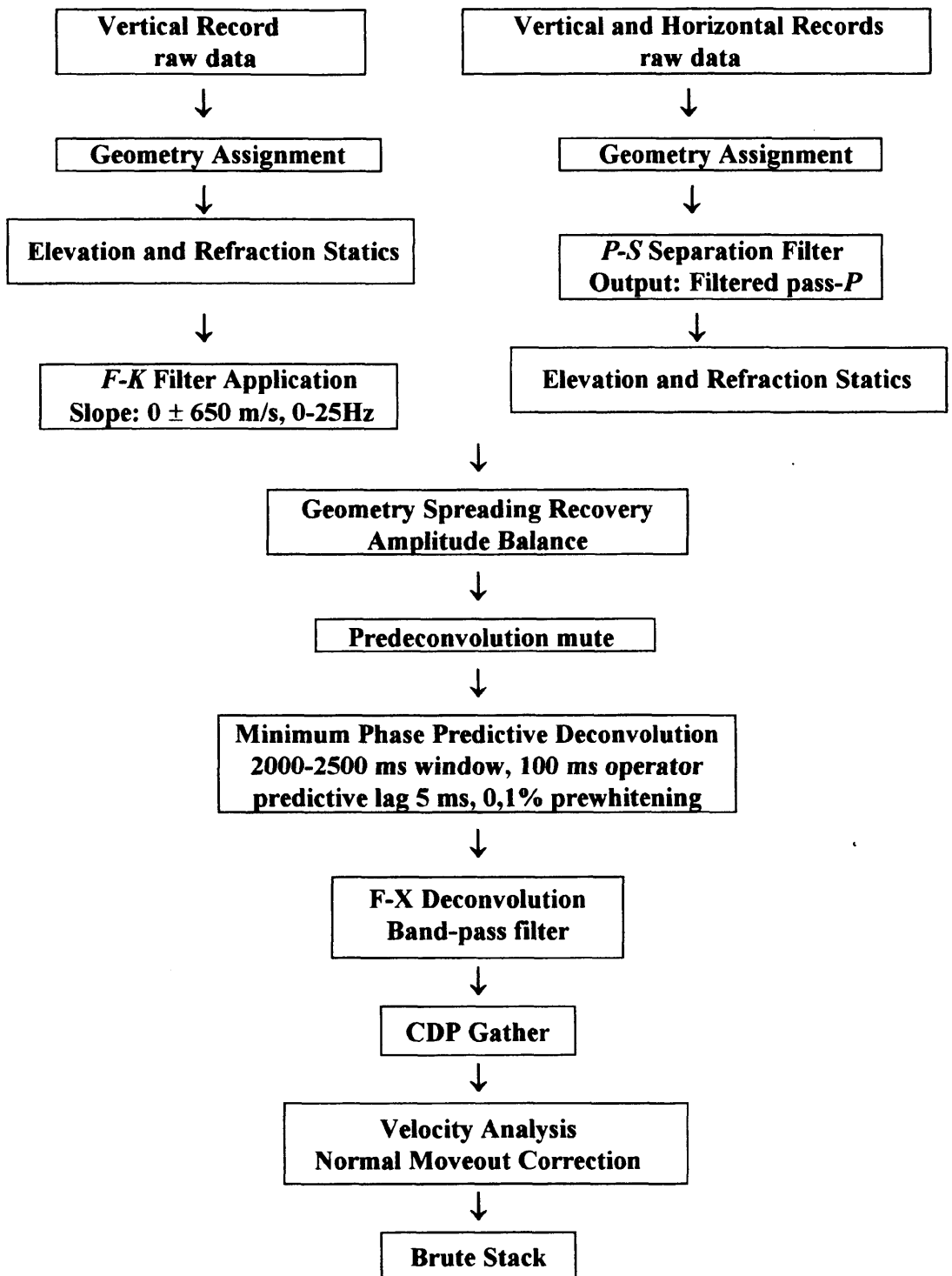


Fig. 2.46. Processing flowchart for *P* wave without and with modal filter.

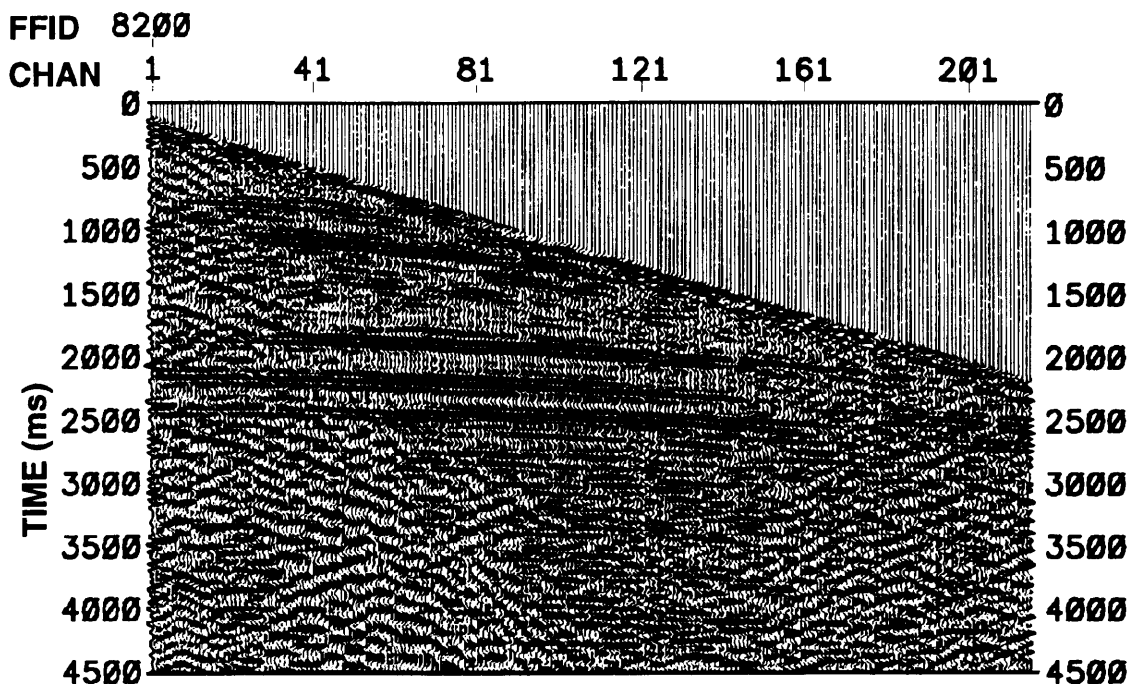


Fig. 2.47a. Shot gather of the vertical component after applying the processing flow shown in Fig. 2.46 without modal filter.

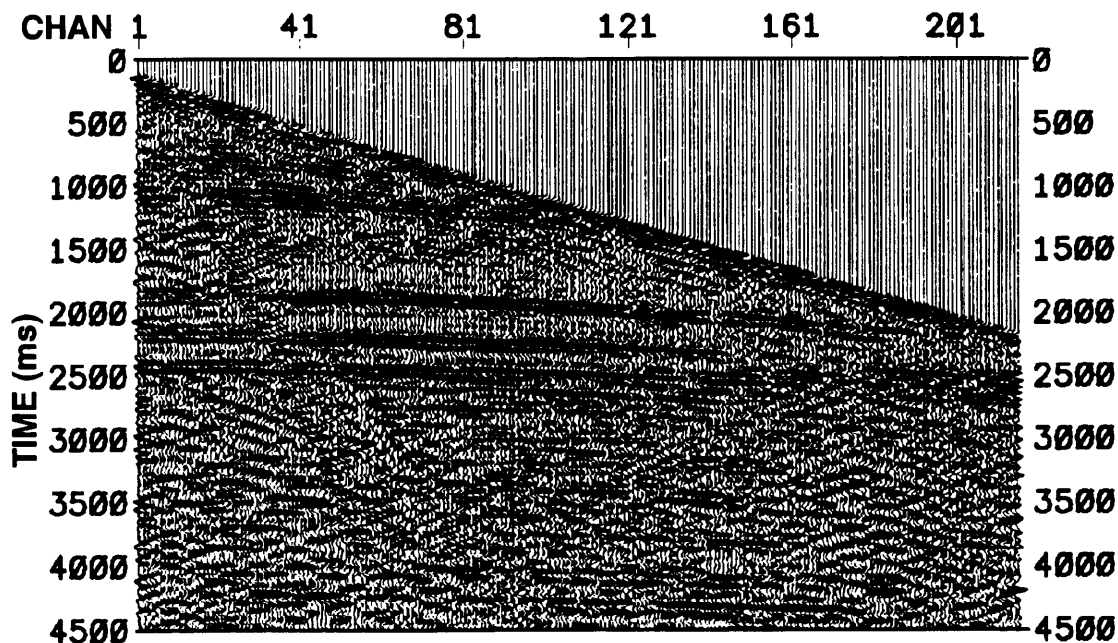


Fig. 2.47b. Pass-*P* output obtained from both vertical and horizontal records (Fig. 2.41) after applying the processing flow shown in Fig. 2.46 with modal filter.

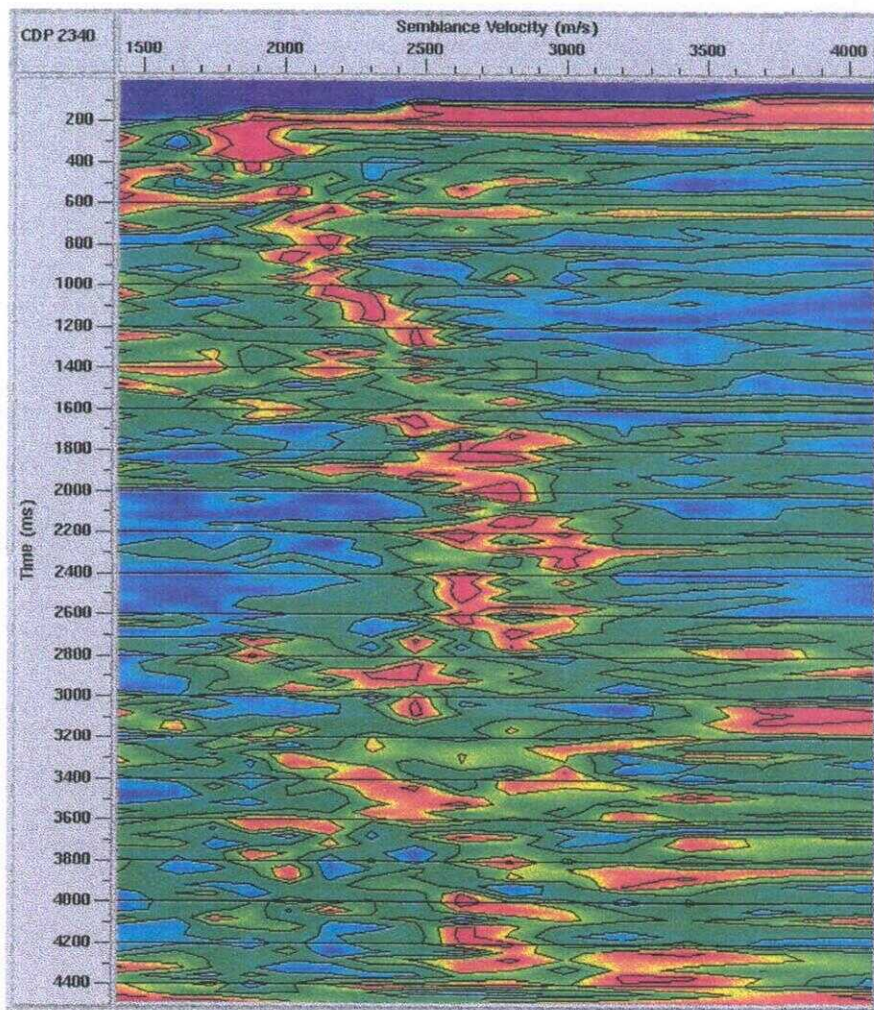


Fig. 2.48a. Velocity analysis for the CDP 2340 without modal filter applied.

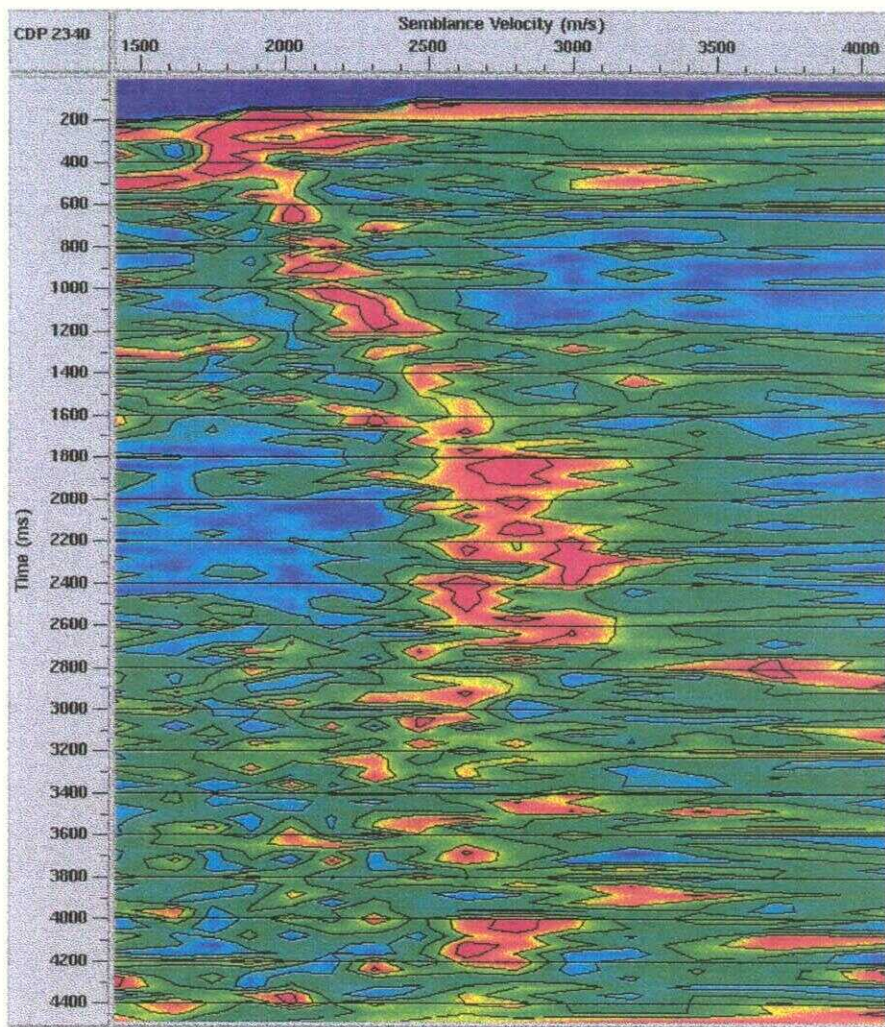


Fig. 2.48b. Velocity analysis for the CDP 2340 after modal filtering.

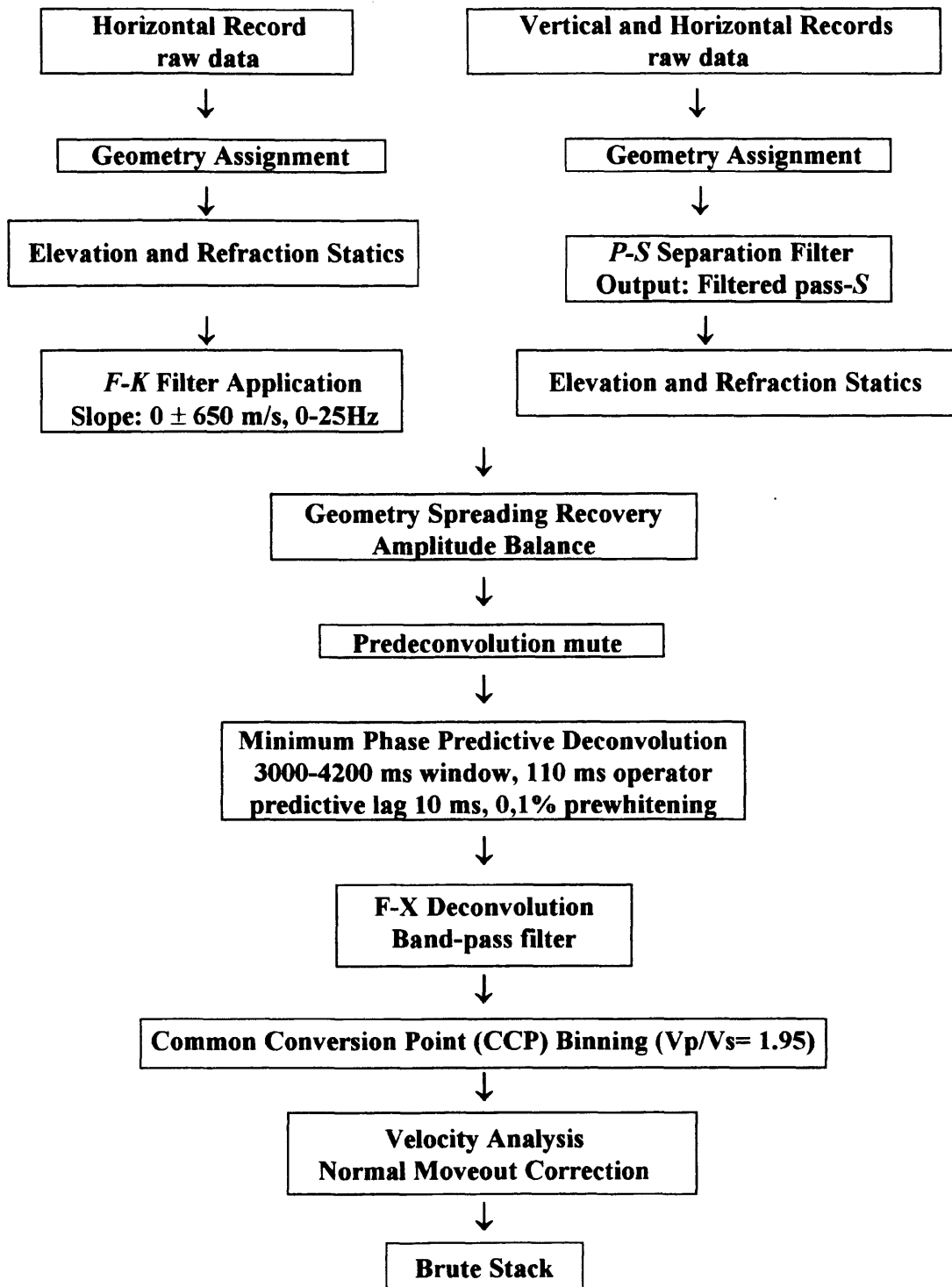


Fig. 2.49. Processing flowchart for *S* waves in the Barinas data without and with modal filter.

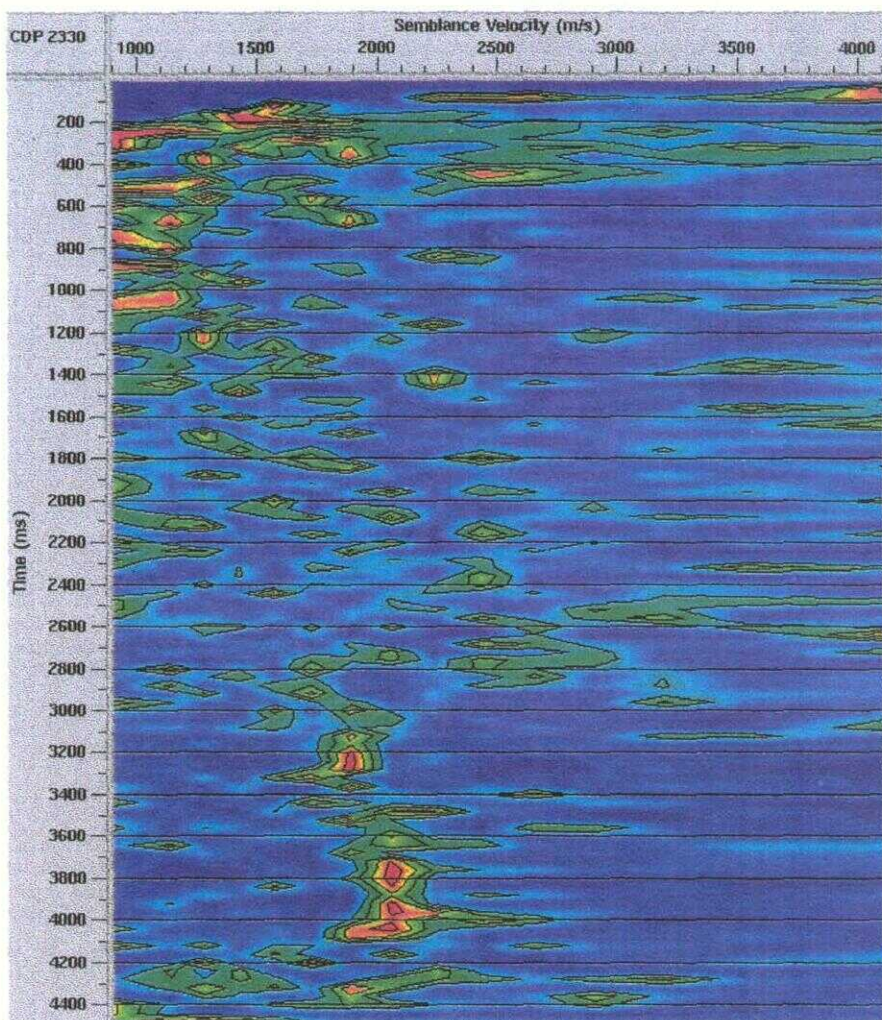


Fig. 2.51a. Velocity analysis for the CCP 2330 without modal filter applied.

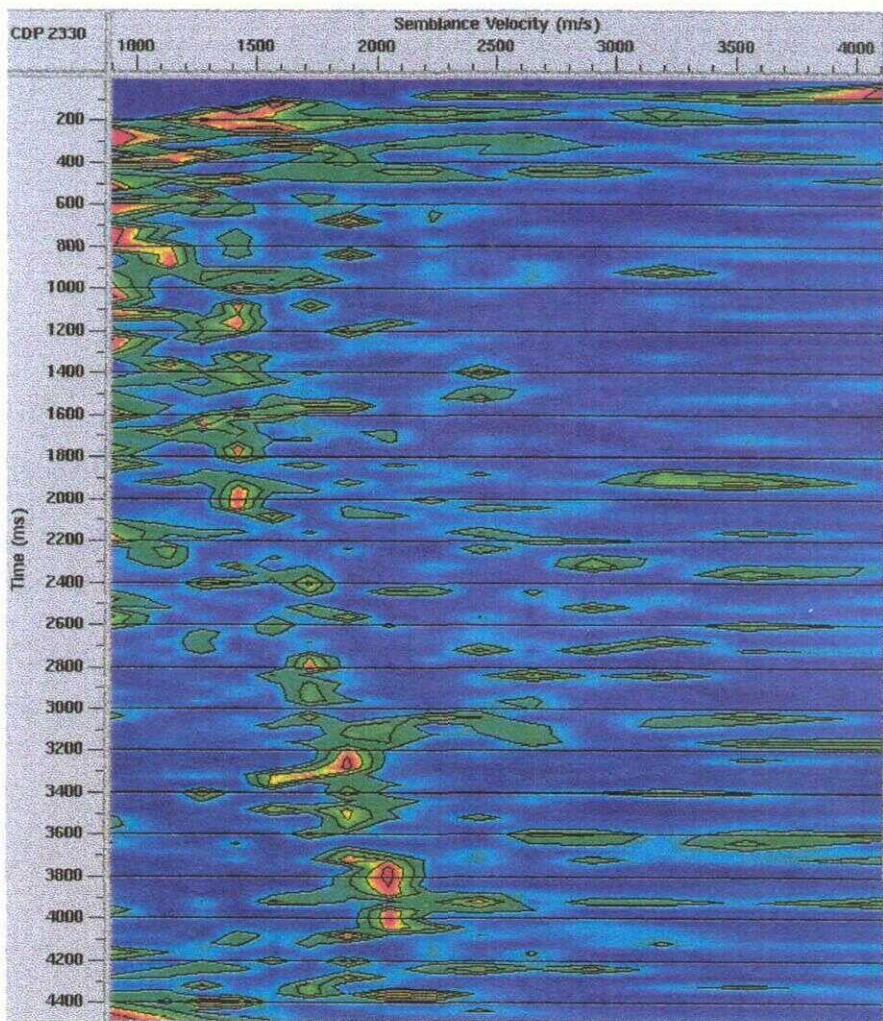


Fig. 2.51b. Velocity analysis for the CCP 2330 after modal filtering.

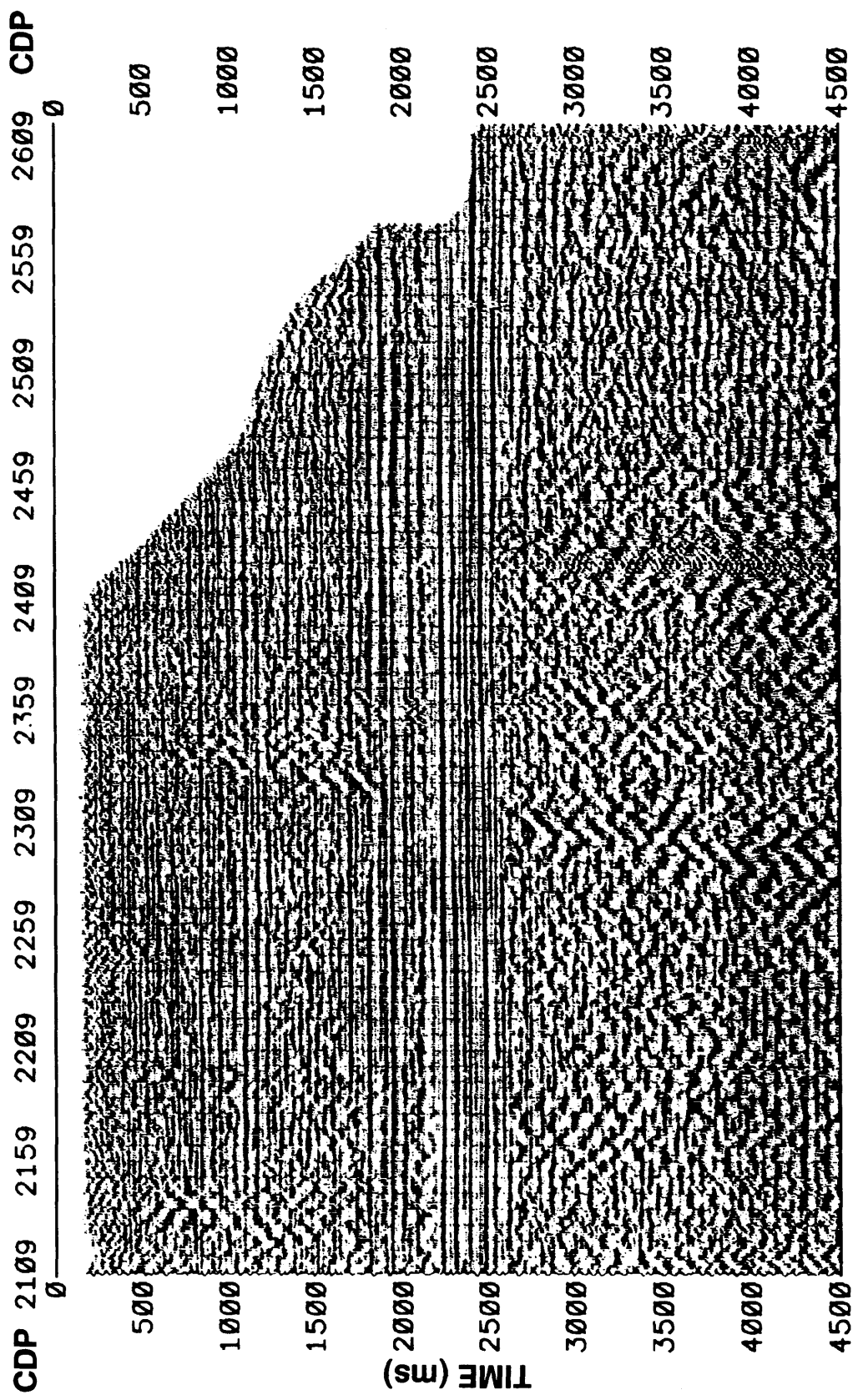


Fig. 2.52. Brute stack of the vertical component data from Barinas, southwest Venezuela, processed without separation filter.

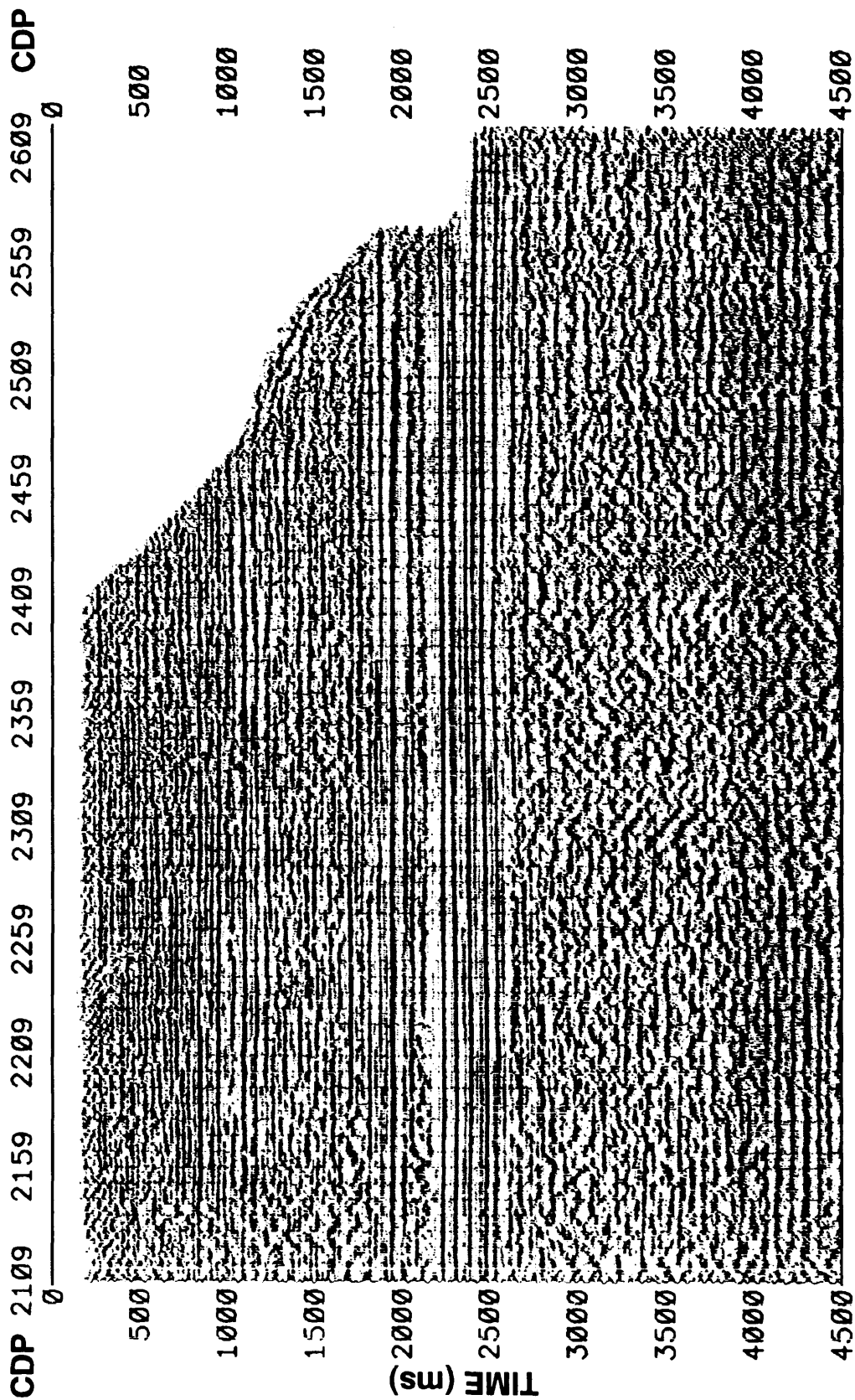


Fig. 2.53. Stacked section of the filtered pass-*P* output obtained from the vertical and horizontal records using $V_p=856$ m/s and $V_s=428$ m/s.

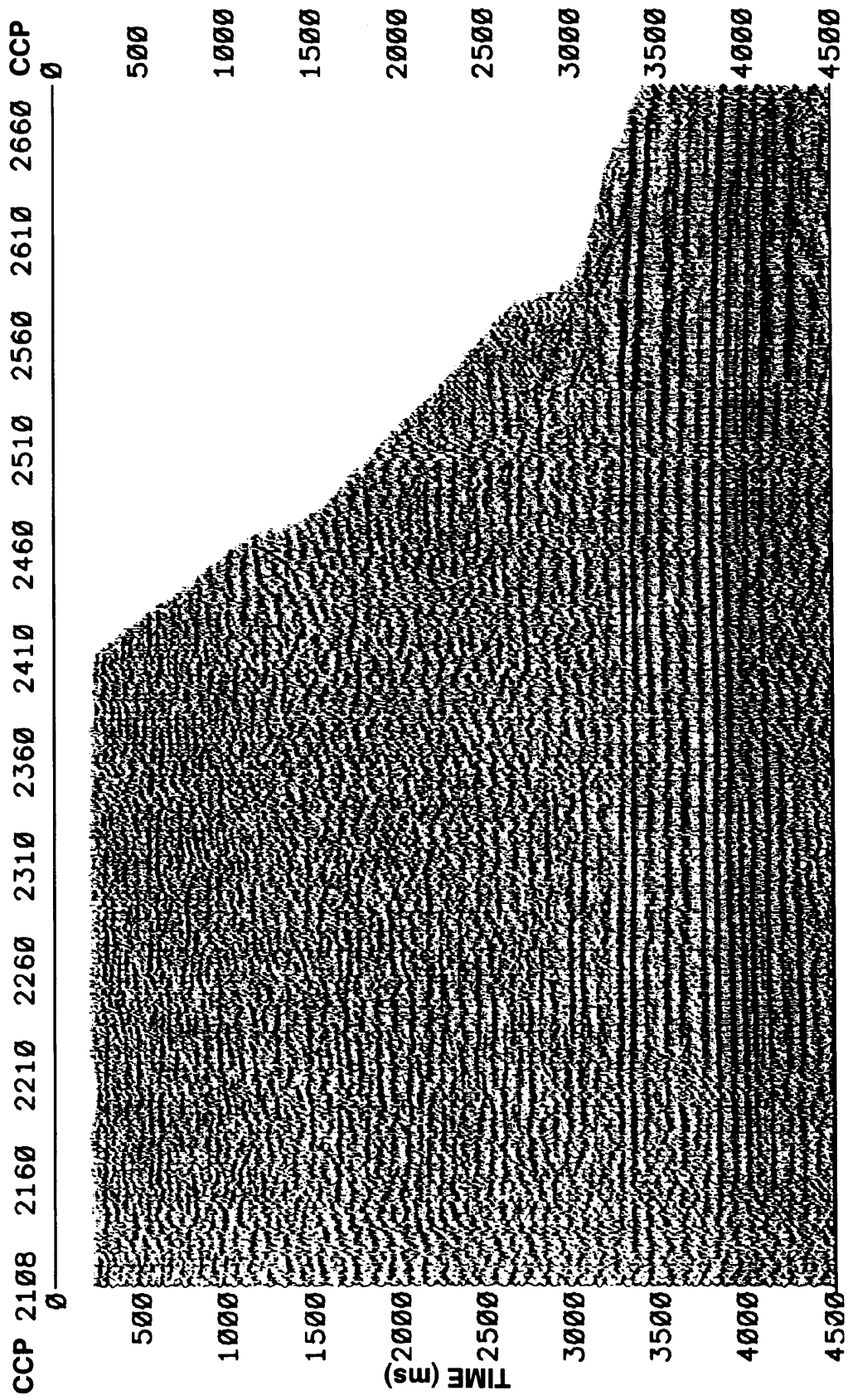


Fig. 2.54. Brute stack of the horizontal component data from Barinas, southwest Venezuela, processed without separation filter.

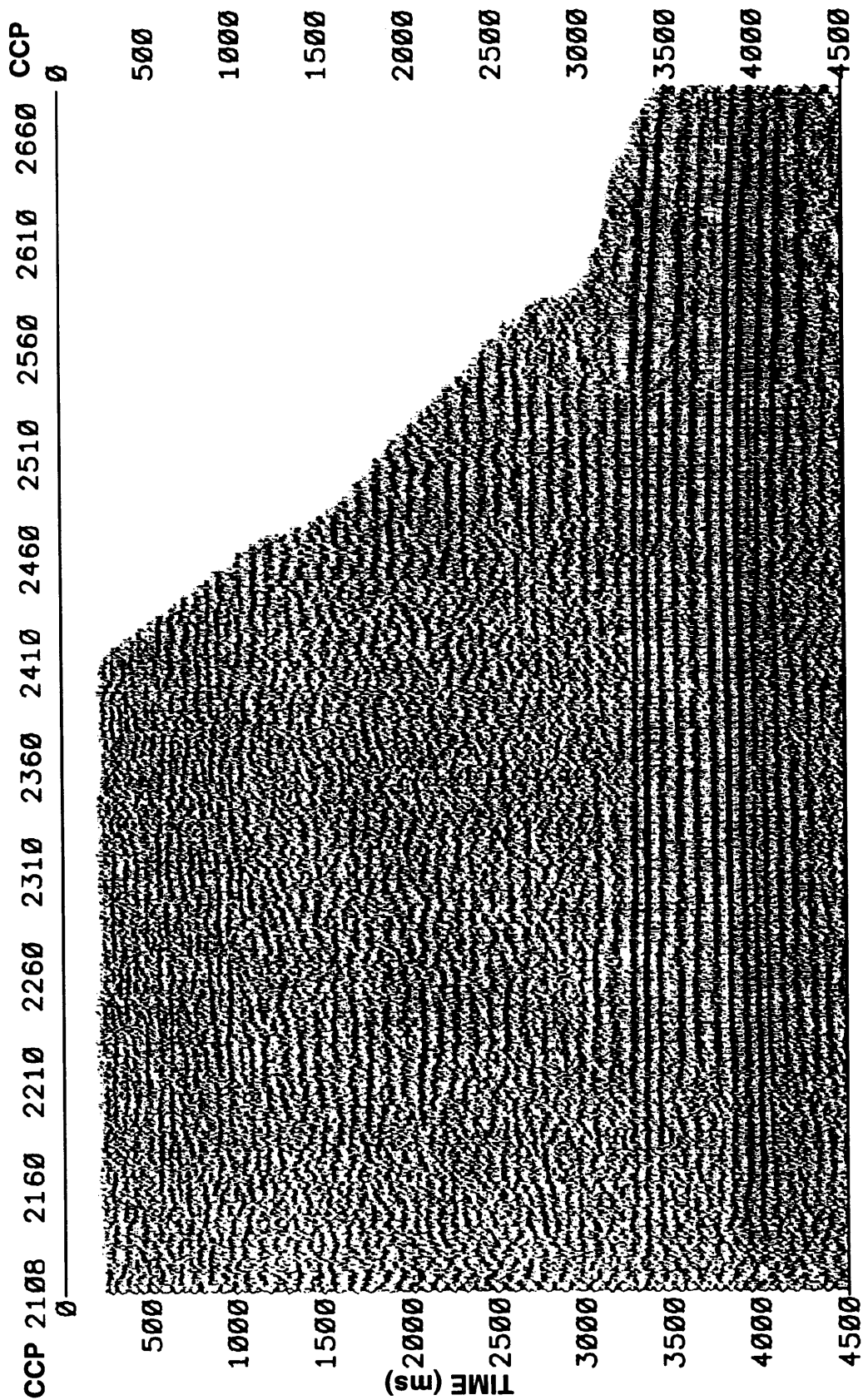


Fig. 2.55. Stacked section of the filtered pass-S output obtained from the vertical and horizontal records using $V_p=856$ m/s and $V_s=428$ m/s.

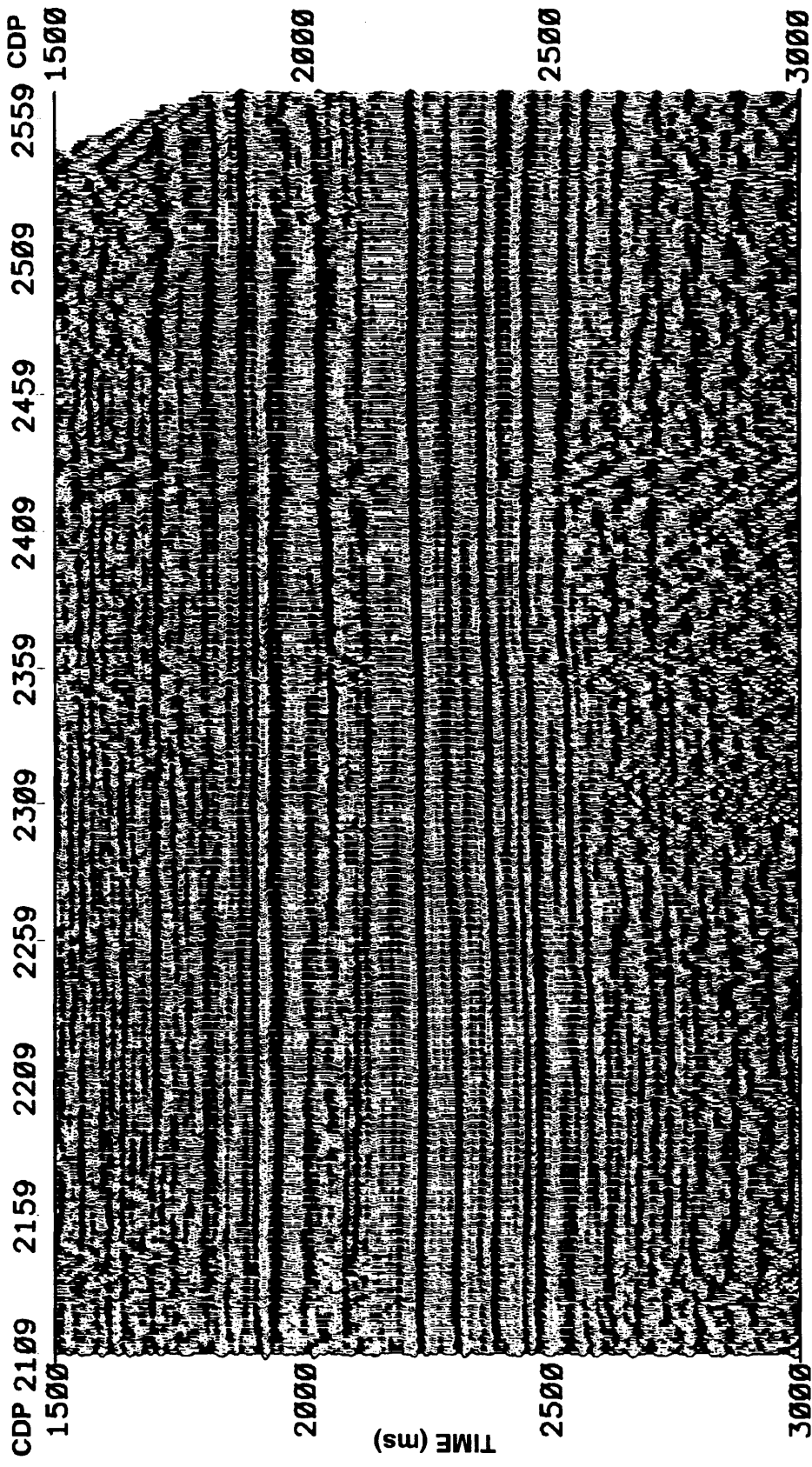


Fig. 2.56a. A detailed picture of the area of interest from the brute stack of the vertical component data acquired in Barinas, southwest Venezuela, processed without separation filter.

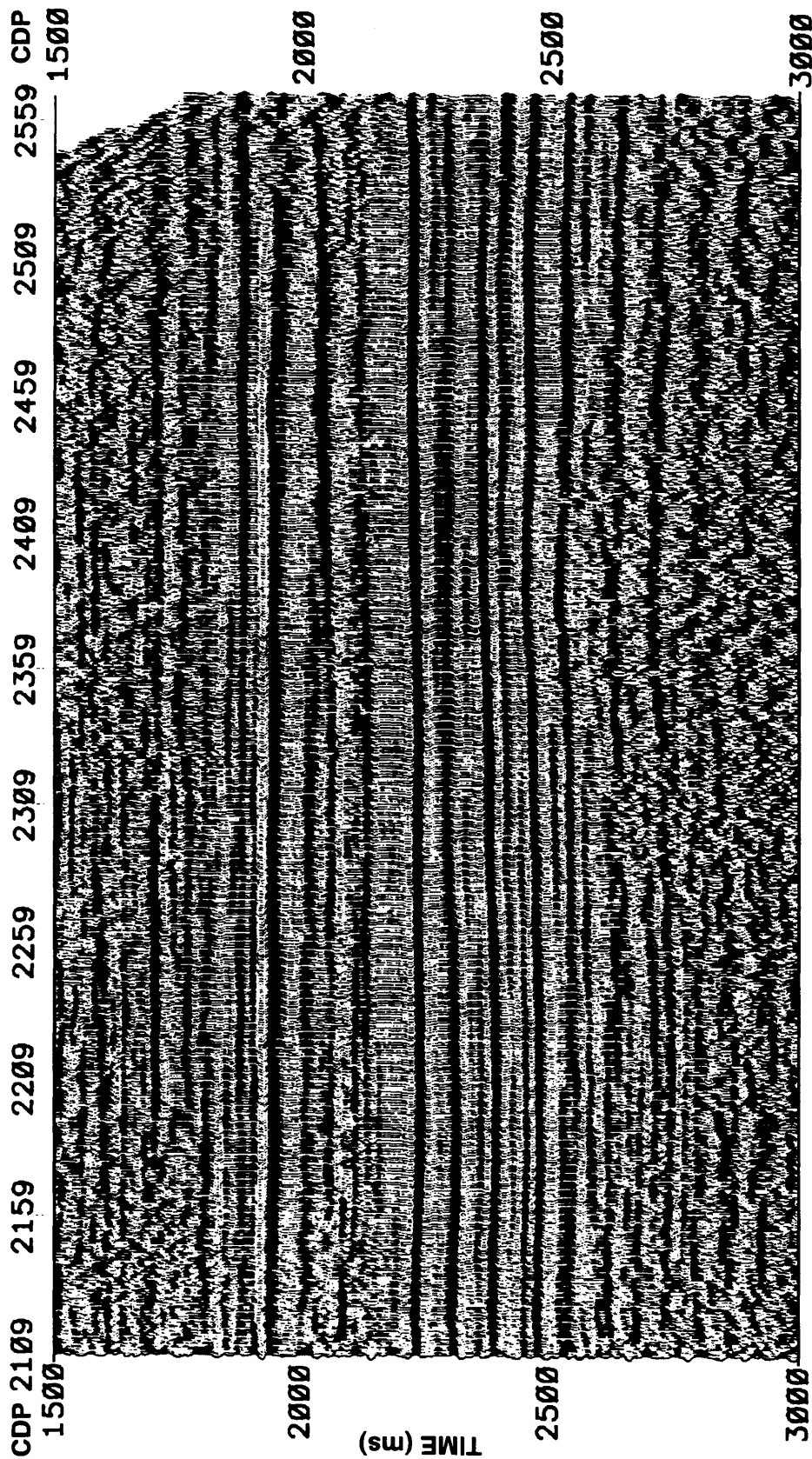


Fig. 2.56b. A detailed picture of the area of interest from the filtered pass- P output obtained from the vertical and horizontal data acquired in Barinas, southwest Venezuela, using $V_p=856$ m/s and $V_s=428$ m/s.

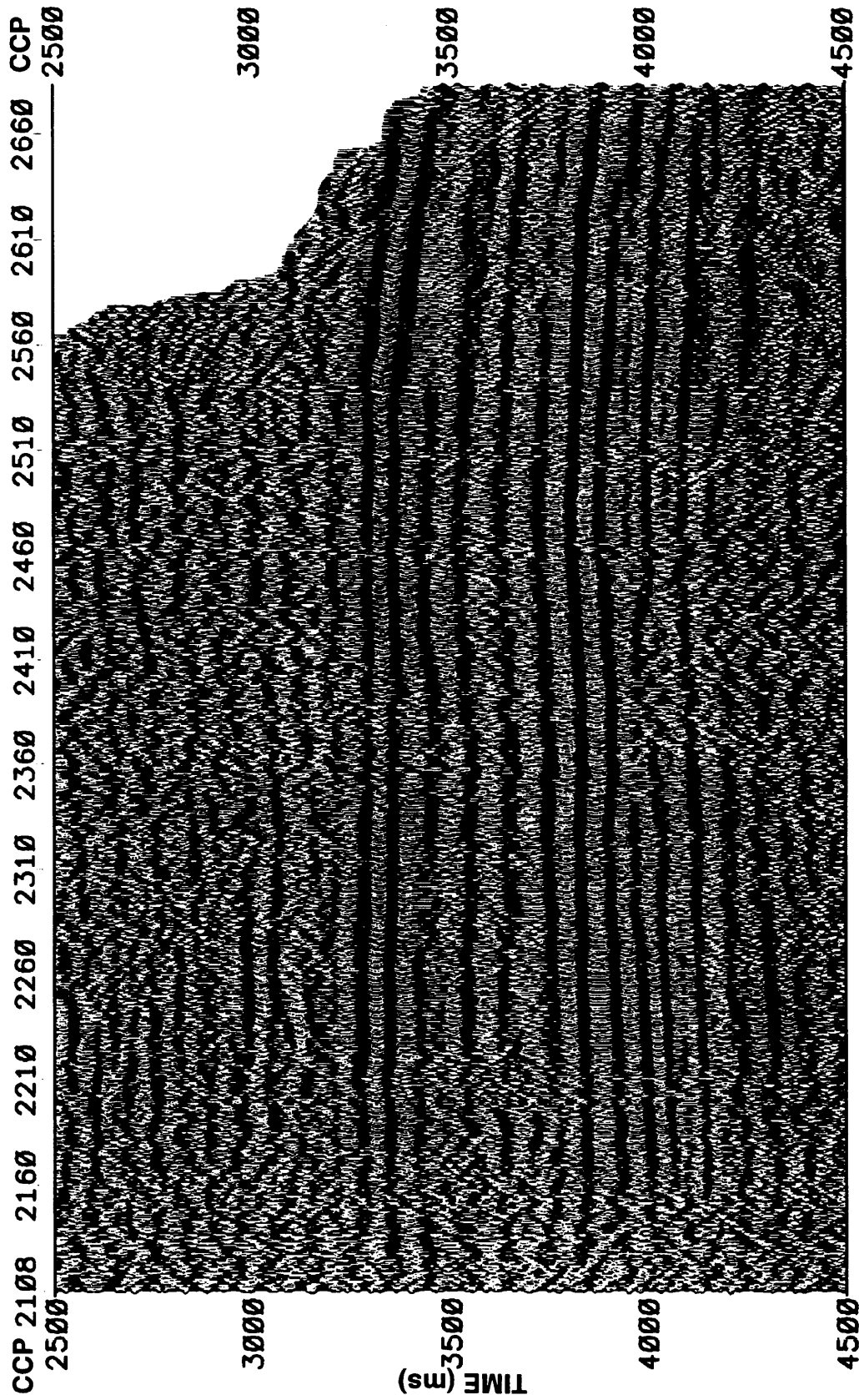


Fig. 2.57a. A detailed picture of the area of interest from the brute stack of the horizontal component data acquired in Barinas, southwest Venezuela, processed without separation filter.

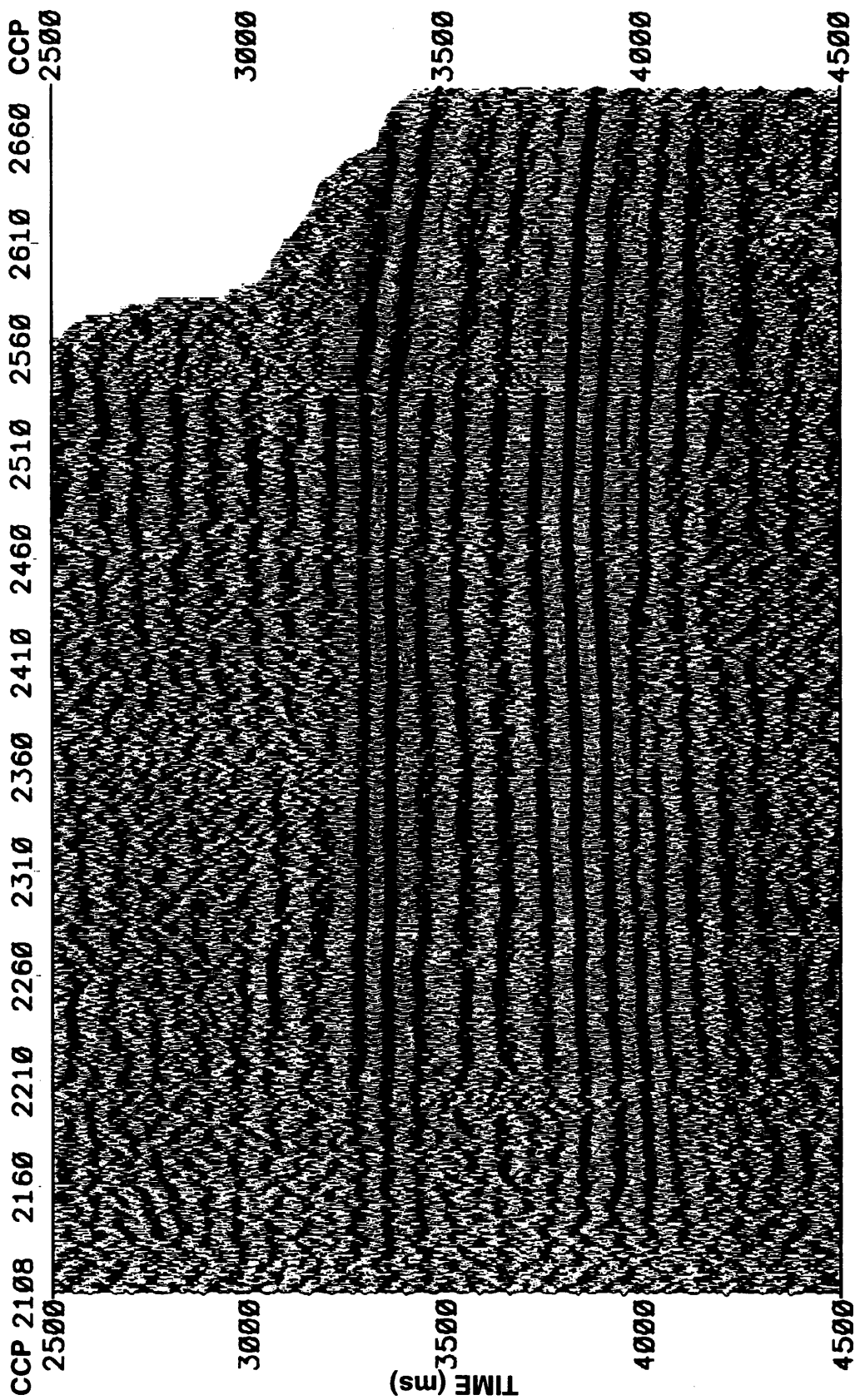


Fig. 2.57b. A detailed picture of the area of interest from the filtered pass-S output obtained from the vertical and horizontal data acquired in Barinas, southwest Venezuela, using $V_p = 856$ m/s and $V_s = 428$ m/s.

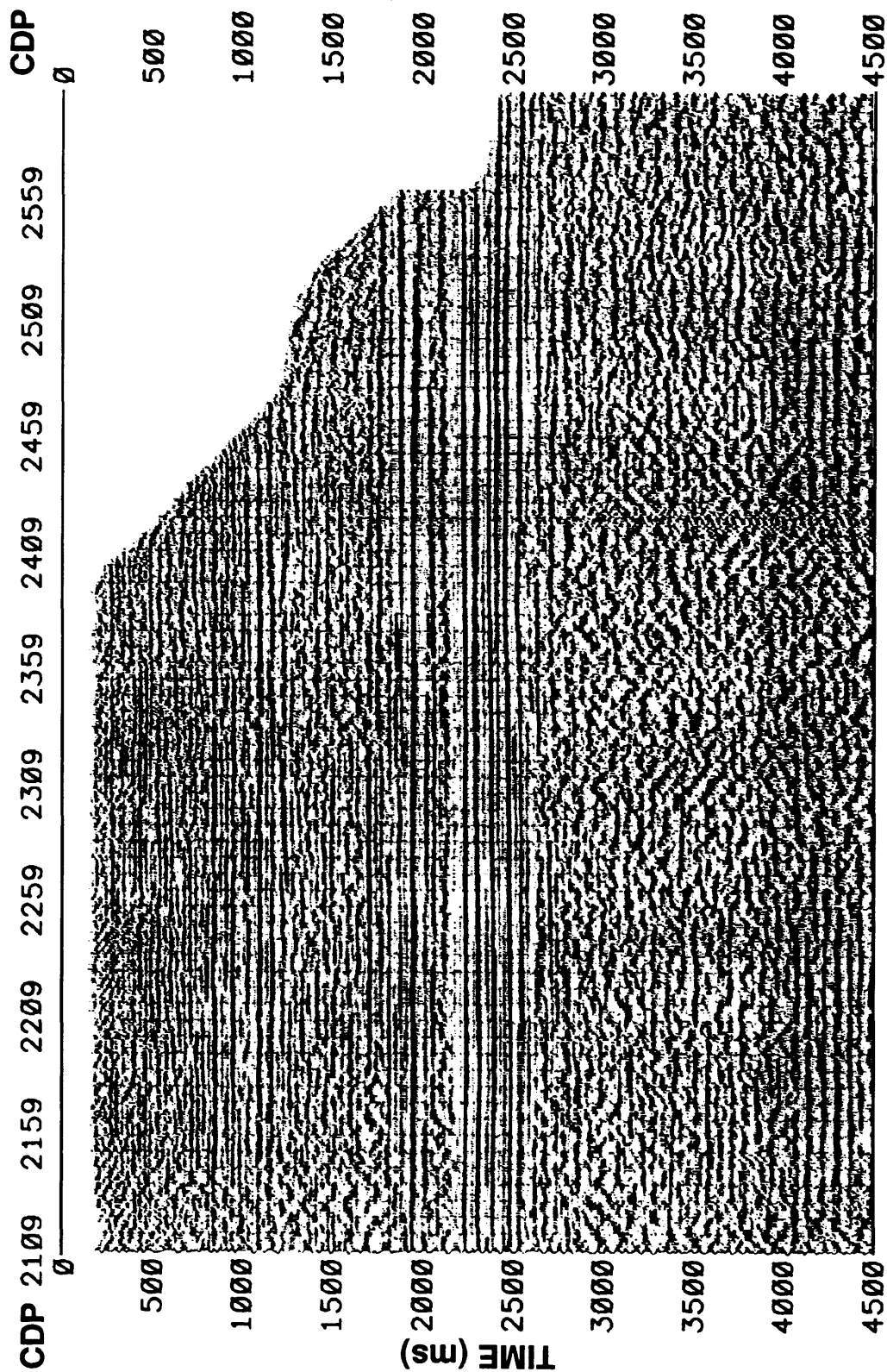


Fig. 2.58a. Stacked section of the filtered pass-P output obtained from the vertical and horizontal records using $V_p=984.4$ m/s and $V_s=492.2$ m/s.

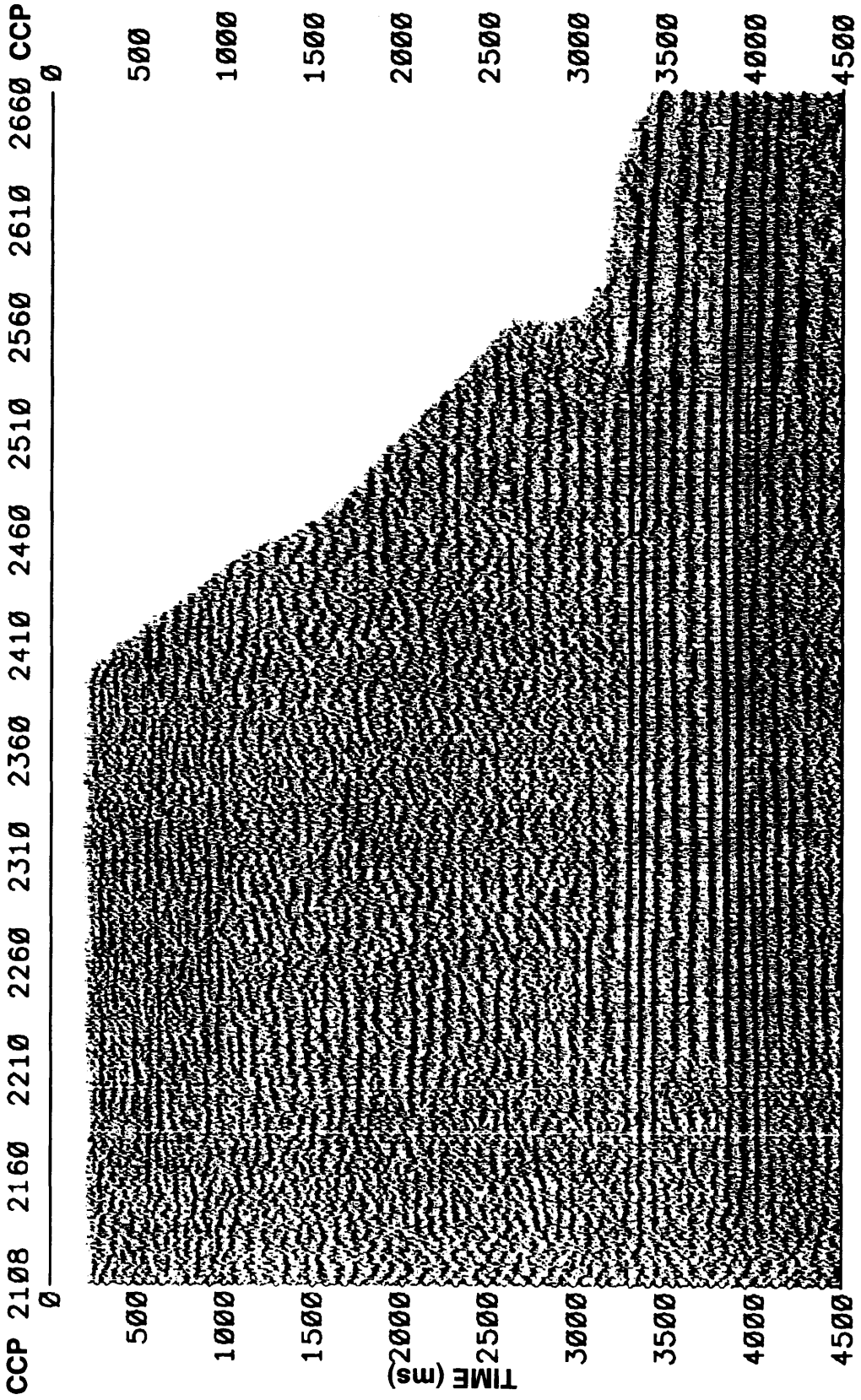


Fig. 2.58b. Stacked section of the filtered pass-S output obtained from the vertical and horizontal records using $V_p=984.4$ m/s and $V_s=492.2$ m/s.

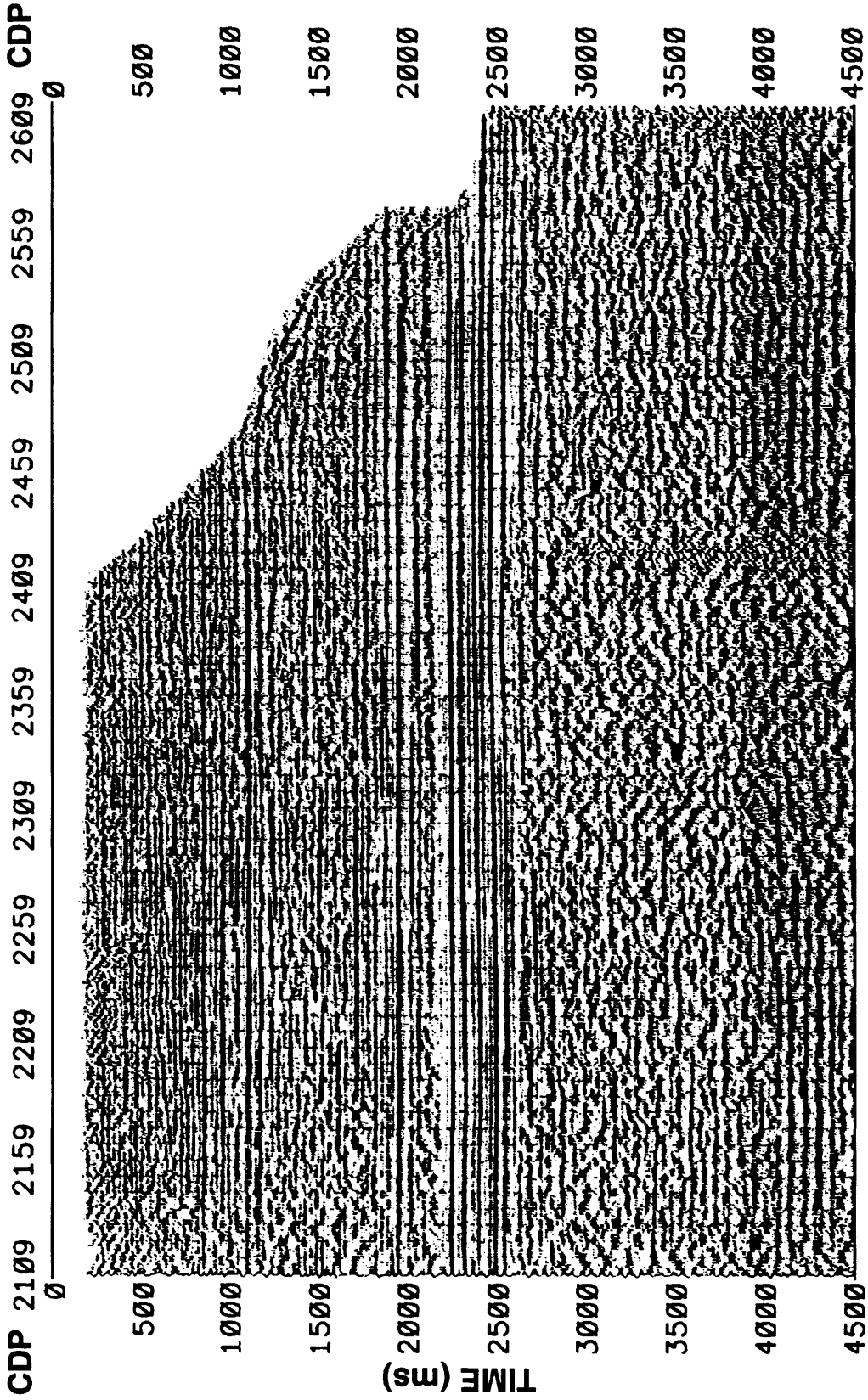


Fig. 2.59a. Stacked section of the filtered pass-P output obtained from the vertical and horizontal records using $V_p=727.6$ m/s and $V_s=363.8$ m/s.

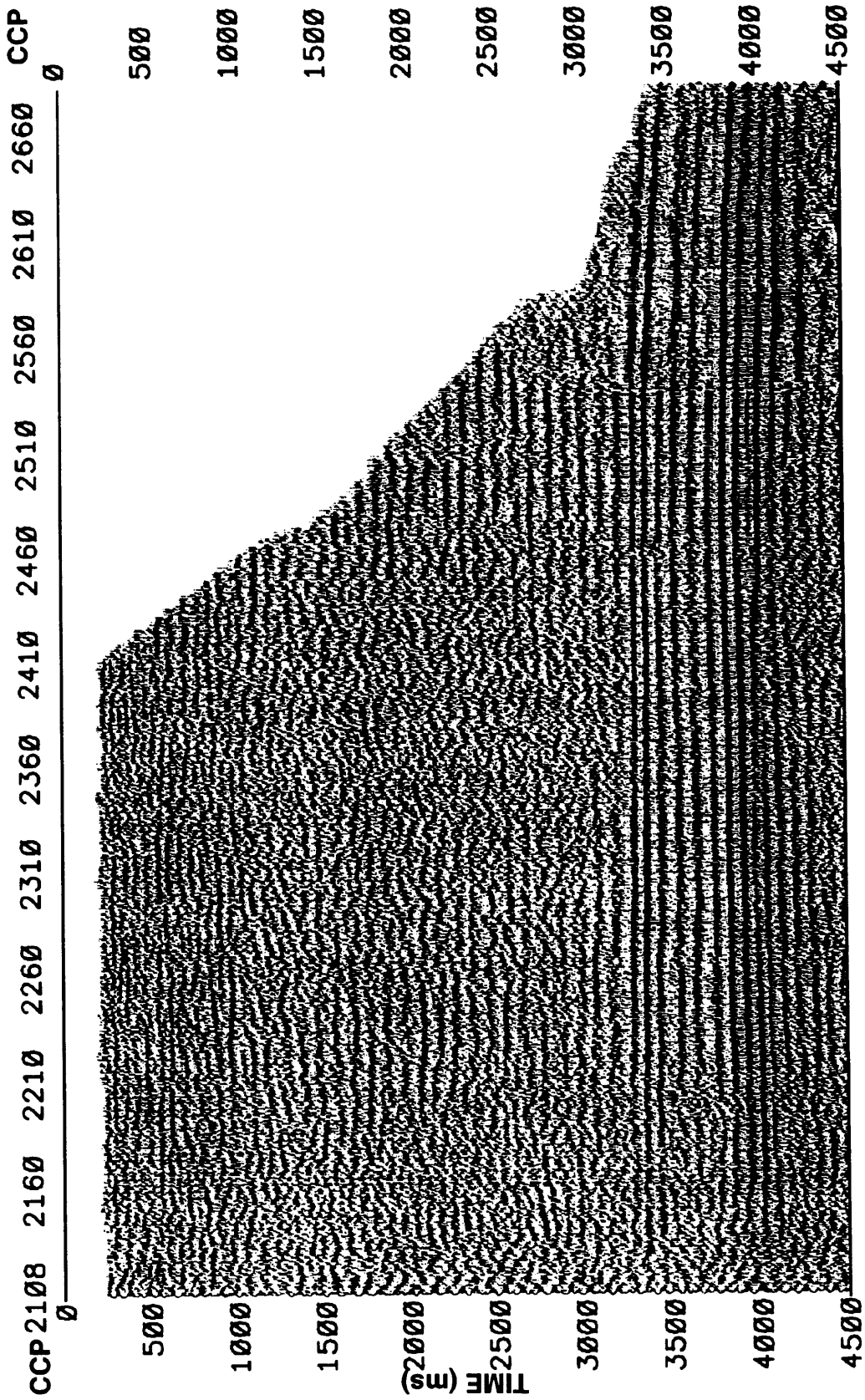


Fig. 2.59b. Stacked section of the filtered pass-S output obtained from the vertical and horizontal records using $V_p = 727.6$ m/s and $V_s = 363.8$ m/s.

use $V_p = 984.4$ m/s and $V_s = 492.2$ m/s which represent an overestimation of 15% on the velocities estimates using the ground information. The filtered sections are shown in Fig. 2.58. Next, an underestimation of 15% in the estimated velocities are used giving $V_p = 727.6$ m/s and $V_s = 363.8$ m/s. The resultant sections are shown in Fig. 2.59. It is evident from these results that the P - S separation filter is robust process and it is not strongly affected for changes in the V_p and V_s velocities values.

Again a detailed image of the carbonates in the area considering wrong values of the velocities at the near-surface is shown in Figs. 2.60 and 2.61 for pass- P and pass- S outputs, respectively. We can compare these images with Figs. 2.56a and 2.57a observing a reasonable good result providing a better definition and clean picture of the reflections

2.6.2.2 Blackfoot, Alberta

A 3C-2D seismic line was acquired over the Blackfoot field near Strathmore, Alberta. The length of the complete line is 4 km. The source was a 6 kg charge of dynamite at 18 m depth. The survey was undertaken to image, using P - S data, a glauconitic sandstone reservoir which is difficult to see on conventional P -wave seismic. The Blackfoot oil pool is in a fluvial/estuarine glauconite sand of the Lower Cretaceous, sands of this type comprise some of the most prolific oil and gas reservoirs in Southern Alberta (Synlonyk, 1995). They are at a depth of about 1550 m and can have thickness up to 43 m. Their importance and potential make them ideal reservoirs to study.

In Fig. 2.62 is presented a plan view of the seismic line and a isopach map of the channel of interest. In this particular study we processed 95 shots located around the area where the channel is located (Shot points: 241 to 150).

Fig. 2.63 shows the raw data for a single shot of the vertical and radial records, respectively. The vertical component shows stronger reflection energy than the radial

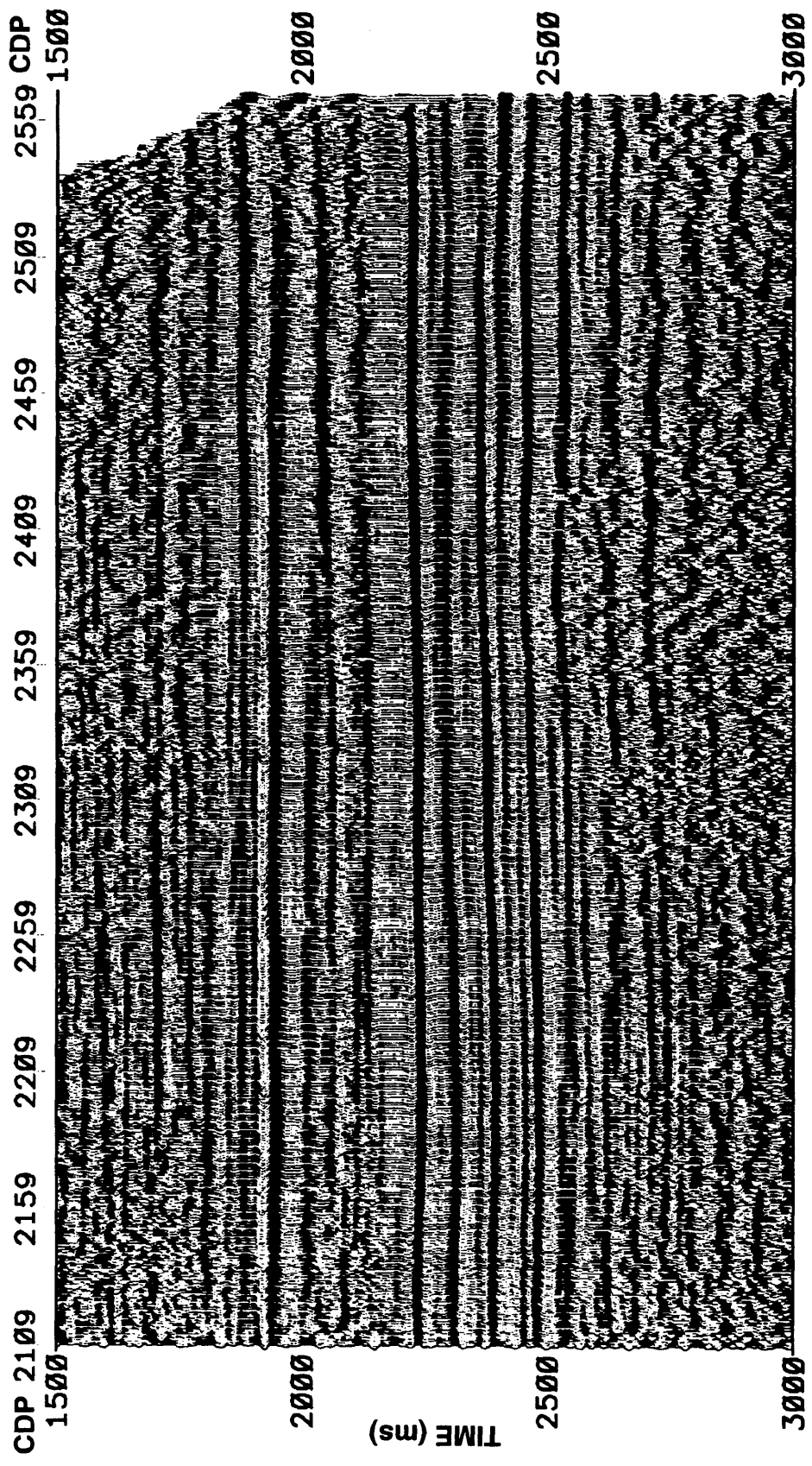


Fig. 2.60a. A detailed picture of the area of interest from the filtered pass-*P* output obtained from the vertical and horizontal data acquired in Barinas, southwest Venezuela, using $V_p=984.4$ m/s and $V_s=492.2$ m/s.

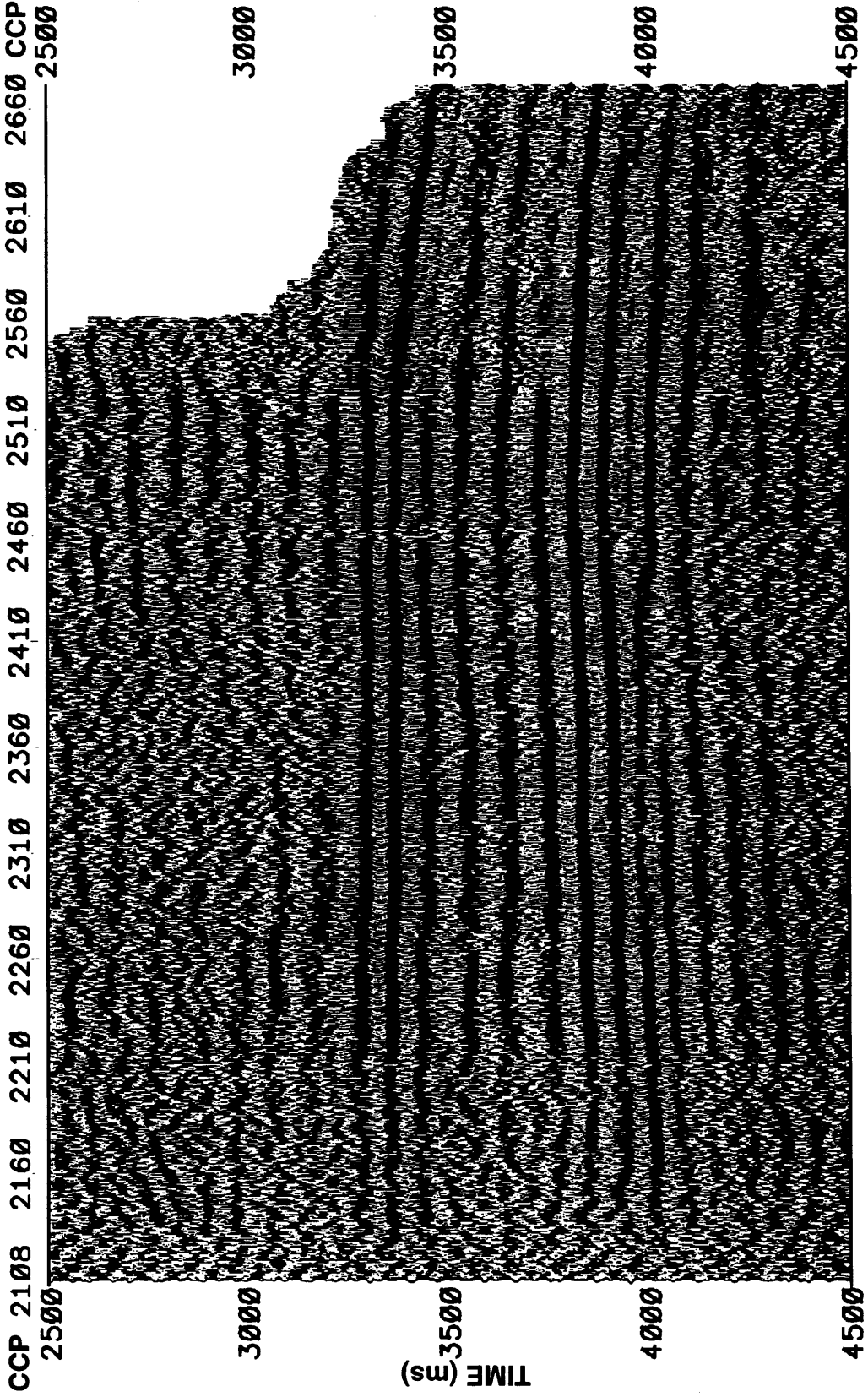


Fig. 2.60b. A detailed picture of the area of interest from the filtered pass-S output obtained from the vertical and horizontal data acquired in Barinas, southwest Venezuela, using $V_p=984.4$ m/s and $V_s=492.2$ m/s.

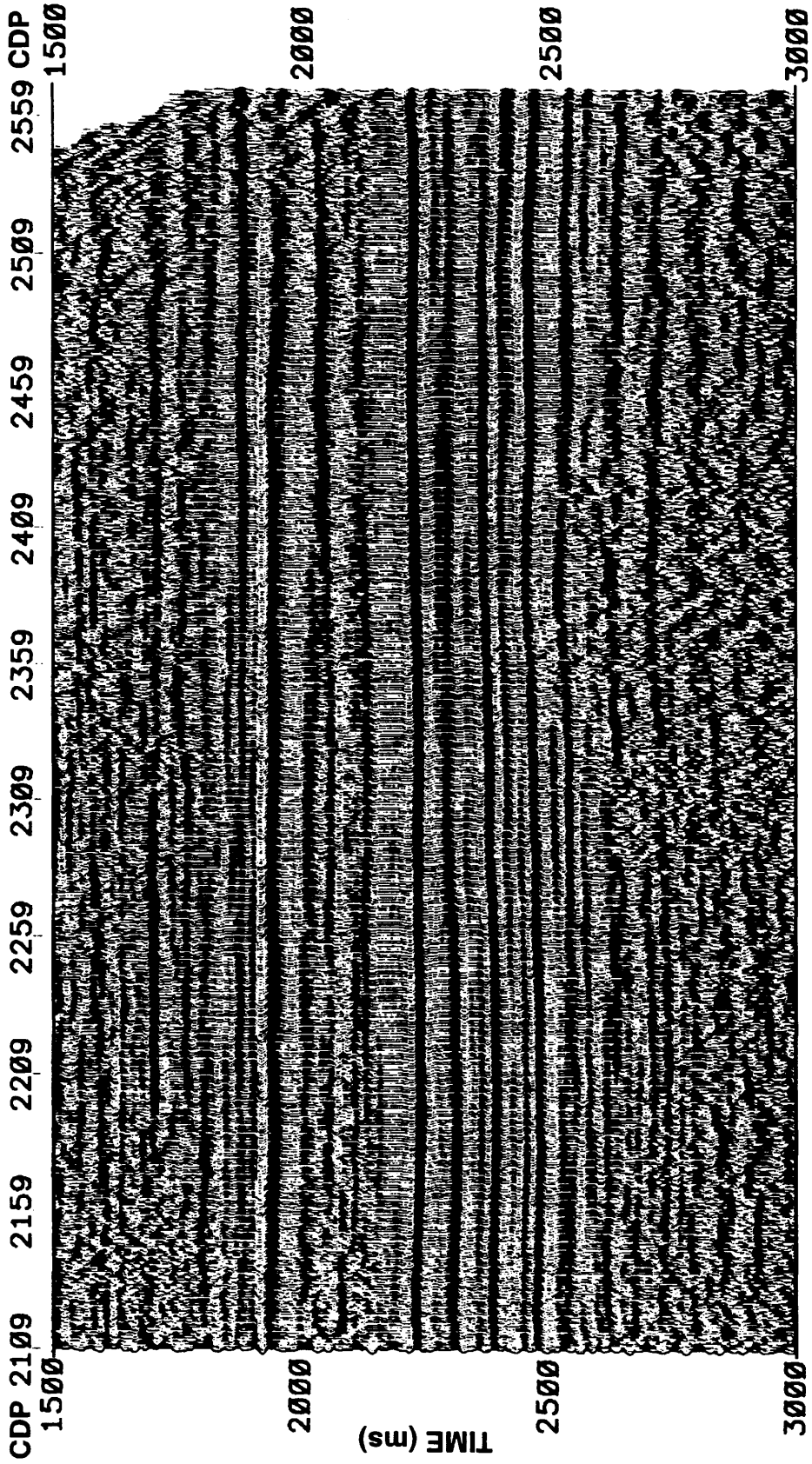


Fig. 2.61a. A detailed picture of the area of interest from the filtered pass-Poutput obtained from the vertical and horizontal data acquired in Barinas, southwest Venezuela, using $V_p= 727.6$ m/s and $V_s= 363.8$ m/s.

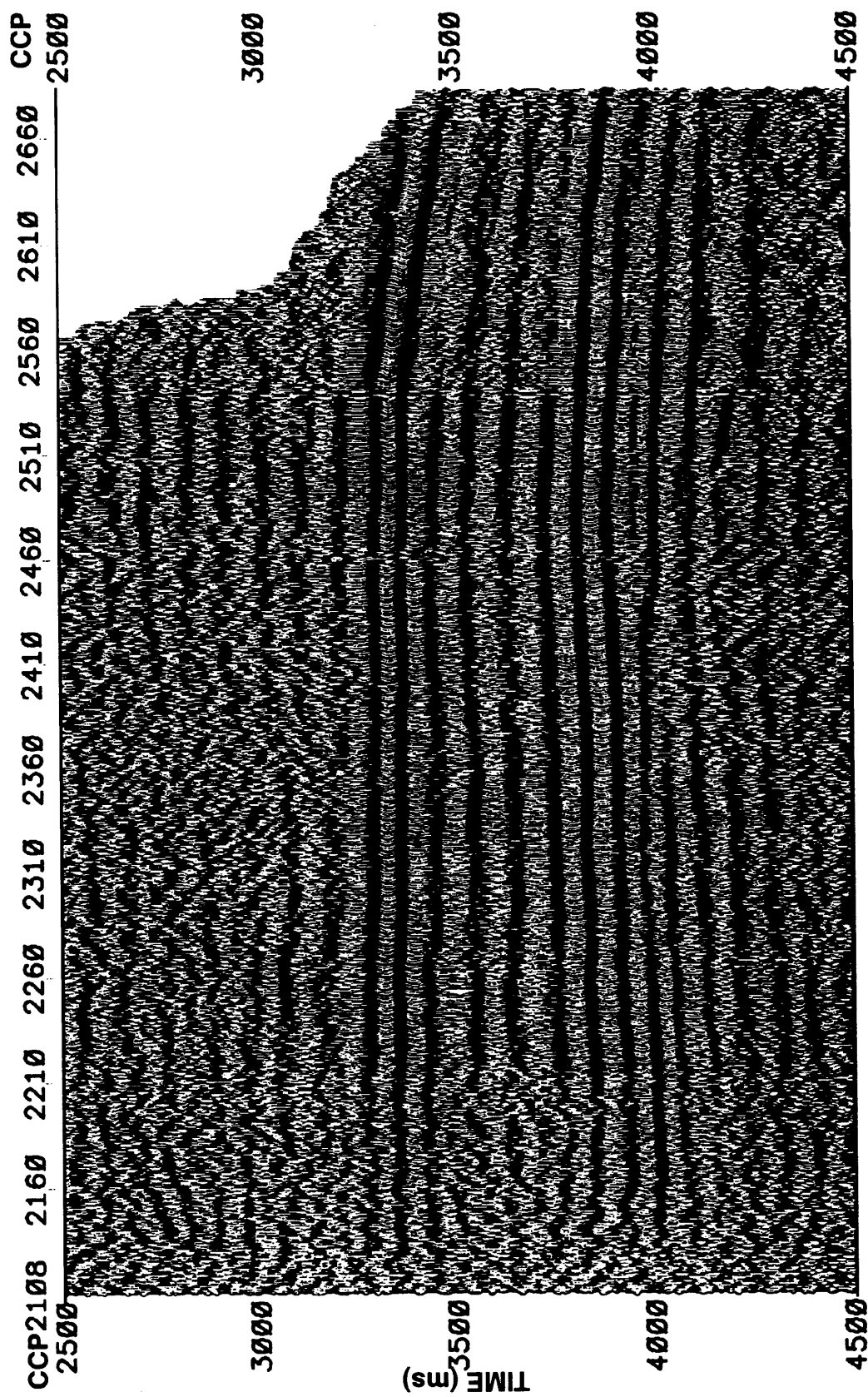


Fig. 2.61b. A detailed picture of the area of interest from the filtered pass-Output obtained from the vertical and horizontal data acquired in Barinas, southwest Venezuela, using $V_p = 727.6$ m/s and $V_s = 363.8$ m/s.

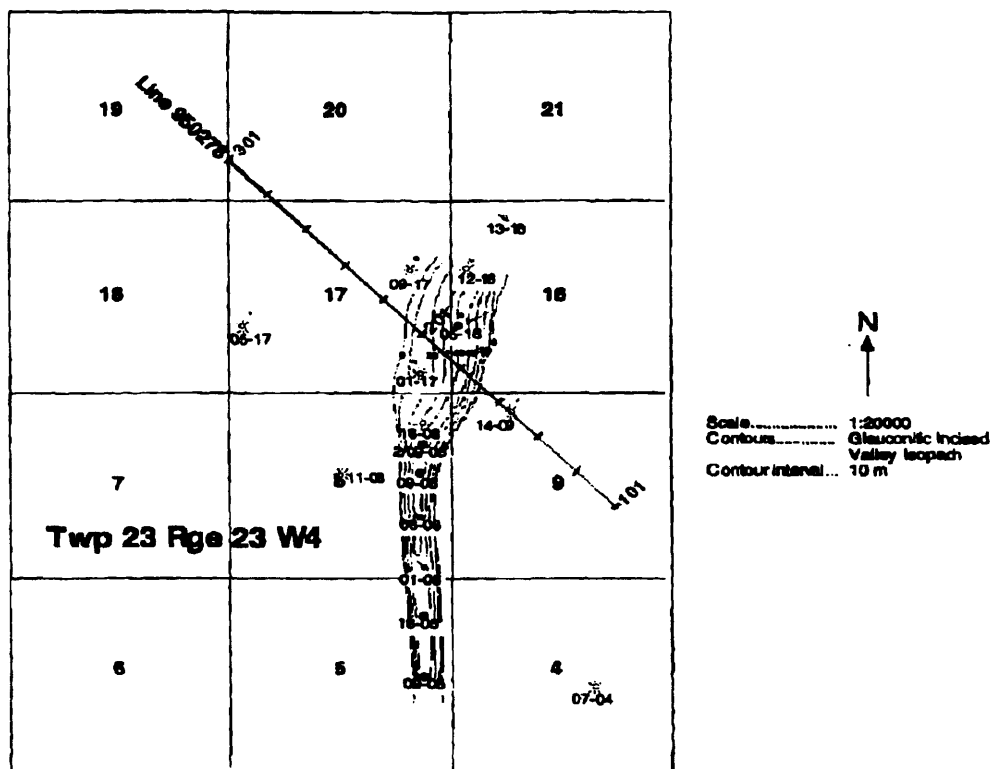


Fig. 2.62. Location of the 3C-2D seismic line 950278, well control and incised valley isopach in Blackfoot area (isopach map from Politylo, 1995).

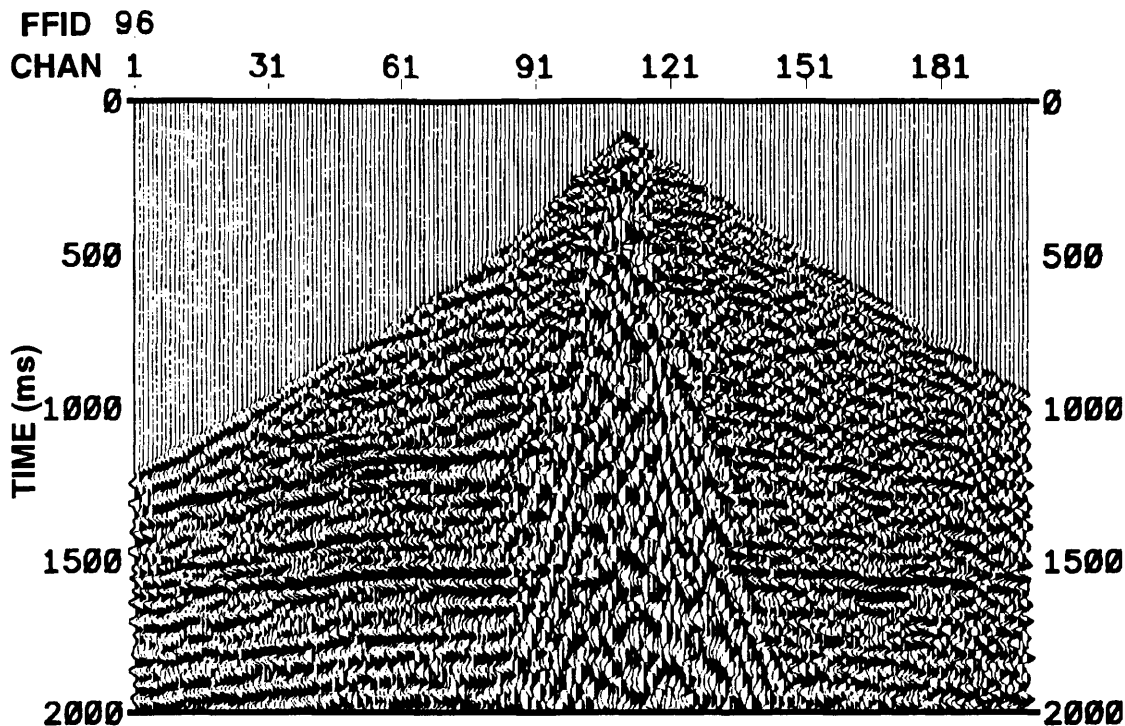


Fig. 2.63a. Raw shot gather from the vertical component showing acquired in Blackfoot, Alberta

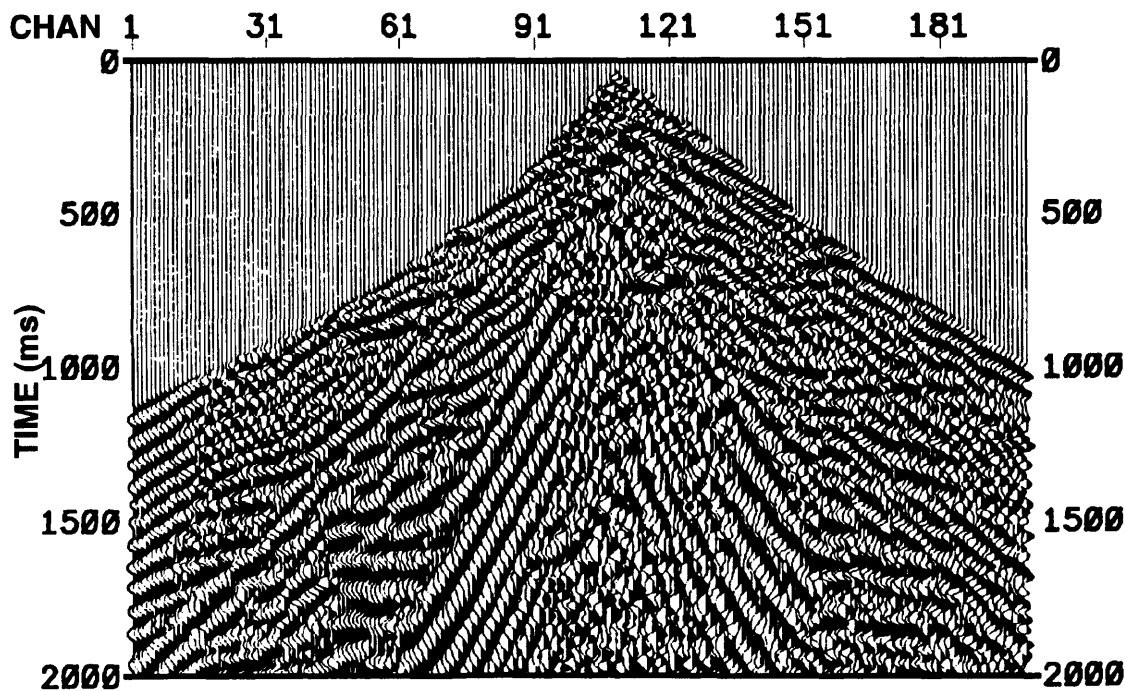


Fig. 2.63b. Raw shot gather from the horizontal component acquired in Blackfoot field.

component. It is evident the strong noise contamination of the data due to the presence of the ground roll. On the radial component the near offsets are strongly contaminated by source noise and converted wave refraction energy. This low velocity coherent energy severely obscures the signal to about one third of the spread length in the zone of interest on the radial recording and provides a challenge to data processing.

Based on log information the porous sand channel is located in time around 1050 ms in the P - P section and 1550 ms for the converted wave data.

The refraction static solutions used in this work were provided by the staff of CREWES Project. The velocity information at the near-surface required for the P - S separation filter was obtained from the uphole time information and the depth of the shots which are shown in Fig. 2.64(a,b).

Taking a mean value of 17.31 m for the depth of the sources, a mean uphole time value 17.57 ms for the enter survey, and assuming $i_n = 0^\circ$ we get that $V_p = 985$ m/s for the P wave and $V_s = 492.58$ m/s for the S wave considering the V_p/V_s ratio equal 2.

The filtered records pass- P and pass- S corresponding to both raw records are shown in Figs. 2.65b and 2.66b obtained using $V_p = 985$ m/s and $V_s = 492$ m/s obtained from the uphole time information and assuming a V_p/V_s ratio of 2.0. In the Fig. 2.65(a,b), it is shown the effect of the P - S separation filter in the τ - p transformation on a single shot from the vertical record which remove the strong amplitudes of the ground roll present in the data, preserve the amplitude and phase of the reflection, and improve the continuity of the reflections. The same results were obtained for a single shot of the radial record are shown in Fig. 2.66(a,b).

Although the analysis of the raw data indicated a low superposition between P and P - S waves, the good performance of the P - S separation filter is evident in isolating the principal P and P - S events. Some remnant P - S in the pass- P data between 1.0 - 1.1 s at large offsets is present. In the same record appears several reflection between 1.5 - 1.6 s that are not evident on the vertical raw record. The analysis of the slopes associated with these reflections seem to indicate any relation with converted waves observed at the same window time on the pass- S record.

We worked with the vertical and radial components until the brute stack stage. Both data sets were processed with and without modal filter for comparing the improvement that could be introduced by the separation filter. For processing the vertical channel we use the processing flow shown in Fig. 2.67.

The f - k filter was applied to the raw data which allows us to eliminate the ground roll, rejecting all noise giving clean records. From the autocorrelograms performed before and after deconvolution we could obtained the best parameters for the deconvolution process which compressed the wavelet and cleaned the data. For the deconvolution we used a minimum phase wavelet with an operator length of 100 ms and prediction lag of 5 ms, and a design window between 800 and 1300 ms. Finally the f - x deconvolution was applied for removing the remnant random noise present improving then the continuity in the data.

A single shot after applying the previous processing sequence without and with the modal filter is shown in Fig. 2.68. Again we can see a good performance of the filter on these real data set defining better the P -wave reflections, cleaning the data and improving continuity.

For obtaining the brute stack was performed a velocity analysis and we found an important difference in the definition of the velocities when it is done on the data process

with the separation filter (Fig. 2.69). With clean and a better focus data we get a better velocities table values.

For the radial component we use the processing flow shown in Fig. 2.70. The $f-k$ filter removed the ground roll, the deconvolution compressed the wavelet and the $f-x$ deconvolution removed the random noise still present in the data. Fig. 2.71 presents the outputs of this flow without and with modal filter. The velocity analysis done on the converted data reveal better results in the converted data processed with the separation filter (Fig. 2.72).

A set of brute stack sections was obtained with and without separation filter for both P and S waves obtained using $V_p = 985$ m/s and $V_s = 492$ m/s. Figs. 2.73 and 2.74 show the brute stacks of the vertical channel and the filtered pass- P data. The brute stacked sections for S waves obtained from conventional and modal filtered processing are shown in Fig. 2.75 and 2.76, respectively. Again we can see from these stacked sections an improvement in the continuity and definition of the $P-P$ and $P-S$ reflections on the modal filtered sections.

A detailed picture of the porous sand channel is shown on Figs. 2.77 and 2.78 for both pass- P and pass- S sections.

The effect on the performance of the $P-S$ separation filter considering wrong estimates of the near-surface velocities V_p and V_s is shown in the Figs. 2.79 and 2.80. The vertical and horizontal records were filtered using erroneous values as follows: first we use $V_p = 1083.5$ m/s and $V_s = 542.3$ m/s which represent an overestimation of 10% on the velocities estimates using the ground information. The filtered sections are shown in Fig. 2.79. Finally, an underestimation of 10% in the estimated velocities are used giving $V_p = 886.5$ m/s and $V_s = 443.7$ m/s. The resultant sections are shown in Fig. 2.80. It is evident

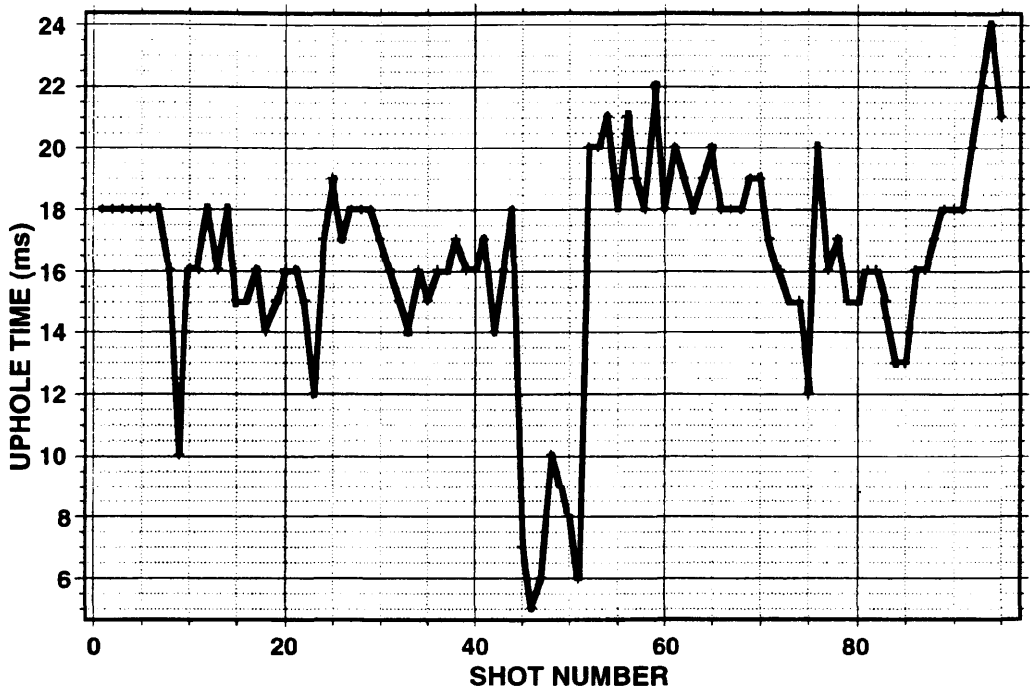


Fig. 2.64a. Uphole time values of the Blackfoot survey.

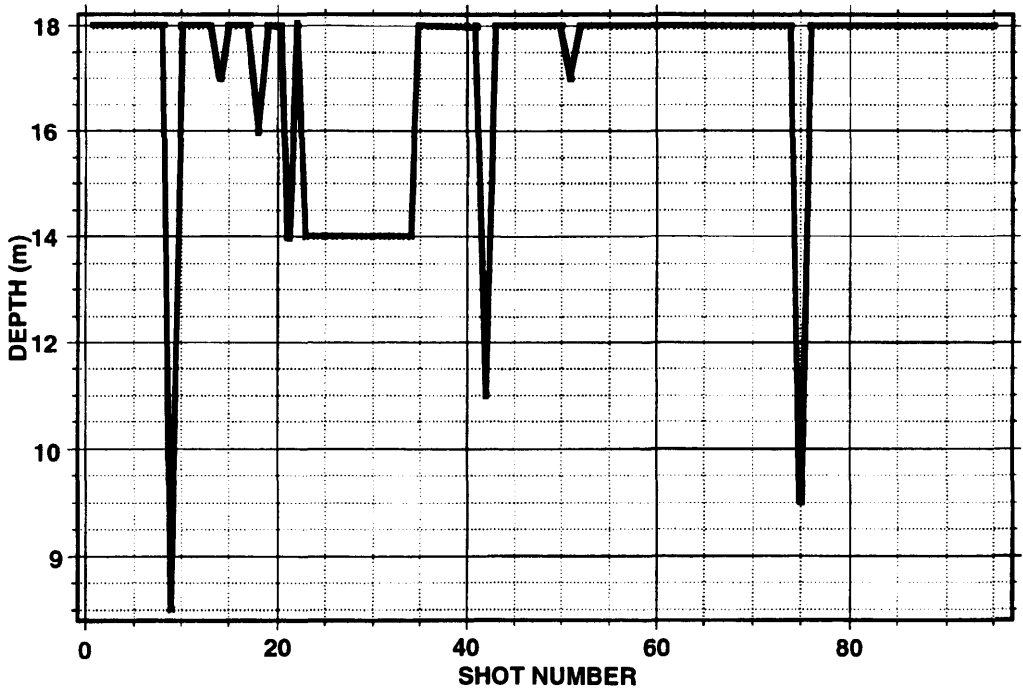


Fig. 2.64b. Source depth in the Blackfoot survey.

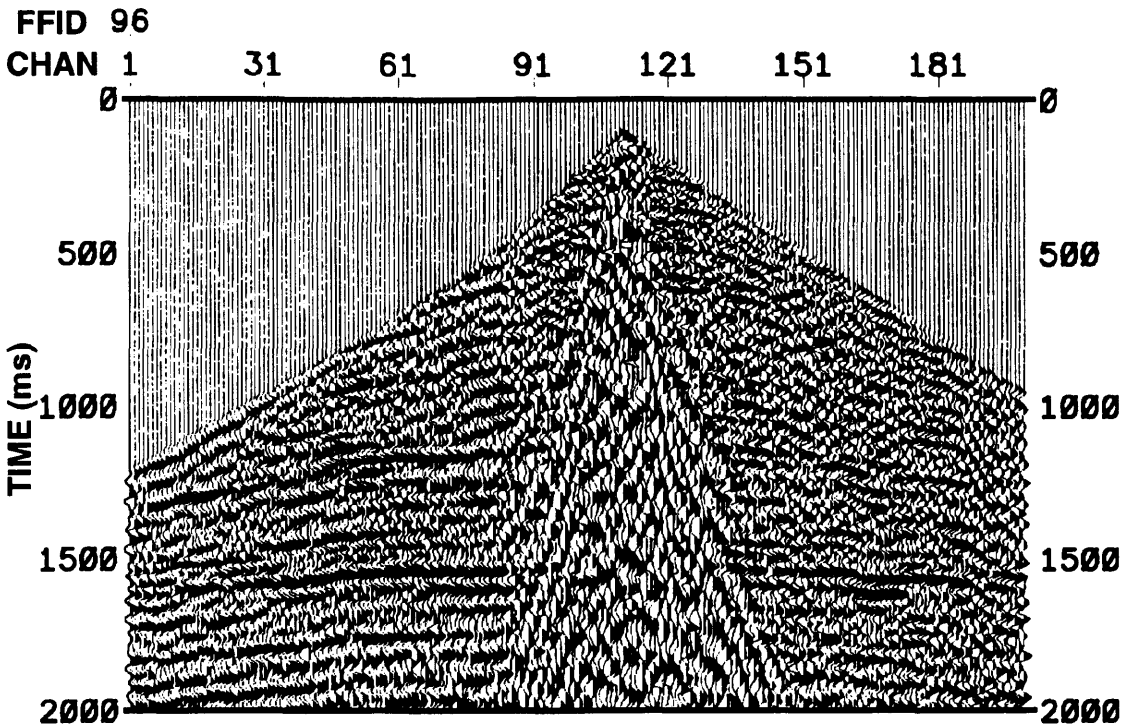


Fig. 2.65a. Raw shot gather from the vertical component.

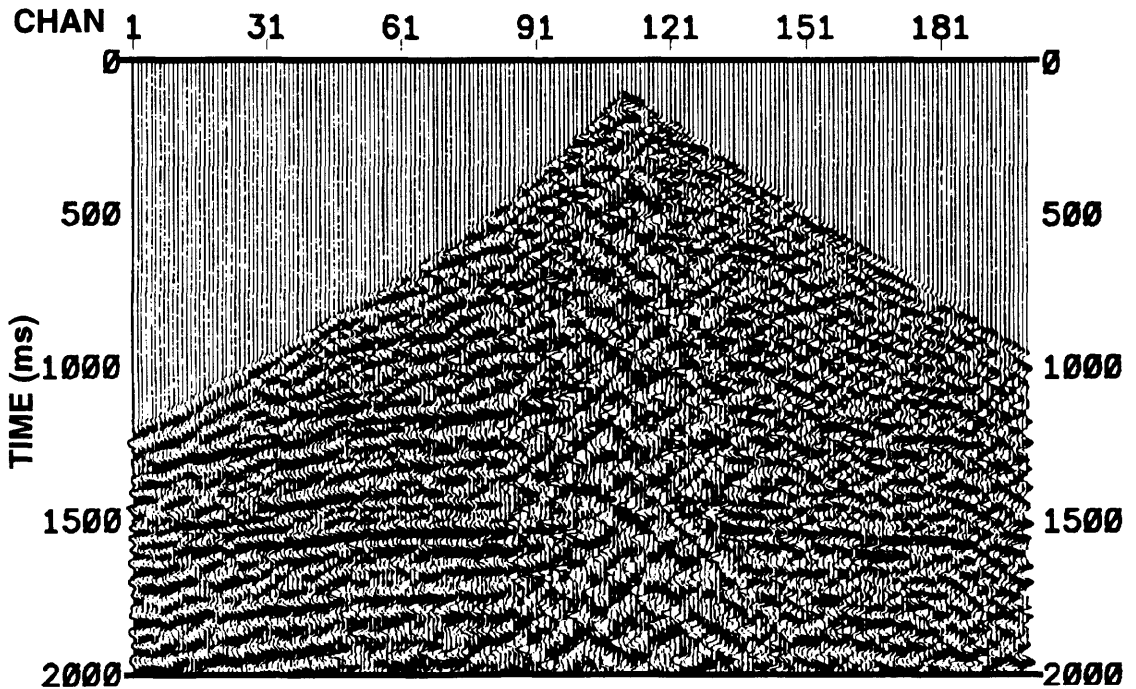


Fig. 2.65b. Filtered pass-*P* record obtained from the vertical and horizontal records (Fig. 2.63) using $V_p = 985$ m/s and $V_s = 492$ m/s.

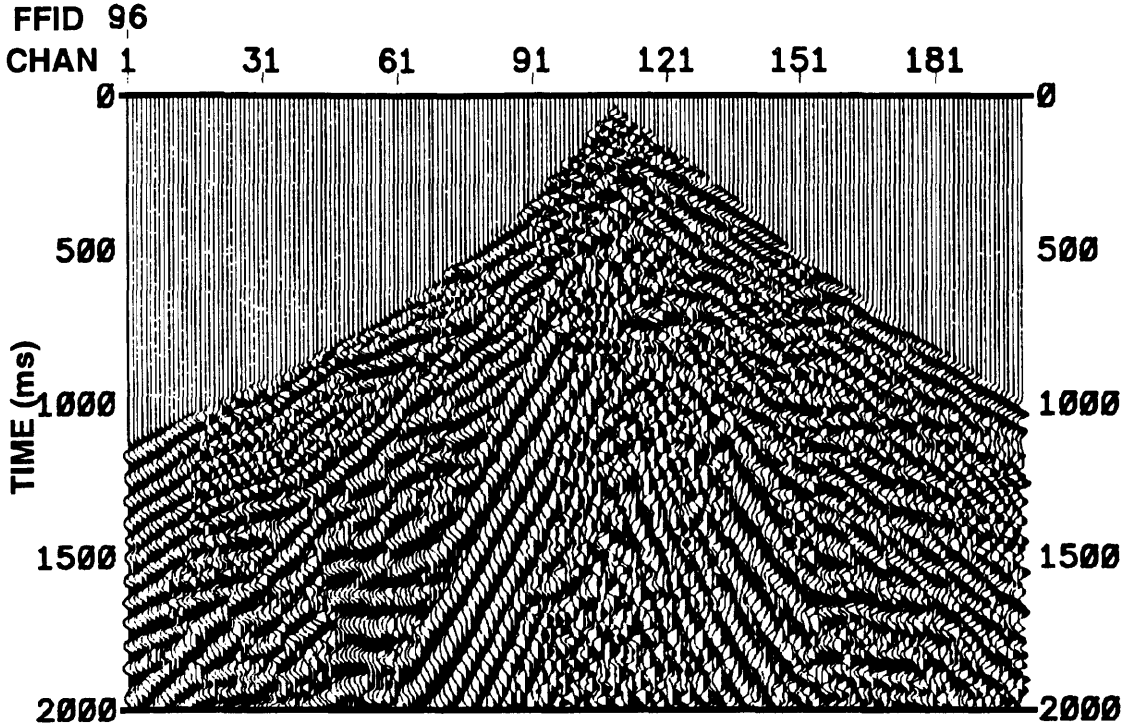


Fig. 2.66a. Raw shot gather from the horizontal component.

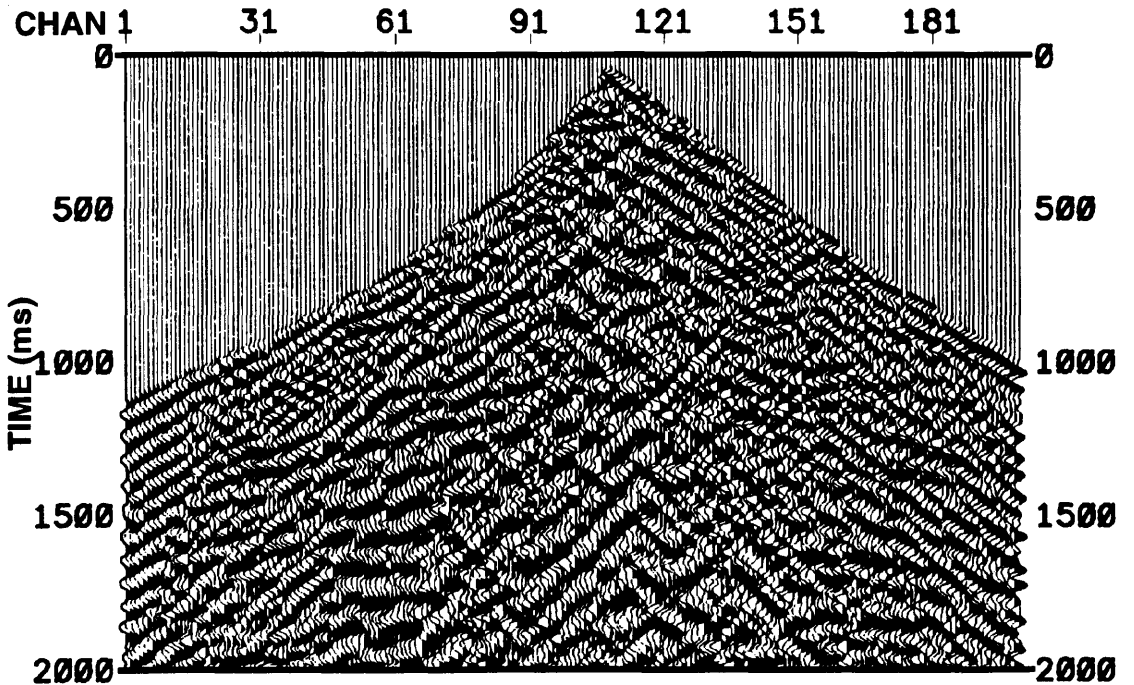


Fig. 2.66b. Filtered pass-S record obtained from the vertical and horizontal records (Fig. 2.63) using $V_p = 985$ m/s and $V_s = 492$ m/s.

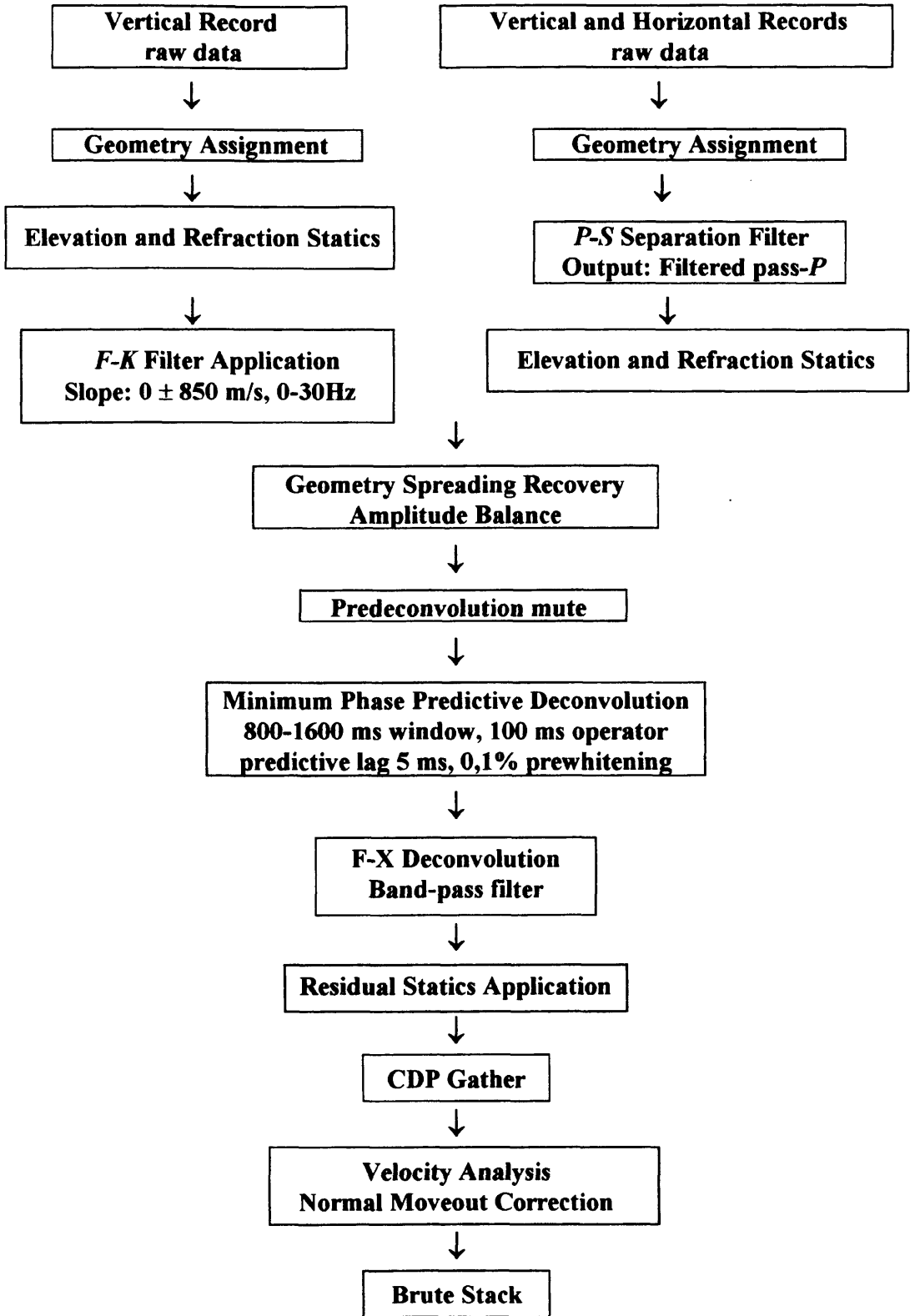


Fig. 2.67. P-wave processing flow for Blackfoot data without and with modal filter.

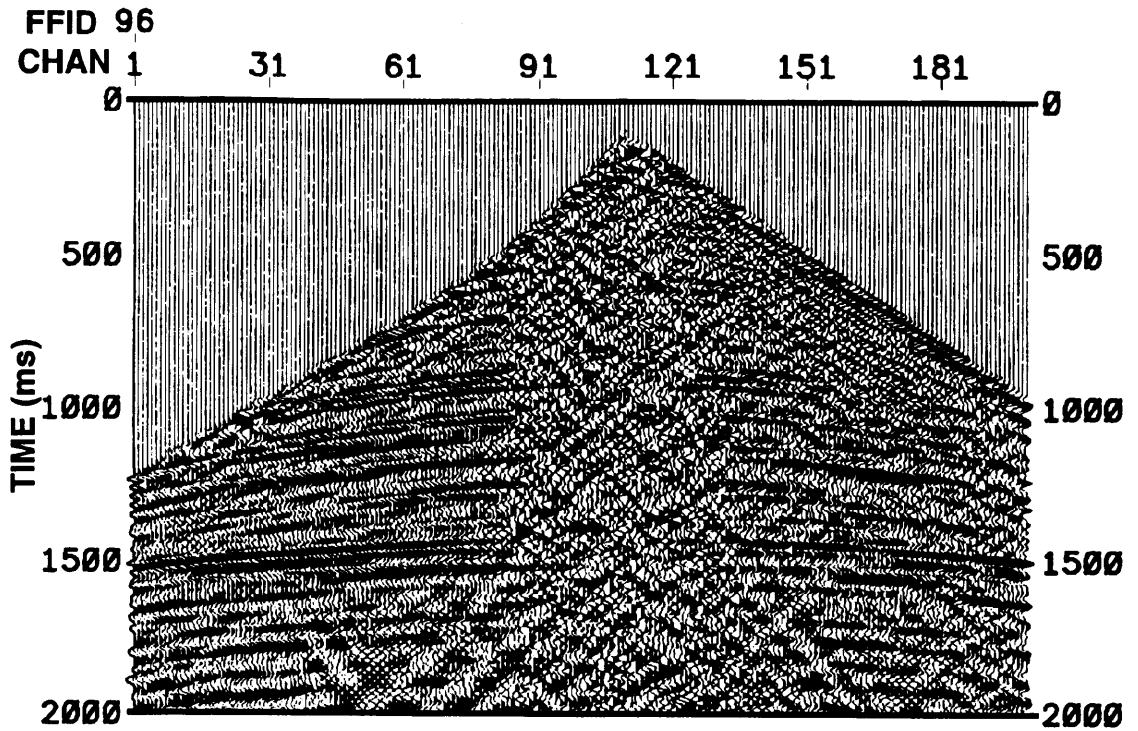


Fig. 2.68a. Shot gather of the vertical component after applying the processing flow shown in Fig. 2.67 without modal filter.

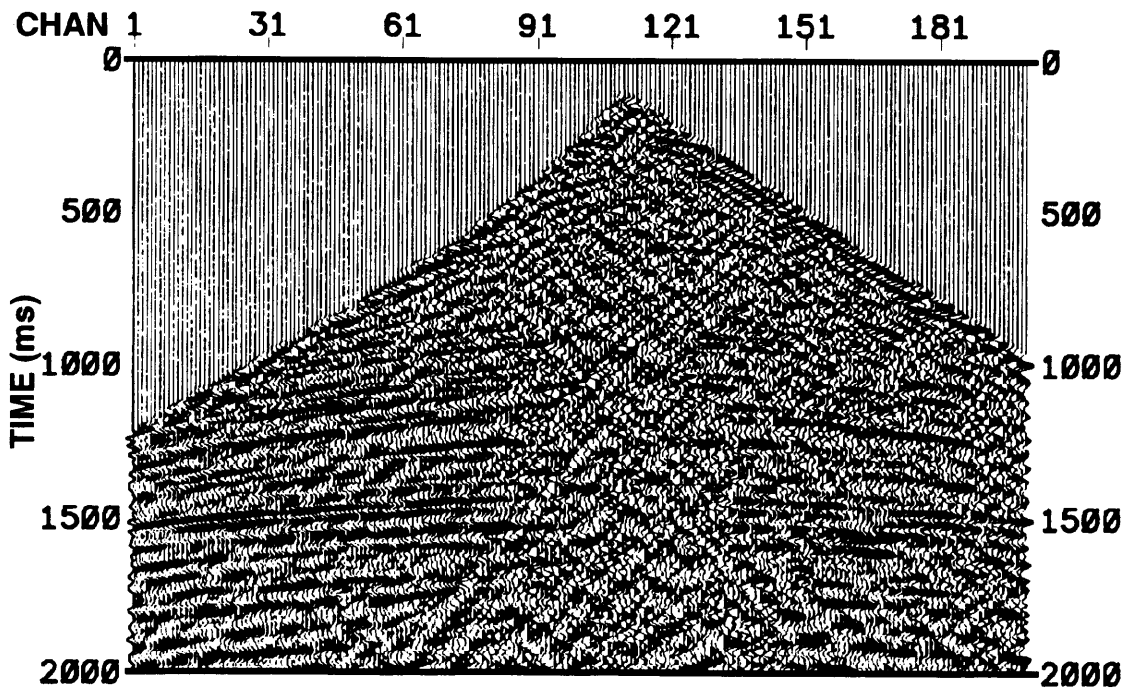


Fig. 2.68b. Pass-*P* output obtained from both vertical and horizontal records (Fig. 2.63) after applying the processing flow shown in Fig. 2.67 with modal filter.

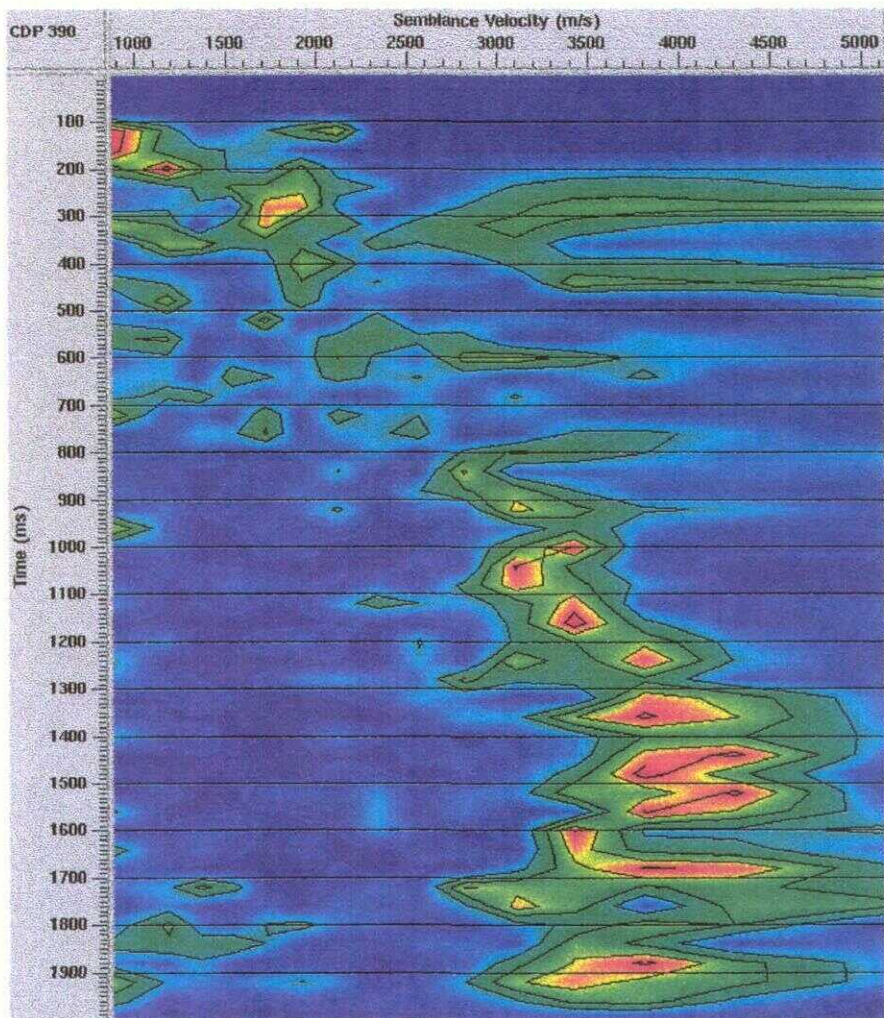


Fig. 2.69a. Velocity analysis for the CDP 390 without modal filter applied.

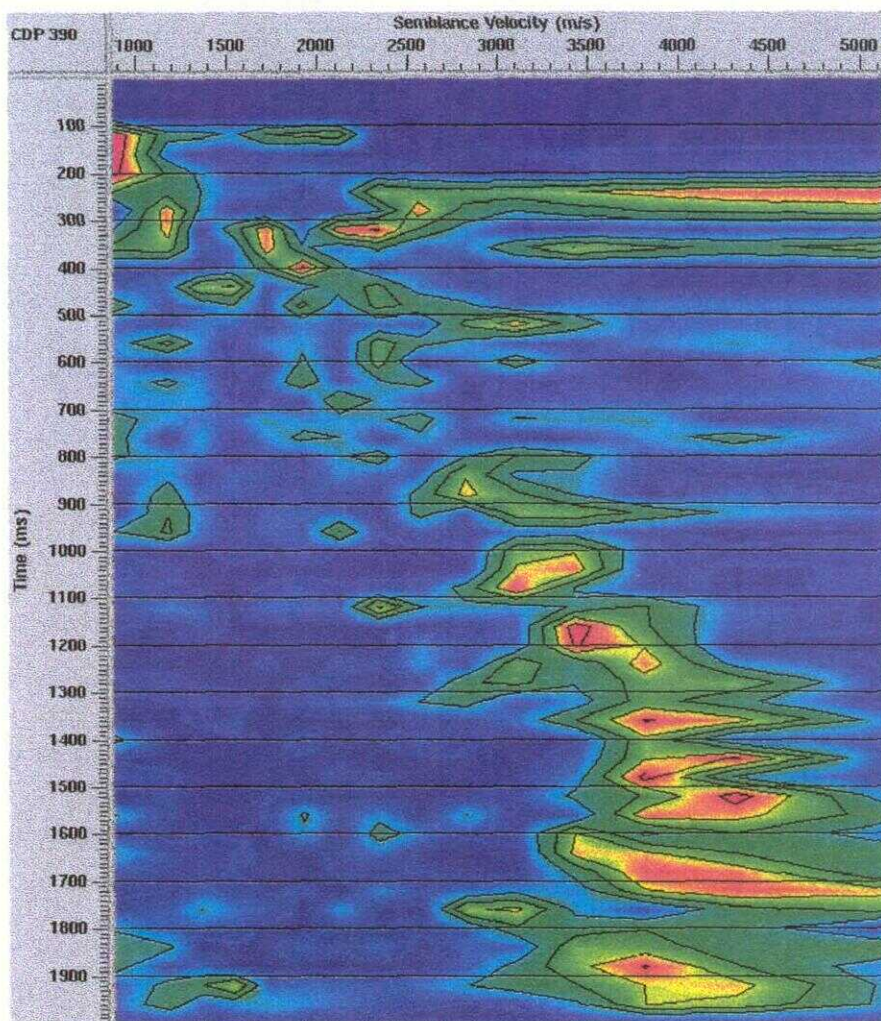


Fig. 2.69b. Velocity analysis for the CDP 390 after modal filtering.

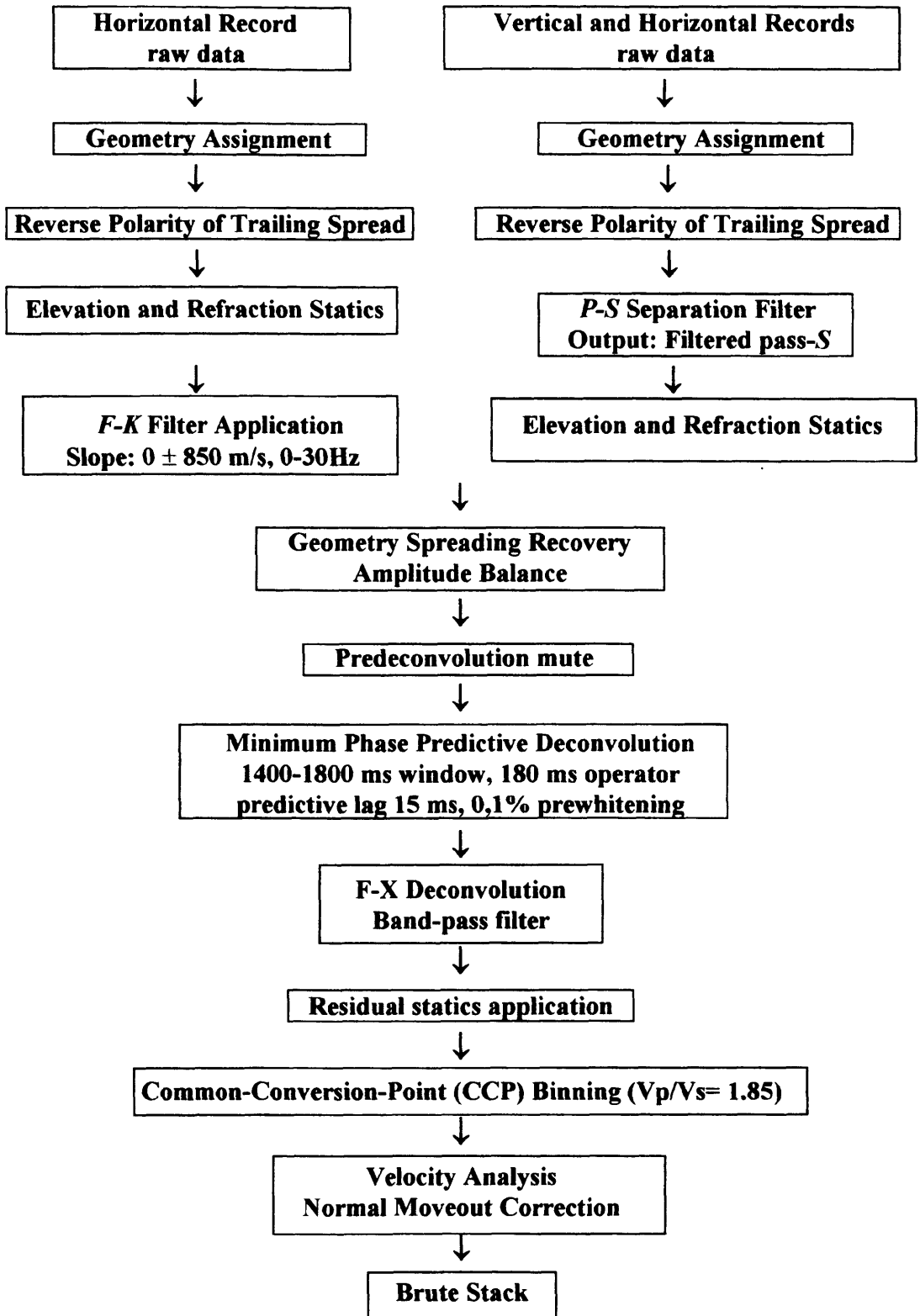


Fig. 2.70. S-wave processing flow for Blackfoot data without and with modal filter.

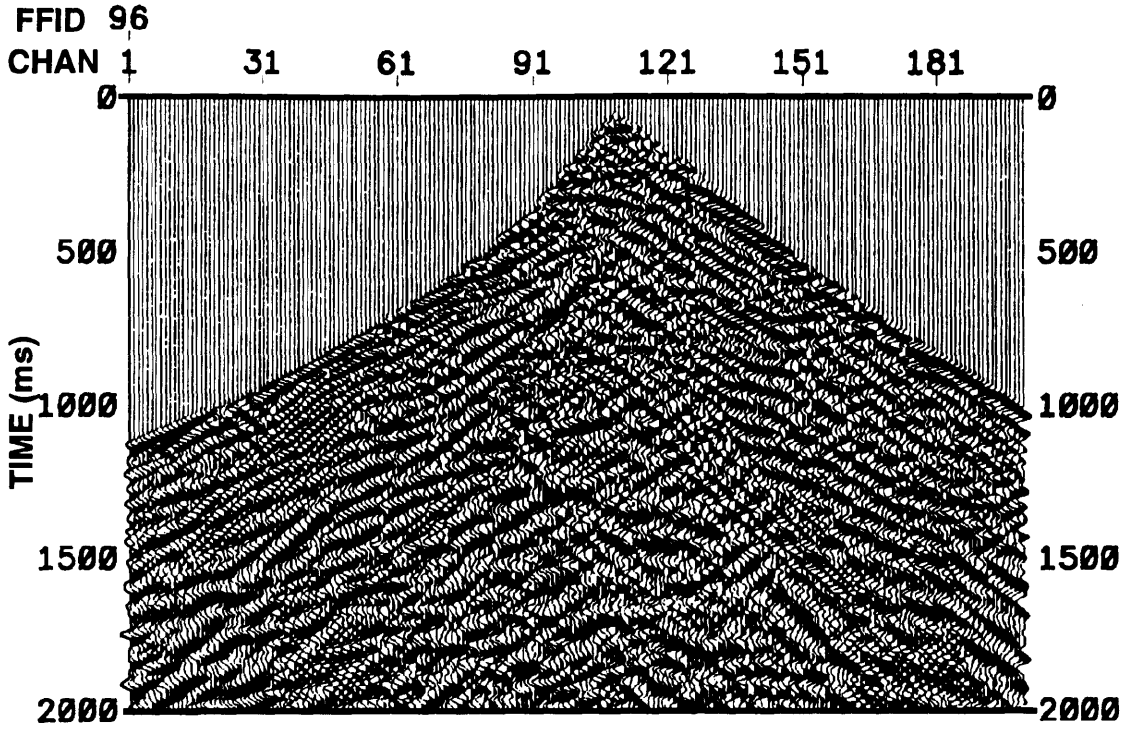


Fig. 2.71a. Shot gather of the horizontal component after applying the processing flow shown in Fig. 2.70 without modal filter.

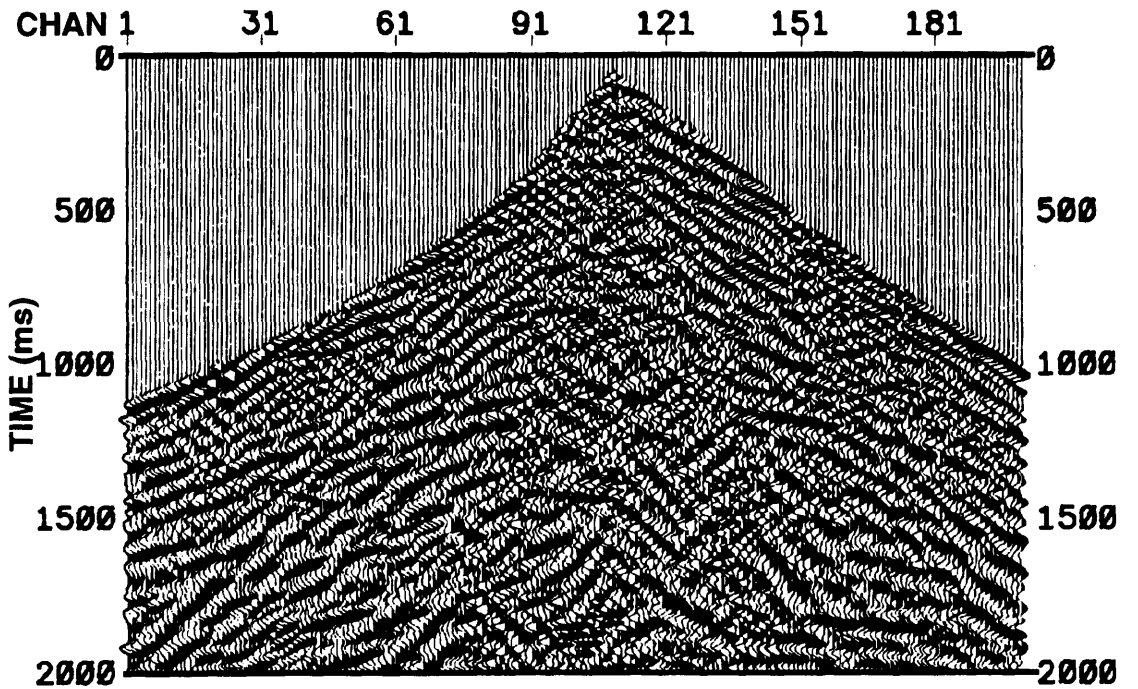


Fig. 2.71b. Pass-S output obtained from both vertical and horizontal records (Fig. 2.63) after applying the processing sequence shown in Fig. 2.70 with modal filter

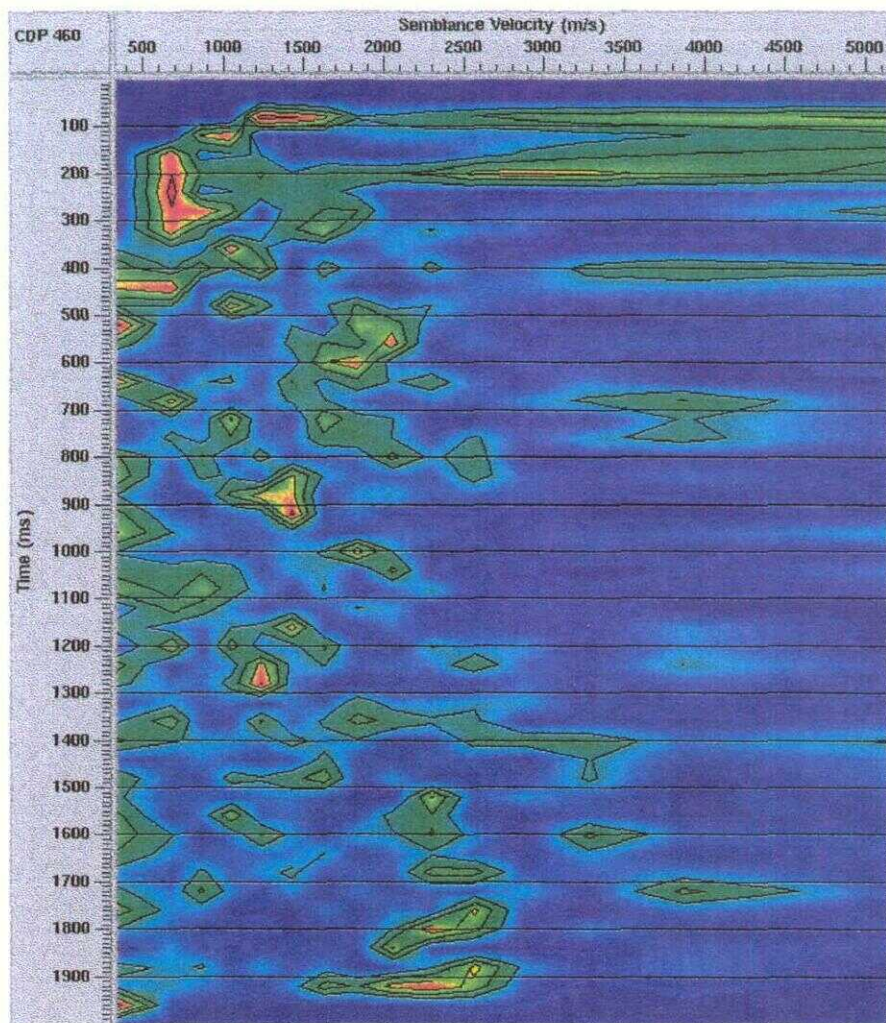


Fig. 2.72a. Velocity analysis for the CCP 460 without modal filter applied.

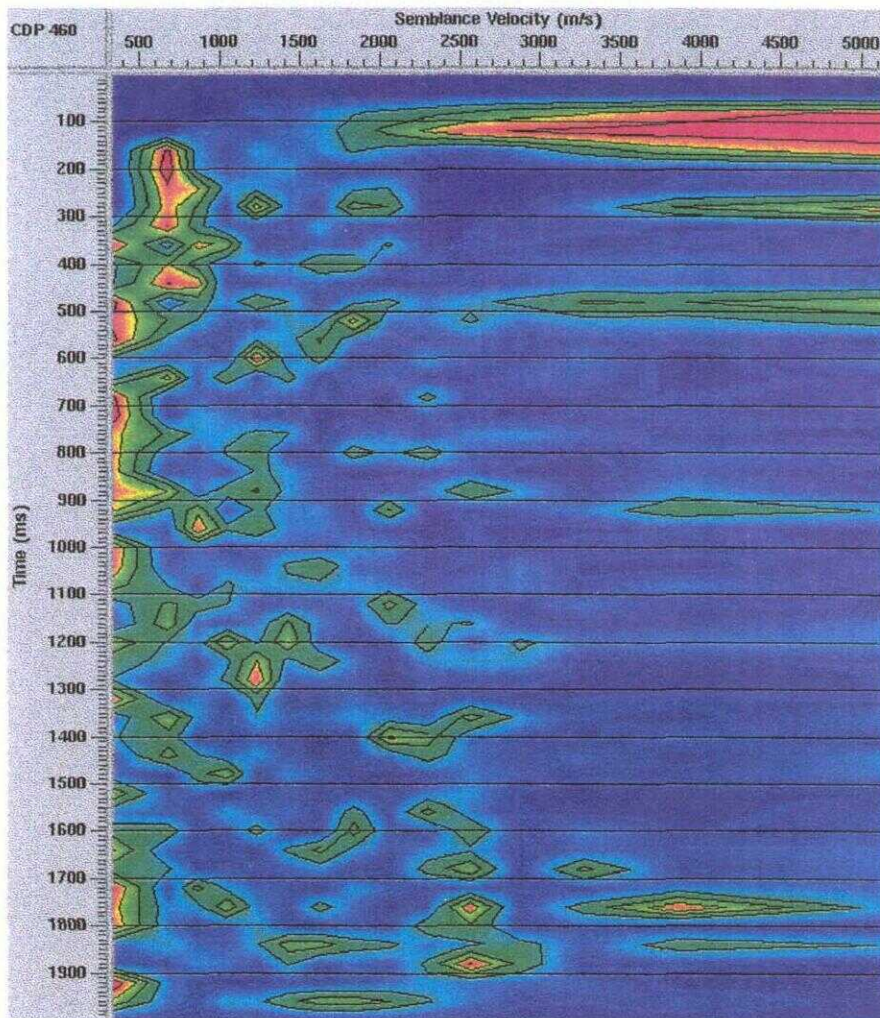


Fig. 2.72b. Velocity analysis for the CCP 460 after modal filtering.

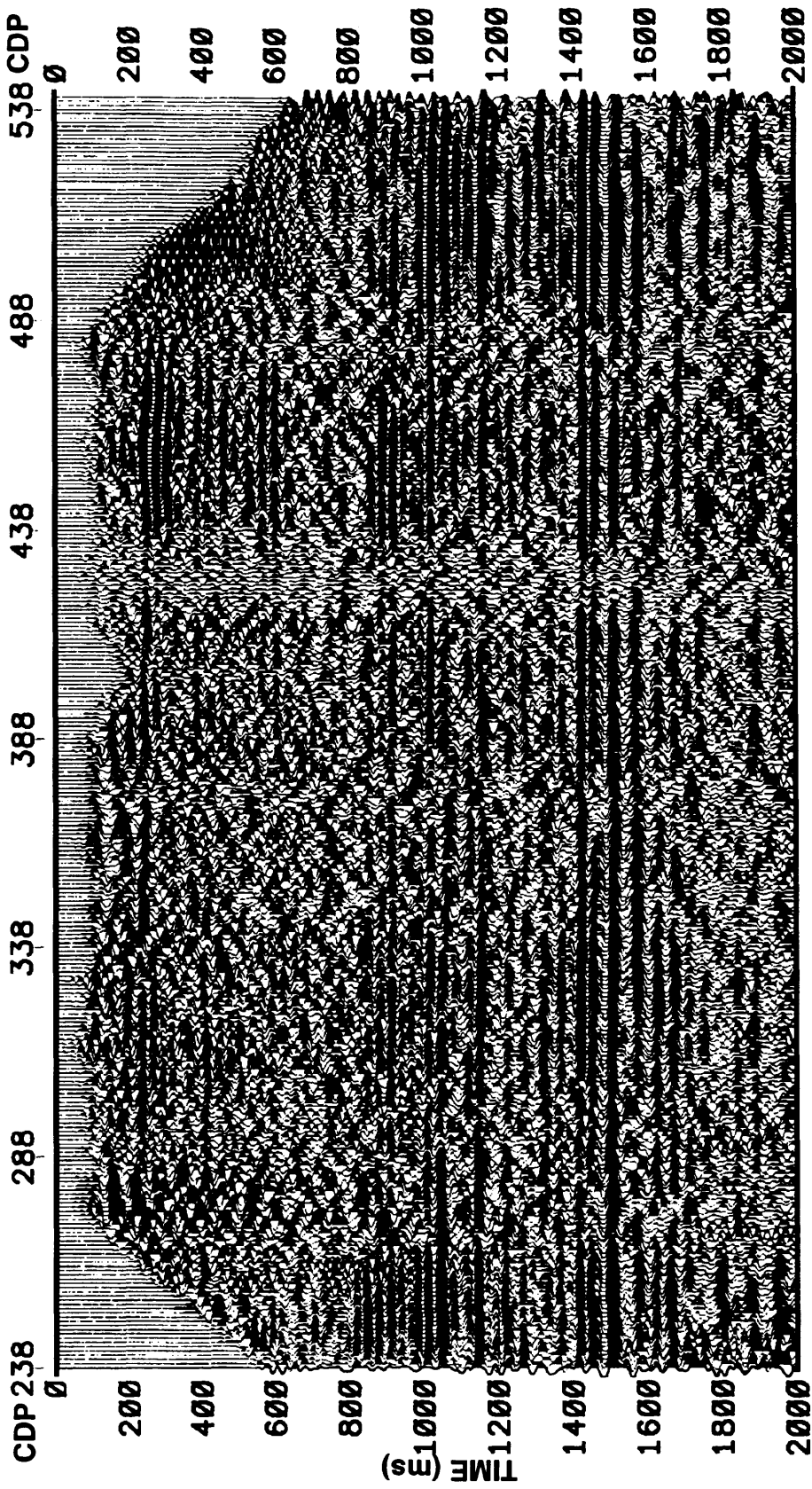


Fig. 2.73. Brute stack of the vertical component data from Blackfoot field, Alberta, processed without separation filter.

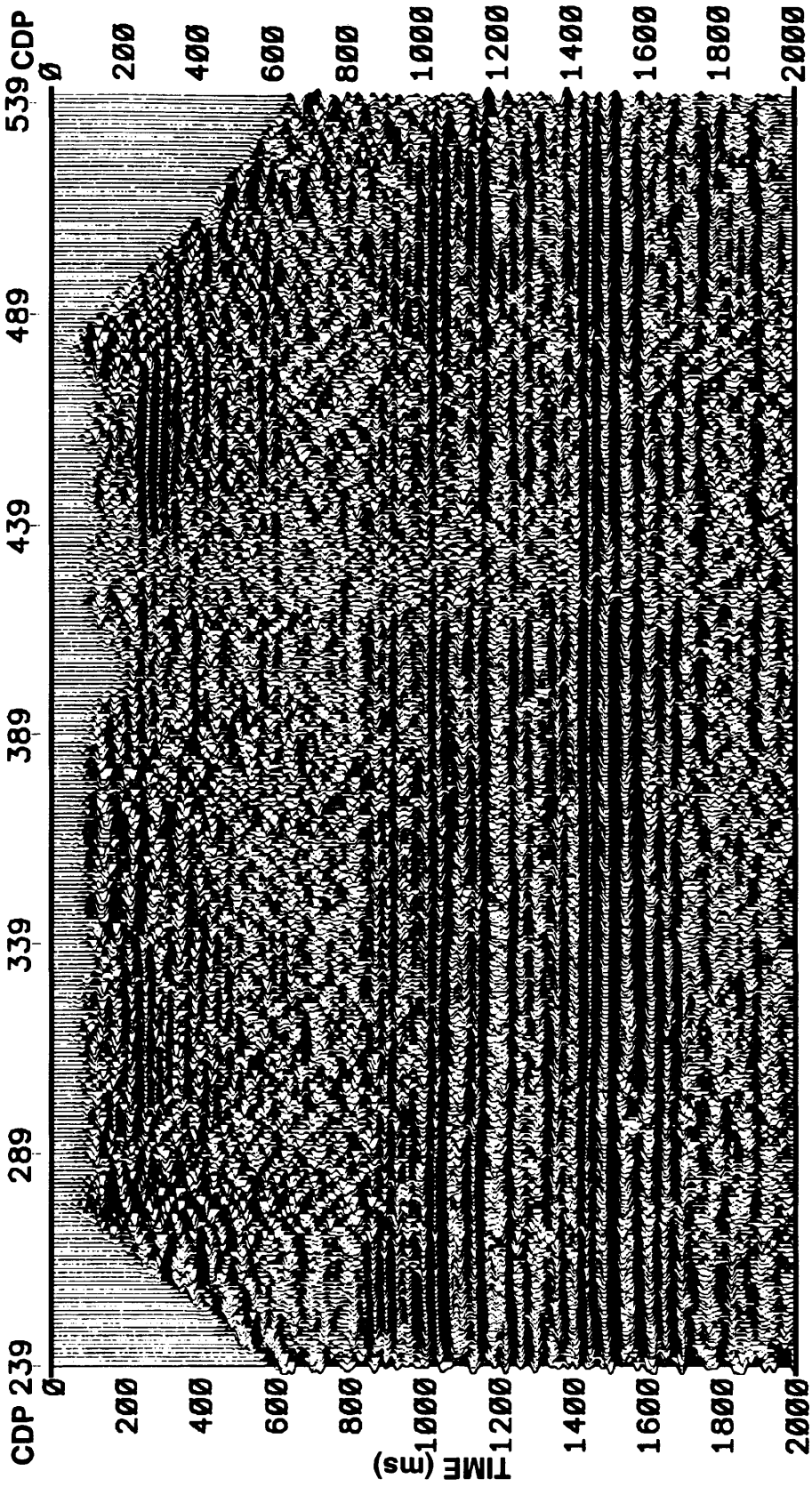


Fig. 2.74. Stacked section of the filtered pass-*P* output obtained from the vertical and horizontal records using $V_p=985$ m/s and $V_s=492$ m/s.

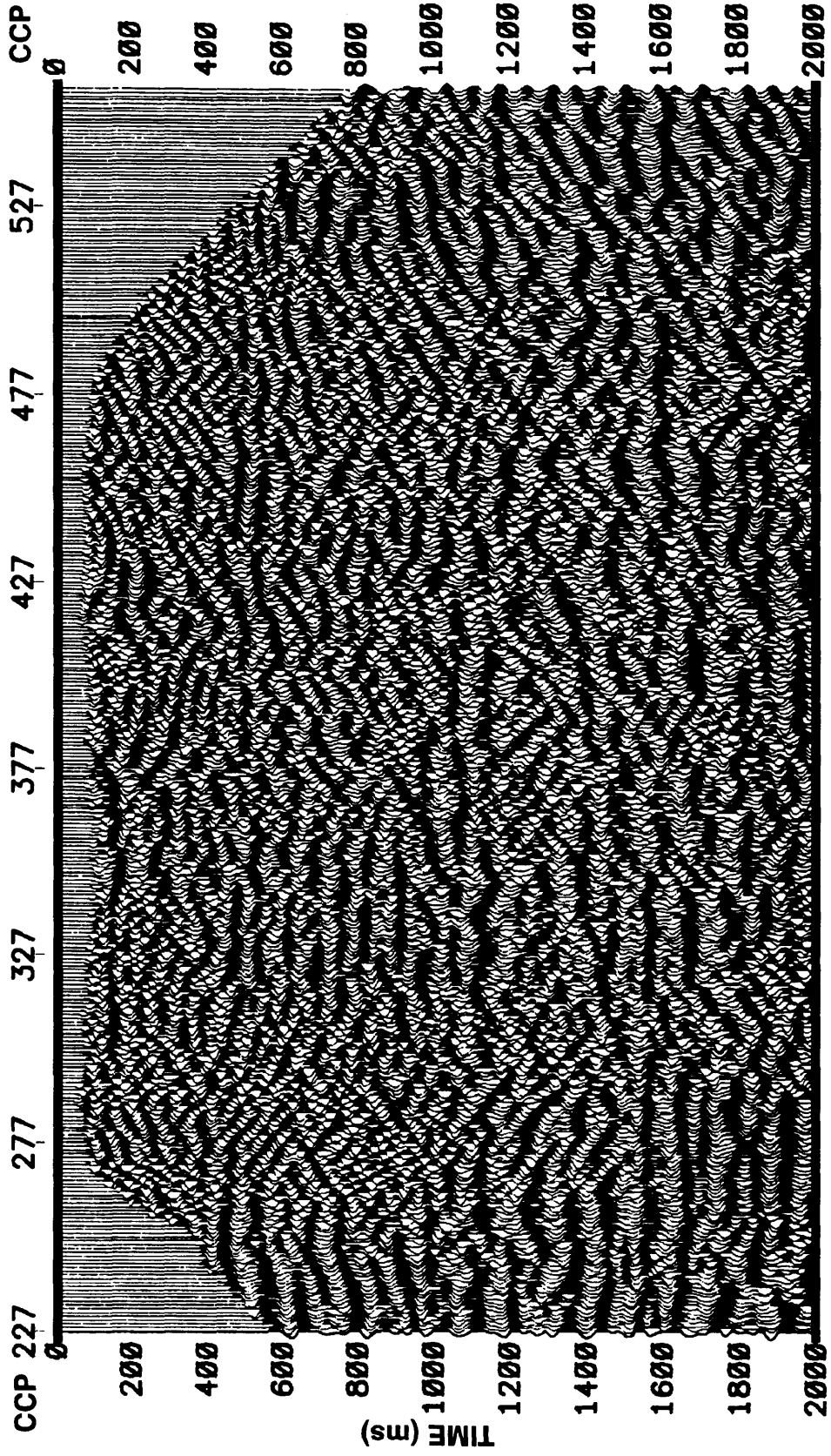


Fig. 2.75. Brute stack of the horizontal component data from Blackfoot field, Alberta, processed without separation filter.

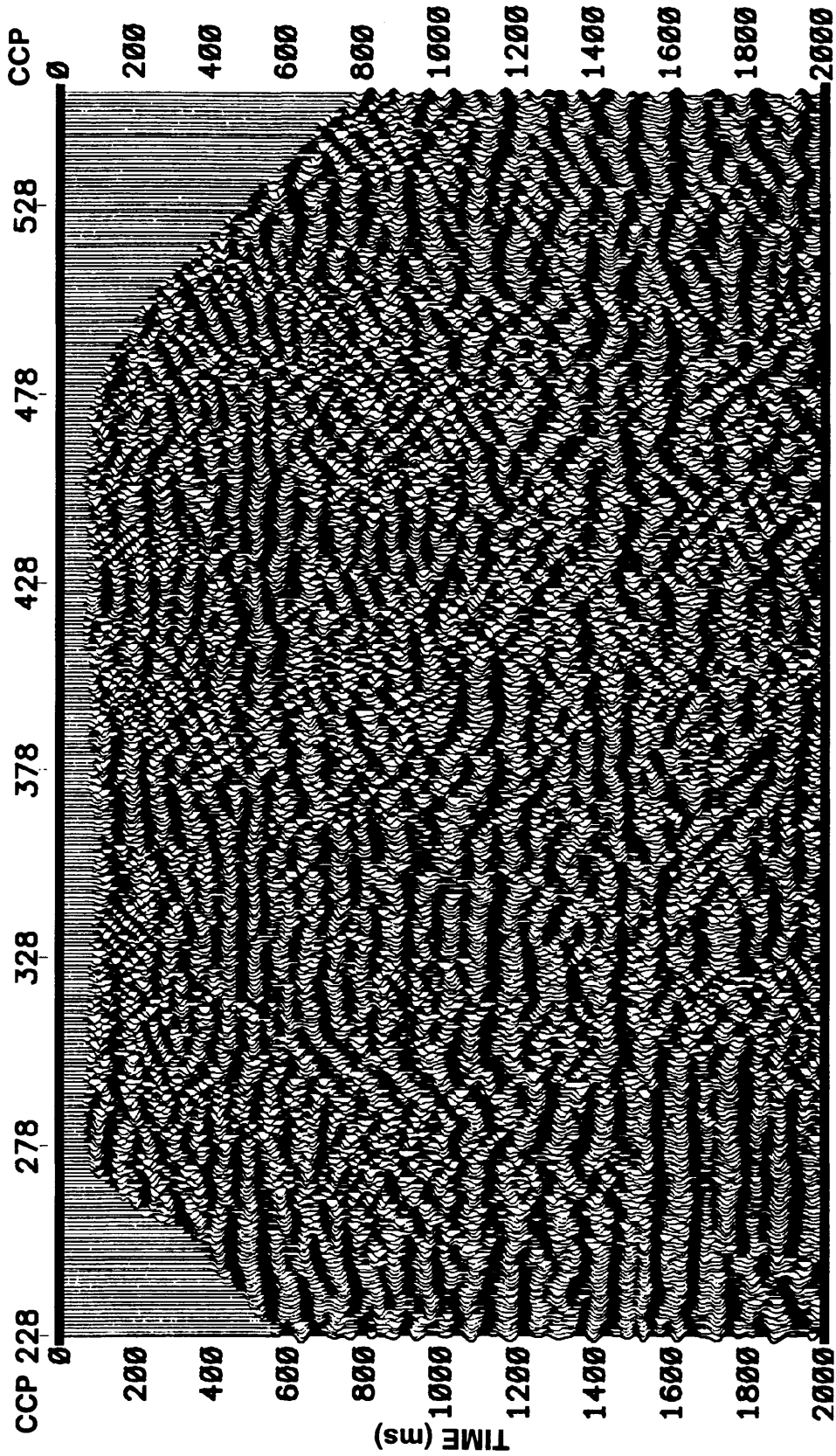


Fig. 2.76. Stacked section of the filtered pass-S output obtained from the vertical and horizontal records using $V_p=985$ m/s and $V_s=492$ m/s.

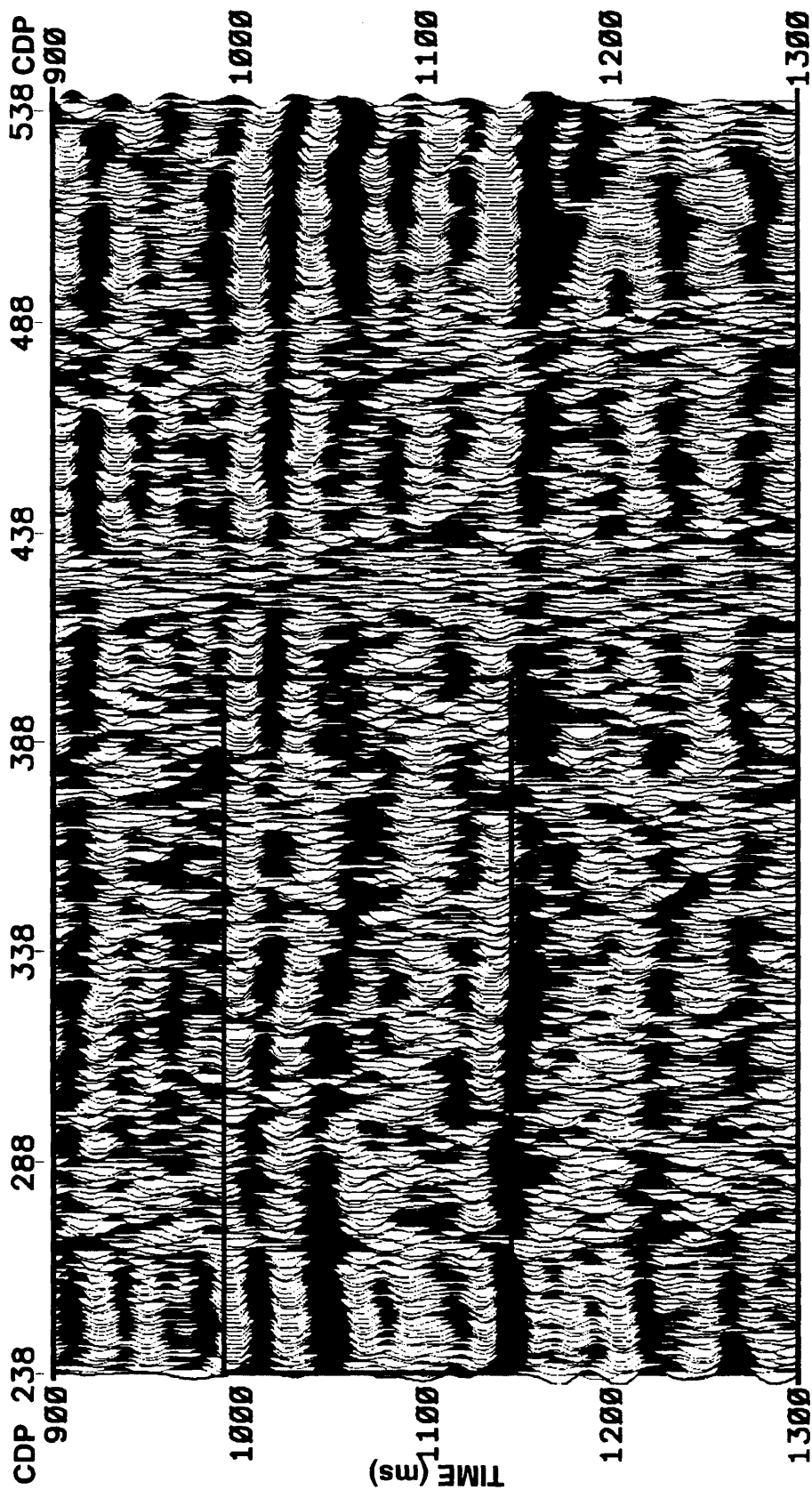


Fig. 2.77a. A detailed picture of the area of interest from the brute stack of the vertical component data acquired in Blackfoot field, Alberta, processed without separation filter.

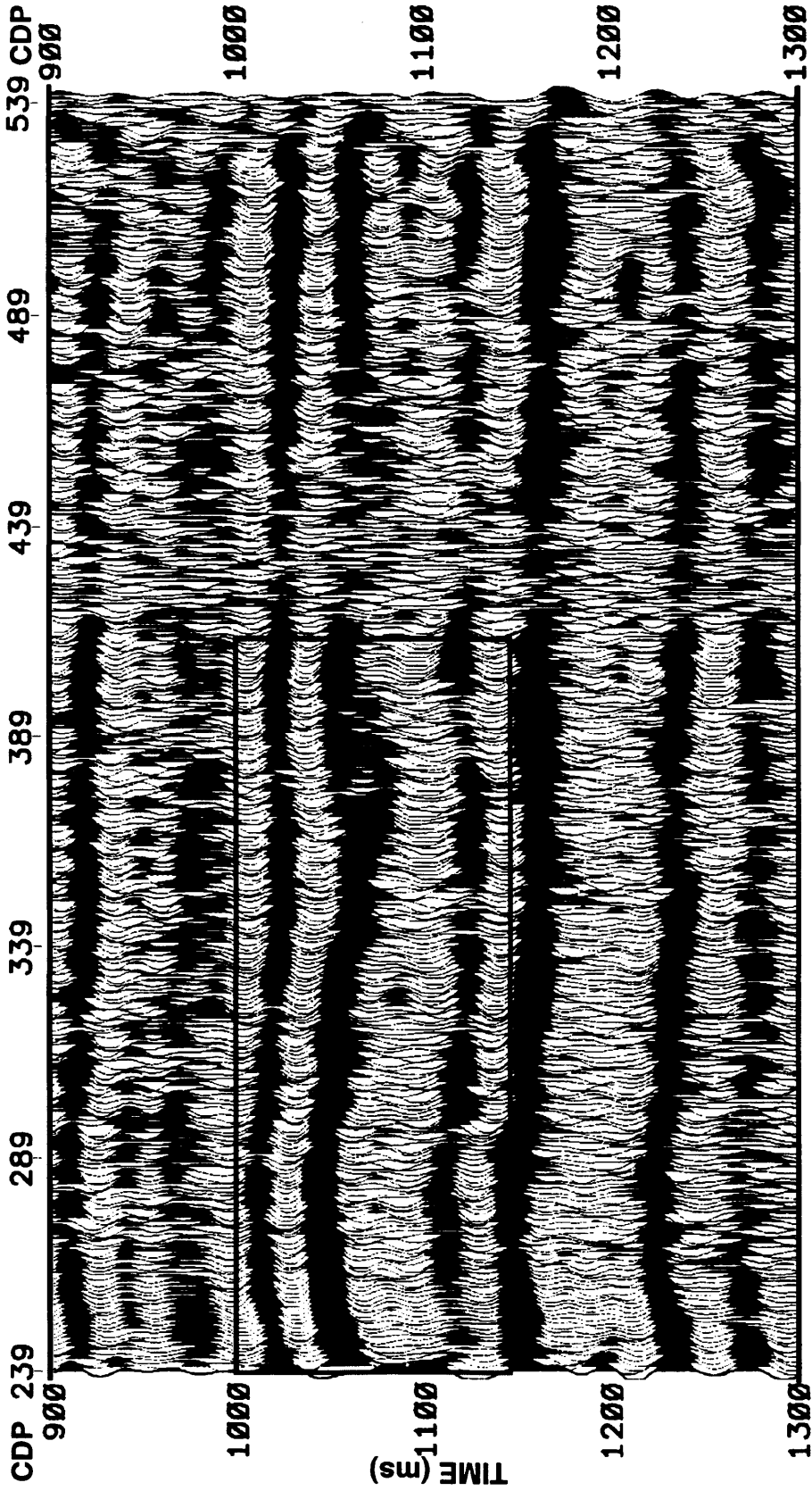


Fig. 2.77b. A detailed picture of the area of interest from the filtered pass-P output obtained from the vertical and horizontal data acquired in Blackfoot field, Alberta, using $V_p=985$ m/s and $V_s=492$ m/s.

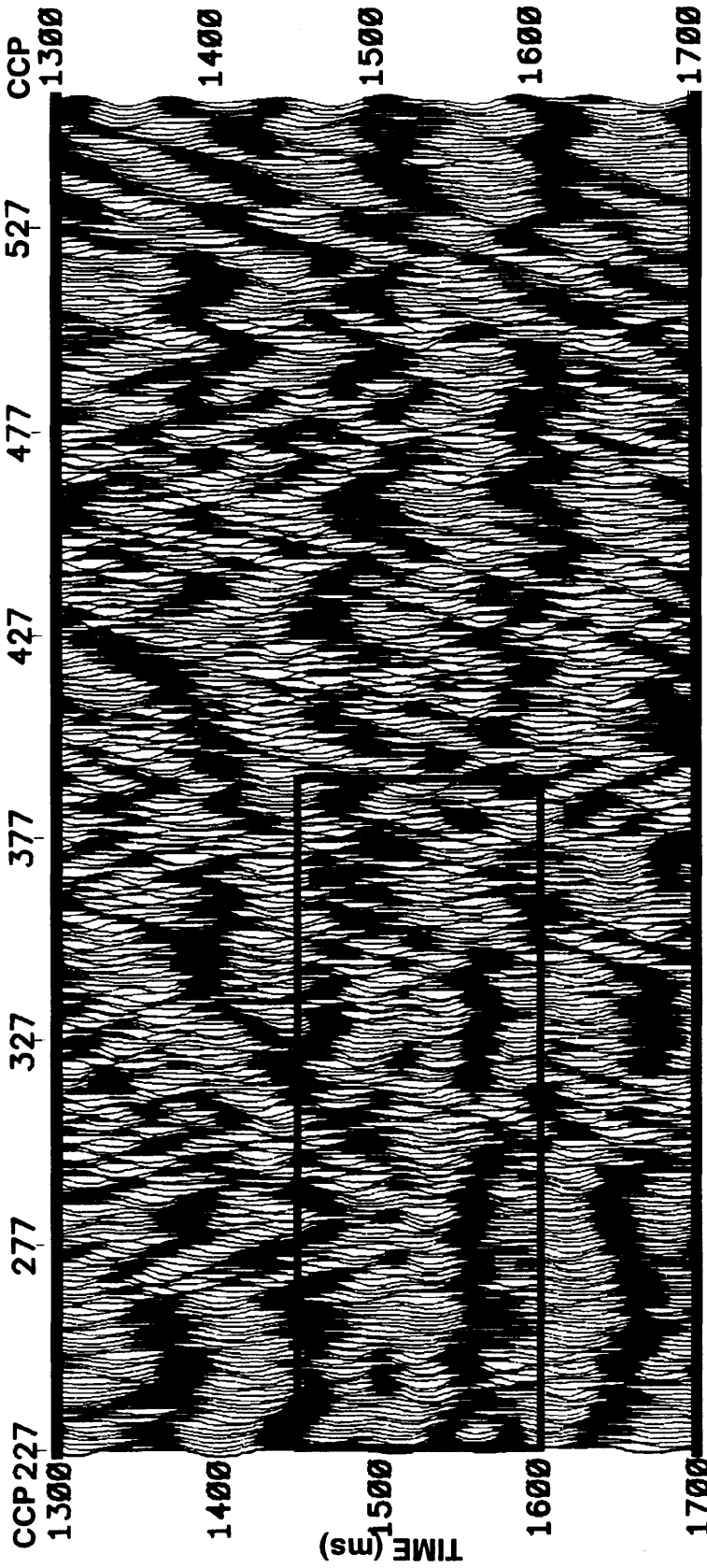


Fig. 2.78a. A detailed picture of the area of interest from the brute stack of the horizontal component data acquired in Blackfoot field, Alberta, processed without separation filter.

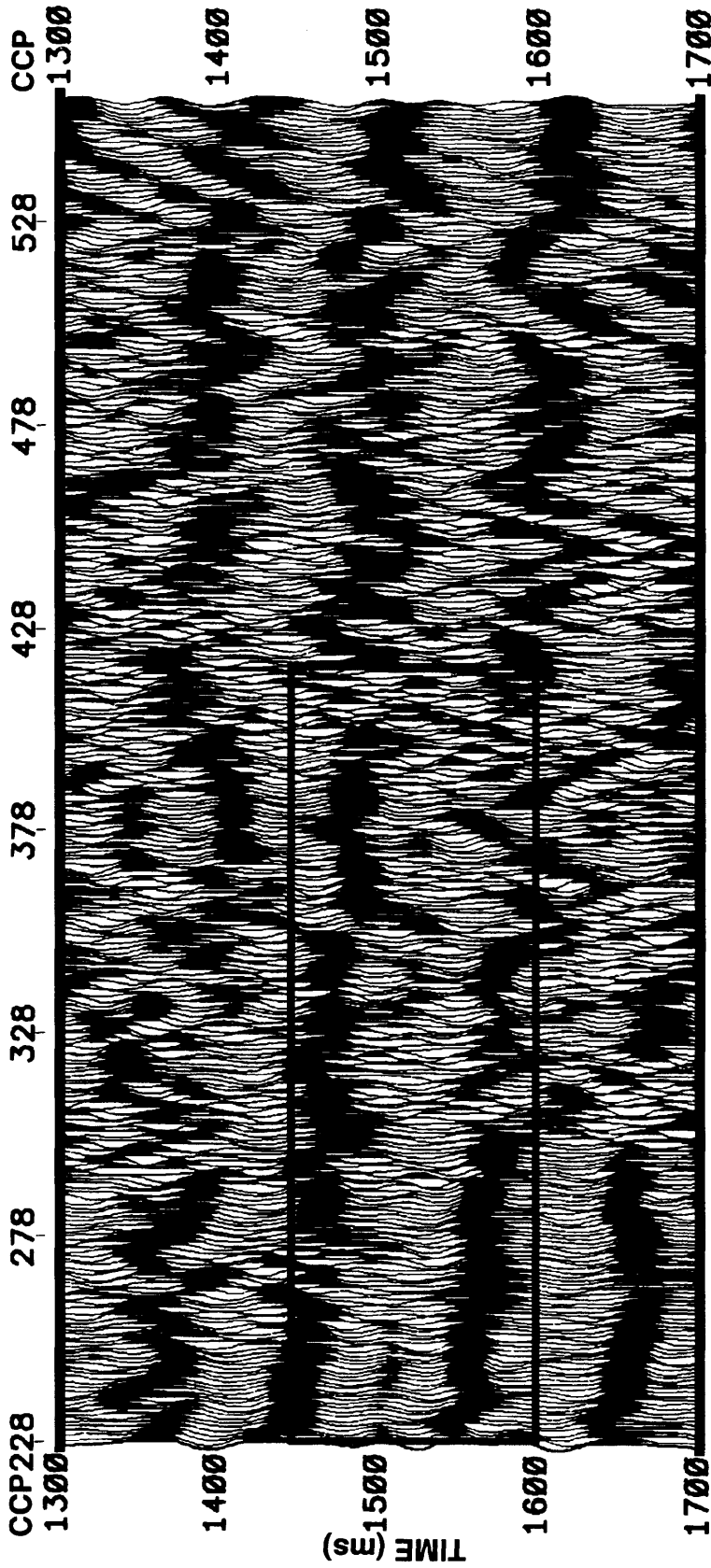


Fig. 2.78b. A detailed picture of the area of interest from the fileref pass-S output obtained from the vertical and horizontal data acquired in Blackfoot field, ALberta, using $V_p=985$ m/s and $V_s=492$ m/s.

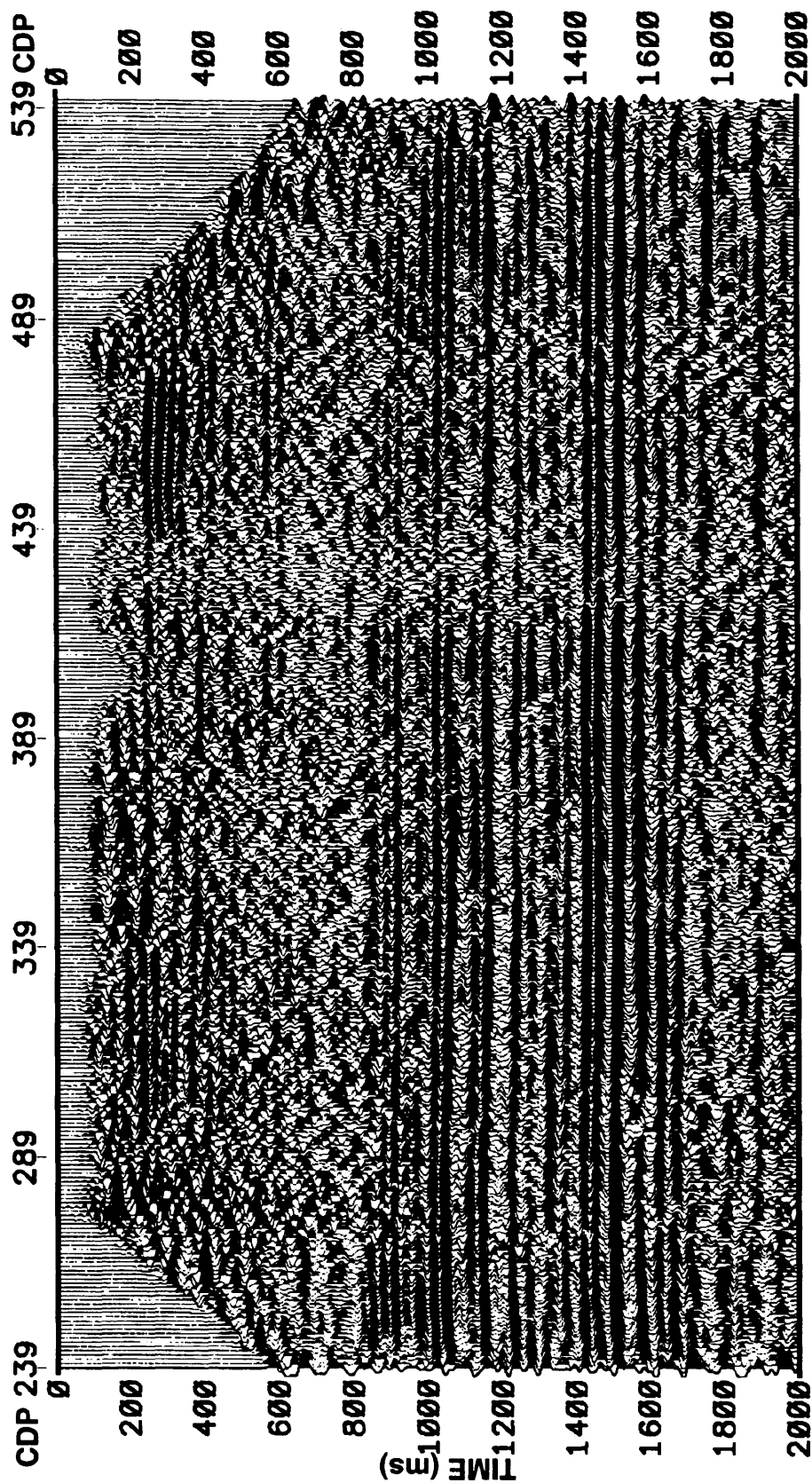


Fig. 2.79a. Stacked section of the filtered pass- P output obtained from the vertical and horizontal records using $V_p=1083.5$ m/s and $V_s=542.3$ m/s.

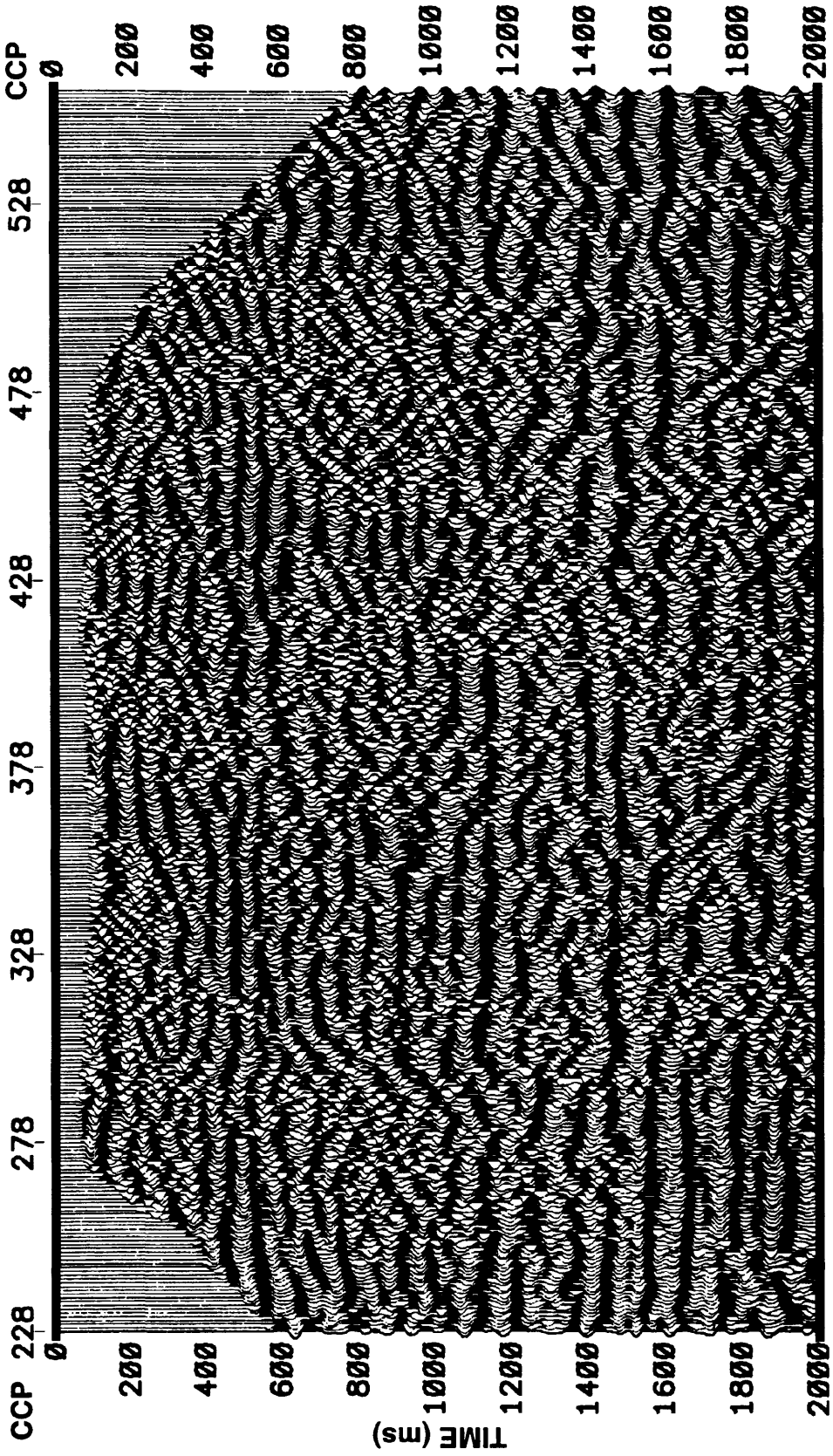


Fig. 2.79b. Stacked section of the filtered pass-S output obtained from the vertical and horizontal records using $V_p=1083.5$ m/s and $V_s=542.5$ m/s.

from these results that the P - S separation filter is robust process and it is not strongly affected for changes in the V_p and V_s velocities values.

Again a detailed image of the porous sand channel in the area considering wrong values of the velocities at the near-surface is shown in Figs. 2.81 and 2.82 for pass- P and pass- S outputs, respectively. We can compare these images with Figs. 2.77a and 2.78a observing a reasonable good result providing a better definition and clean picture of the reflections

2.7 Discussion

The P - S separation filter in the τ - p domain has shown very good performance on synthetic data showing degrees of superposition of P and S arrivals. The filter appears stable with respect to errors in the selection of the values of near-surface V_p and V_s velocities, but the pass- S filtered seems to be more sensible than pass- P filtered record.

The filter was tested under noise and refraction conditions showing handle properly the P and S waves providing reasonable good solutions. These results could guarantee the good performance in real data where we have noise and in many occasions refractions statics problems specially for the converted waves.

The use of τ - p within the process let us eliminate noise like ground-roll, perhaps we don't need to apply previous filtering to the data before entering to the P - S separation filter.

The results obtained from the separation filter in the τ - p domain on real data show its applicability and robustness into 2-D sequence of converted wave processing and its future application in 3-D data.

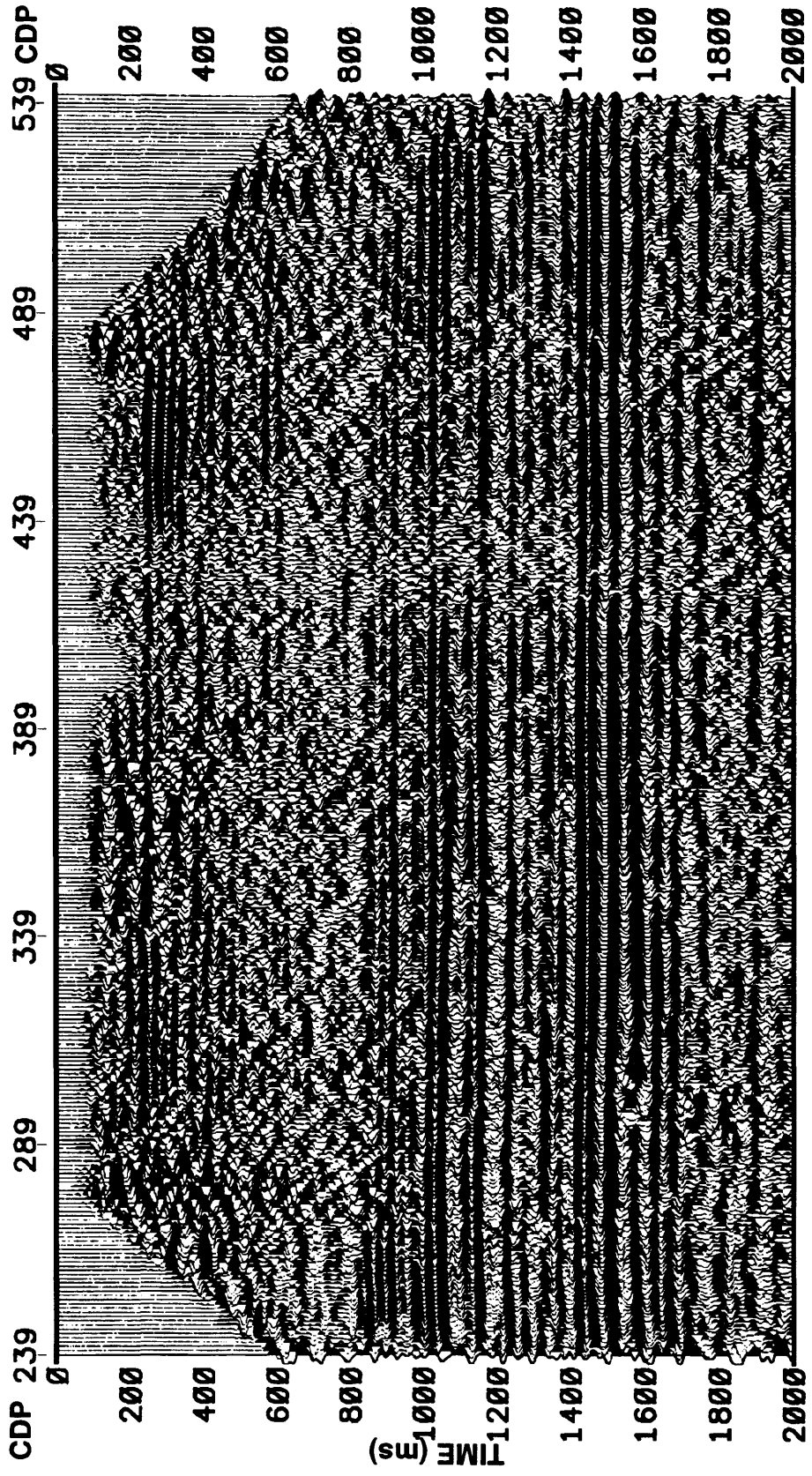


Fig. 2.80a. Stacked section of the filtered pass-P output obtained from the vertical and horizontal records using $V_p=886.5$ m/s and $V_s=443.7$ m/s.

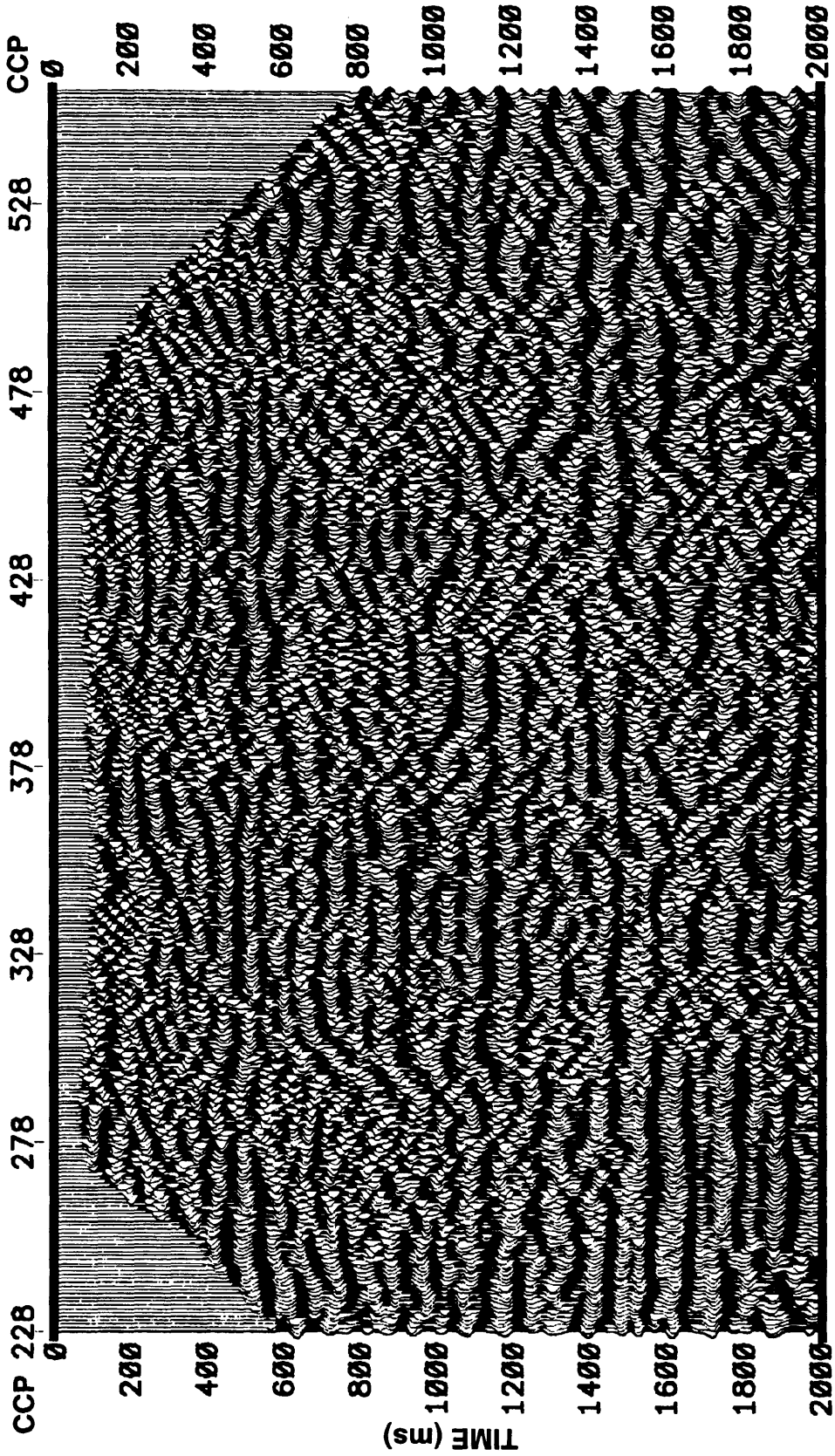


Fig. 2.80b. Stacked section of the filtered pass-S output obtained from the vertical and horizontal records using $V_p=886.5$ m/s and $V_s=443.7$ m/s.

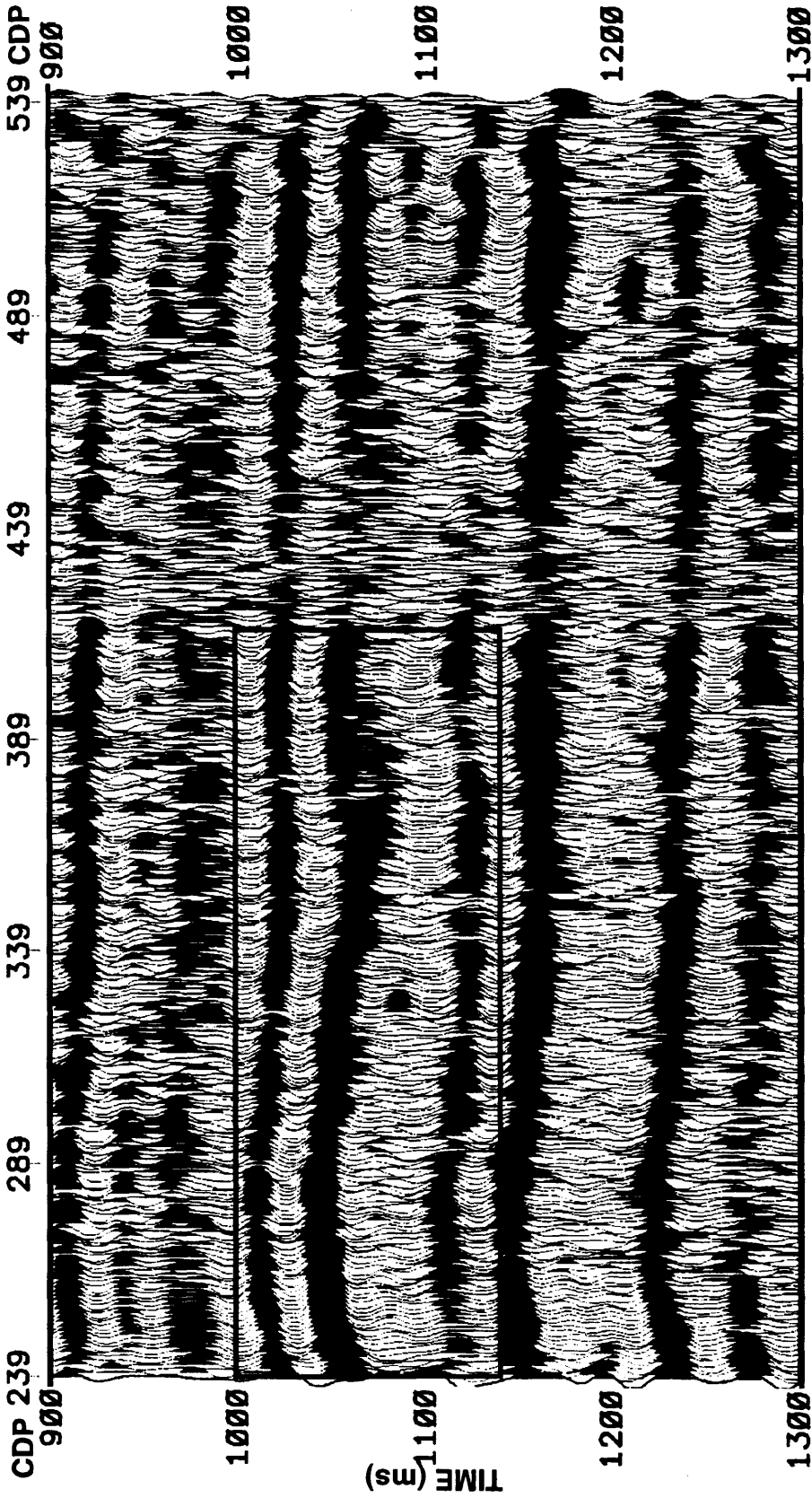


Fig. 2.81a. A detailed picture of the area of interest from the filtered pass-P output obtained from the vertical and horizontal data acquired in Blackfoot field, Alberta, using $V_p = 1083.5$ m/s and $V_s = 542.3$ m/s.

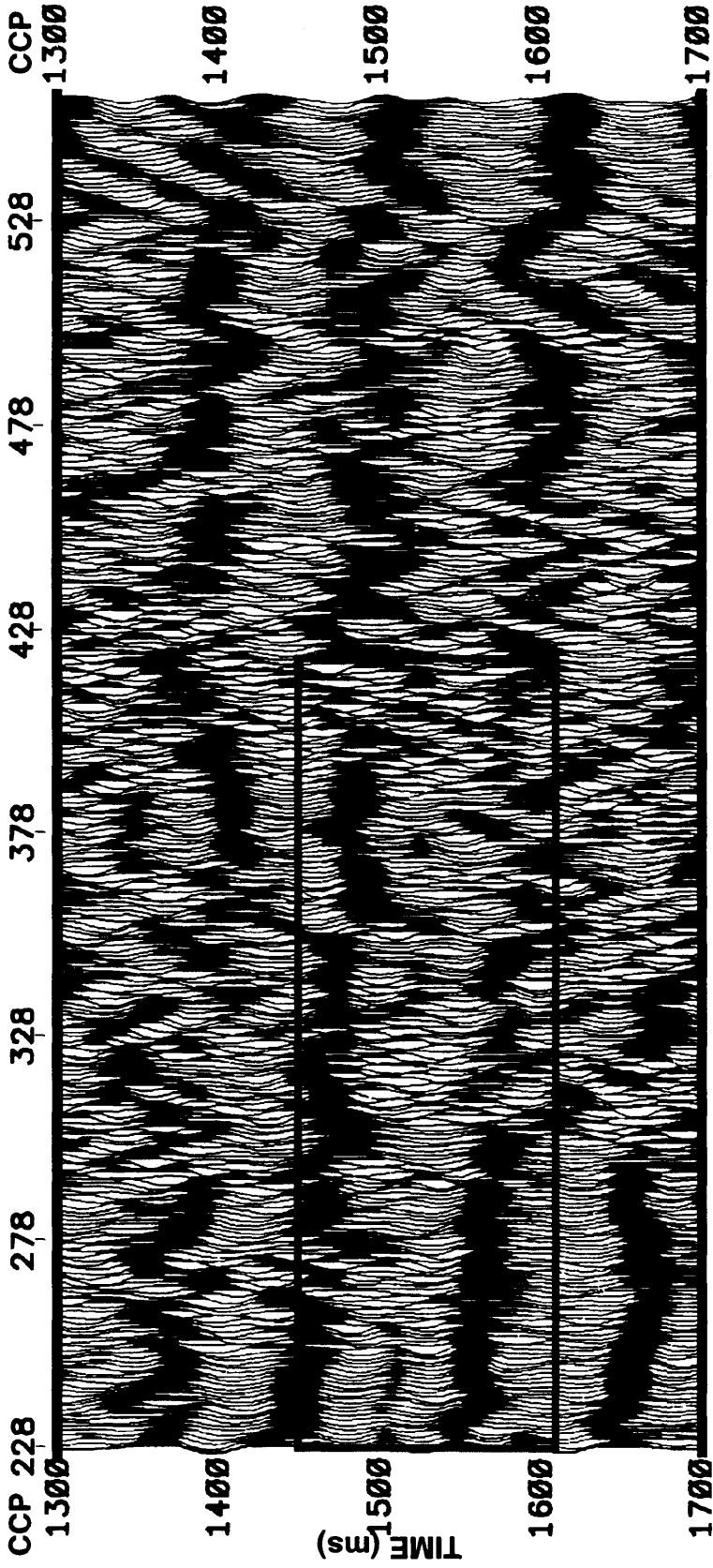


Fig. 2.81b. A detailed picture of the area of interest from the filtered pass-S output obtained from the vertical and horizontal data acquired in Blackfoot field, Alberta, using $V_p=1083.5$ m/s and $V_s=542.3$ m/s.

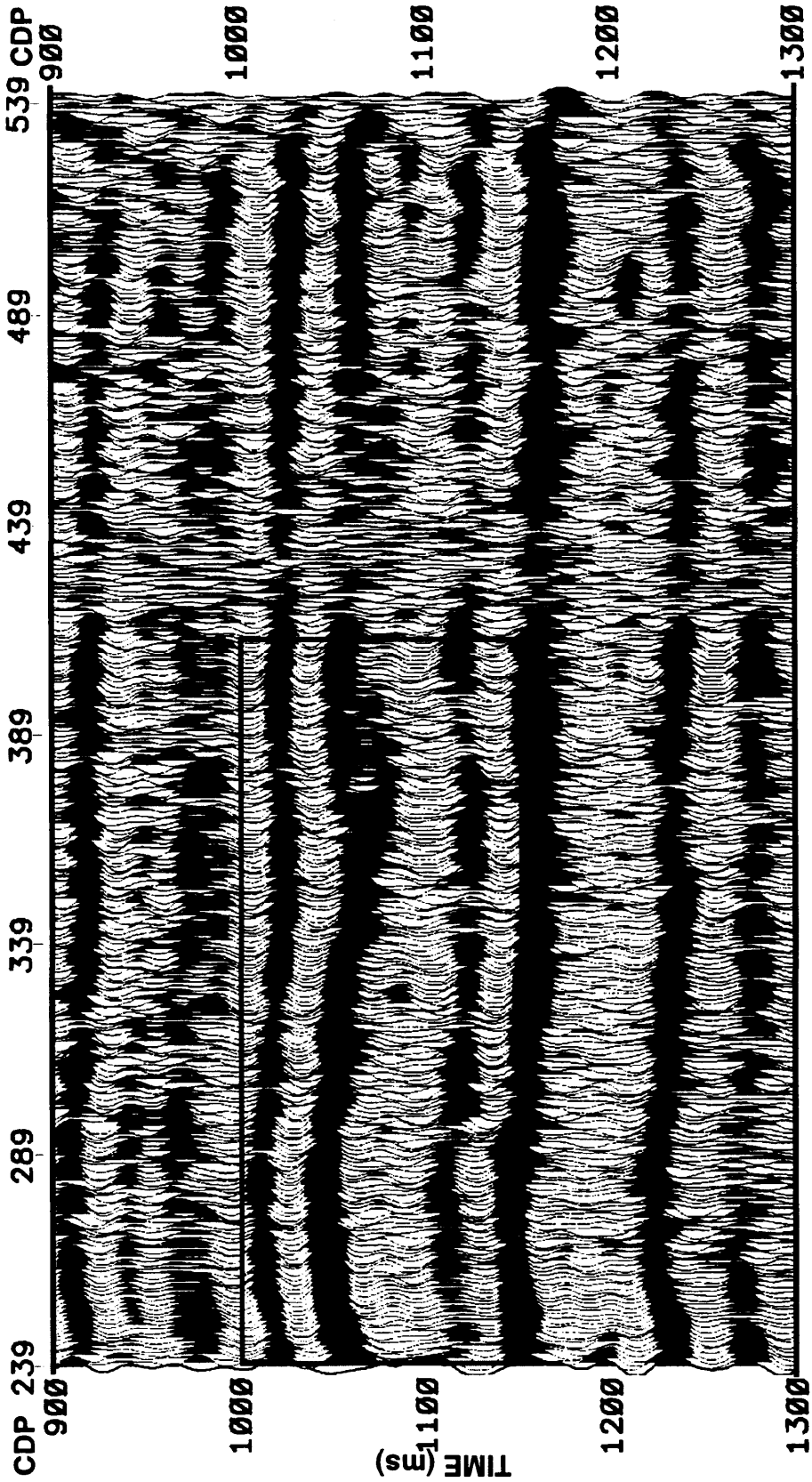


Fig. 2.82a. A detailed picture of the area of interest from the filtered pass-P output obtained from the vertical and horizontal data acquired in Blackfoot field, Alberta, using $V_p = 886.5$ m/s and $V_s = 443.7$ m/s.

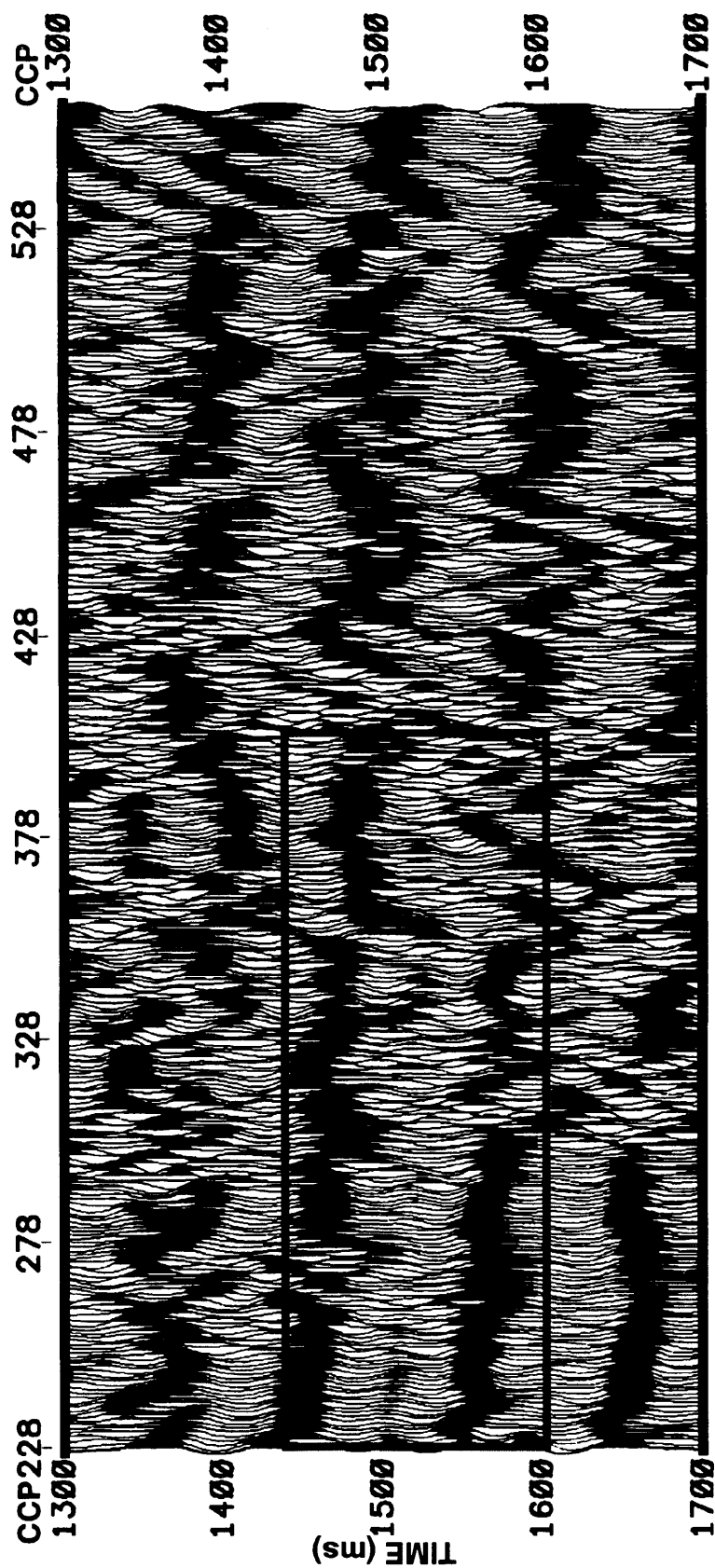


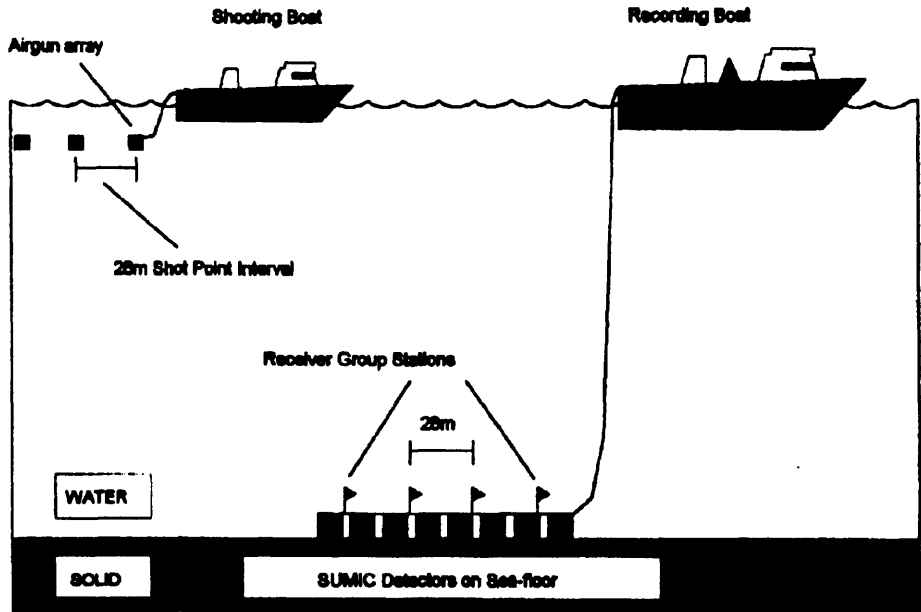
Fig. 2.82b. A detailed picture of the area of interest from the filtered pass-S output obtained from the vertical and horizontal data acquired in Blackfoot field, Alberta, using $V_p = 886.5$ m/s and $V_s = 443.7$ m/s.

CHAPTER 3 - MODAL SEPARATION OF 3C-2D SUBSEA SEISMIC DATA

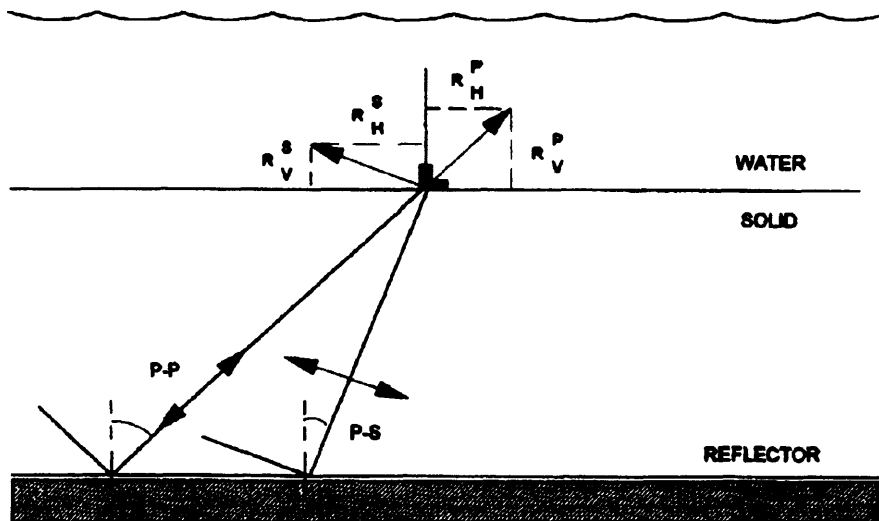
3.1 Introduction

P and S seismic waves impinging on a liquid-solid interface give rise to energy on both horizontal and vertical geophones. The response of the vertical geophone at an interface is quite similar to that on a free surface. The horizontal geophone has a stronger response to impinging P waves and a smoother response to incident S waves. Presented here is a filtering method operating in the τ - p domain, that separates P and S waves by taking into account the geophone response. The filter requires estimates of the near-interface P and S wave velocities but is robust with respect to errors in these velocities. The P - S separation filter is tested on synthetic elastic-wave data and performs the wave type separation well.

The quest for a more detailed and confident description of the subsurface has led to the rise of three-component (3-C) seismic surveying. Considerable effort is currently being expended to make and use converted-wave (P -to- S reflection) seismic sections from these 3-C recordings. Most of the effort to date has been with land recordings. However, with the advent of the SUMIC (subsea seismic) survey and its very promising early results (Berg et al., 1994; Granli et al., 1995), more attention is focusing on the marine 3-C case (Fig. 3.1). A fundamental aspect of deciphering 3-C records from the ocean bottom is to understand how seismic waves interact with a geophone at a fluid-solid interface. This paper reviews the basic theory of the geophone response at the water bottom and proposes a new filter to separate P and S waves so recorded. The separation filter is based on the methods of Dankbaar (1985) and Labonte (1990). The separated waves (pure P and S) are then further processed into their respective sections.



(a)



(b)

Fig. 3.1. (a) Schematic SUMIC (subsea seismic) 2-D acquisition (after Berg et. al., 1994). (b) Geometry of waves impinging on a vertical and horizontal geophone at the fluid-solid interface (after Ferber, 1989).

3.2 Theory

The P - S separation method here uses the water-bottom geophone response as developed by White (1965). The geophone response describes the P and S amplitudes output from a receiver due to an incident wave of “unit” size. This output varies with the angle of incidence of the impinging waves. In the elastic case considered here, four responses are involved, distinct for vertical and horizontal geophones and for incident P and S waves.

To derive the P - S separation filter, we first express the full horizontal and vertical geophone records in terms of the response to incident P and S waves (Dankbaar, 1985). As shown before, these responses are a function of horizontal slowness, thus it is advantageous to decompose the data into plane waves, i.e. to transform the data to the τ - p domain. Then the expressions become straightforward:

$$U_V(\tau, p) = P_{in}(\tau, p)R_V^P(p) + S_{in}(\tau, p)R_V^S(p), \quad (3.1)$$

$$U_H(\tau, p) = P_{in}(\tau, p)R_H^P(p) + S_{in}(\tau, p)R_H^S(p), \quad (3.2)$$

where U_V and U_H are the vertical and horizontal geophone records transformed to the τ - p domain, P_{in} and S_{in} the incident P and S wavefields, and R_V^P , R_V^S , R_H^P and R_H^S the geophone responses, respectively.

3.3 Geophone response definitions and characteristics

The expressions for the response of a single geophone located at a liquid-solid contact (White, 1965) can be written as a function of horizontal slowness p , which is

defined as the reciprocal of velocity along the horizontal direction ($p = \sin\theta/V$, θ is the incidence angle measured from the vertical). The vertical geophone response $R_V^P(p)$ from an impinging P wave, at angle ϕ , with horizontal slowness p is given below, where primed quantities are related to the liquid:

$$R_V^P(p) = 2\gamma^{-1}\xi (2V_s^2 p^2 - 1) / R_o(p), \quad (3.3)$$

where $\gamma = V_s/V_p$, $\xi = (\gamma^2 - V_s^2 p^2)^{1/2}$, and

$$R_o(p) = \frac{\rho V_p' (1 - V_p'^2 p^2)^{1/2}}{\rho V_p (1 - V_p'^2 p^2)^{1/2}} + 4\gamma^3 \sin^2 \phi \cos \phi (1 - \gamma^2 \sin^2 \phi)^{1/2} + (1 - 2\gamma^2 \sin^2 \phi).$$

The response from an impinging S wave is:

$$R_V^S(p) = 4V_s p \eta \xi / R_o(p). \quad (3.4)$$

where $\eta = (1 - V_s^2 p^2)^{1/2}$.

Similarly the horizontal geophone response from an impinging P wave is:

$$R_H^P(p) = 2V_p p \left[\frac{\rho V_p' (1 - V_p'^2 p^2)^{1/2}}{\rho V_p (1 - V_p'^2 p^2)^{1/2}} + 2\xi \eta \right] / R_o(p), \quad (3.5)$$

and the horizontal geophone response from S wave is:

$$R_{H}^S(\rho) = 2\eta \left[\frac{\rho V_p (1 - V_p^2 \rho^2)^{1/2}}{\rho V_p (1 - V_p^2 \rho^2)^{1/2} + (1 - 2V_s^2 \rho^2)} \right] / R_o(\rho), \quad (3.6)$$

To view the geophone responses, let us take a specific case where the solid has elastic values: $\rho = 1.6$ g/cc, $V_p = 1500$ m/s, and $V_s = 650$ m/s, and the fluid has values: $\rho = 1.135$ g/cc and $V_p = 1455$ m/s. The geophone responses are shown as functions of angle of incidence in Fig. 3.2. We can compare these responses with those from a geophone on a free surface. Using the same solid values and the expressions of the response on a free surface (White, 1965), we calculated the plots in Fig. 3.3. Figs. 3.2a and 3.3a show the behavior of the vertical geophone for a stress-free solid and liquid-solid contact, respectively. We see that the magnitudes of the geophone responses at a liquid-solid contact are reduced as compared with the stress-free solid. The S -wave response in the fluid case is also relatively smaller compared to the P -wave.

The horizontal geophone responses for a liquid-solid and stress-free solid contact are plotted in Figs. 3.2b and 3.3b. We see that R_H^S is modified somewhat by the presence of the liquid: the principal effects being the elimination of the nulls at 45° , and the increased sensitivity to the incident P waves.

Figs 3.4 (a,d) shown the geophone characteristics for single vertical and horizontal geophone in the liquid-solid contact considering difference elastic parameters in both mediums. From these figures it is evident the dependence of the geophone responses on the P -wave and S -wave velocities, and both incident P and incident S waves are observed on vertical and horizontal geophone records due to the overlapping of the radiation characteristics associated with both waves for certain angles of incidence ($30^\circ - 60^\circ$).

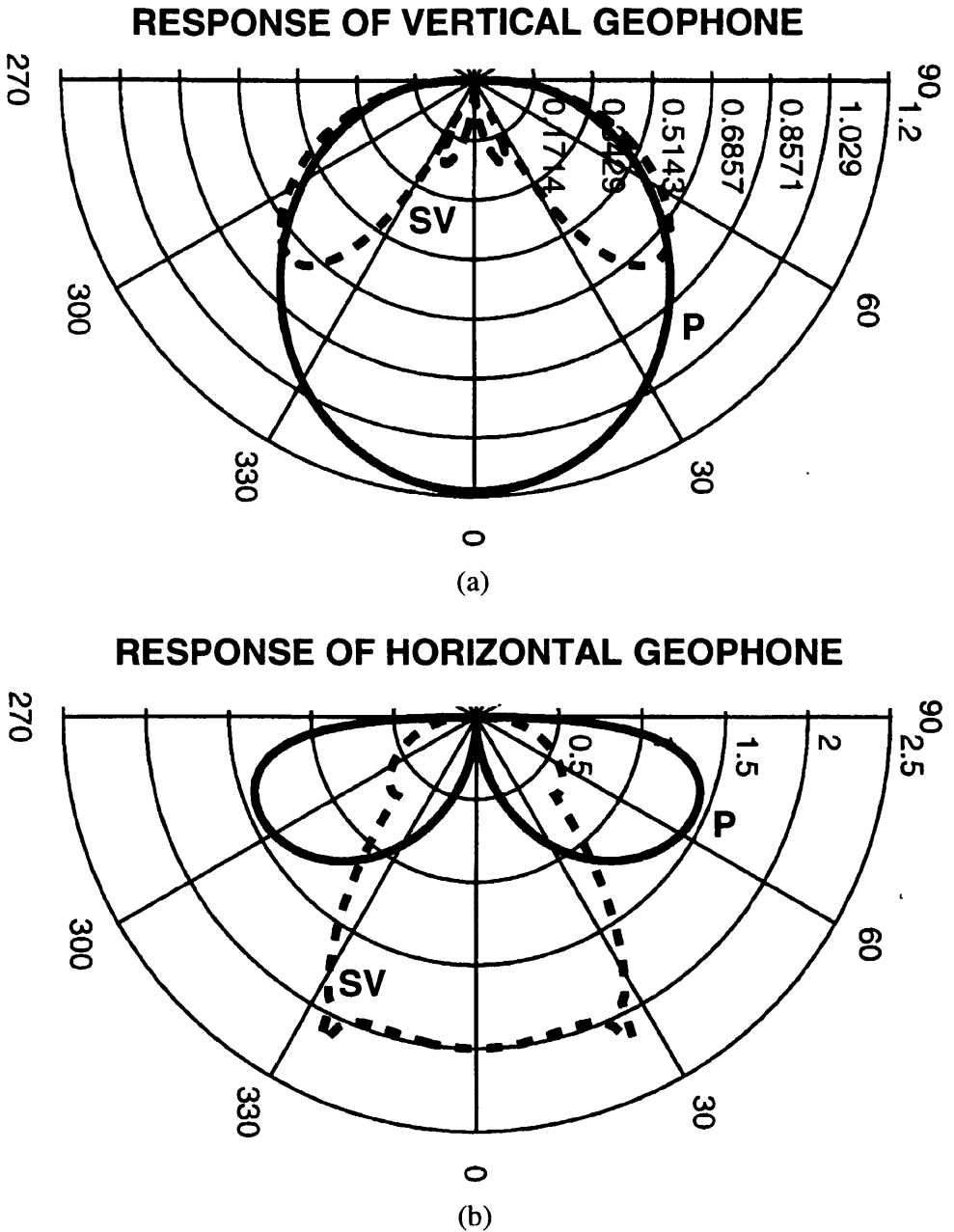


Fig. 3.2. Response, in polar diagram form, of the vertical (a) and horizontal (b) geophones, located at a liquid-solid contact, for P waves and S waves as a function of angle of incidence. Parameter values for this case are: $V_p = 1500$ m/s, $V_s = 650$ m/s, and $\rho = 1.6$ g/cc (in the solid), and $V_p = 1455$ m/s and $\rho = 1.135$ g/cc in the liquid.

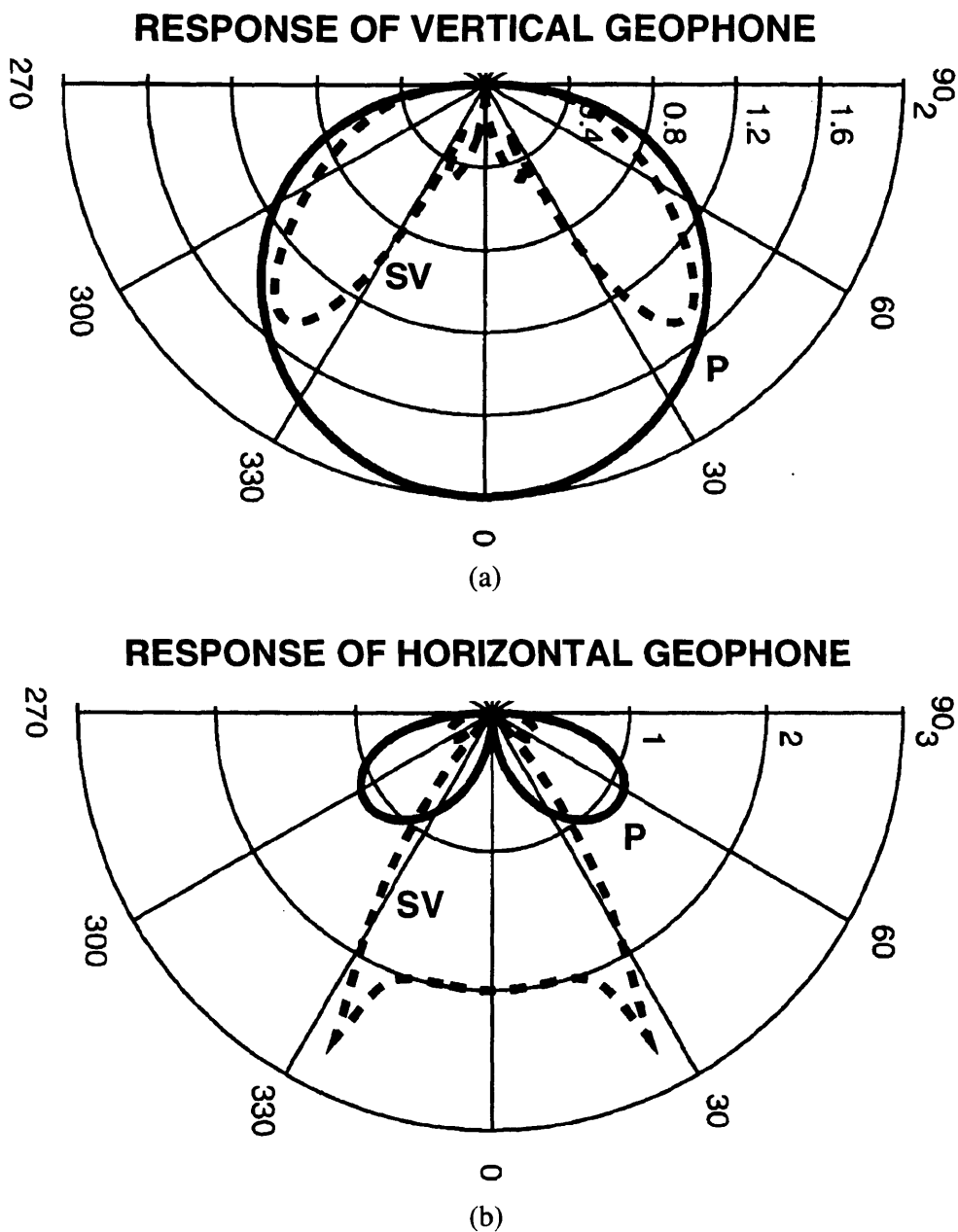


Fig. 3.3. Response, in polar diagram form, of the vertical (a) and horizontal (b) geophones located on the surface of a solid (stress-free) for P waves and S waves as a function of angle of incidence. Parameter values are: $V_p = 1500$ m/s, $V_s = 650$ m/s and $\rho = 1.6$ g/cc.

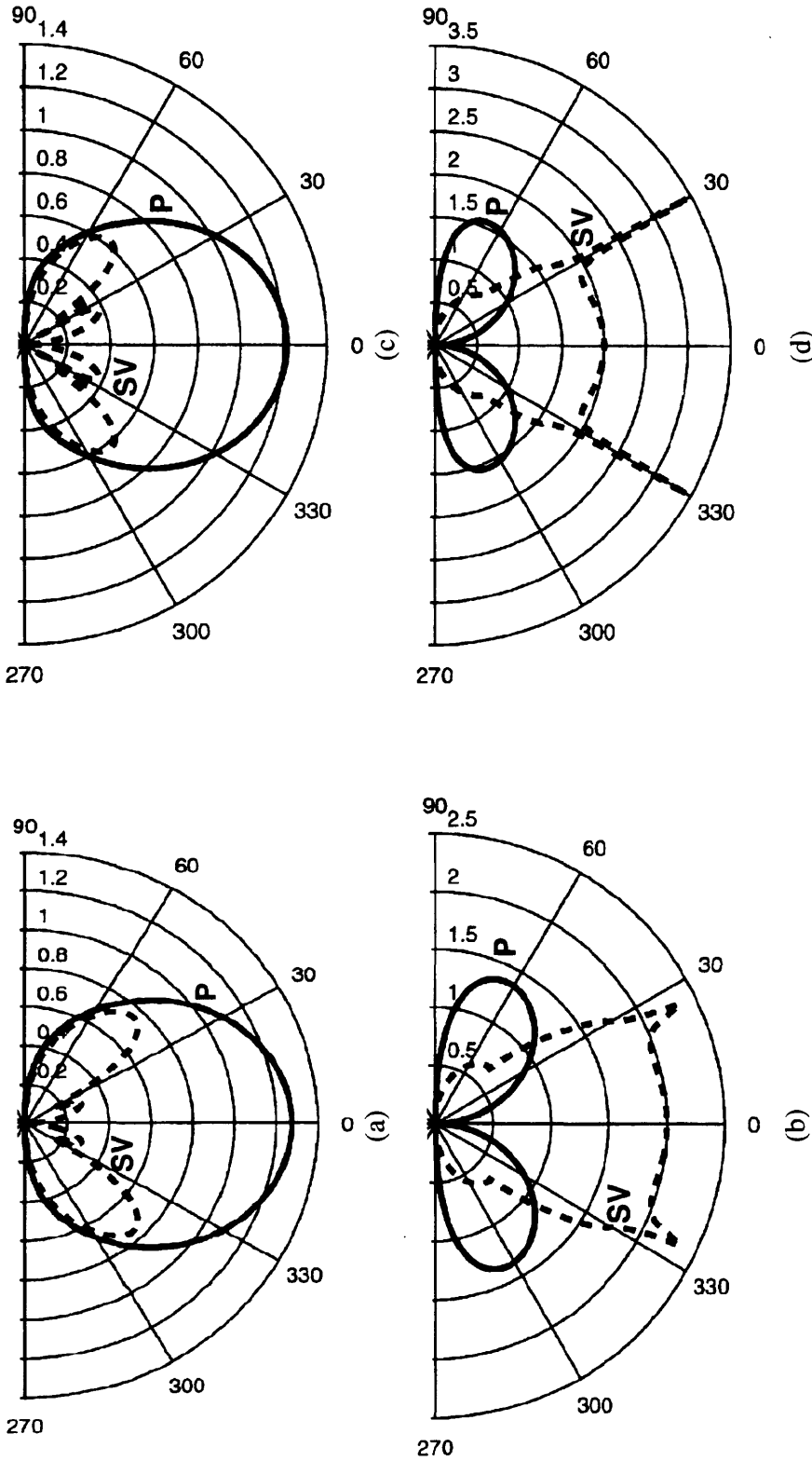


Fig. 3.4. (a,b) Response, in polar diagram form, of the vertical (a) and horizontal (b) geophones, located at a liquid-solid contact, for P and S waves as a function of the angle of incidence. Parameter values for this case are: $V_p = 1650$, $V_s = 715$ m/s and $\rho = 1.76$ g/cc (in the solid), and $V_p = 1455$ m/s and $\rho = 1.135$ g/cc (in the liquid). (c,d) Response, in polar diagram form, of the vertical (c) and horizontal (d) geophones, located at a liquid-solid contact, for P and S waves as a function of the angle of incidence. Parameter values for this case are: $V_p = 1600$, $V_s = 800$ m/s and $\rho = 1.3$ g/cc (in the solid), and $V_p = 1350$ m/s and $\rho = 1.0$ g/cc (in the liquid).

3.4 Filter coefficients

3.4.1 Raw filter coefficients

If we have records from both horizontal and vertical geophones (U_H and U_V), then we have two equations with two unknowns (the incident P and incident S waves). The equations can be solved for P and S waves:

$$P_{in}(\tau, p) = F_V^P(p)U_V(\tau, p) + F_H^P(p)U_H(\tau, p), \quad (3.7)$$

$$S_{in}(\tau, p) = F_V^S(p)U_V(\tau, p) + F_H^S(p)U_H(\tau, p), \quad (3.8)$$

The coefficients F are functions of geophone responses R and are considered as filter coefficients. The subscripts V or H indicate that the coefficients operate on vertical or horizontal geophone data, superscript P or S , respectively, indicates coefficients for the pass- P or pass- S mode. The full expressions for the F functions are given below:

$$F_V^P(p) = \frac{-R_H^S}{R_H^P R_V^S - R_V^P R_H^S} = \frac{-\gamma (m_o + (1 - 2V_s^2 p^2))}{2\xi} \quad (3.9)$$

$$F_H^P(p) = \frac{R_V^S}{R_H^P R_V^S - R_V^P R_H^S} = \gamma^2 V_p^2 p \quad (3.10)$$

$$F_V^S(p) = \frac{-R_H^P}{R_H^S R_V^P - R_V^S R_H^P} = \frac{V_s p (m_o + 2\xi\eta)}{2\xi\eta} \quad (3.11)$$

$$F_{H}^{S}(p) = \frac{R_{V}^{P}}{R_{H}^{S}R_{V}^{P} - R_{V}^{S}R_{H}^{P}} = \frac{(1 - 2V_{s}^{2}p^{2})}{2\eta} \quad (3.12)$$

$$\text{where } m_o = \rho'_{V_p} (1 - V_p^2 p^2)^{1/2} / \rho V_p (1 - V_p^2 p^2)^{1/2}$$

The geophone responses and thus the filter coefficients are only functions of p and the fluid and solid elastic parameters.

3.4.2 Instabilities

The behavior of the coefficients F_V^P , F_V^S , F_H^P , and F_H^S using $V = 1500$ m/s, $V_s = 650$ m/s and $\rho = 1.6$ g/cc for the solid, and $V = 1455$ m/s and $\rho = 1.135$ g/cc for the liquid is shown in the Fig. 3.5a. It is evident that the filter coefficients F_V^P and F_H^S can reach anomalous values in comparison with F_V^P and F_H^S . As consequence, the relations that express the pass- P and pass- S wavefield (eqs. (3.7) - (3.8)) are strongly affected altering the coupled relation between both equation. The ideal situation is indicated in Fig 3.5b where the coefficients are limited between -2 and +2 range where it is guaranteed the stability of the filter coefficients. An additional condition on slowness p values for P waves it is included to limit the behavior for F_V^P and F_H^P .

3.4.3 Tapered filter coefficients

Fig. 3.6a shows the four tapered filter coefficients as functions of slowness for the elastic parameters as in Figs. 3.2 and 3.3. The maximum slowness displayed corresponds to that of incident S waves. These results can be compared with the four filter coefficients

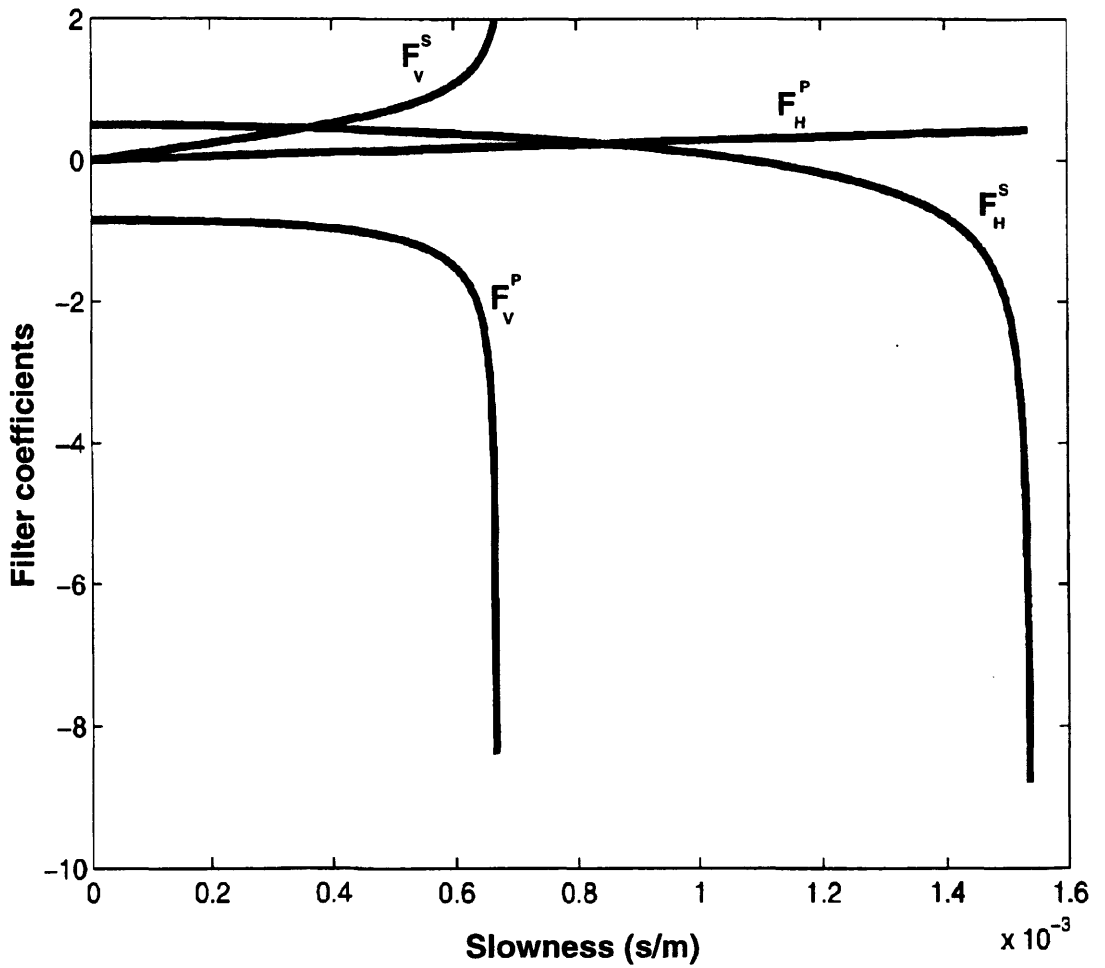


Fig. 3.5. Value of the filter coefficients F as a function of horizontal slowness for pass- P and pass- S filter considering $V_p= 1500$ m/s, $V_s= 650$ m/s and $\rho= 1.6$ m/s (in the solid), and $V_p= 1455$ m/s and $\rho= 1.135$ g/cc (in the liquid), without constrains.

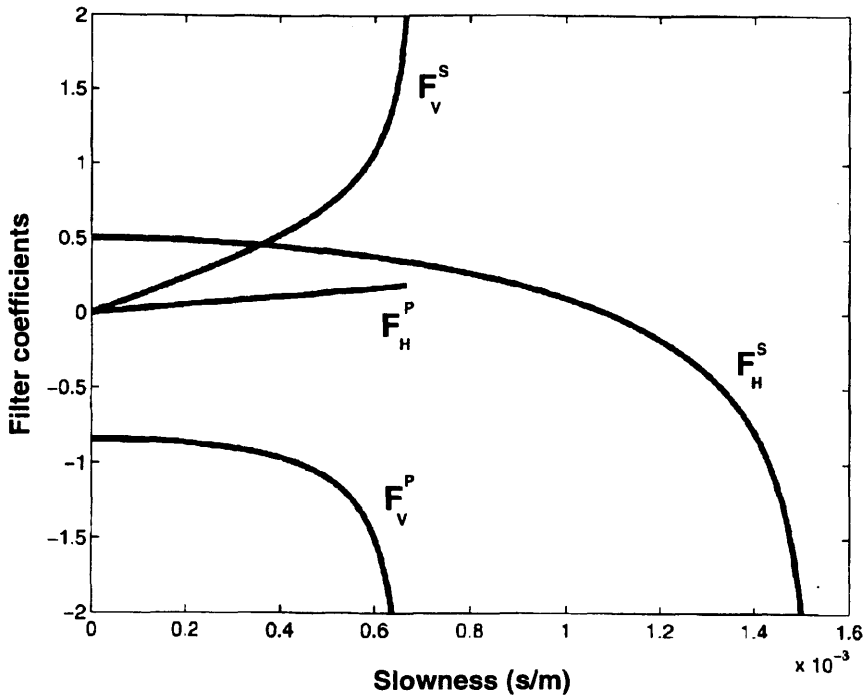


Fig. 3.6a. Filter coefficients F as a function of horizontal slowness for pass- P and pass- S filter for a geophone located at a liquid-solid contact as described in Fig. 3.2.

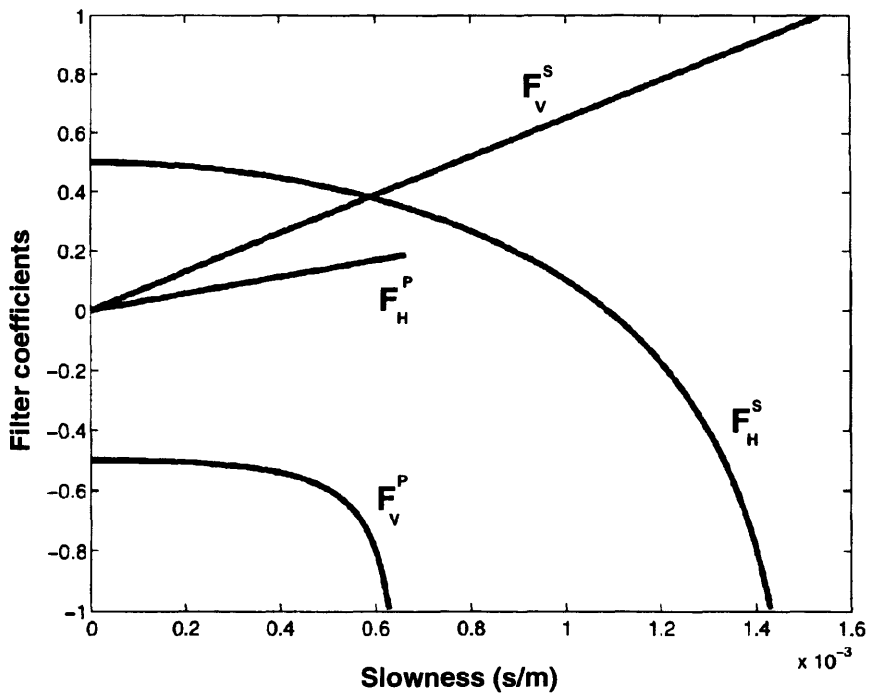


Fig. 3.6b. Filter coefficients F as a function of horizontal slowness for pass- P and pass- S filter for a geophone on the surface at a solid (stress-free case) using the model of Fig. 3.3

of the P - S separation filter related to stress-free solid (Fig. 3.6b). The filter coefficients have similar shapes except for F_V^S which shows a non-linear behavior with the horizontal slowness p due to the additional term $V_s pm_o / 2\xi\eta$, and becomes large at the maximum slowness of the incident P waves. Also, the coefficients F_V^S and F_V^P for the fluid-solid interface are affected by the variable m_o which contains information on the elastic properties of both media. In both cases, the F_H^P and F_V^P filter coefficients are limited by the maximal slowness of the incident P waves which represents horizontal incidence. The values of the filter coefficients for the liquid-solid contact have been limited to avoid instabilities in the P - S separation filter similar to what is done in the stress-free interface case (Labonte, 1990) (Fig. 3.6a,b).

Figs. 3.7(a,b) shown the behavior of the coefficients F_V^P , F_V^S , F_H^P , and F_H^S considering different values of the elastic parameters in the solid and liquid media. We can see how the shape of these coefficients change with the changes in the P -wave and S -wave velocities evidencing the dependence of the filter coefficients on the near-surface velocities.

The filter is operated in pass- P or pass- S mode. In pass- P mode, the output consists of all waves arriving at the liquid-solid contact as P waves: S wave energy is removed. In pass- S mode, the output is the incident S wavefield, with P wave energy removed. To return to the x - t domain, an inverse τ - p transform is applied.

Fig. 3.8 shows the basic steps followed by the P - S separation filter in the τ - p domain. The procedure followed for calculating the direct and inverse τ - p transformation is similar to Wade and Gardner (1988).

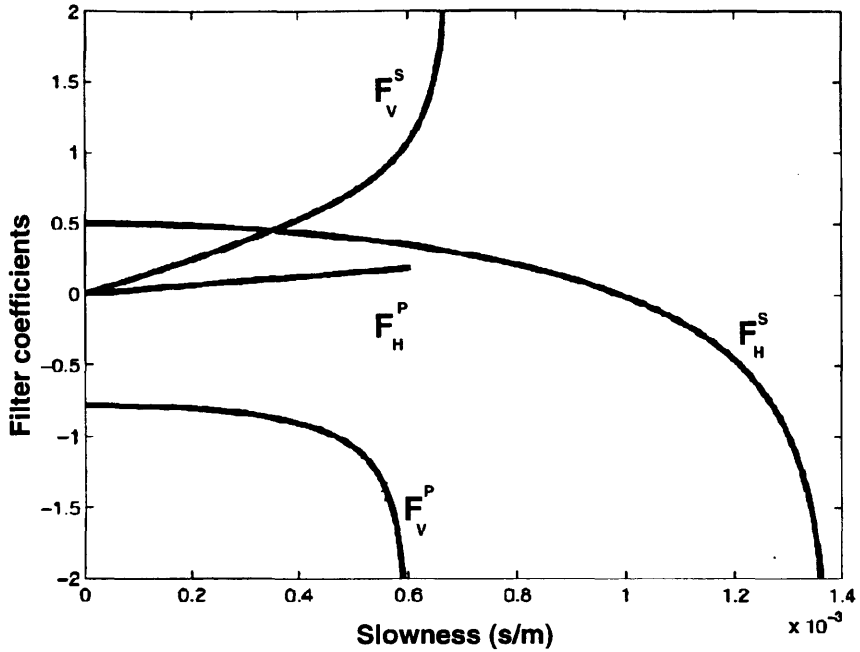


Fig. 3.7a. Value of the filter coefficients F as a function of horizontal slowness for pass- P and pass- S filter considering $V_p= 1650$ m/s, $V_s= 715$ m/s and $\rho= 1.76$ g/cc (for the solid), and $V_p= 1455$ m/s and $\rho= 1.135$ g/cc (for the liquid), with constrains.

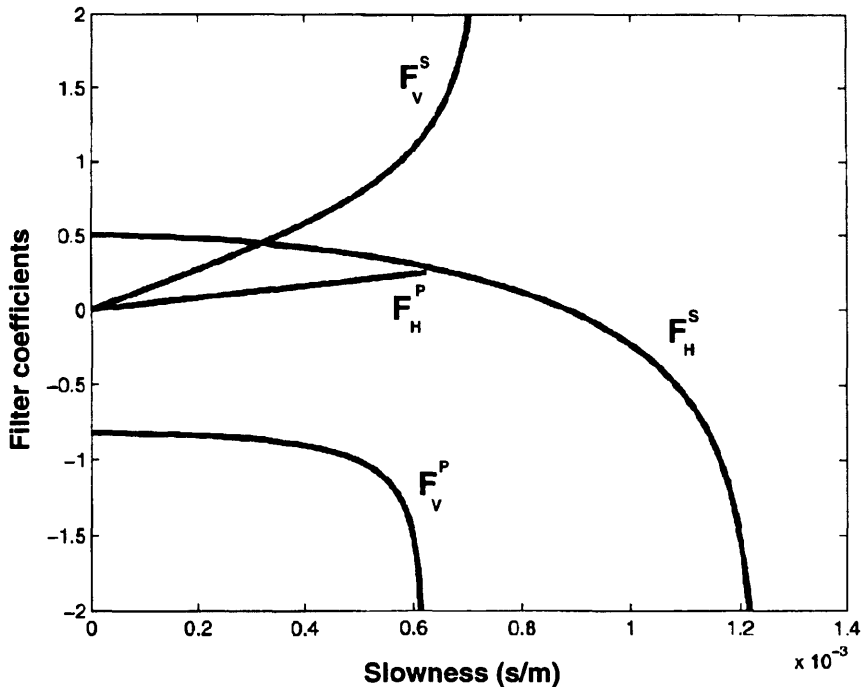


Fig. 3.7b. Value of the filter coefficients F as a function of horizontal slowness for pass- P and pass- S filter considering $V_p= 1600$ m/s, $V_s= 800$ m/s and $\rho= 1.3$ g/cc (for the solid), and $V_p= 1350$ m/s and $\rho= 1.0$ g/cc (for the liquid), with constrains.

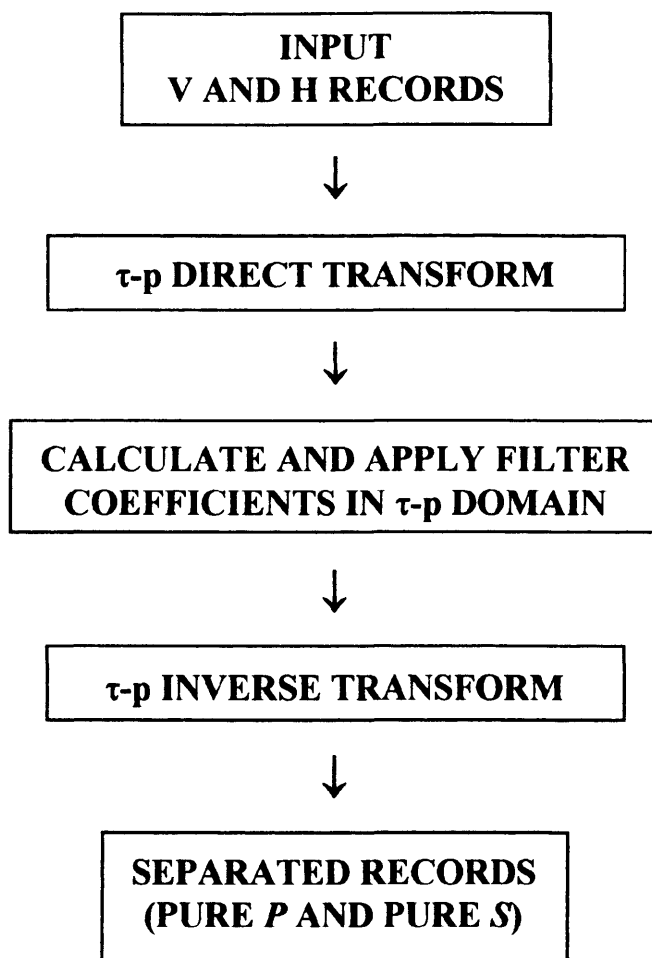


Fig. 3.8. Flowchart of the P - S separation filter in the τ - p domain.

3.5 Application of the filter in the tau-p domain

3.5.1 Synthetic application

Some examples of the filter operation on two synthetic data models follow. The first one is a horizontally layered earth model (after Dankbaar, 1985) which is shown in Fig. 3.9. There are six flat homogeneous layers on top of a half-space. The first layer consists of a water layer 10 m deep and the maximum reflector depth in this model is 210 m. Geophone offsets are from 5 - 200 m spaced 5 m (Fig. 3.9).

First, we consider the source located at the top of the water layer and the receivers on the bottom of the water layer and the top of layer 2 (solid). In this case, an explosive source (P waves only) radiated energy uniformly from 0° to 180° downward. Only P - P and P - S primary reflections are considered. Fig. 3.10a shows the P - P and P - S seismograms without geophone responses, where there are only P wave arrivals on the vertical geophone and only S wave arrivals on the horizontal geophone. The P - P and P - S seismograms were generated using a minimum phase wavelet with a center frequency of 45 Hz. Then, the P - P seismogram represents the response of the vertical geophone taking R_V^S equal zero; likewise with the P - S seismogram with R_H^P equal zero. Next, taking into account the geophone responses (Fig. 3.2) and using incident P and converted waves gives traces as shown in the Figs. 3.10b. On the horizontal geophone record all P - P and P - S reflections are evident.

The filtered pass- P and pass- S are shown in Fig. 3.10c. They can be compared with the incident seismograms (Fig. 3.10a). There is reasonable agreement between the corresponding records indicating fairly good wave-type separation.

The effect on the filter of erroneous estimates of the layer 2 velocities is shown in Fig. 3.11. The vertical and horizontal geophone records from Fig. 3.10b were filtered

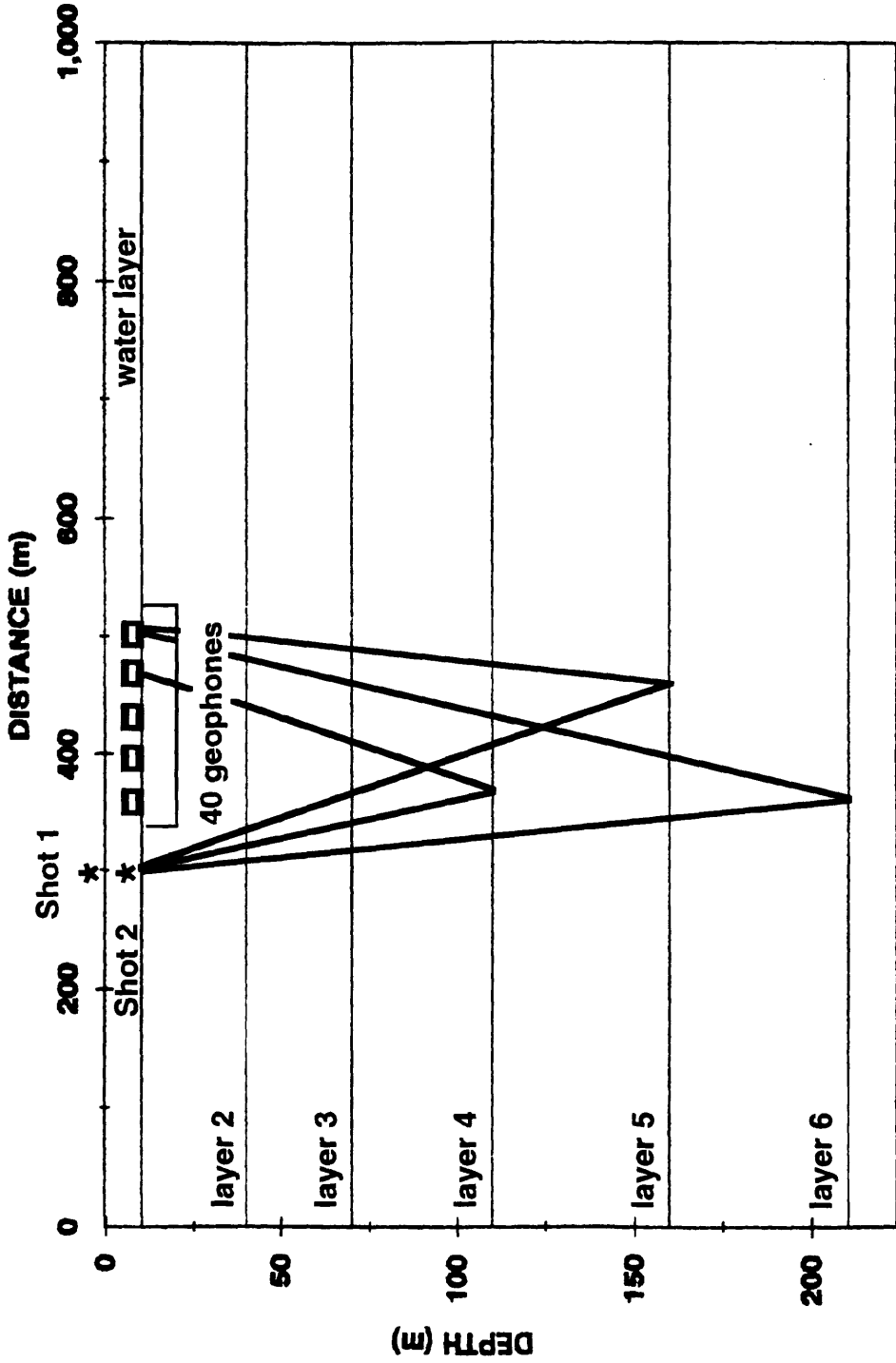


Fig. 3.9. Subsurface model used for synthetic data calculation (after Dankbaar, 1985).

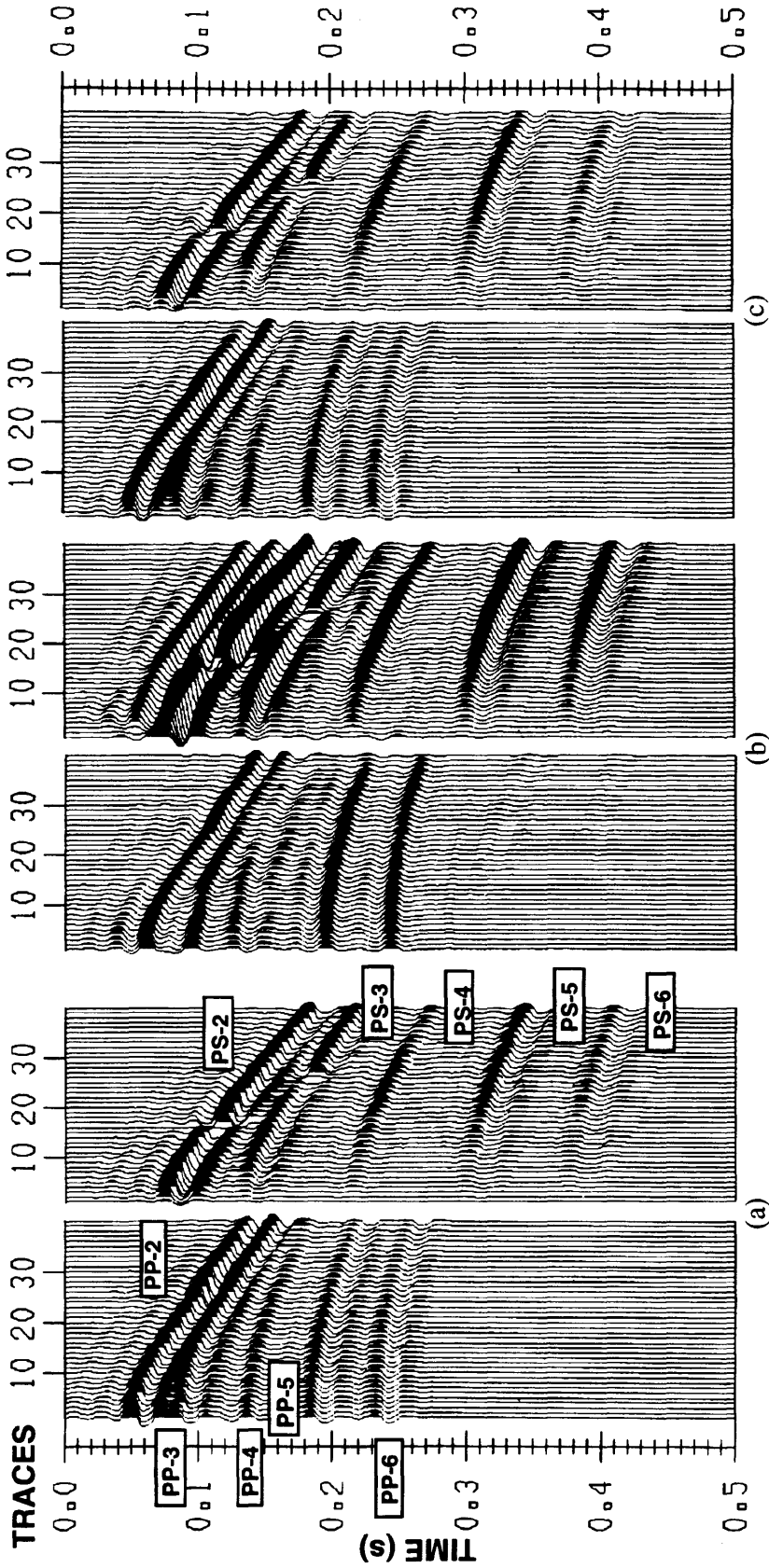


Fig. 3.10. Vertical and horizontal geophone response from the model of Fig. 3.9

(a) *P-P* and *P-S* reflections, with no receiver response.

(b) Vertical an horizontal geophone output from incident *P-P* and *P-S* reflections.

(c) Pass-*P* and pass-*S* sections obtained from both vertical and horizontal records (Fig. 3.10b) using $V_p=1500\text{m/s}$, $V_s=650\text{ m/s}$, and $\rho=1.6\text{ g/cc}$ (in the solid) and $V_p=1455\text{ m/s}$ and $\rho=1.135\text{ g/cc}$ (in the liquid).

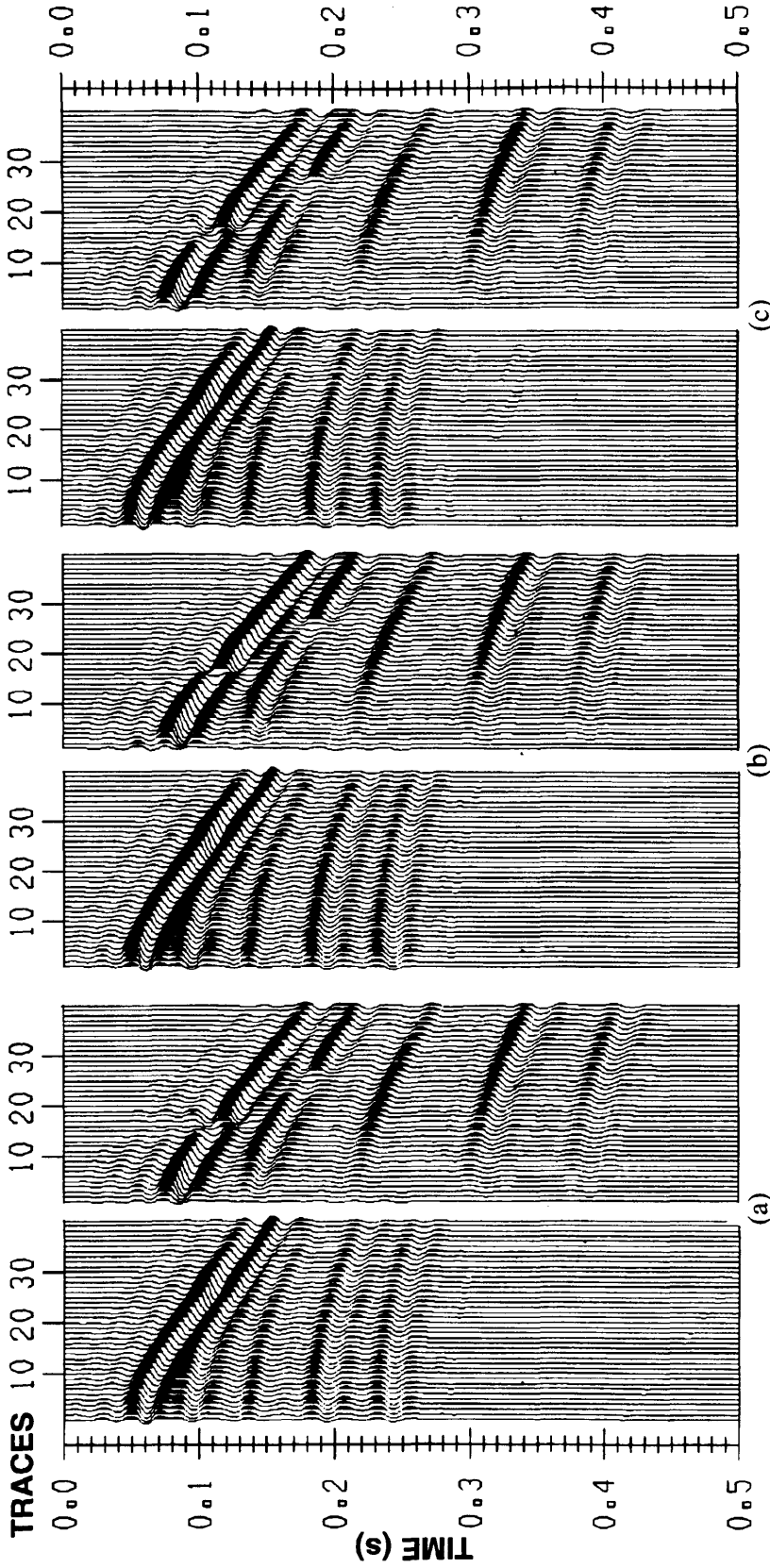


Fig. 3.11. (a) Filtered pass-P and pass-S records, respectively, obtained using $V_p=1650$ m/s, $V_s=715$ m/s, and $\rho=1.76$ g/cc (in the solid), and $V_p=1455$ m/s and $\rho=1.135$ g/cc (in the liquid).
 (b) Filtered pass-P and pass-S records, respectively, obtained using $V_p=1350$ m/s, $V_s=585$ m/s, and $\rho=1.44$ g/cc (in the solid), and $V_p=1455$ m/s and $\rho=1.135$ g/cc (in the liquid).
 (c) Filtered pass-P and pass-S records, respectively, obtained using $V_p=1600$ m/s, $V_s=800$ m/s, and $\rho=1.3$ g/cc (in the solid), and $V_p=1350$ m/s and $\rho=1.0$ g/cc (in the liquid).

using erroneous values as follows: first we use $V_p = 1650$ m/s and $V_s = 715$ m/s for layer 2 (which represent a over estimation of 10% in the velocities), and density $\rho = 1.76$ g/cc for the solid, and $V_p = 1455$ m/s and $\rho = 1.135$ g/cc for the liquid. The filtered sections are shown in Fig. 3.10a. Next, an underestimation of 10% in the velocities are used in the layer 2 velocities giving $V_p = 1350$ m/s and $V_s = 585$ m/s, and density $\rho = 1.44$ g/cc for the solid, and $V_p = 1455$ m/s and $\rho = 1.135$ g/cc for the liquid. The resultant sections are shown in Fig. 3.11b. Finally, perturbed parameters in velocity and density are used with $V_p = 1600$ m/s and $V_s = 800$ m/s and density $\rho = 1.3$ g/cc for the solid, and $V_p = 1350$ m/s and $\rho = 1.0$ g/cc for the liquid. The filtered sections are shown in Fig. 3.11c.

The results presented in Figs. 3.11a,c can be compared with the records from Fig. 3.10a. The similar results of the filter when using erroneous velocities and densities for the calculation indicate a robust operation. We see that the pass- P record is less effected by errors in the velocities than the pass- S record, where there is still some residual P - wave energy.

Real data contain noise and the filter was tested with random noise added. Fig. 3.12a shows the same P - P and P - S seismograms as in Fig. 3.10a, but now with 10% random noise added. Fig. 3.12b shows how these incident waves are observed on vertical and horizontal geophones. These records were again filtered pass- P and pass- S . The result is shown in Fig. 3.12c and can be compared with the incident wave records from Fig. 3.10a. Apparently, the filter is not affected by noise in the data. The noise has even decreased at larger offset.

The effect on the filter of erroneous estimates of the layer 2 velocities was tested on the vertical and horizontal records shown in Fig. 3.12b. Figs. 3.13(a,c) display the

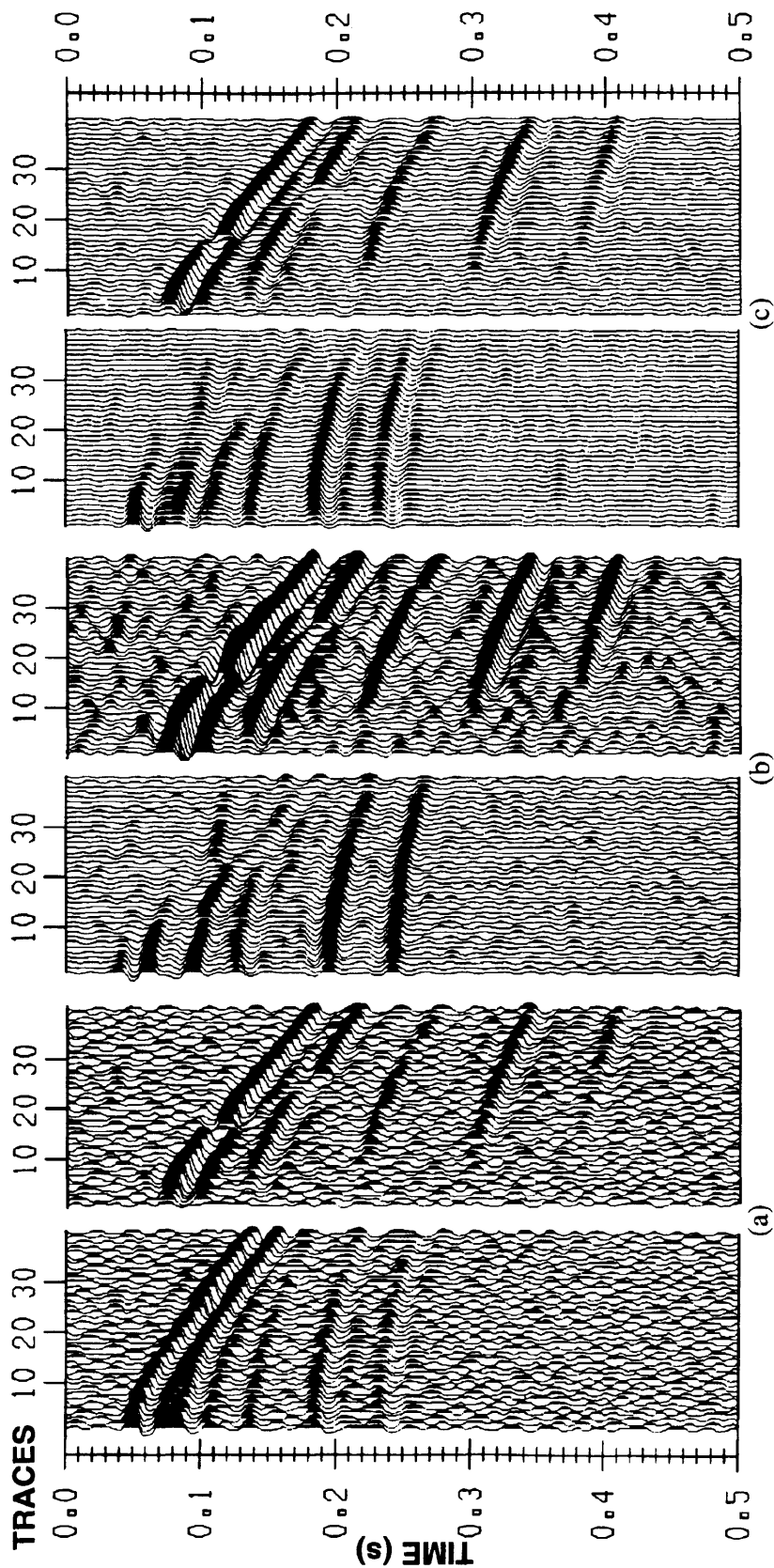


Fig. 3.12. Vertical and horizontal geophone response from the model of Fig. 3.9

(a) *P-P* and *P-S* reflections with 10 % of random noise added, no receiver response considered.

(b) Vertical an horizontal geophone output from incident *P-P* and *P-S* reflections.

(c) Pass-*P* and pass-*S* sections obtained from both vertical and horizontal records (Fig. 3.12b) using $V_p = 1500$ m/s, $V_s = 650$ m/s, and $\rho = 1.6$ g/cc (in the solid) and $V_p = 1455$ m/s and $\rho = 1.135$ g/cc (in the liquid).

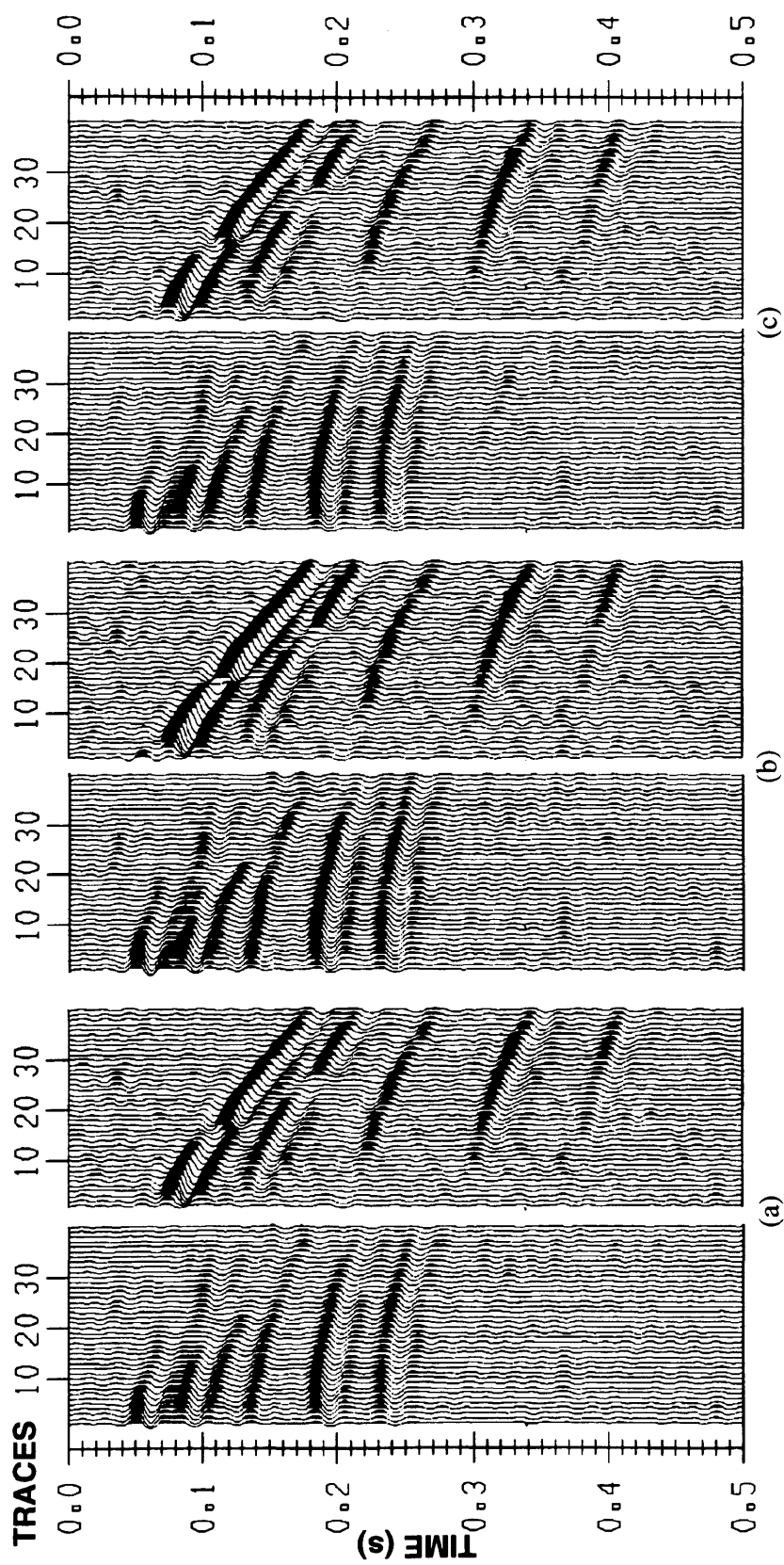


Fig. 3.13. (a) Filtered pass-P and pass-S records, respectively, obtained using $V_p=1650$ m/s, $V_s=715$ m/s, and $\rho=1.76$ g/cc (in the solid), and $V_p=1455$ m/s and $\rho=1.135$ g/cc (in the liquid).
 (b) Filtered pass-P and pass-S records, respectively, obtained using $V_p=1350$ m/s, $V_s=585$ m/s, and $\rho=1.44$ g/cc (in the solid), and $V_p=1455$ m/s and $\rho=1.135$ g/cc (in the liquid).
 (c) Filtered pass-P and pass-S records, respectively, obtained using $V_p=1600$ m/s, $V_s=800$ m/s, and $\rho=1.3$ g/cc (in the solid), and $V_p=1350$ m/s and $\rho=1.0$ g/cc (in the liquid).

filtering effects when erroneous velocities V_p and V_s are used. Once again, the filter is robust with respect to errors in the velocity estimates.

In the second case, we consider both the source and the receivers located on the liquid-solid contact. First, only P - P and S - S reflections were calculated, where both P and S waves were radiated by the source. Fig. 3.14a shows the incident P and S waves at the liquid-solid contact with no geophone responses. The incident S waves have zero points at certain offsets, followed by a nearly 180° phase shift for larger offsets. The vertical and horizontal geophone records are shown in the Fig. 3.14b. All P and S arrivals appear on both records. The shallow SS -3 reflection interferes with the PP -4 and PP -5 reflections and P reflections complicate the horizontal response.

The result of the separation filter applied on both vertical and horizontal records is shown in the Fig. 3.14c. The filter used near-surface velocities $V_p = 1500$ m/s and $V_s = 650$ m/s, and density $\rho = 1.6$ g/cc for the solid and velocity $V_p = 1455$ m/s and density $\rho = 1.135$ g/cc for the liquid, as corresponds to the velocities for the liquid and first solid layer in the synthetic model.

The comparison of the filtered pass- P and pass- S records with the incident seismograms shows a reasonable performance. Most of the S -wave energy is removed from the pass- P section. However, there is some P wave leakage onto the pass- S section. This is largely due to errors of the τ - p transform and some instabilities in the filter coefficients. Some noise is present on both pass- P and pass- S records as consequence of the limitations during the summation process in the τ - p domain.

The same experiment performed in Figs. 3.11a,c (with erroneous layer 2 values) is now applied on the horizontal and vertical geophone records shown in Fig. 3.14b. Figs.

3.15a,c display the filtering effects when erroneous velocities V_P and V_S are used. Once again, the filter is robust with respect to errors in the velocity estimates.

Fig. 3.16a shows the result of adding 10% of random noise to the incident waves shown in Fig. 3.14a. The vertical and horizontal records generated using incident waves shown in Fig. 3.16a and eqs. (3.1) and (3.2) are shown in Fig. 3.16b. These records were filtered and the results are shown in Fig. 3.16c. The same experiment performed in Figs. 3.13a,c (with erroneous elastic parameters values for layer 2) is now applied on the horizontal and vertical geophone records shown in Fig. 3.16c, and the results are shown in Figs. 3.17(a,c). From these results it is evident some leakage of P wave data in the pass- S output, however the filter shows to be robust in the presence of both noise and errors in the elastic parameters at the near-surface.

The last example presents a more complex situation in separating P and S waves. Again both source and receivers are located at the bottom of the water layer, but converted P - S and S - P reflections are included. Fig. 3.18a shows the incident P - P and S - P and incident S - S and P - S waves. The S - P converted reflections have quite low amplitudes in comparison with the converted P - S waves. Fig. 3.18b shows the vertical and horizontal geophone records resulting from the incident P and S waves. The resultant pass- P and pass- S (Fig. 3.18c) can be compared with the incident seismograms (Fig. 3.18a). There is good agreement between the corresponding records. The incident P and S waves are retrieved correctly, although SS -3 and SS -4 have slightly lower amplitudes after the filtering process.

Figs. 3.19a,c shows the results of testing the stability of the filter against errors in the P and S velocity. These results can be compared with the incident P and S waves in Fig. 3.18a. We see that the separation of P and S waves is still successful. The PP -3 reflection is somewhat larger than when filtering with the correct velocity specified.

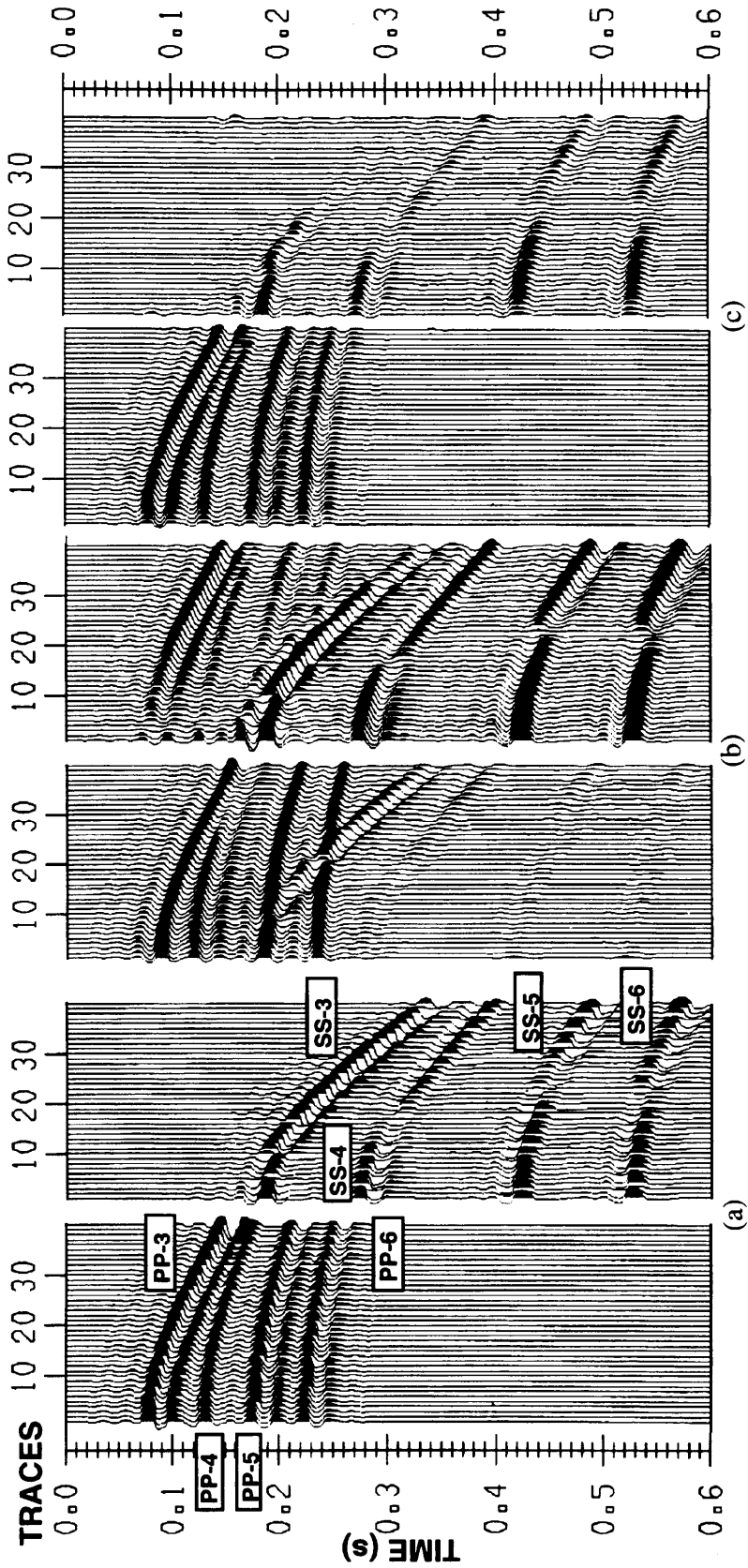


Fig. 3.14. Vertical and horizontal geophone response with source and receivers on the fluid-solid interface from the model of Fig. 3.9

(a) *P-P* and *S-S* reflections, with no receiver response.

(b) Vertical an horizontal geophone output from incident *P-P* and *S-S* reflections.

(c) Pass-*P* and pass-*S* sections obtained from both vertical and horizontal records (Fig. 3.14b) using $V_p = 1500 \text{ m/s}$, $V_s = 650 \text{ m/s}$, and $\rho = 1.6 \text{ g/cc}$ (in the solid) and $V_p = 1455 \text{ m/s}$ and $\rho = 1.135 \text{ g/cc}$ (in the liquid).

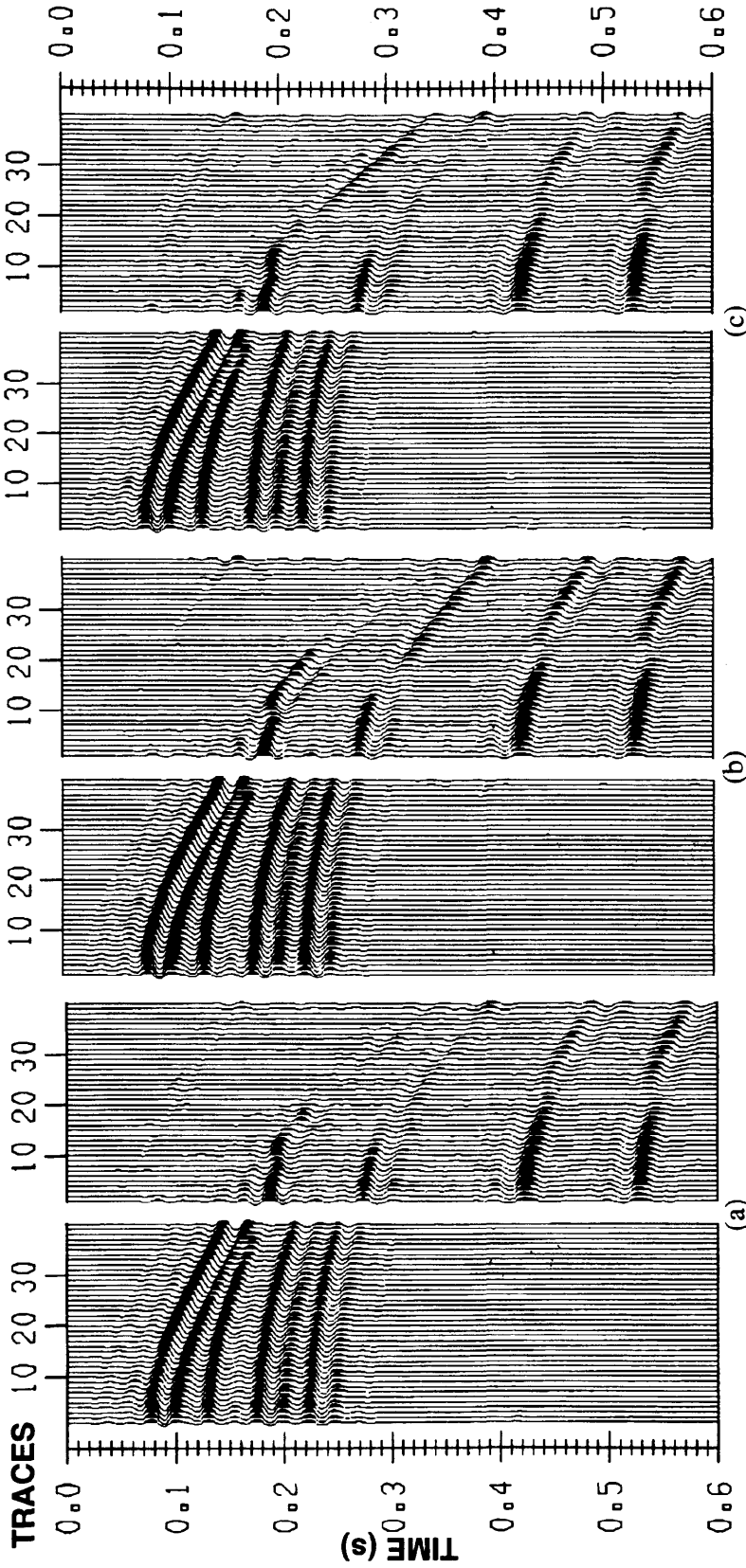


Fig. 3.15. (a) Filtered pass- P and pass- S records, respectively, obtained using $V_p=1650$ m/s, $V_s=715$ m/s, and $\rho=1.76$ g/cc (in the solid), and $V_p=1455$ m/s and $\rho=1.135$ g/cc (in the liquid).
 (b) Filtered pass- P and pass- S records, respectively, obtained using $V_p=1350$ m/s, $V_s=585$ m/s, and $\rho=1.44$ g/cc (in the solid), and $V_p=1455$ m/s and $\rho=1.135$ g/cc (in the liquid).
 (c) Filtered pass- P and pass- S records, respectively, obtained using $V_p=1600$ m/s, $V_s=800$ m/s, and $\rho=1.3$ g/cc (in the solid), and $V_p=1350$ m/s and $\rho=1.0$ g/cc (in the liquid).

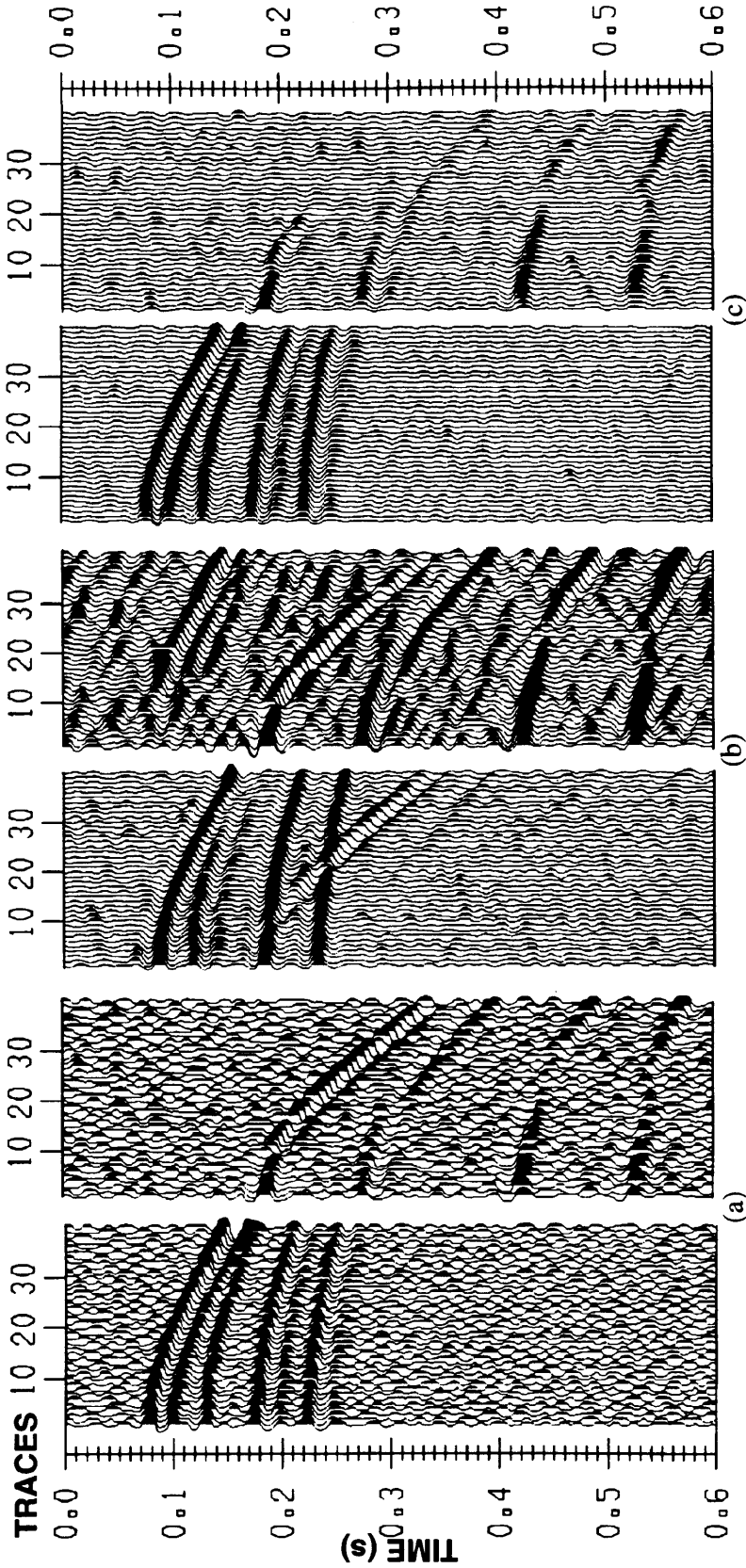


Fig. 3.16. Vertical and horizontal geophone response with source and receivers on the fluid-solid interface from the model of Fig. 3.9

(a) P - P and S - S reflections with 10% of random noise added, no receiver response considered.

(b) Vertical an horizontal geophone output from incident P - P and S - S reflections.

(c) Pass- P and pass- S sections obtained from both vertical and horizontal records (Fig. 3.16b) using $V_p = 1500$ m/s, $V_s = 650$ m/s, and $\rho = 1.6$ g/cc (in the solid) and $V_p = 1455$ m/s and $\rho = 1.135$ g/cc (in the liquid).

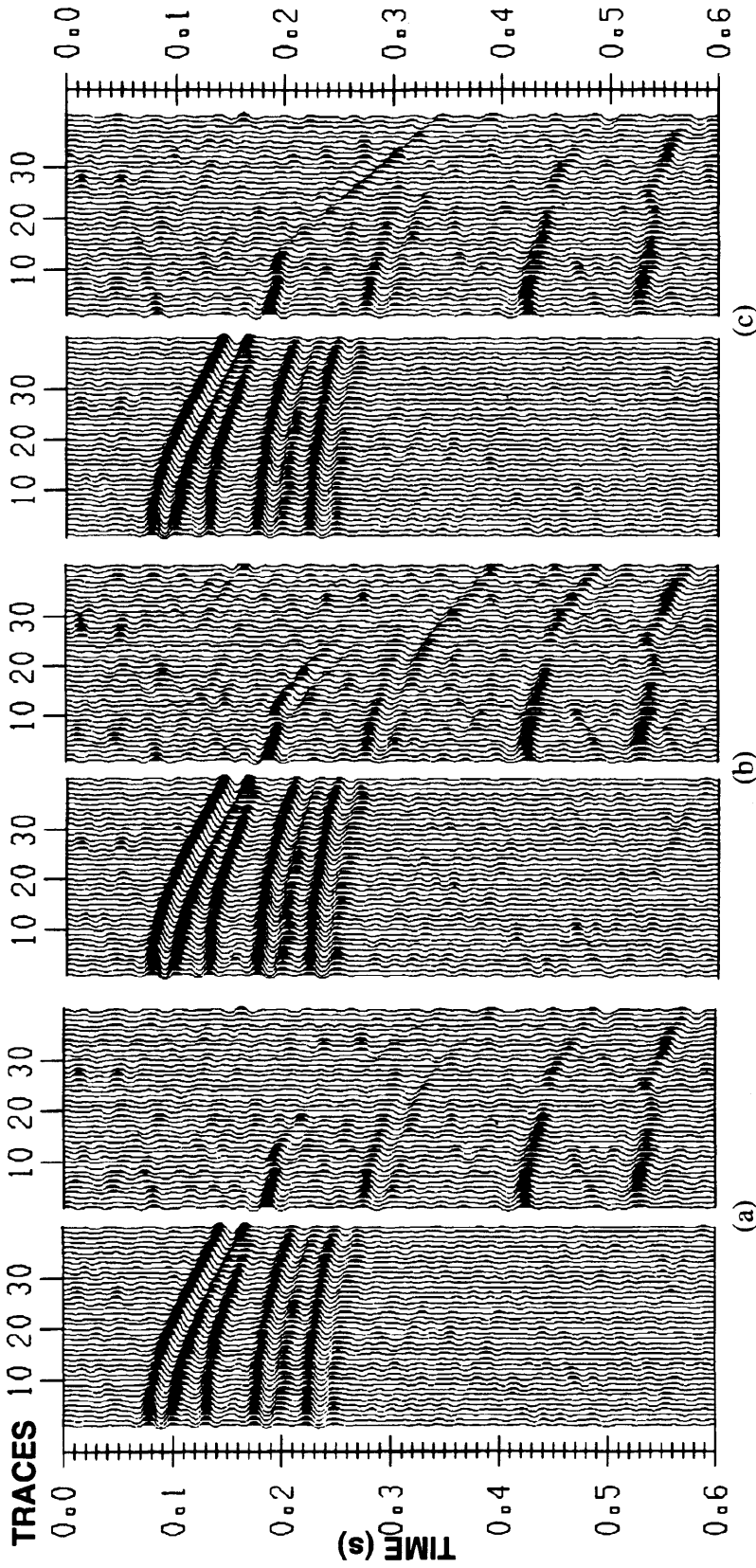


Fig. 3.17. (a) Filtered pass- P and pass- S records, respectively, obtained using $V_p=1650$ m/s, $V_s=715$ m/s, and $\rho=1.76$ g/cc (in the solid), and $V_p=1455$ m/s and $\rho=1.135$ g/cc (in the liquid).
 (b) Filtered pass- P and pass- S records, respectively, obtained using $V_p=1350$ m/s, $V_s=585$ m/s, and $\rho=1.44$ g/cc (in the solid), and $V_p=1455$ m/s and $\rho=1.135$ g/cc (in the liquid).
 (c) Filtered pass- P and pass- S records, respectively, obtained using $V_p=1600$ m/s, $V_s=800$ m/s, and $\rho=1.3$ g/cc (in the solid), and $V_p=1350$ m/s and $\rho=1.0$ g/cc (in the liquid).

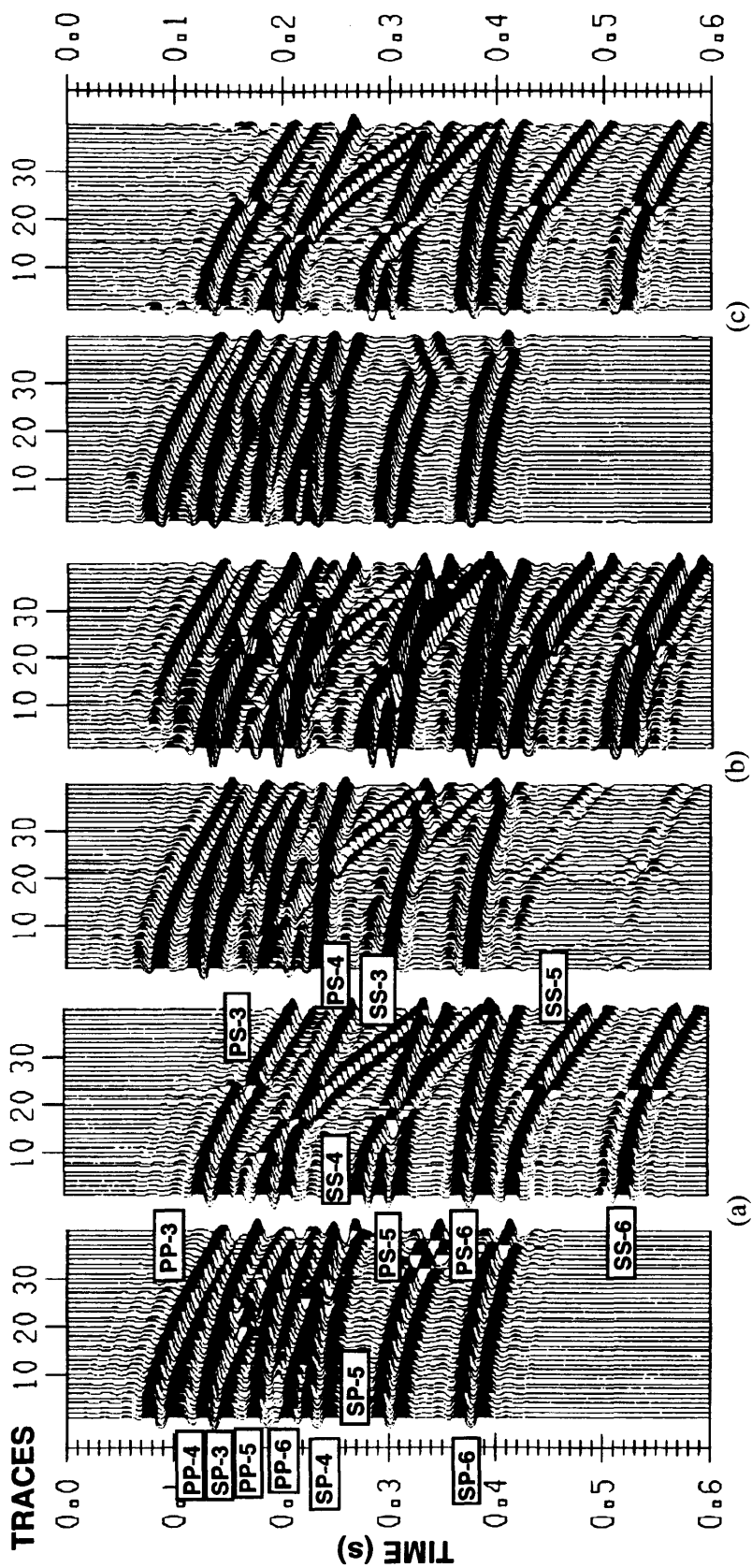


Fig. 3.18. Vertical and horizontal geophone response with source and receivers on the fluid-solid interface from the model of Fig. 3.9

(a) P - P , S - P , S - S , and P - S reflections, with no receiver response.

(b) Vertical an horizontal geophone output from incident P - P , S - S , P - S , and S - P reflections.

(c) Pass- P and pass- S sections obtained from both vertical and horizontal records (Fig. 3.18b) using $V_p = 1500$ m/s, $V_s = 650$ m/s, and $\rho = 1.6$ g/cc (in the solid) and $V_p = 1455$ m/s and $\rho = 1.135$ g/cc (in the liquid).

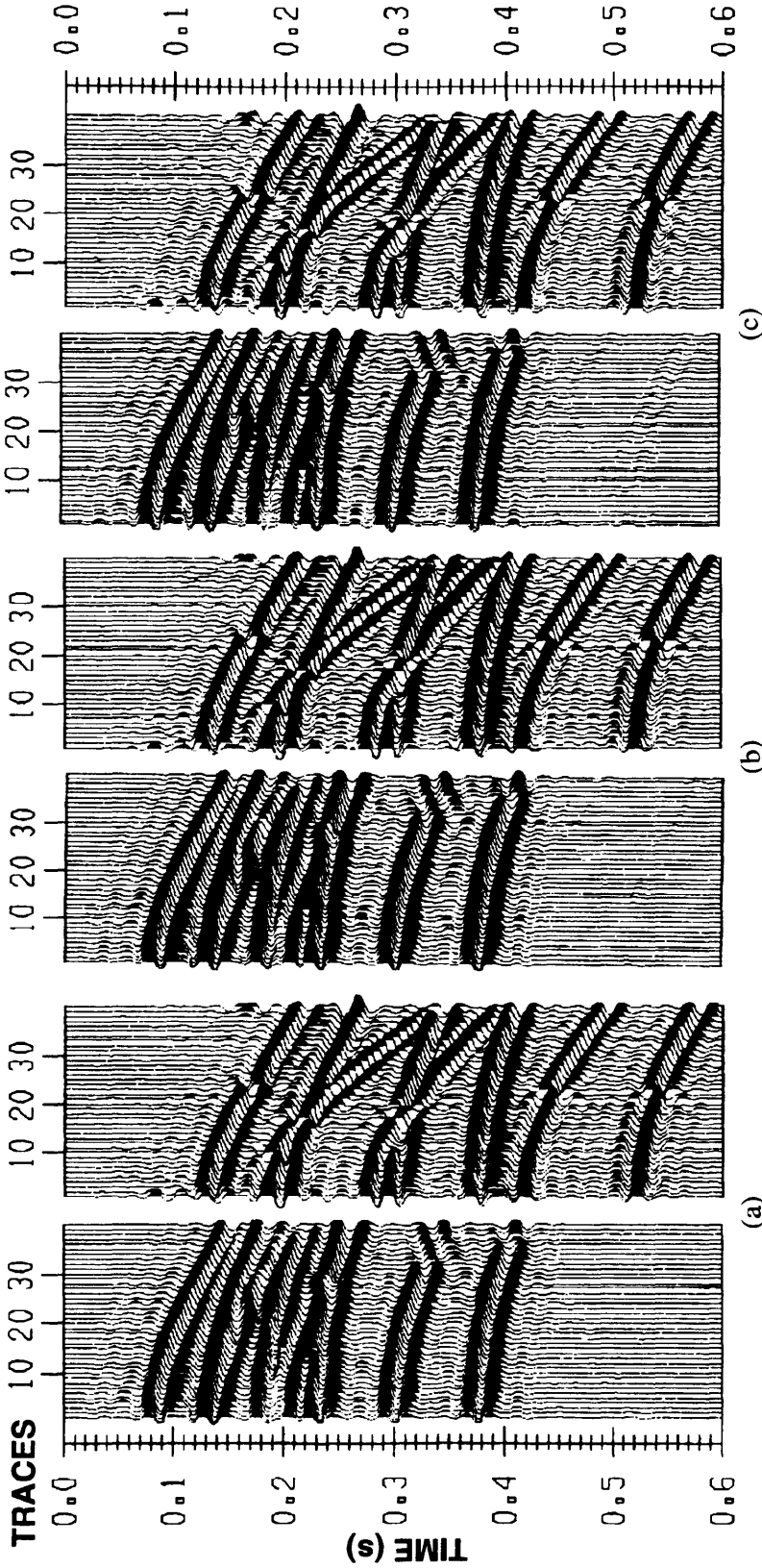


Fig. 3.19. (a) Filtered pass-*P* and pass-*S* records, respectively, obtained using $V_p=1650$ m/s, $V_s=715$ m/s, and $\rho=1.76$ g/cc (in the solid), and $V_p=1455$ m/s and $\rho=1.135$ g/cc (in the liquid).

(b) Filtered pass-*P* and pass-*S* records, respectively, obtained using $V_p=1350$ m/s, $V_s=585$ m/s, and $\rho=1.44$ g/cc (in the solid), and $V_p=1455$ m/s and $\rho=1.135$ g/cc (in the liquid).

(c) Filtered pass-*P* and pass-*S* records, respectively, obtained using $V_p=1600$ m/s, $V_s=800$ m/s, and $\rho=1.3$ g/cc (in the solid), and $V_p=1350$ m/s and $\rho=1.0$ g/cc (in the liquid).

Adding 10% of random noise to the $P(PP$ and $SP)$ and $S(SS$ and $PS)$ seismograms shown in Figs. 3.18a were generated the seismograms shown in Fig. 3.20a. The correspondent vertical and horizontal records are shown in Fig. 3.20b where it is evident the superposition of the noisy P and S waves. The pass- P and pass- S outputs considering the correct and the wrong elastic parameters in the near-surface are shown in the Figs. 3.20c and 3.21(a,c), respectively. Again the separation filter provides good results.

The second model used contains a relatively thin lens. This model has six layers where the first consists of a water layer 30 m deep; all layers are laterally homogeneous except for a thin lens - like unit near the center (Fig. 3.22). A 3C-2D data set was acquired. The survey consists in 25 shots extended from 500 to 5500 m on the model, separated 200 each other and located in the top of the water. For each shot we have 80 geophones, spaces every 25 m, located in the bottom of the water layer. A sketch of the survey is shown in the Fig. 3.22.

We modeled only $P-P$ and $P-S$ reflections using SIERRA modeling package. The stacked sections of both incident waves are shown in Fig. 3.23(a,b). The processing sequence applied for both $P-P$ and $P-S$ 25 shots gathers consists basically in geometry application, spherical divergence correction, CDP or CCP gathering, velocity analysis and stack. In both sections we can see a good definition of the thin-lens.

Next, taking into account the geophone responses and using incident P and converted waves gives the vertical and horizontal stacked sections shown in Fig. 3.24(a,b) where it is evident the presence and superposition of both incident $P-P$ and $P-S$ waves.

The stacked filtered pass- P and pass- S are shown in Fig. 3.25(a,b). They can be compared with the incident seismograms (Fig. 3.23(a,b)). There is reasonable agreement between the corresponding records indicating fairly good wave-type separation.

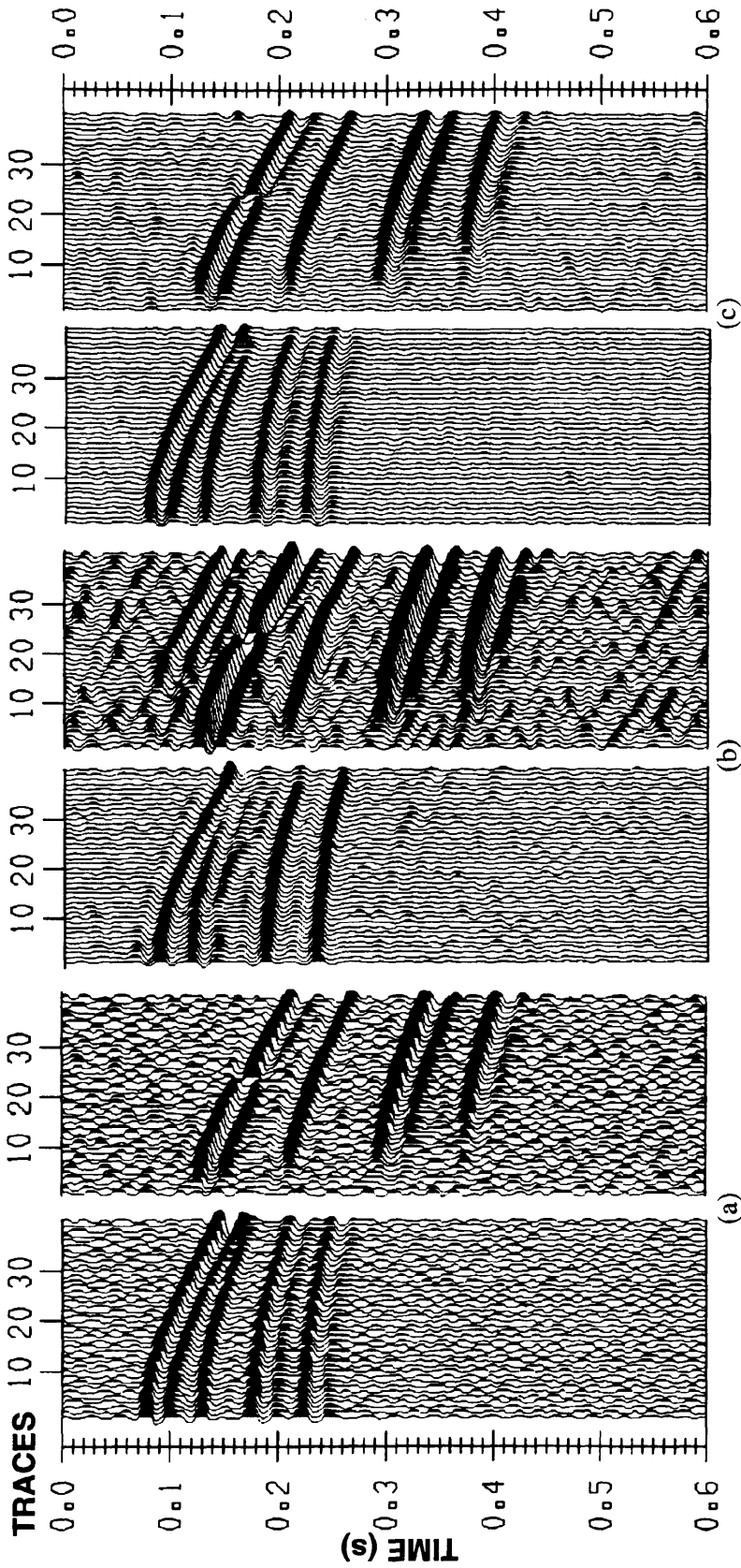


Fig. 3.20. Vertical and horizontal geophone response with source and receivers on the fluid-solid interface from the model of Fig. 3.9

(a) P - P , S - P , S - S , and P - S reflections with 10% of random noise added, no receiver response considered.

(b) Vertical an horizontal geophone output from incident P - P , S - S , P - S , and S - P reflections.

(c) Pass- P and pass- S sections obtained from both vertical and horizontal records (Fig. 3.20b) using $V_p = 1500$ m/s, $V_s = 650$ m/s, and $\rho = 1.6$ g/cc (in the solid) and $V_p = 1455$ m/s and $\rho = 1.135$ g/cc (in the liquid).

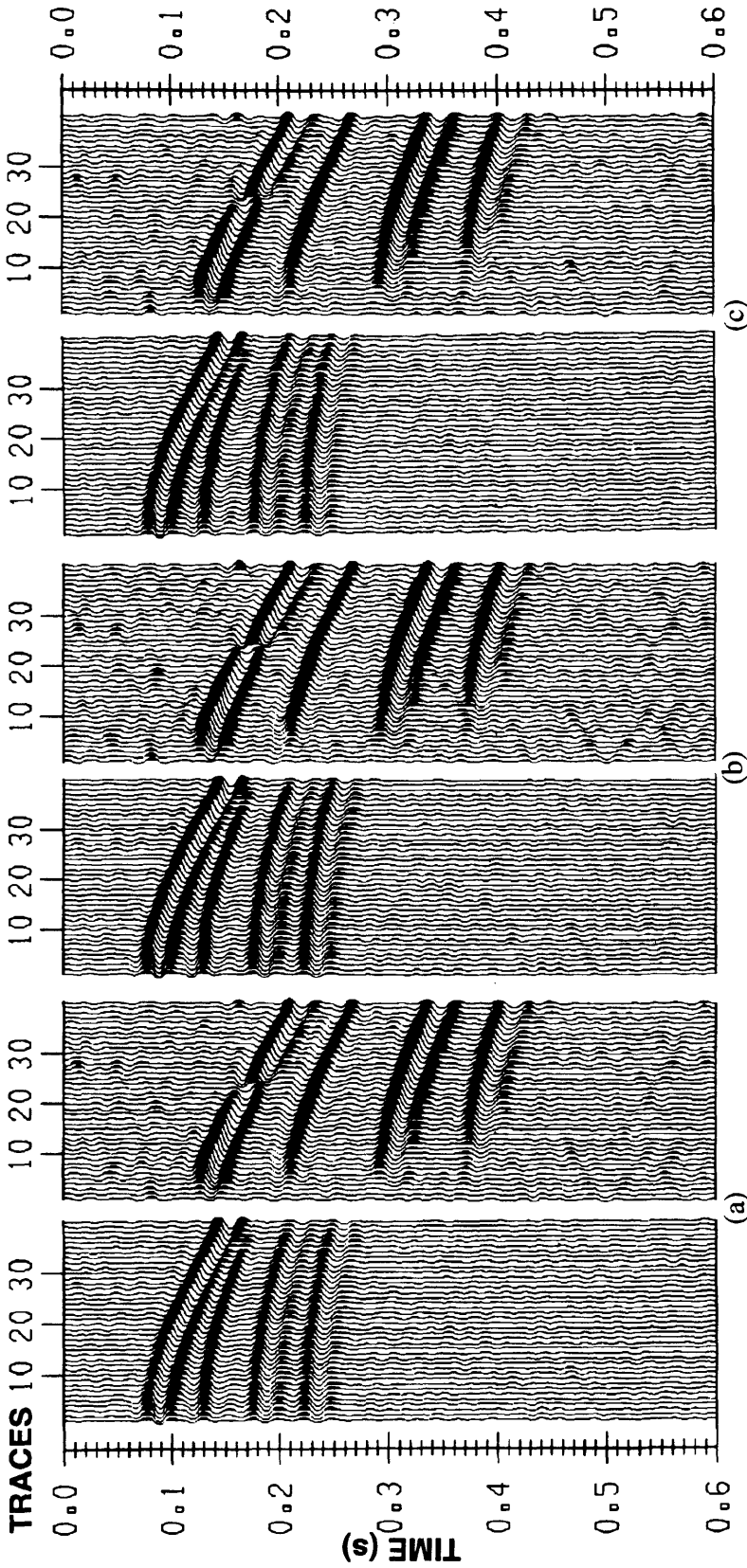


Fig. 3.21. (a) Filtered pass- P and pass- S records, respectively, obtained using $V_p=1650$ m/s, $V_s=715$ m/s, and $\rho=1.76$ g/cc (in the solid), and $V_p=1455$ m/s and $\rho=1.135$ g/cc (in the liquid).
 (b) Filtered pass- P and pass- S records, respectively, obtained using $V_p=1350$ m/s, $V_s=585$ m/s, and $\rho=1.44$ g/cc (in the solid), and $V_p=1455$ m/s and $\rho=1.135$ g/cc (in the liquid).
 (c) Filtered pass- P and pass- S records, respectively, obtained using $V_p=1600$ m/s, $V_s=800$ m/s, and $\rho=1.3$ g/cc (in the solid), and $V_p=1350$ m/s and $\rho=1.0$ g/cc (in the liquid).

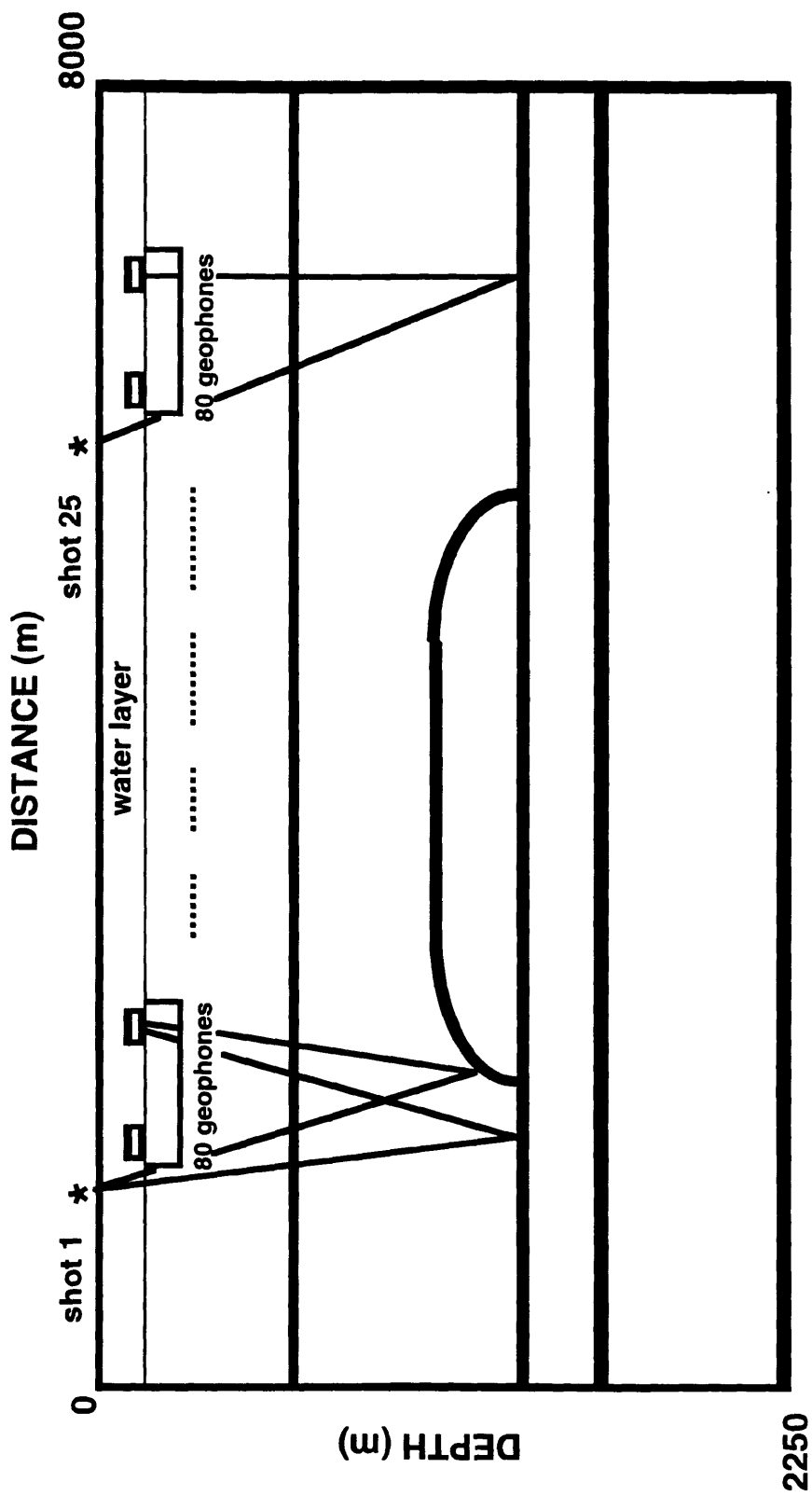


Fig. 3.22. Depth model with a thin-lens used for synthetic data calculation (after McCormack and Tatham, 1989).

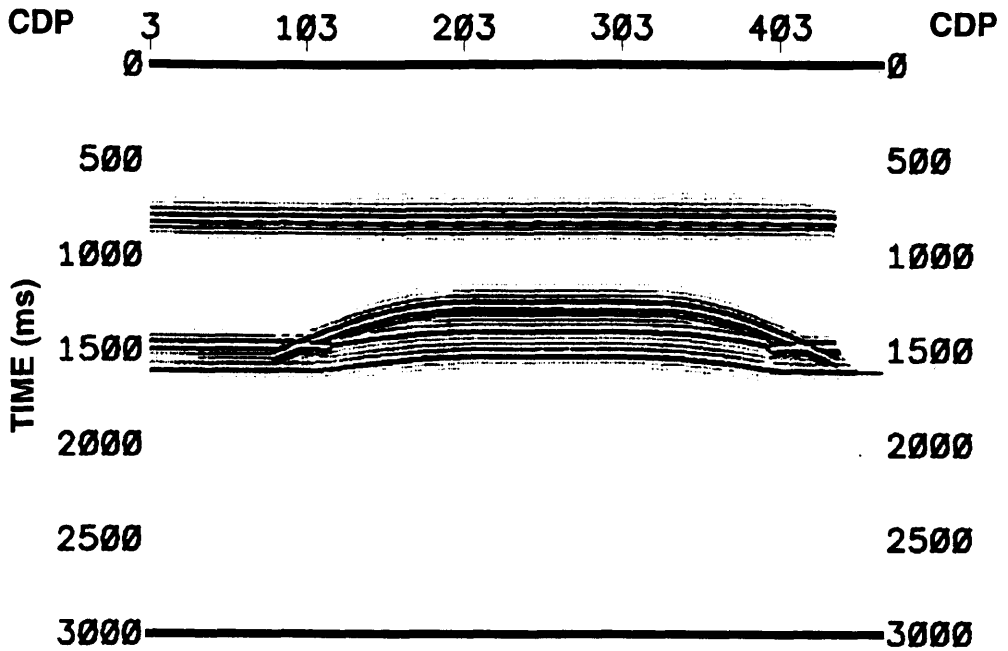


Fig. 3.23a Stacked section of the *P-P* reflections, with no receiver response.

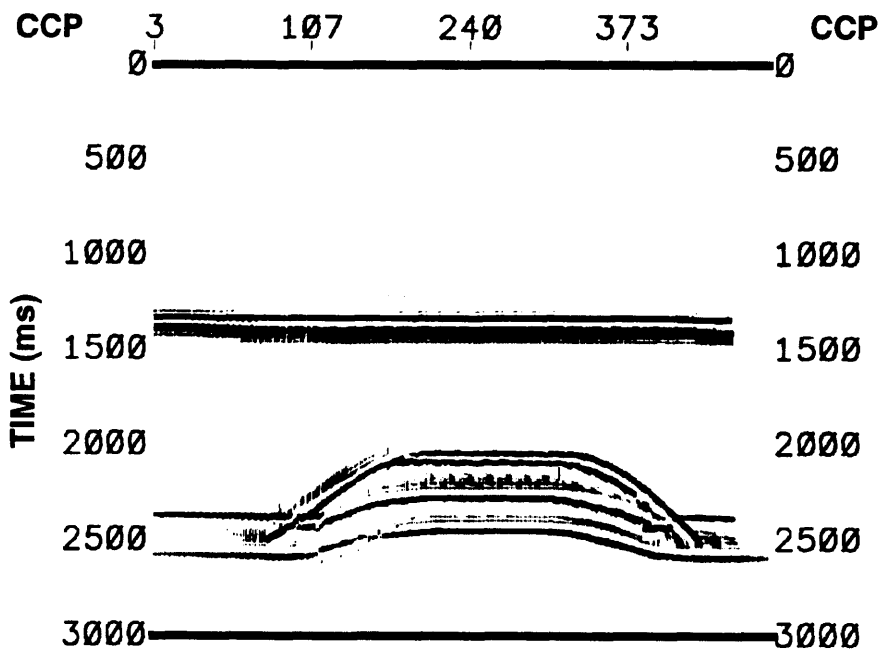


Fig. 3.23b. Stacked section of the *P-SV* reflections, with no receiver response.

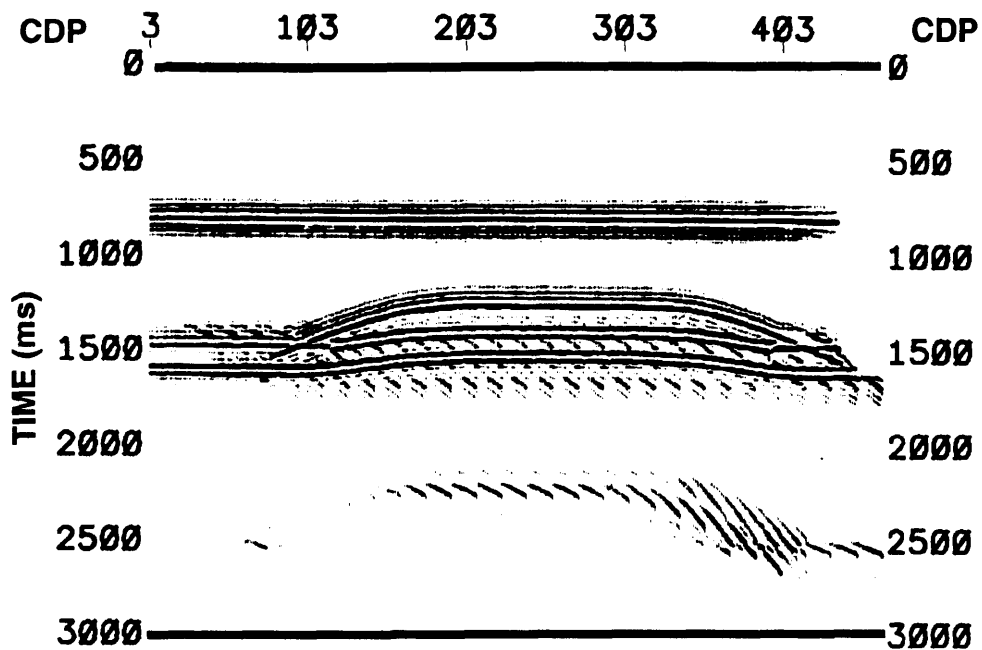


Fig. 3.24a. Stacked section of the vertical records.

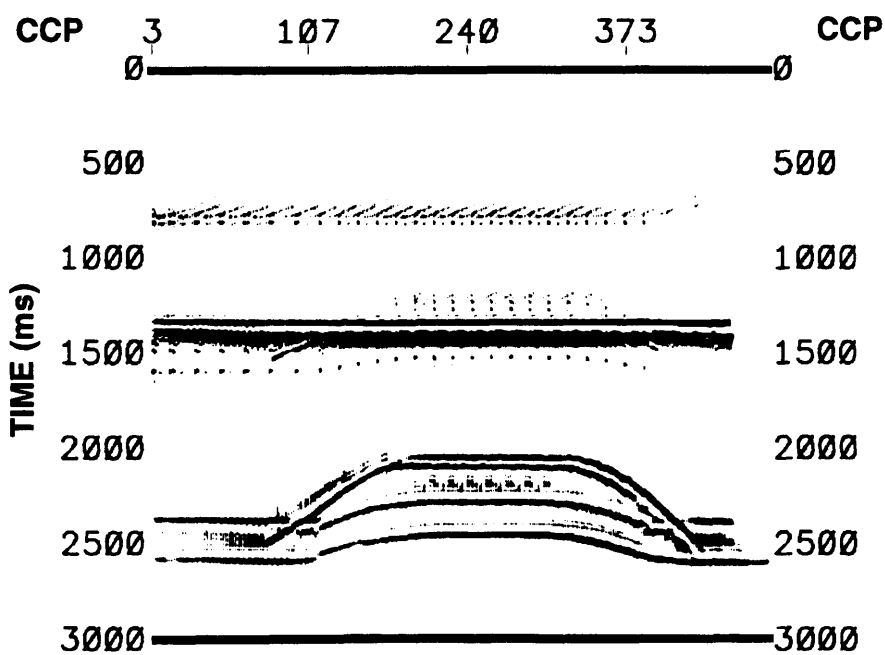


Fig. 3.24b. Stacked section of the horizontal records.

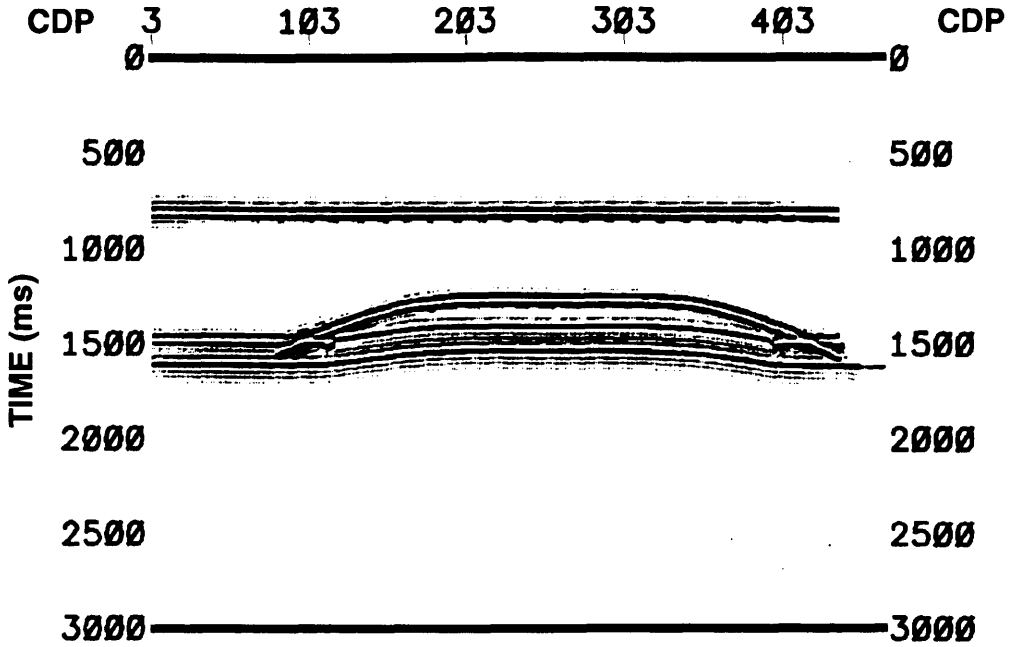


Fig. 3.25a. Stacked section of the filtered pass- P output obtained using $V_p= 2273$ m/s, $V_s= 947$ m/s and $\rho= 1.6$ g/cc (for the solid), and $V_p= 1455$ m/s and $\rho= 1.135$ g/cc (for the liquid).

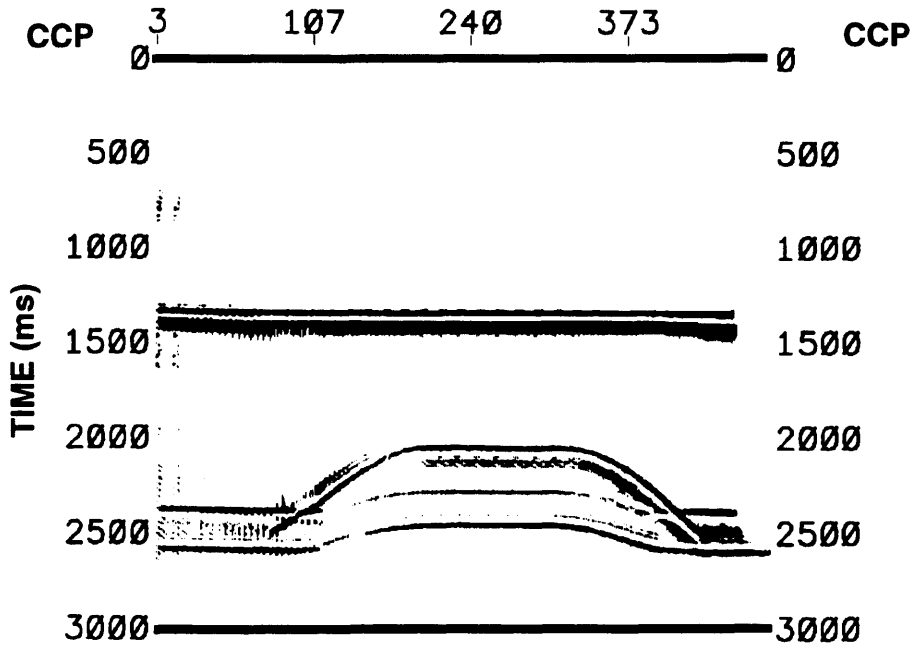


Fig. 3.25b. Stacked section of the filtered pass- S output obtained using $V_p= 2273$ m/s, $V_s= 947$ m/s and $\rho= 1.6$ g/cc (for the solid), and $V_p= 1455$ m/s and $\rho= 1.135$ g/cc (for the liquid).

The effect on the filter of erroneous estimates of the layer 2 velocities is shown in Figs. 3.26 and 3.27. The vertical and horizontal geophone records were filtered using erroneous values as follows: first we use $V_p = 2499$ m/s and $V_s = 1042$ for layer 2 (which represent a 10% error), and $\rho = 1.6$ g/cc for the solid, and $V_p = 1455$ m/s and $\rho = 1.135$ g/cc for the liquid. The filtered sections are shown in Fig. 3.26(a,b). Next 25% errors are used in the layer 2 elastic parameters giving $V_p = 1875$ m/s, $V_s = 813$ m/s and $\rho = 2.0$ g/cc for the solid, and $V_p = 1455$ m/s and $\rho = 1.135$ g/cc for the liquid. The resultant sections are shown in Fig. 3.27(a,b). It is important to indicate that both stacked and stacked filtered sections were generated using the processing sequence described previously.

The results presented can be compared with the stacked seismograms sections from Fig. 3.23(a,b) indicating a robust operation. We see that the stacked pass- P section is less effected by errors in the velocities than the stacked pass- S section, where there is still some residual P -wave energy

3.6 Discussion

This chapter reviews the response of a two-component geophone at a fluid-solid interface and presents a filtering method to separate incident P and S waves. We find that there are some differences between the responses of a geophone located on a stress-free solid and geophone located at a liquid-solid contact. The response of the vertical channels are reduced in the liquid-solid case compared to the free surface. There is also a smoother response for shear waves on the horizontal channel in the fluid-solid case.

A P - S separation filter is developed which uses the geophone responses and operates in the τ - p domain. It performs well on synthetic data when the source is located on the top of the water layer and the receivers located at the bottom of the water layer. It

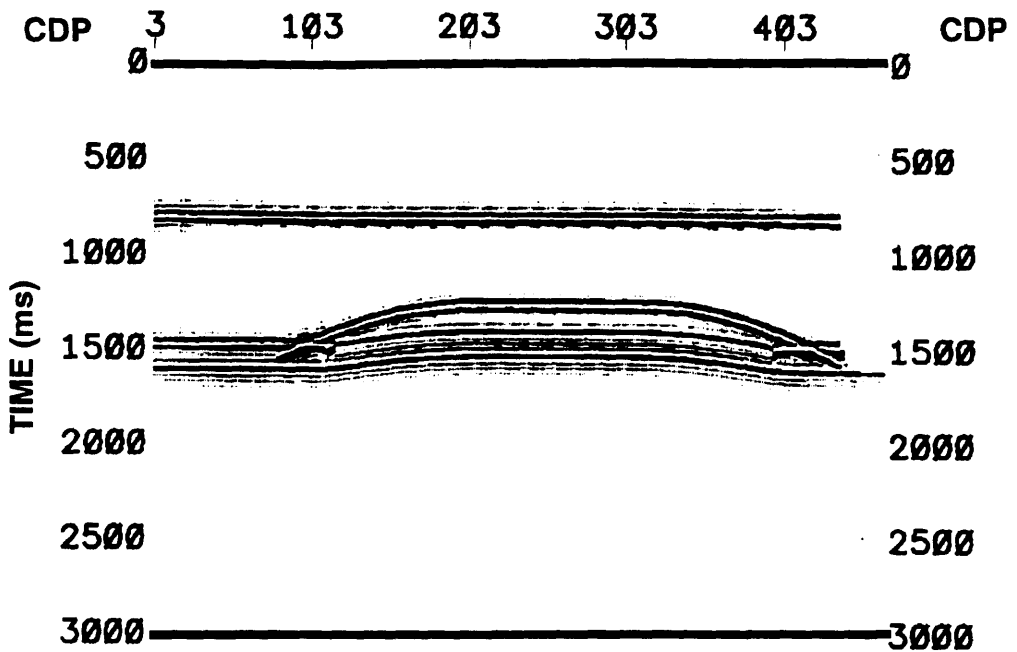


Fig. 3.26a. Stacked section of the filtered pass- P output obtained using $V_p= 2499$ m/s, $V_s= 1042$ m/s and $\rho= 21.6$ g/cc (for the solid), and $V_p= 1455$ m/s and $\rho= 1.135$ g/cc (for the liquid).

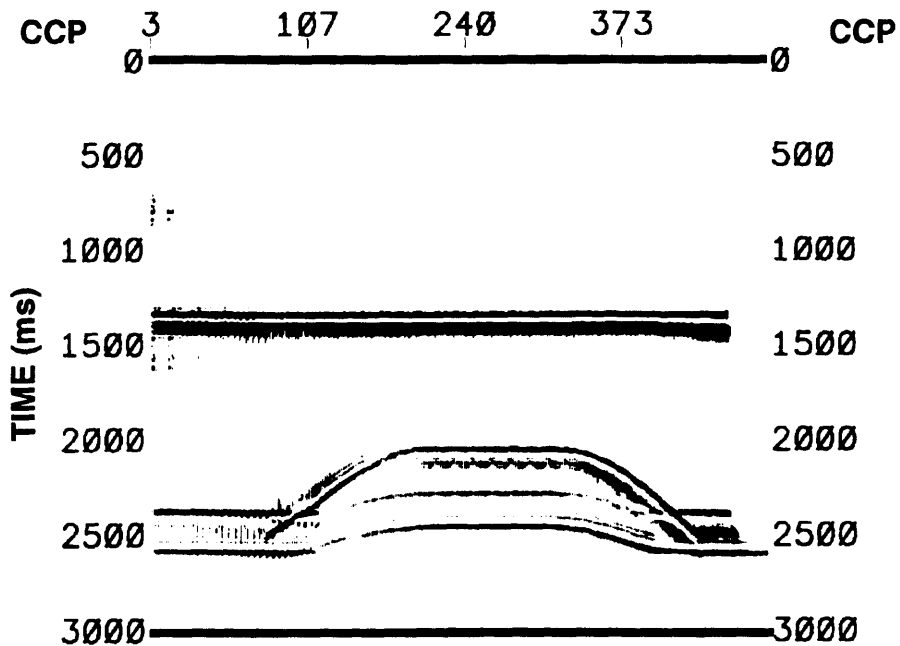


Fig. 3.26b. Stacked section of the filtered pass- S output obtained using $V_p= 2499$ m/s, $V_s= 1042$ m/s and $\rho= 1.6$ g/cc (for the solid), and $V_p= 1455$ m/s and $\rho= 1.135$ g/cc (for the liquid).

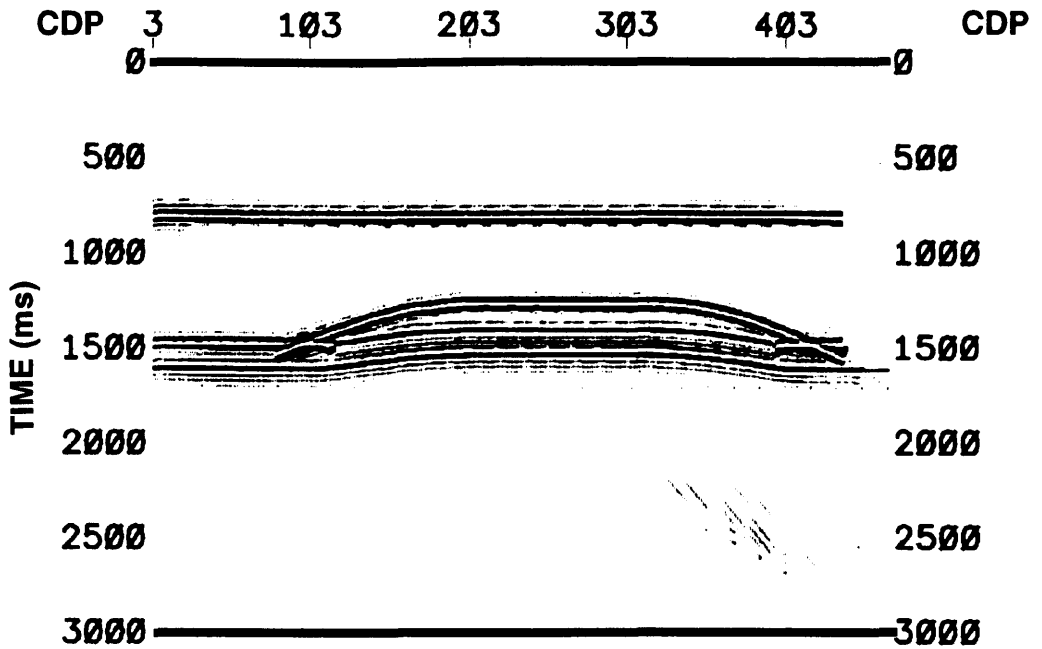


Fig. 3.27a. Stacked section of the filtered pass- P output obtained using $V_p=1875$ m/s, $V_s=813$ m/s and $\rho=2.0$ g/cc (for the solid), and $V_p=1455$ m/s and $\rho=1.135$ g/cc (for the liquid).

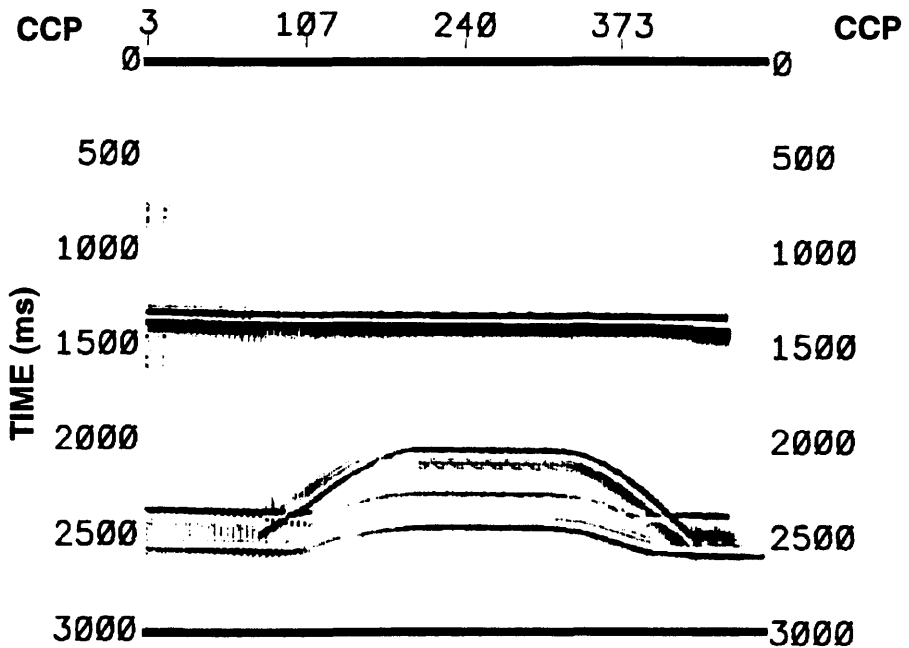


Fig. 3.27b. Stacked section of the filtered pass- S output obtained using $V_p=1875$ m/s, $V_s=813$ m/s and $\rho=2.0$ g/cc (for the solid), and $V_p=1455$ m/s and $\rho=1.135$ g/cc (for the liquid).

also provides good results for data recorded with both source and receivers located on the bottom of the water layer. The filter is stable with respect to errors in the elastic values of layer under the fluid, and with respect to noise present in the data. Because of the S -wave energy on the vertical channel and P -wave energy on the horizontal channel, it will be very useful to separate wave types before proceeding on to make pure P and S wave section.

CHAPTER 4 - CONCLUSIONS

The P - S separation filter in the τ - p domain has provided very good performance on synthetic data showing different degrees of superposition of P and S arrivals. The filter appears stable with respect to errors in the selection of the values of near-surface V_p and V_s velocities, although the pass- S filtered result seems to be more sensitive than pass- P filtered record.

The filter was tested using noise and refraction problems. The results show that the P - S filter keeps its accuracy in separating P and S waves. These results promise good performance in real data where noise is generally present. These noise and refraction statics problems, especially for the converted waves, are some of the more challenging processing problems.

The use of τ - p transform within the P - S separation filter lets us eliminate coherent noise like ground-roll, improving the quality of the seismic data before applying the filter without considering more extensive seismic pre-processing for noise elimination.

The results obtained from the separation filter in the τ - p domain on real data show its applicability and robustness into 2-D sequence of converted wave processing.

Analyzing the response of a two-component geophone at a fluid-solid interface and the filter performance to separate incident P and S waves, it is found that there are some differences between the responses of a geophone located on a stress-free solid and geophone located at a liquid-solid contact. The response of the vertical channels are reduced in the liquid-solid case compared to the free surface. There is also a smoother response for shear waves on the horizontal channel in the fluid-solid case.

Also, the P - S separation filter performs well on synthetic data when the source is located on the top of the water layer and the receivers located at the bottom of the water layer. It also provides good results for data recorded with both source and receivers located on the bottom of the water layer. The filter is stable with respect to errors in the elastic values of layer under the fluid, and with respect to noise present in the data. Because of the S -wave energy on the vertical channel and P -wave energy on the horizontal channel, it will be very useful to separate wave types before proceeding on to make pure P and S wave section.

Also presented is a 3-D τ - p transform which does not require assumptions of any geometric symmetry in the wavefield contained in the seismic data. The 3-D τ - p transform (forward and inverse) works in the k - w domain by expressing the slant stack process as a four-fold sequence of Fourier transforms which convert the (x, y, t) data to (p_x, p_y, w) data. Considerable disk space required for performing the necessary Fourier transforms but very fast processing results. Although, the 3-D τ - p transforms were applied only on 3-D synthetic data, the obtained results show promise for noise elimination when applied on real data.

CHAPTER 5 - FUTURE WORK

Having already tested the P - S modal filter on synthetic data for the liquid-solid case and based on the good results obtained the next step is to apply this filter on data acquired on physical modeling and real data. This experiment will provide us information about how stable and robust the filter is working.

Improve the inverse of the τ - p transform will improve the outputs of the separation filter removing the artifacts introduced by the inverse transform.

Based on the results obtained by the separation filter with 3C-2D data, the next step is extend the P - S separation filter to a 3C-3D data set by removing the three-dimensional geophone responses in the 3-D tau-p domain. The separation of the individual P and S arrivals in the 3-D case may be considered a problem since the P and S data are recorded in the vertical, horizontal and transverse geophones. In this approach we will consider the three-component geophones at a solid interface (free-surface case). The filter will operate in pass- P and pass- S (SV , SH or S_1 and S_2 for an anisotropic case) let us to separate incident P and S waves. In pass- P mode, the output consists of all waves arriving at the geophone as P waves where S wave energy is removed. In the pass- S mode, the output is the incident S waves with P wave energy removed.

The P - S separation filter for 3C-3D data will be tested on data acquired on physical modeling data and the 3C-3D data set acquired in Blackfoot area. Also, it will give us the opportunity of verifying our expectations about the 3-D τ - p transform for eliminating coherent noise and multiples.

APPENDIX - 3-D TAU-P

A.1 Introduction

Generally, the 3-D τ - p process is applied on 3-D seismic data by considering some specific symmetry on the data with the goal of doing this process more useful in real situations.

In this appendix is introduced a τ - p transform algorithm for 3-D seismic data which does not require any geometrical symmetry on the wavefield contained in the seismic data. It only requires to have the data regularly spaced. This algorithm express the τ - p transform by a four-fold sequence of 1-D Fourier transforms in time and spatial coordinates as indicated by McCowan and Brysk (1989) for a point source in an arbitrary medium.

The 3-D τ - p transform is developed as an integration process of different two-dimensional τ - p transforms, each one representing a particular picture of the propagating wave field, along inline and crossline directions. The two-dimensional τ - p transform (back and forward) is performed in the k - ω domain using the algorithm published by Wade and Gardner (1988) and Gardner and Lu (1991) based on the "Fourier slice theorem" or "Projection slice theorem" (Kak and Rosenfeld, 1982), which is explained in Chapter 2, section 2.4.2.

The 3-D τ - p transform algorithm is tested on synthetic data simulating a shot acquired on an horizontally layered earth model. The synthetic data includes P and converted waves. The results show the robustness of the algorithm for recovering the events of interest and removing random and coherent noise from the original shot gathers.

A.2 Expressions, development and characteristics of the tau-p transform in the 3-D domain

A seismic section in the τ - p domain offers an alternative view in which all subsurface reflectors are illuminated by incident energy of a fixed ray-parameter range. One advantage of working in the τ - p domain is that we can study the different wave modes as function of their corresponding slowness values ($p=1/v$), where v is the propagation velocity. Then, the τ - p transform is an useful processing tool because it provides an increased separation between different seismic waves (i.e., multiples, ground-roll, P and S waves among others), a simplified interpretation of field records and better noise suppression.

This transformation has been used world-wide and has been the subject of considerable research for two-dimensional seismic data analysis during the last several decades. For 3-D data there are some mathematical developments and several approaches taking advantage of particular symmetries in the data (Evans, 1991).

The application of slant stacking to decompose plane wavefields into their component waves is well documented (Chapman, 1978; Stoffa et al., 1981, Diebold and Stoffa, 1981 among others). Commonly, the slant stack is defined as:

$$\psi(p, \tau) = \int_{-\infty}^{\infty} u(\tau + px, x) dx \quad (\text{A.1})$$

where $u(t, x)$ are the data at time t , and horizontal range, x . In seismic field, $u(t, x)$ represents any two dimensional seismic data recorded as a function of travelttime, t , and source-receivers offset, x , as result of a point-source excitation. The variable $t=\tau+px$ represents a line in the x - t plane with slope p (or slowness, $1/v$) and vertical intercept time τ (Fig. A.1). Conceptually, the slant stack represents a process that maps the summed amplitudes along a given line with slope p and intercept time τ in the x - t domain into a

point in the τ - p domain (Fig. A.1). In this way, summing amplitudes, of a given event, along lines with different p and τ values we can represent this event as an ellipse in the τ - p domain (Fig. A.2).

The generalization of the slant stack to the 3-D case is straightforward if we consider now that the slowness vector p has two components (p_x, p_y) . Then, the 3-D τ - p transform can be expressed for a point source acting at the origin of a uniform medium as follows:

$$\psi(\tau, p_x, p_y) = \int_{-\infty}^{\infty} \int_{-\infty}^{\infty} u(\tau + p_x x + p_y y, x, y) dy dx \quad (\text{A.2})$$

where $u(t, x, y)$ represent the seismic data distributed over an areal coverage at time, t , without assuming any geometric symmetry and represent the orthogonal components of the slowness p (Chapman, 1981; McCowan and Brysk, 1989).

When we are defining a 3-D slant stack over surface data we have to consider an areal coverage in the acquisition; the data are acquired not only at different offsets r , but also in all directions θ . In cylindrical coordinates both in space and in p variables are reduced as

$$(x, y) = (r \cos \theta, r \sin \theta) \quad \left(p_x, p_y \right) = (p \cos \alpha, p \sin \alpha) \quad (\text{A.3})$$

Retaining the same symbols, the eq. (A.2) is reformulated as a function of the cylindrical coordinates, as follows

$$\psi(\tau, p, \alpha) = \int_0^{\infty} r dr \int_{-\pi}^{\pi} u(\tau + pr \cos(\theta - \alpha), r, \theta, 0) d\theta \quad (\text{A.4})$$

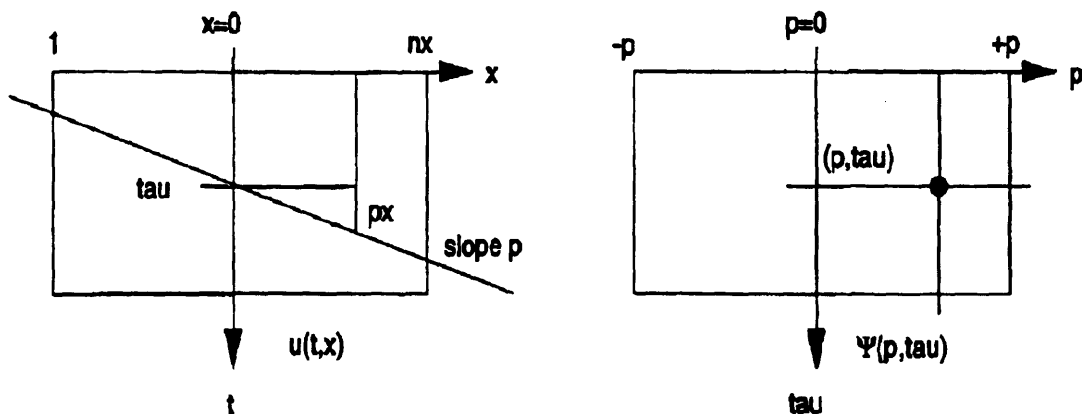


Fig. A.1. The slant stack $\Psi(p, \tau)$ at any point (p, τ) is obtained by adding $u(x, t)$ along the line $t = \tau + px$. The value of the Ψ at the points where the line intersects each trace of u is obtained by interpolation (after Wade and Gardner, 1988).

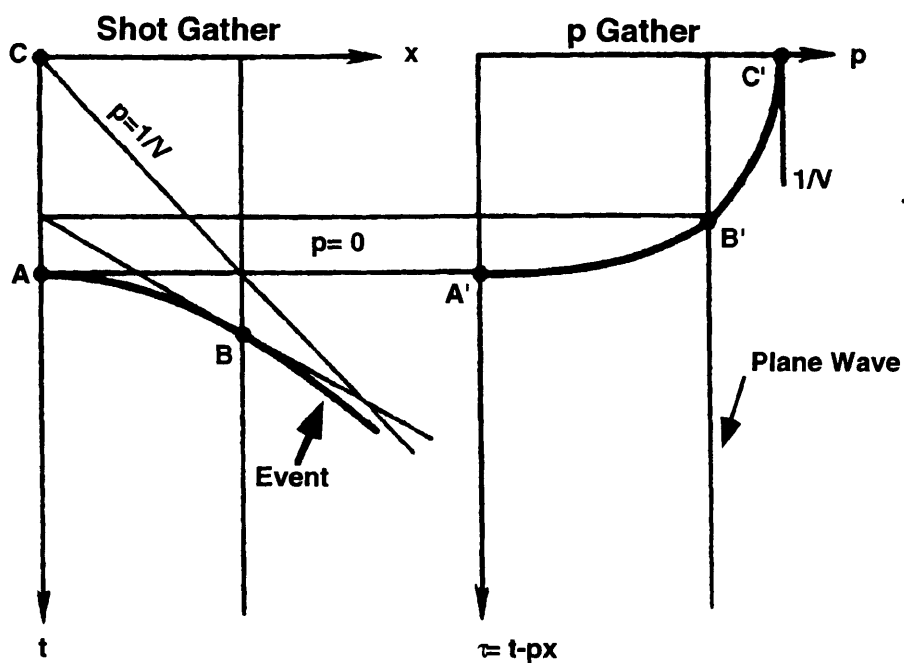


Fig. A.2. A hyperbola on a shot gather maps onto an ellipse on the p -gather (after Yilmaz, 1987).

The θ integral in eq. (A.4) extends over a ring (on the surface) of radius r about the source; it involves stacking the traces located on the ring (with interpolation as necessary) with different time shift applied to each trace depending upon its azimuth (Fig. A.3a). For a given slant stack (fixed direction of propagation α and Snell's parameter p), the time shift is the product of p and the projection of the position vector (of magnitude r) along the direction α .

In an axisymmetric problem, the data are expected to depend upon offset but not upon direction, so that

$$u(t, r, \theta, z) = u(t, r, 0, z) = u(t, r, \alpha, z) \quad (\text{A.5})$$

by taking $\theta' = \theta - \alpha$ as the integration variable instead of θ and using the symmetry properties of the cosine, eq.(A.4) can be rewritten as

$$\psi(\tau, p, \alpha) = 2 \int_0^{\infty} r dr \int_0^{\pi/2} \left[u(\tau + pr \cos \theta', r, 0, 0) + u(\tau - pr \cos \theta', r, 0, 0) \right] \quad (\text{A.6})$$

If $p=0$ the integration is trivial

$$\psi(t, 0, \alpha) = \pi \int_{-\infty}^{\infty} u(t, x, 0, 0) |x| dx \quad (\text{A.7})$$

For $p>0$ we can change variables from θ' to $p' = p \cos \theta'$. Then,

$$dp' = -p \sin \theta' d\theta' = -\left(p^2 - p'^2\right)^{1/2} d\theta' \quad (\text{A.8})$$

and

$$\psi(\tau, p, \alpha) = 2 \int_0^p (p^2 - p'^2)^{1/2} dp' \int_{-\infty}^{\infty} u(\tau + p'x, x, 0, 0) |x| dx \quad (\text{A.9})$$

If axial symmetry is assumed, we can imagine the existing trace t at offset r (or the *average of the two existing traces*) to be repeated at every θ grid point on the ring. The θ integration consists of stacking multiple copies of the existing trace at offset r , each time shifted a different amount according to the θ value assigned to it. Whether areal coverage is real or simulated, the r integration consists simply of stacking the stacked traces *obtained at each offset again by the θ integral procedure*, where each stacked trace is multiplied by the offset.

The procedure just outlined permits us to relate the cylindrical slant stack directly to the line-source slant stack when there is axial symmetry. Considering a seismic line along the x axis, with a shotpoint at $x=0$. Multiply each trace by the magnitude of its offset. Perform a conventional slant stack upon the rescaled traces (appropriate for a line source along the y -axis) (*Fig. A.3b*). *The result is precisely the x integral in eqs. (A.7) and (A.9), for Snell's parameter p' .* The outer integral of eq. (A.9) then expresses the cylindrical slant stack for p as a superposition of the line-source slant stacks (using traces to which linear offset gain has been applied) for all p' close to p . For a axisymmetric problem, the value of u is independent of θ . The remaining θ integration is just the integral representation of the Bessel function.

The procedures presented previously are time consuming and are valid only if we have a symmetric problem which in real cases generally does not apply. Perhaps, we need to develop a more general algorithm that could be applied on any kind of data without limitations and let us remove noise and multiples while preserving the target reflections.

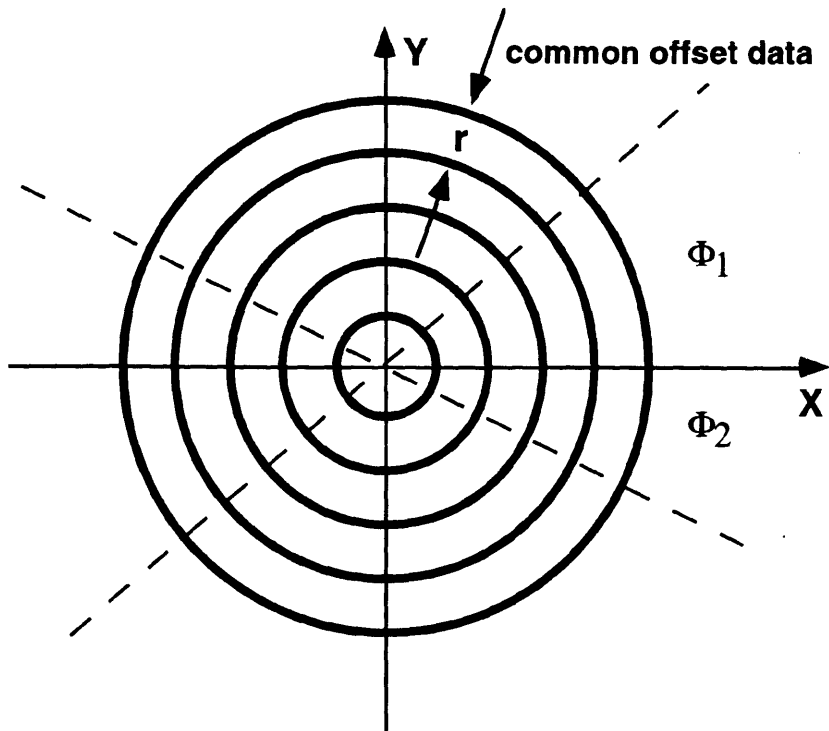


Fig. A.3a. Schematic view of a 3-D slant stack defined over a surface data.

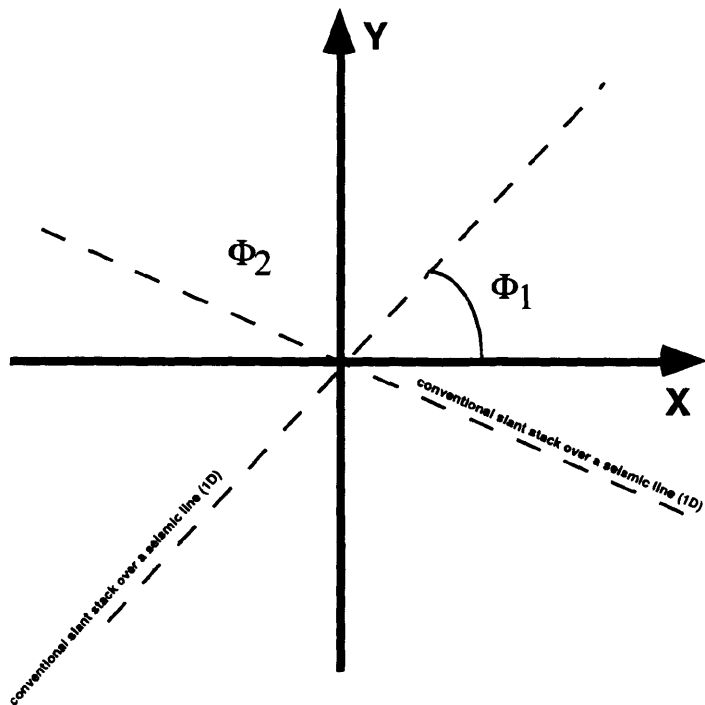


Fig. A.3b. Schematic view of a 3-D slant stack defined over a surface data considering axial symmetry.

A.3 Theory

The reciprocal slant-stack operation for reconstructing (x, t) data from (p, τ) data corresponding to eq. (A.2) is given by:

$$u(t, x, y, z) = -\frac{1}{4\pi^2} \frac{d^2}{dt^2} \int_{-\infty}^{\infty} dp_x \int_{-\infty}^{\infty} dp_y \Psi(t - p_x x - p_y y - qz, p_x, p_y) \quad (\text{A.10})$$

A more convenient way to express the 3-D τ - p transform and its reciprocal is to use direct and inverse Fourier transforms. In fact, the slant stack is reduced to a sequence of 1-D Fourier transforms as follows:

$$\Psi(\tau, p_x, p_y) = \frac{1}{2\pi} \int_{-\infty}^{\infty} e^{-i\omega\tau} d\omega \int_{-\infty}^{\infty} e^{-i\omega p_x x} dx \int_{-\infty}^{\infty} e^{-i\omega p_y y} dy \int_{-\infty}^{\infty} e^{i\omega t} u(t, x, y) dt \quad (\text{A.11})$$

where $\omega (= 2\pi f)$ is the angular frequency. In the same way, the reciprocal operation is achieved by Fourier transforming back four times (McCowan and Brysk, 1989). The only consideration is that the transform variable for x is ωp_x and y it is ωp_y , so that an additional factor of ω^2 appears during the operation $u(t, x, y)$ thus has the form:

$$u(t, x, y) = \frac{1}{8\pi^3} \int_{-\infty}^{\infty} d\omega e^{-i\omega t} \omega^2 \int_{-\infty}^{\infty} dp_x e^{i\omega p_x x} \int_{-\infty}^{\infty} dp_y e^{i\omega p_y y} \int_{-\infty}^{\infty} d\tau e^{i\omega\tau} \Psi(\tau, p_x, p_y) \quad (\text{A.12})$$

In other words, the slant stack can be performed either directly as a double integral over time-shifted traces (eq. (A.9)), or by four-fold sequence of Fourier transforms (eq. (A.11)); so can its reciprocal, except for the differentiation (with reference to eq. (A.10) and (A.12)).

Then, for obtaining the τ - p transform we use the following procedure: i.) first, we convert the 3-D input data from x - t domain to x - w domain (space-frequency domain) by direct Fourier transform, ii.) second, we pick out the volume long crossline direction and apply to each inline data a Fourier transform from x to $w p_x$, iii.) third, the last procedure is again apply on the data picked out from y to $w p_y$, and iv.) fourth, we convert the resulting (w, p_x, p_y) volume using the inverse Fourier transform. All of this sequence is performed shot by shot for all the inline and cross-line lines of each shot. Physically, with the inner integrations in the last line of eq. (A.11), we expanded the propagating plane waves and picked out the particular plane wave with a frequency w and a wavenumber with x and y components $w p_x$ and $w p_y$. With the last integration in the same equation, we superpose a collection of such plane waves to build up a new wavelet following the criteria: They all have the same components of the Snell's parameter p_x and p_y ; in other words, they all have the same direction of incidence into the medium, but different frequencies and wavenumbers. Hence, the slant stack represents a wavelet entering the medium with a specific orientation (McCowan and Brysk, 1989).

The inverse operation for recovering the original (t, x, y) volume is performed reversing the above sequence.

A.4 3-D tau-p transform algorithm

The process for obtaining the 3-D τ - p transform as a sequence of Fourier transforms was implemented by modifying the forward and inverse 2-D τ - p algorithms published by Gardner and Lu (1991) and discussed in detail in Chapter 2. Both algorithms work in the k - w domain taking advantage of the projection slice theorem (Wade and Gardner, 1988). This theorem says that the 1-D temporal coefficients of (τ, p) are identical to the coefficients in the 2-D Fourier transform of $u(t, x)$ picked out long the radial line

$k=pw$, where k is the frequency corresponding to x and w , the frequency corresponding to t . The forward slant stack process is indicated in the Fig. A.4a. Basically, it is used the fact that any radial line in the $k-w$ domain is a column in the $p-w$ domain (Wade and Gardner, 1988). This last property lets us reconstruct the (k, w) data from the (p, w) data by simply picking out values for k constant (along a hyperbola) as illustrated in Fig. A.4b.

The extension for 3-D of these algorithms is indicated graphically in the Fig. A.5. First, a (w, p_x, y) volume is obtained after applying the forward 2-D $\tau-p$ transform in the $k-w$ domain along the crossline direction. Second, the forward 2-D $\tau-p$ transform is again applied along the inline direction (value of p_y constant) for obtaining the final (w, p_x, p_y) volume. An inverse Fourier transform is applied on the resultant volume for reconstructing the original (t, x, y) data. For obtaining a 1:1 mapping, i.e., each coefficient for ψ comes from a unique coefficient for u , it was applied a high-cut frequency filtering process for muting the (p, w) data outside the interval $(2\pi/wdx)$ for each frequency. The resulting (p, τ) slant stack contains enough information to recover the original $u(t, x, y)$ without aliasing.

A.5 Synthetic modeling

To test the 3-D $\tau-p$ transform algorithm a horizontally layered earth mode with three flat homogeneous layers was used. A single 3-D shot record was acquired on this synthetic model which consists on 60 receivers distributed along six inlines in the North-South direction and ten crosslines oriented East-West. Fig. A.6(a,b) show the depth model and a plan view of the geometry used. Five different experiments were performed for evaluating the algorithm in reconstructing the original wavefield under noise-free, noisy conditions, and ground-roll contamination. Also were considered pure P and converted waves. These experiments are described as follows.

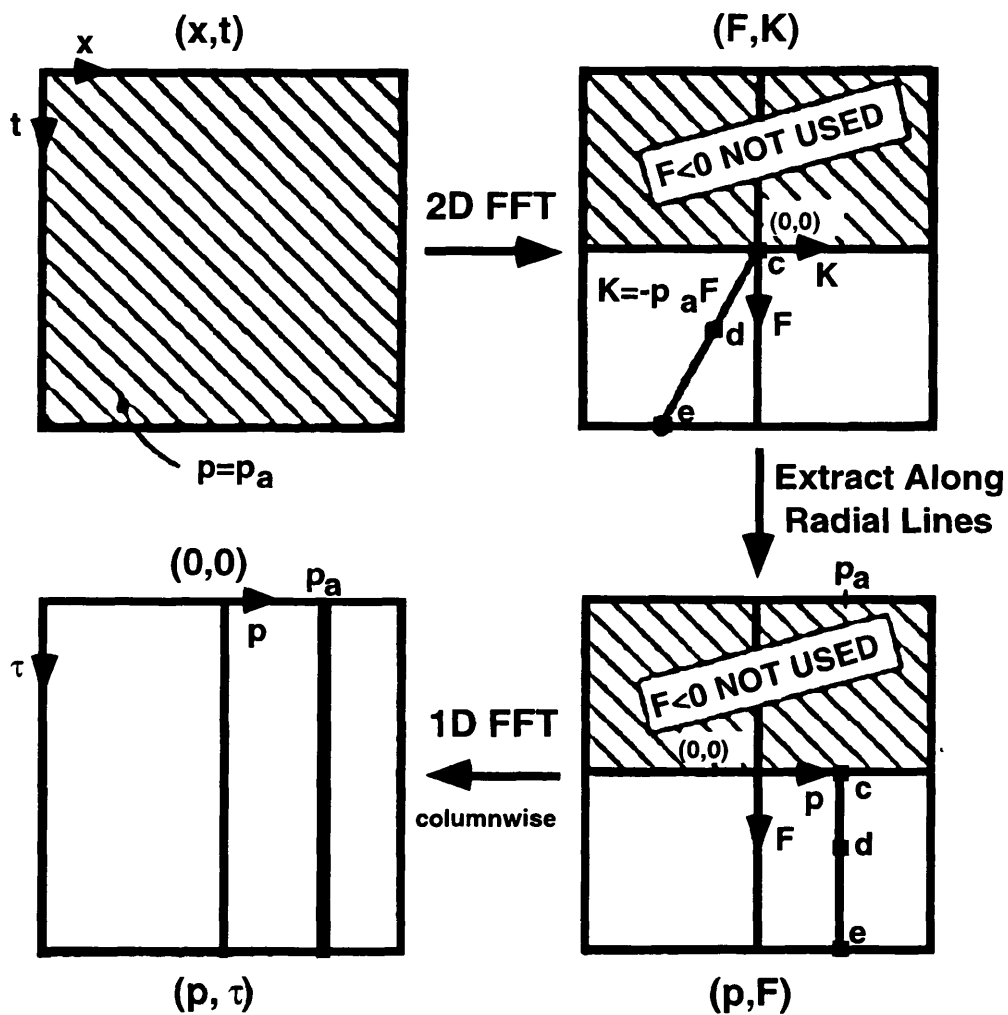


Fig. A.4a. Scheme for constructing slant stack with 2-D Fourier transforms (after Wade and Gardner, 1988).

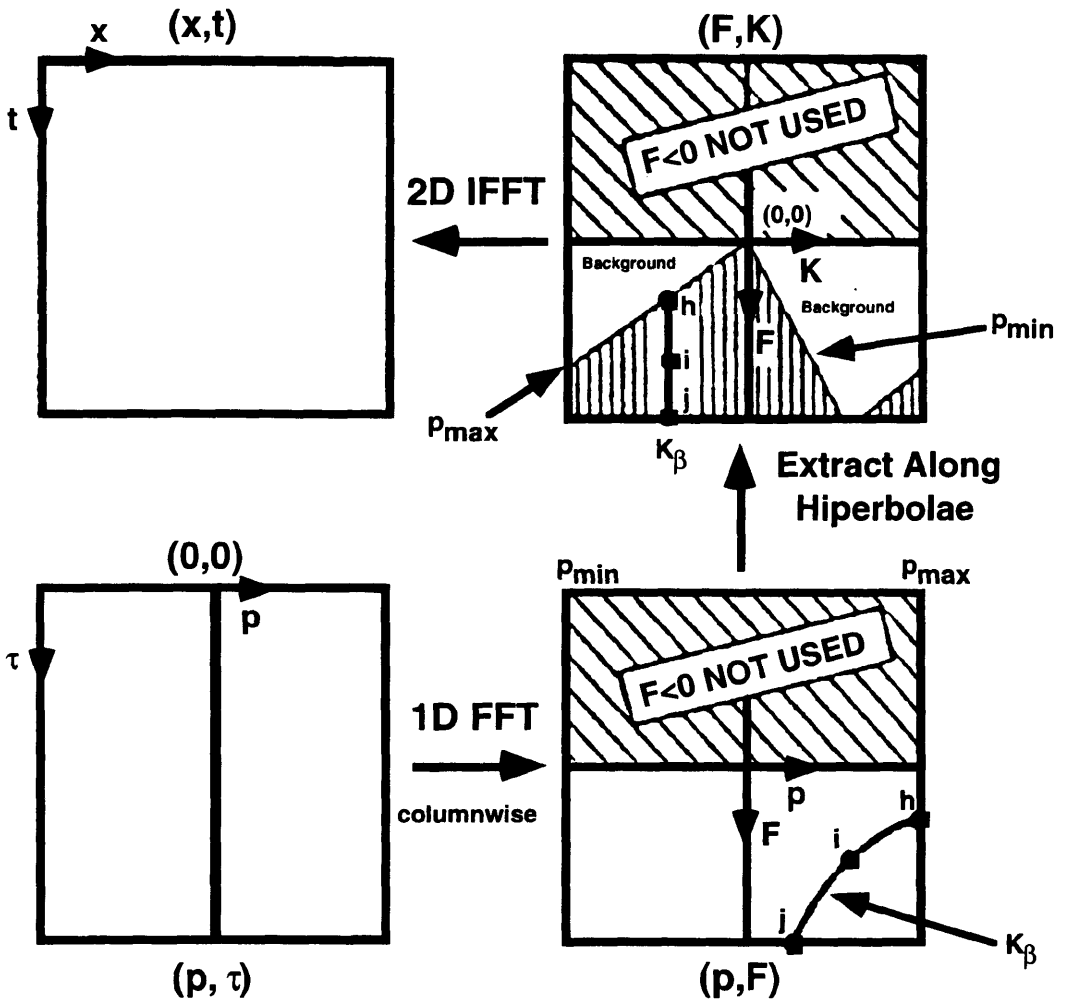


Fig. A.4b. Scheme for reconstructing (x, t) data from (τ, p) data with 2-D Fourier transforms (after Wade and Gardner, 1988).

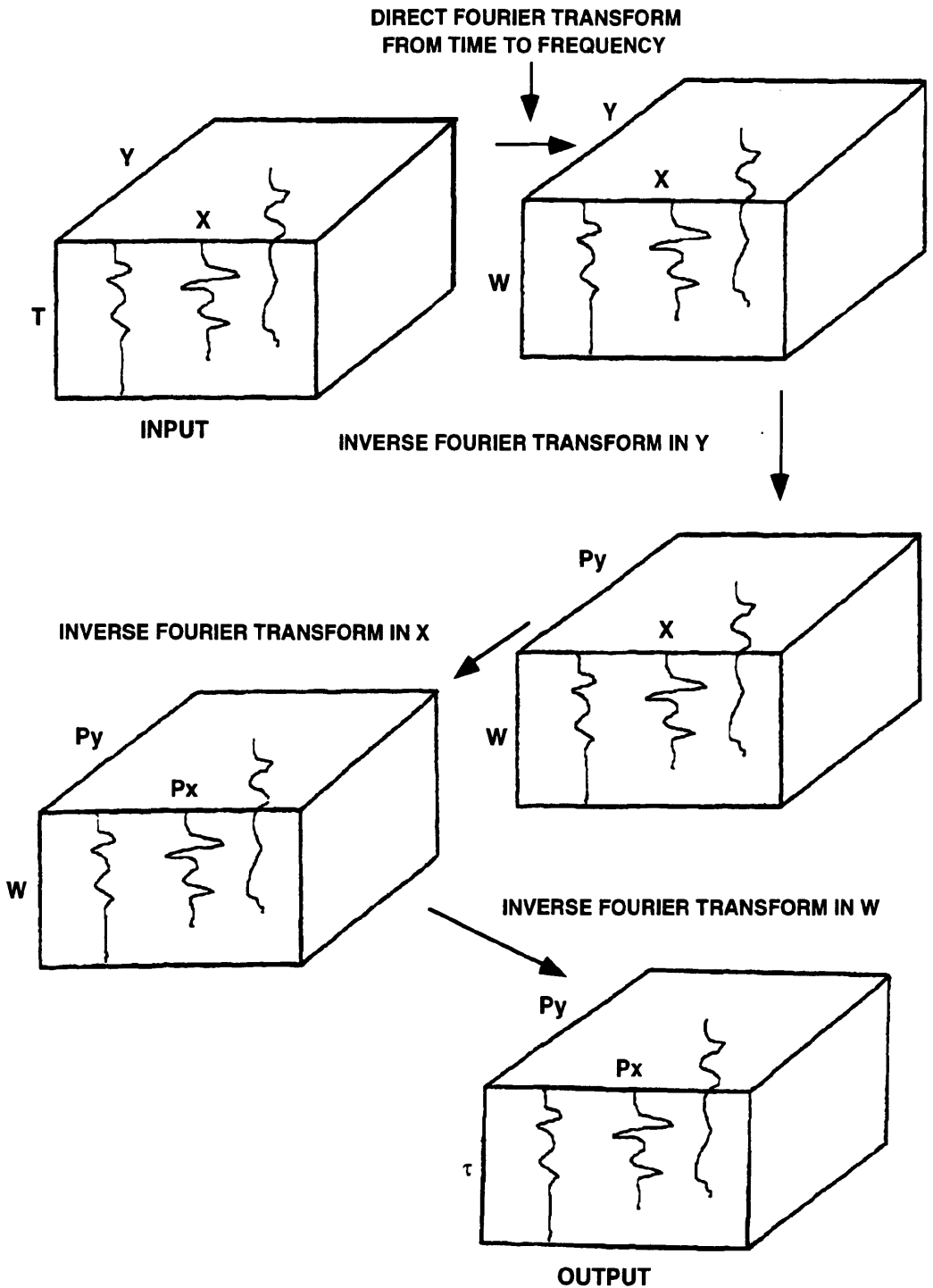


Fig. A.5. Schematic view of 3-D τ - p transform applied on data distributed over an areal coverage without assuming any geometric symmetry.

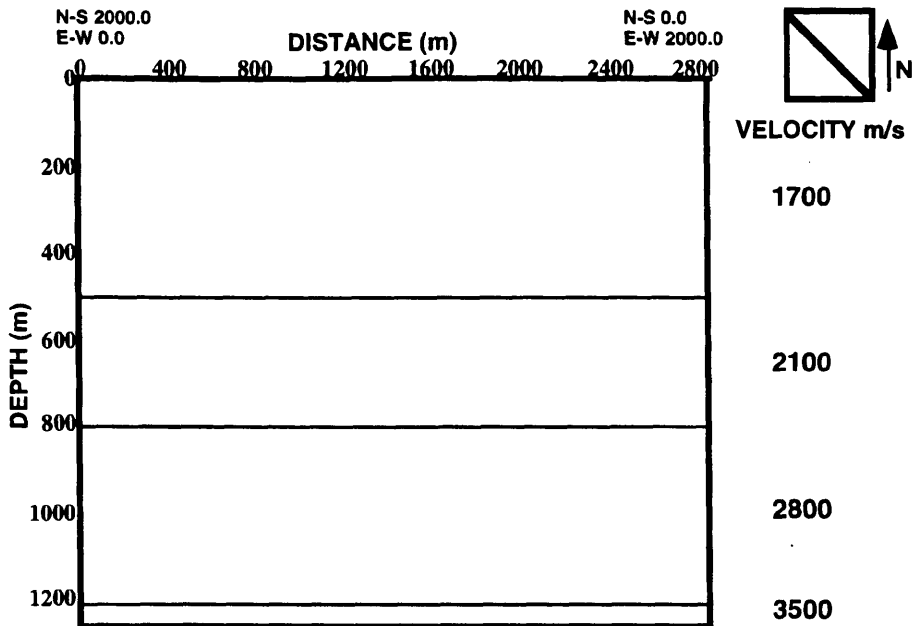


Fig. A.6a. Depth model representing a horizontally layered earth with constant P and S wave velocities

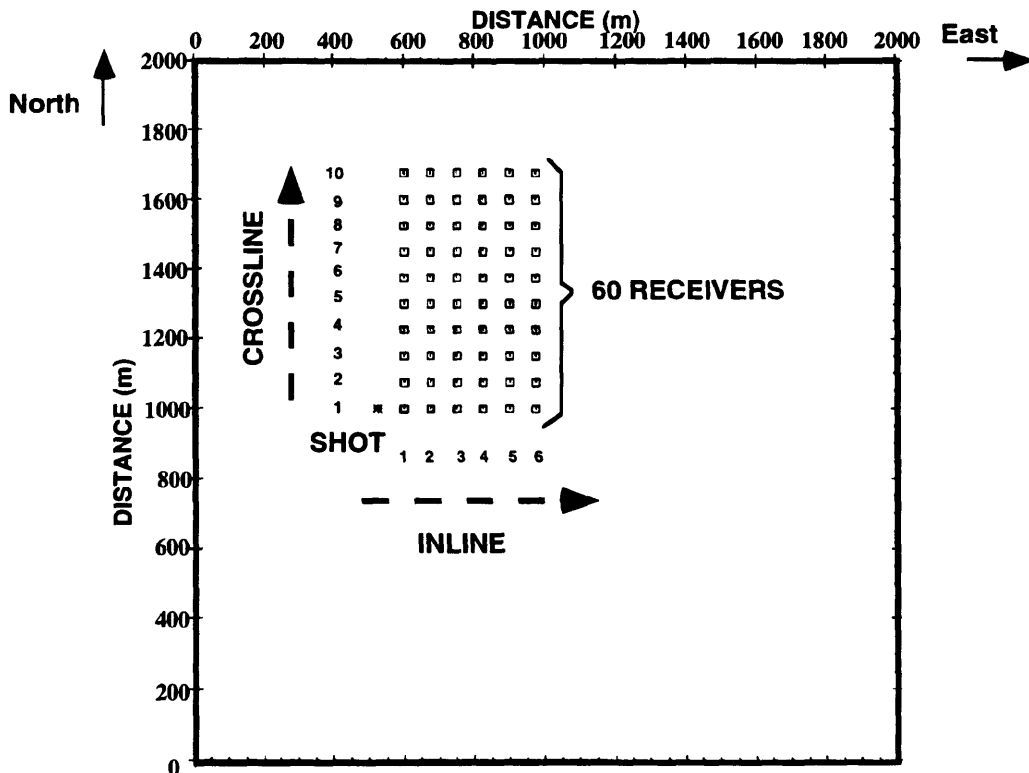


Fig. A.6b. Acquisition geometry for a 3-D shot record. The inlines are oriented along the North-South direction and crosslines along the East-West direction. The source is represented by the symbol (*) and the receivers by (#) on the display.

Experiment 1

It represents synthetic 3-D P - P shot record of the three flat horizons of the depth model (Fig. A.7a). The reconstructed shot record is indicated in the figure A.7c for 50 values of slowness, p (50 for p_x and 50 for p_y). It represents a p increment of 0.0000134 s/m with a range of p values between 0 - 0.00067 s/m equivalent to a minimum P wave velocity of 1500 m/s for both inline and crossline directions. It is obvious the good performance of the algorithm during the reconstruction of the input shot. Some noise is left on the record after applying the algorithm. Fig. A.7d shows the result of the reconstruction increasing the total number of p values by a factor of 2. The remnant noise was practically eliminated. It indicates that a more fine sampling in the slowness p let us obtain a better wavefield reconstruction. The correspondent representation of the original shot record in the τ - p transform is indicated in the Fig. A.7c. The shot spread used in the acquisition produces linear noise interfering with the ellipses associated with the events. In fact, as indicated by Phinney et al. (1981) slant stacks of lines of finite-length discrete data do not transform exactly into points regardless of the method used for obtaining the direct and inverse τ - p transform.

In addition, a very small signal deterioration is observed at large offsets producing aliasing in the data. It can be explained by the limitation of the 3-D τ - p transform when we are using a coarse p interval. Maroof (1984) indicates that the ray parameter increment (Δp) must be small enough to avoid aliasing. The Fig. A.7d shows how is reduced this effect by considering a more fine p interval.

Experiment 2

In this case, 15% percent random noise was added in the 3-D P - P shot record (Fig. A.8a). We can see the reflections associated with the first and second flat reflectors but the reflection from the last one is masked by the noise background. The reconstructed

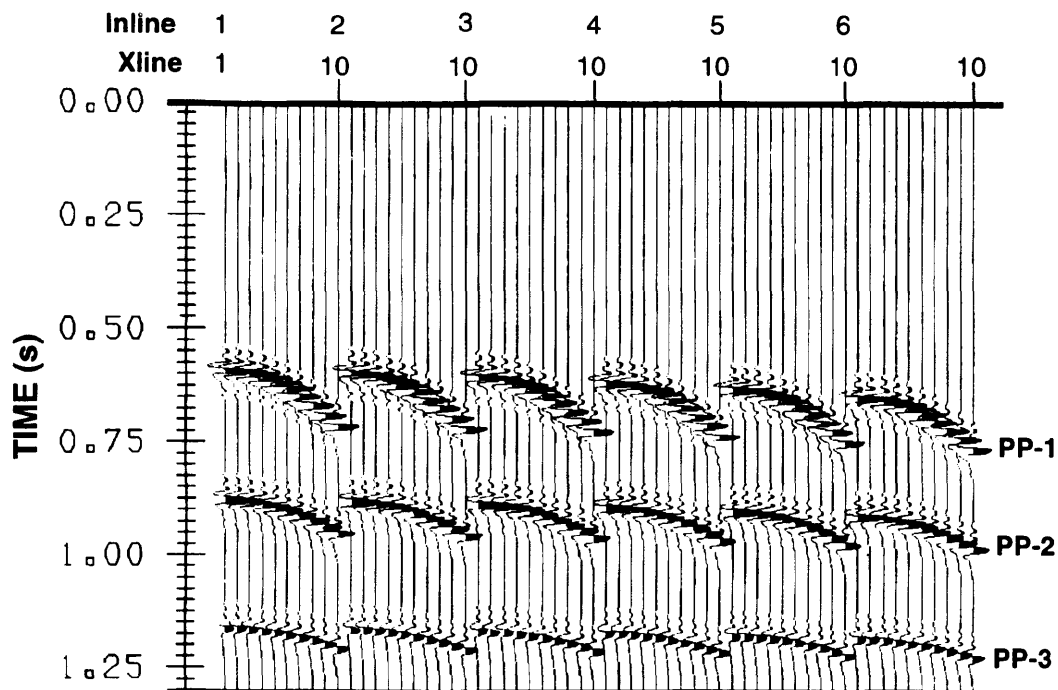


Fig. A.7a. 3-D shot record showing the P - P arrivals.

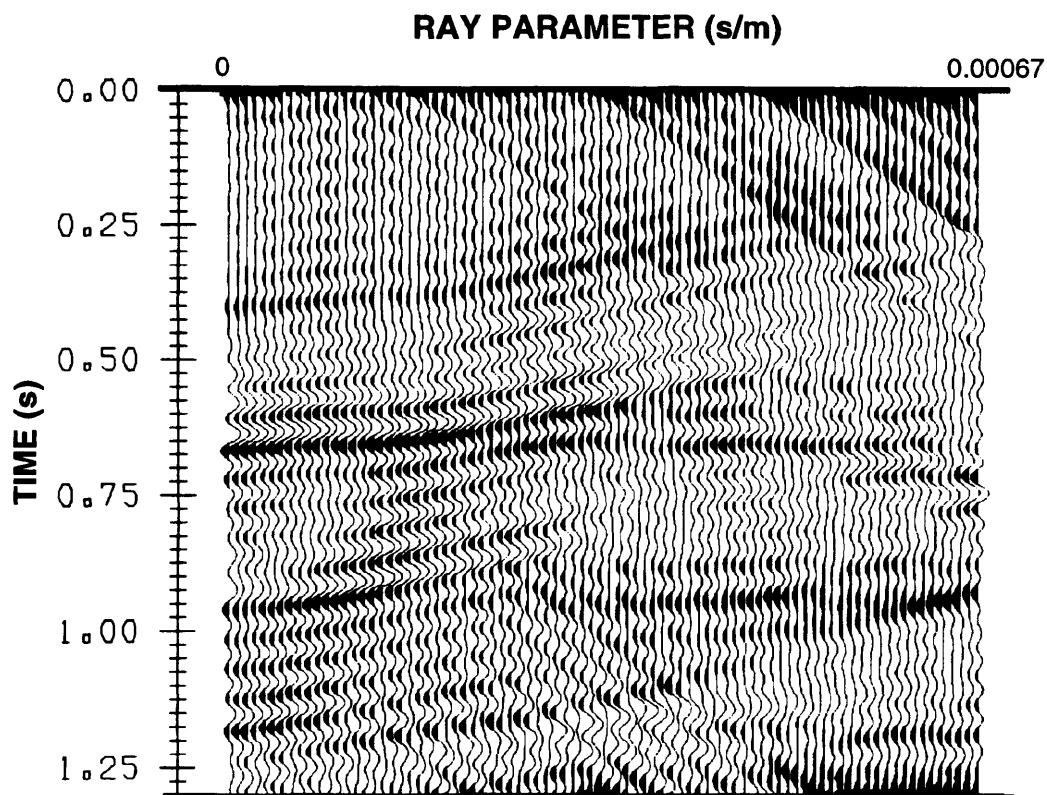


Fig. A.7b. Representation of the 3-D shot record (Fig. A.7a) for the inline number 1 in the τ - p domain.

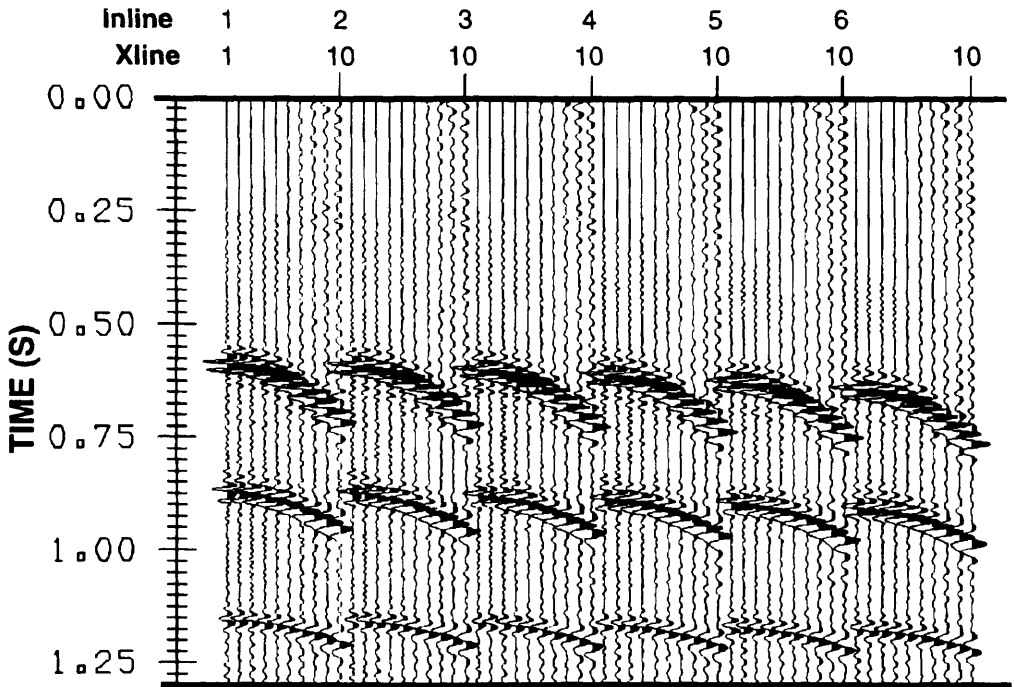


Fig. A.7c. Reconstructed 3-D shot after applying the 3-D τ - p transform considering 50 slowness values in each x and y direction.

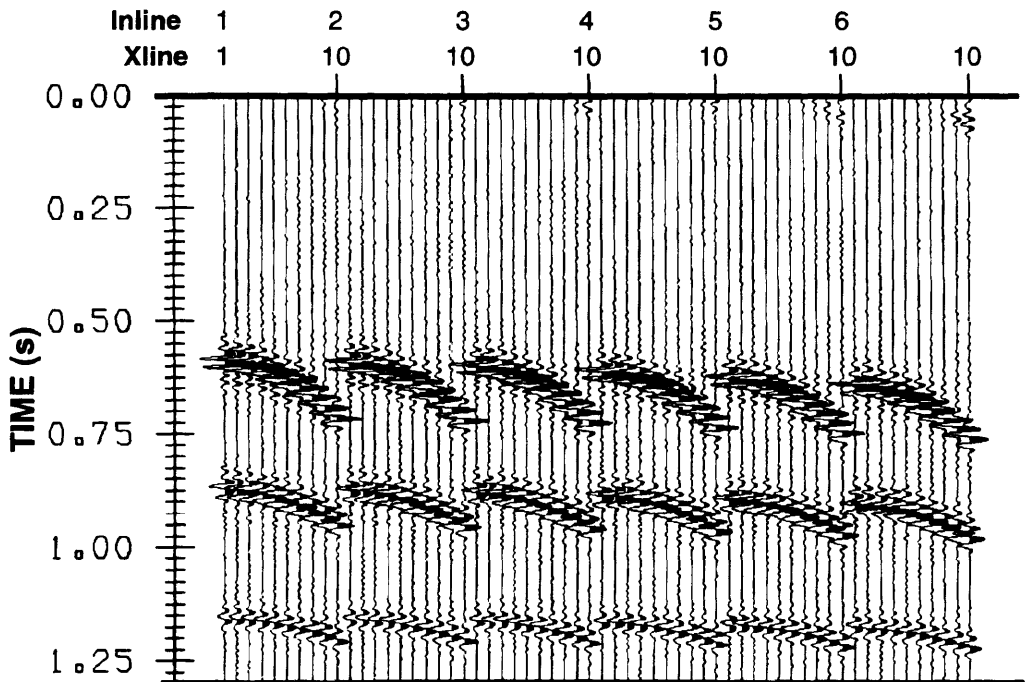


Fig. A.7d. Reconstructed 3-D shot after applying the 3-D τ - p transform considering 100 slowness values in each x and y direction.

shot record (Fig. A.8b), using the same spacing between p traces in the τ - p domain shown in experiment 1, shows an excellent recovering of the three events in presence of noise. Although, the amplitudes of the events are diminished after the reconstruction is possible to denote the two upper P wave events. The last event associated with the deepest layer have been recovered too but it is partially masked by the noise.

Experiment 3

The goal of this experiment is evaluate the reconstruction of a shot record containing converted waves (Fig. A.9a). The reconstructed record is indicated in the figure A.9b, the reconstruction of the P - P and P - SV waves is very good but noisy. Here, the reflections associated with the converted waves appear with less amplitude due to superposition of the P and SV energies in the τ - p domain as consequence of the finite-length or shot offset of the spread in the x - t domain. As the energy associated with the P -wave is stronger than the SV -wave energy; it masks the SV events specially those arriving at longer traveltime.

Experiment 4

The effect of the random noise on the reconstruction of the 3-C converted wave records is considered (Fig. A.10a). The noise level is kept at 15 percent as experiment 2. The result after applying the 3-D τ - p transform process is shown in the Fig. A.10b. It is obvious that the 3-D τ - p transform recover the shallow SV wave events but the deeper ones are affected by the residual noise. It can be explained due to its energy is less than the noise present in the data. Then, the reconstruction of the SV waves is effected by the P - P and P - SV interference and the low S/N ratio. *The P -wave energy is more coherent in the τ - p domain and it permits a better performance of the algorithm.*

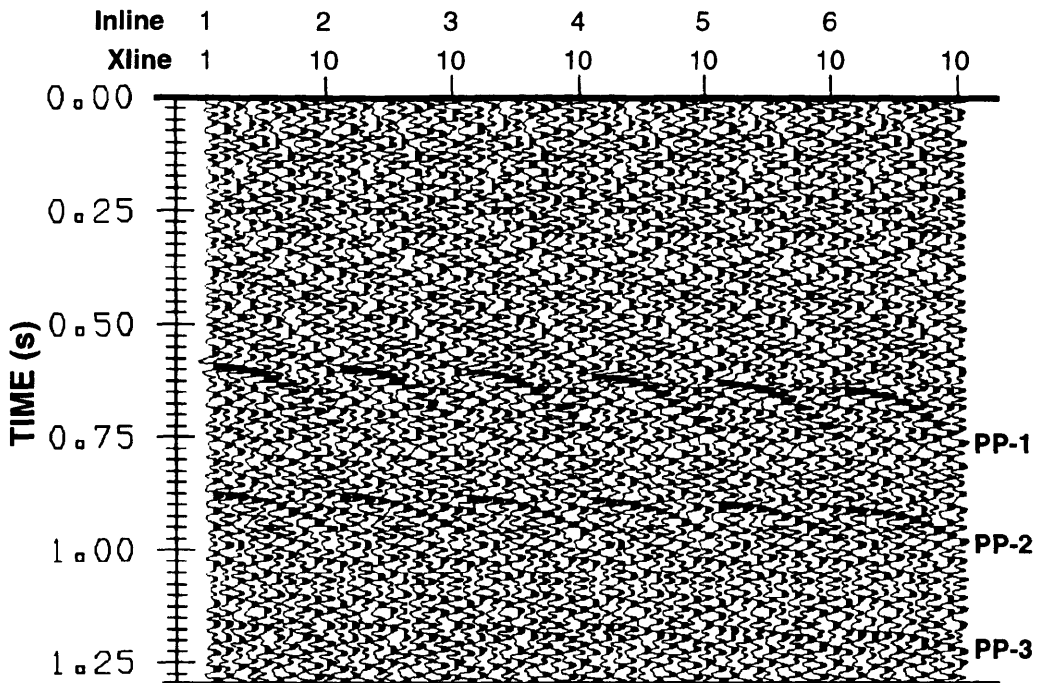


Fig. A.8a. 3-D shot record input showing the P - P arrivals with 15% of background noise added for the three flat layers in the depth model shown in Fig. A.6a.

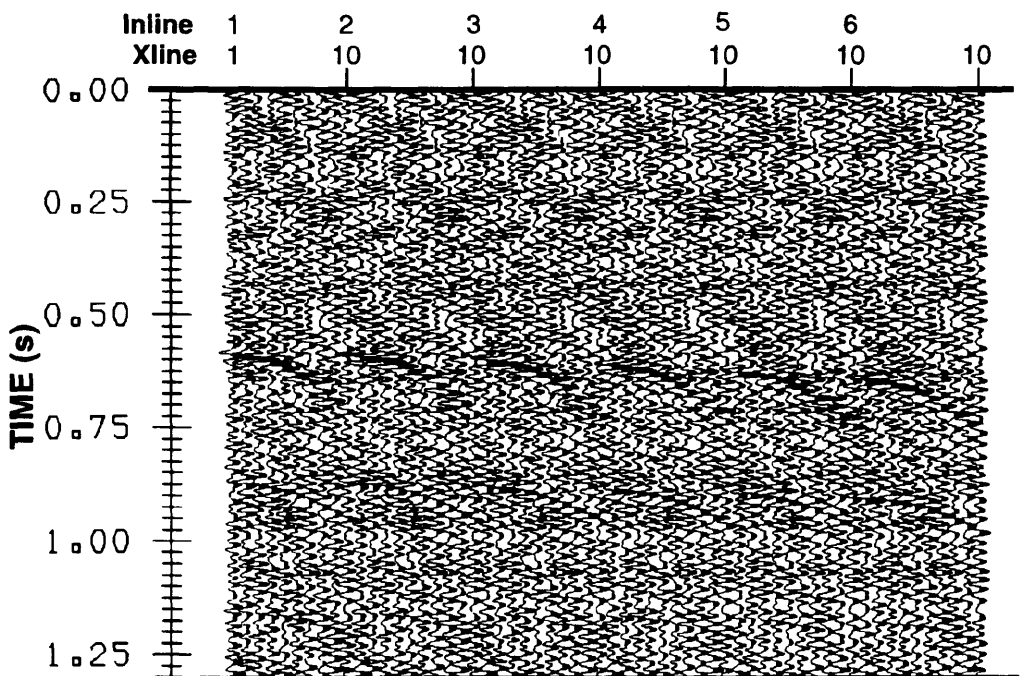


Fig. A.8b. Reconstruction of the 3-D shot record shown in Fig. A.8a after applying the 3-D τ - p transform in the presence of noise.

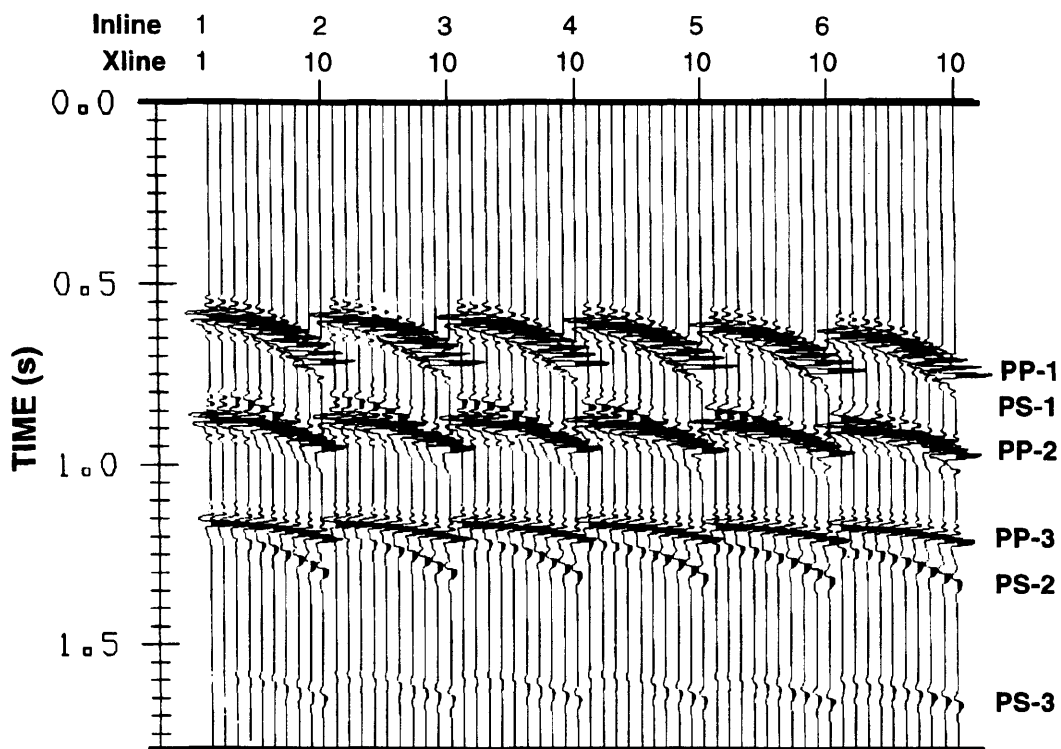


Fig. A.9a. 3-D shot record showing the P - P and P - SV arrivals (free-noise condition).

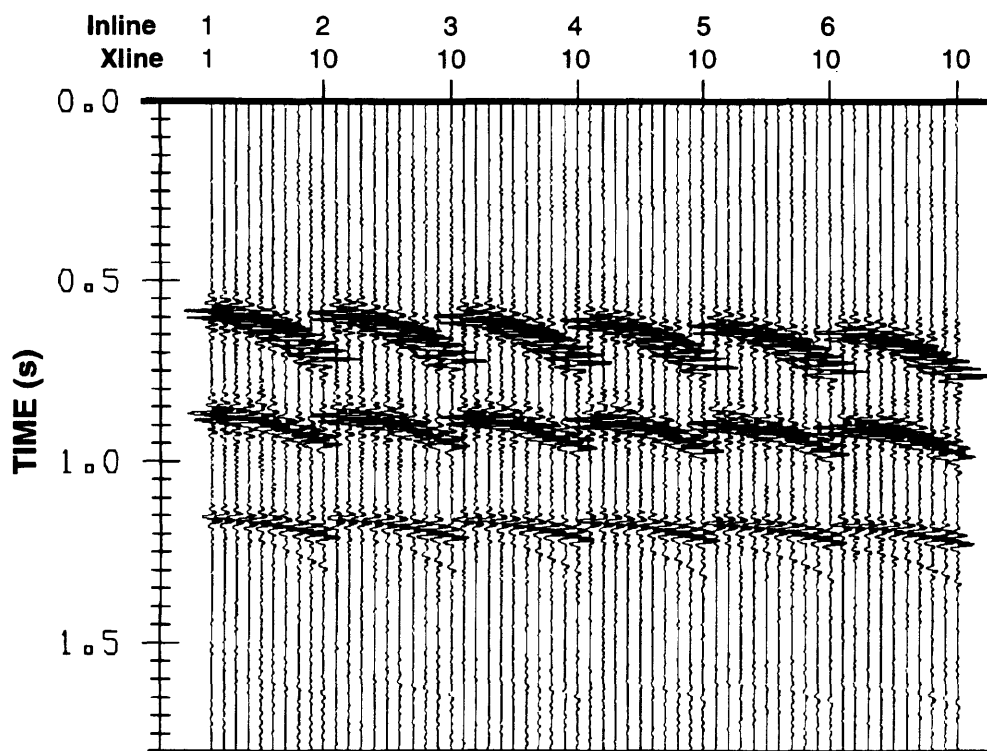


Fig. A.9b. Reconstructed 3-D shot record after applying the 3-D τ - p transform.

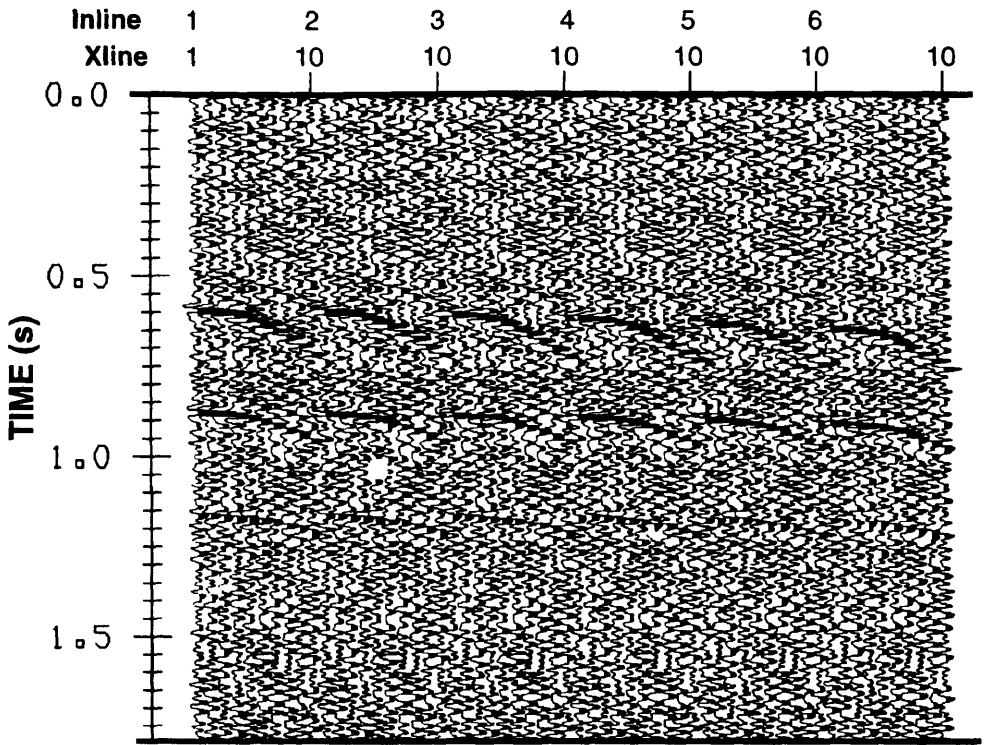


Fig. A.10a. 3-D shot record showing the P - P and P - SV arrivals with 15% of random noise added for the three layers in the depth model shown in Fig. A.6a.

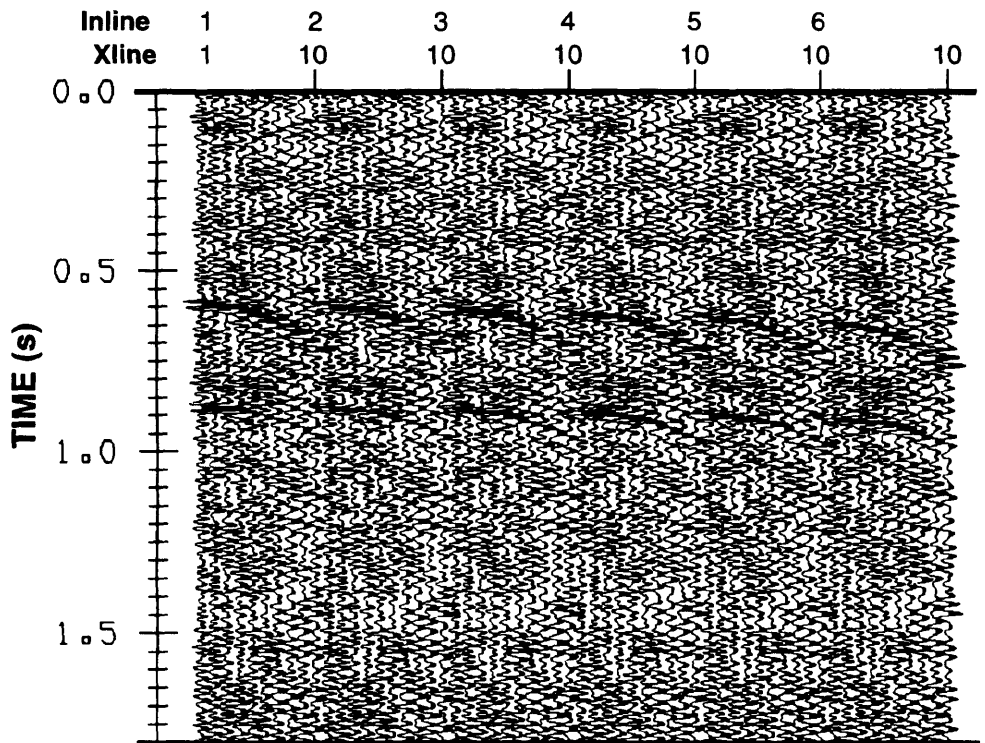


Fig. A.10b. Reconstructed 3-D shot record after applying 3-D τ - p transform in the presence of noise.

Experiment 5

In this experiment the algorithm was tested in removing linear noise (i.e. field ground-roll from a Venezuelan survey) which was added to the 3-D shot described in the experiment 1 (Fig. A.11a). It shows a dispersive ground-roll interfering with the principal reflections along inline direction. Mutes were applied in the f - p_x and f - p_y domains for rejecting the p range containing this noise. The mute selection was based on the observed apparent velocities for the ground-roll. The three reflections have been recovered with considerable attenuation of the ground-roll minimizing the ground-roll interference (Fig. A.11b). A similar result is obtained along crossline direction.

A.6 Discussion

Has been presented a 3-D τ - p transform which not requires to assume any geometric symmetry in the wavefield contained in the seismic data.

The 3-D τ - p transform (forward and inverse) works in the k - w domain by expressing the slant stack process as a four-fold sequence of Fourier transforms which convert the (x, y, t) data to (p_x, p_y, w) data. This is trade-off for the expense disk space required for performing the necessary Fourier transforms, but these are typically very fast.

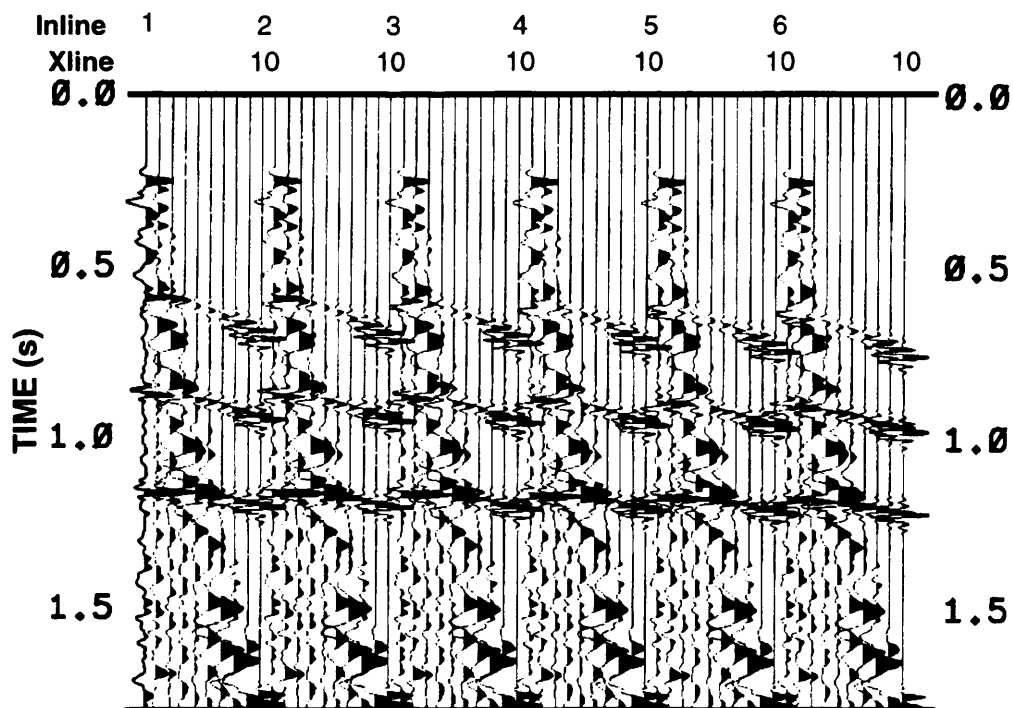


Fig. A.11a. 3-D shot record from the depth model shown in Fig. A.6a with ground roll noise added.

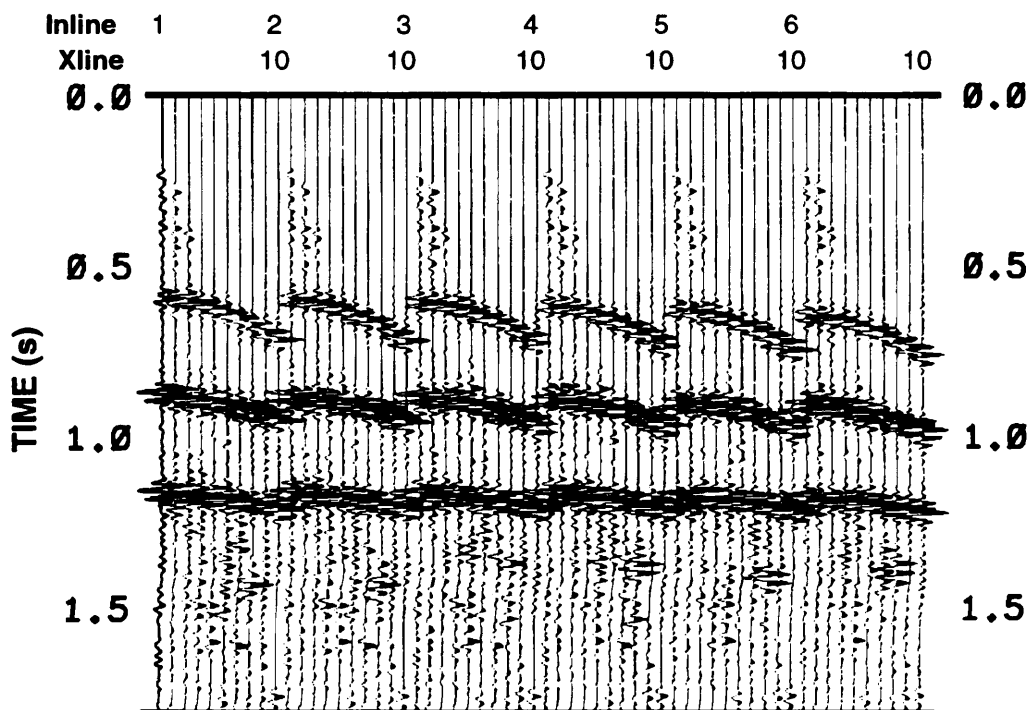


Fig. A.11b. Reconstructed 3-D shot record after applying 3-D τ - p transform under the presence of ground roll.

REFERENCES

- Ameely, L., Edelman, A.H.K., and Fertig, J., 1985, How do shear wave affect normal P-wave records?: *Geophys. Prosp.*, v. 33, p. 201-211.
- Behrens, J., and Waniek, L., 1972, Modellseismik, *J. Geophys.* 38, 1-44.
- Chapman, C.H., 1978, A new method for computing synthetic seismograms: *Geophys. J. Roy. Astr. Soc.*, v. 54, p. 481-518.
- Chapman, C.H., 1981, Generalized radon transforms and slant stacks: *Geophys. J. Roy. Astr. Soc.*, v. 66, p. 445-453.
- Cherry, J.T. Jr., 1962, The azimuthal and polar radiation patterns obtained from a horizontal stress applied at the surface of an elastic half space: *Bull. Seismological Soc. Am.*, v. 52, p. 27-36.
- Claerbout, J.F., 1978, Snell waves: Stanford Exploration Project Report, No 15, p. 57-72, Stanford University.
- Claerbout, J.F., 1985, Imaging of earth's interior: Black-well Scientific Publications.
- Dankbaar, J.W.M., 1985, Separation of P- and S-waves: *Gephys. Prosp.*, v. 33, p. 970-986.
- Diebold, J.B. and Stoffa, P.L., 1981, The travelttime equation, tau-p mapping and inversion common midpoint data: *Geophysics*, v. 46, p. 238-254.
- Evans, B., 1991, ET-a slant-stack transform of three dimensional data: *Expl. Geophys.*, v. 22, p. 135-142.
- Helbig, K. and Mesdag, C.S., 1982, The potential of shear-wave observations: *Geophys. Prosp.*, v. 30, p. 413-431.
- Kak, C. and Rosenfield, A., 1982, Digital picture processing - Volume 1: Academic Press, Inc.
- Love, A.E.H., 1944, A treatise on the mathematical theory of elasticity, 4th edition, Dover Publications, Inc., New York.
- Lu, L., 1991, Aplication of the local slant-stack to trace interpolation. In Gardner, G. H. F. and Lu, L. (Eds.): *Slant-Stack Processing*, Geophysical reprint series, No. 14, 302-303.

- Maroof, S. I. and Gravely, C. J., 1984, Aliasing and $t-p$: Presented at the 54th Annual SEG Meeting, Atlanta.
- McCowan, D.W. and Brysk, H., 1989, Cartesian and cylindrical slant stacks, Paul L. Stoffa (ed.), *Tau-p: A Plane Wave Approach to the Analysis of Seismic Data*, p. 1-33.
- Meissner, R. and Hegazy, M.A., 1981, The ratio of the PP- to the SS-reflection coefficient as a possible future method to estimate oil and gas reservoirs: *Geophys. Prosp.*, v. 29, p. 533-540.
- Miller, G.F., and Pursey, H., 1954, The field and radiation impedance of mechanical radiation on the free surface of a semi-infinite isotropic solid: *Proc. Roy. Soc. London, Ser. A*, v. 223, p. 521-541.
- Palmer, D., 1986, *Refraction Seismics: The lateral resolution of structure and seismic velocity*, Geophysical Press, London.
- Pan, N.D. and Gardner, G.H.F., 1984, Forward and inverse p-tau transformations using k-f transforms: *Seismic Acoustics Laboratory Semi-Annual Progress Review*, v. 14, p. 241-270.
- Phinney, R.A., Chowdhury, K.R., and Frazer, L.N., 1981, Transformation and analysis of record sections: *J. Geoph. Res.*, 86, pp. 359-377. Tatham, R.H., 1984, Multidimensional filtering of seismic data: *Proceedings of the IEEE*, 72, No. 10, Oct.
- Stoffa, P.L., Buhl, P., Diebold, J.B., and Wenzel, F., 1981, Direct mapping of seismic data to the domain of intercept time and rayparameter—a plane wave decomposition, *Geophysics*, v. 46, p. 25-267.
- Wade, J.C. and Gardner, G.H.F., 1988, Slant-stack inversion by hyperbolae extraction in the Fourier domain: 58th Ann. Internat. Mtg., Soc. Expl. Geophys., Expanded Abstracts, p. 676-679.
- Wade, J.C. and Lu, L., 1991, Some fundamentals of slant-stack methods: *Slant-stack processing, SEG (Appendix 1)*, p. 457-481.
- White, J.E., 1965, *Seismic waves radiation, transmission and attenuation*, McGraw-Hill, Inc., New York.
- Yilmaz, O., *Seismic data processing*, 1987: SEG.